

Fall 2013

Mass Spectrometric Studies on the Primary Products of Fast Pyrolysis of Carbohydrates and the Molecular Structures of Asphaltenes, and the Development of a Rastering Probe for Laser-Induced Acoustic Desorption into an Atmospheric Pressure Chemical Ionization Source

Matthew Robert Hurt
Purdue University

Follow this and additional works at: https://docs.lib.purdue.edu/open_access_dissertations

 Part of the [Analytical Chemistry Commons](#)

Recommended Citation

Hurt, Matthew Robert, "Mass Spectrometric Studies on the Primary Products of Fast Pyrolysis of Carbohydrates and the Molecular Structures of Asphaltenes, and the Development of a Rastering Probe for Laser-Induced Acoustic Desorption into an Atmospheric Pressure Chemical Ionization Source" (2013). *Open Access Dissertations*. 140.
https://docs.lib.purdue.edu/open_access_dissertations/140

This document has been made available through Purdue e-Pubs, a service of the Purdue University Libraries. Please contact epubs@purdue.edu for additional information.

PURDUE UNIVERSITY
GRADUATE SCHOOL
Thesis/Dissertation Acceptance

This is to certify that the thesis/dissertation prepared

By Matthew R. Hurt

Entitled **MASS SPECTROMETRIC STUDIES ON THE PRIMARY PRODUCTS OF FAST PYROLYSIS OF CARBOHYDRATES AND THE MOLECULAR STRUCTURES OF ASPHALTENES, AND THE DEVELOPMENT OF A RASTERING PROBE FOR LASER-INDUCED ACOUSTIC DESORPTION INTO AN ATMOSPHERIC PRESSURE CHEMICAL IONIZATION SOURCE**

For the degree of Doctor of Philosophy

Is approved by the final examining committee:

Hilkka Kenttämäa

Chair

Mahdi Abu-Omar

Mary Wirth

Yu Xia

To the best of my knowledge and as understood by the student in the *Research Integrity and Copyright Disclaimer (Graduate School Form 20)*, this thesis/dissertation adheres to the provisions of Purdue University's "Policy on Integrity in Research" and the use of copyrighted material.

Approved by Major Professor(s): Hilkka Kenttämäa

Approved by: R. E. Wild

Head of the Graduate Program

10/9/2013

Date

MASS SPECTROMETRIC STUDIES ON THE PRIMARY PRODUCTS OF FAST
PYROLYSIS OF CARBOHYDRATES AND THE MOLECULAR STRUCTURES OF
ASPHALTENES, AND THE DEVELOPMENT OF A RASTERING PROBE FOR
LASER-INDUCED ACOUSTIC DESORPTION INTO AN ATMOSPHERIC
PRESSURE CHEMICAL IONIZATION SOURCE

A Dissertation

Submitted to the Faculty

of

Purdue University

by

Matthew R. Hurt

In Partial Fulfillment of the

Requirements for the Degree

of

Doctor of Philosophy

December 2013

Purdue University

West Lafayette, Indiana

To my wife Deepali for all of her support and love

To my parents, John and Tammy, for the endless encouragement throughout the years

To my parents-in-law, Nikhil and Nimisha, who also have encouraged me since the first
day we met

ACKNOWLEDGMENTS

First, I would like to express my gratitude to my advisor, Professor Hilikka Kenttämäa, for her guidance during my graduate career, and for allowing me the freedom to pursue many of my own ideas in my research projects. Under her direction, I have gained advanced scientific knowledge and independent thinking skills that allow me to be a successful analytical chemistry scientist. Her passion, open-mindedness, and knowledge greatly helped push me to expand my potential and abilities as an independent scientist. I am very thankful for the opportunity to work with this research group and to be her student.

I owe many thanks to Dr. David Borton II who mentored me when I first started at Purdue and whom I worked extensively with for my first three years of graduate school. David taught me much that helped me get through my graduate career, namely, how to fix any of our instruments and how to analyze some of the nastiest and complex mixtures in the world, asphaltenes.

Numerous other members of the Kenttämäa group have contributed to my success as a scientist and a person, including Dr. Enada Archibold, Dr. Jennifer Reece, Dr. Ben Owen, Dr. Fanny Widjaja, Dr. George Pates, Sabir Aqueel, Padmaja Narra, Dr. Lucas Amundson, Dr. Jinshan Gao, Dr. Nelson Vinueza, Dr. Vanessa Gallardo, Tiffany Jarrell, Weijuan Tang, Huaming Sheng, Dr. Linan Yang, Chris Marcum, Peggy Williams, Priya

Murria, Alex Dow, Ashley Wittrig, and James Riedeman, along with other former and present group members.

I also need to thank Mr. Weldon Vaughn, Mr. Mark Carlsen, and the rest of the Amy Instrumentation Facility for their extensive help and support with the maintenance and development of instrumentation. If it was not for their help, much of my work would not have been possible or would still be ongoing for years to come. Their extensive expertise and willingness to help made working with them a great and fruitful experience. I must also thank Dr. Piotr Gawecki and John Degenstein who are both chemical engineers that I have had the opportunity to work with extensively throughout my graduate career. They have taught me much about how engineers think about problems, which has provided me new better ways to interpret and solve problems.

I would like to thank my family for the unlimited support they have provided me throughout my life. My wife, Deepali, has been an amazing source of help and comfort. Her tolerance, patience, and support of me for the last four years have been remarkable and the time has been full of her unrelenting love. I wish to thank my parents, John and Tammy Hurt, for their love and guidance that have transformed me into the man I am today, and for showing me that it is possible to do anything if I set my mind to it. My brother, Steve, is thanked for all the brotherly love he has shown me through the years. I am also grateful for my parents-in-law, Nikhil and Nimisha, who have treated me like their own son from day one. I would like to truly thank my advisor, coworkers, family, friends, and all of you. Without your support, I would not be here today.

TABLE OF CONTENTS

	Page
LIST OF TABLES	ix
LIST OF FIGURES	x
ABSTRACT	xx
LIST OF PUBLICATIONS	xxiii
CHAPTER 1: INTRODUCTION AND OVERVIEW	1
1.1 Introduction	1
1.2 Overview	3
1.3 References	5
CHAPTER 2: FOURIER-TRANSFORM ION CYCLOTRON RESONANCE AND LINEAR QUADRUPOLE ION TRAP MASS SPECTROMETRY: INSTRUMENTAL AND EXPERIMENTAL CONSIDERATIONS	7
2.1 Introduction	7
2.2 Ionization Methods	8
2.2.1 Atmospheric Pressure Chemical Ionization (APCI)	9
2.2.2 Electrospray Ionization (ESI)	10
2.3 Linear Quadrupole Ion Trap (LQIT) Mass Spectrometry	11
2.3.1 Instrument Overview	12
2.3.2 Ion Motion	15
2.3.2.1 Radial Motion	15
2.3.2.2 Axial Motion	18
2.3.3 Ion Ejection and Detection	20
2.3.4 Tandem Mass Spectrometry in LQIT	23
2.3.4.1 Ion Isolation	23
2.3.4.2 Collision-Activated Dissociation (CAD)	25
2.4 Liquid Chromatography-Mass Spectrometry (LC-MS)	26

2.5	Fourier Transform Ion Cyclotron Resonance (FT-ICR) Mass Spectrometry ..	27
2.5.1	Instrumentation Overview	27
2.5.2	Ion Motion	30
2.5.2.1	Cyclotron Motion.....	30
2.5.2.2	Trapping Motion.....	32
2.5.2.3	Magnetron Motion	32
2.5.3	Ion Excitation for Detection and Ejection	35
2.6	Laser Induced Acoustic Desorption (LIAD).....	39
2.6.1	Generation of Acoustic Waves	39
2.6.2	Metal Substrate	42
2.6.3	Sample Preparation	44
2.6.4	LIAD Probes	45
2.6.4.1	Fiber LIAD Probe	45
2.6.4.2	Fiberless LIAD Probe	46
2.7	References.....	48
CHAPTER 3: ON-LINE MASS SPECTROMETRIC METHODS FOR THE DETERMINATION OF THE PRIMARY PRODUCTS OF FAST PYROLYSIS OF CARBOHYDRATES AND FOR THEIR GAS-PHASE MANIPULATION.....		55
3.1	Introduction.....	55
3.2	Experimental.....	57
3.3	Results and Discussion	61
3.4	Conclusions.....	71
3.5	References.....	74
CHAPTER 4: COMPARISON OF MOLECULES' STRUCTURES IN COAL AND PETROLEUM ASPHALTENES BY USING MASS SPECTROMETRY.....		78
4.1	Introduction.....	78
4.2	Experimental.....	80
4.3	Results and Discussion	81
4.4	Conclusions.....	94
4.5	References.....	97

CHAPTER 5: COMPARISON OF THE STRUCTURES OF MOLECULES IN PETROLEUM ASPHALTENES BEFORE AND AFTER MILD AND HARSH HYDROCRACKING	101
5.1 Introduction.....	101
5.2 Experimental.....	103
5.3 Results and Discussions.....	105
5.4 Conclusions.....	113
5.5 References.....	115
CHAPTER 6: A MASS SPECTROMETRIC STUDY COMPARING THE MOLECULAR STRUCTURE OF FIELD DEPOSIT ASPHALTENES AND HEPTANE PRECIPITATED ASPHALTENES	118
6.1 Introduction.....	118
6.2 Experimental.....	119
6.3 Results and Discussions.....	120
6.4 Conclusions.....	128
6.5 References.....	129
CHAPTER 7: EXAMINATION OF SOLVENT/REAGENT EFFECTS ON ATMOSPHERIC PRESSURE CHEMICAL IONIZATION OF ASPHALTENES IN A SEARCH FOR A REPLACEMENT FOR CARBON DISULFIDE	132
7.1 Introduction.....	132
7.2 Experimental.....	135
7.3 Results and Discussions.....	136
7.4 Conclusions.....	148
7.5 References.....	149
CHAPTER 8: DEVELOPMENT OF A HIGH-THROUGHPUT LASER-INDUCED ACOUSTIC DESORPTION PROBE WITH RASTER SAMPLING COUPLED TO ATMOSPHERIC PRESSURE CHEMICAL IONIZATION	154
8.1 Introduction.....	154
8.2 Experimental.....	156
8.3 Novel High Throughput LIAD probe	157
8.3.1 New LIAD Probe Performance.....	159
8.4 Novel High-Throughput LIAD Raster Assembly.....	161
8.4.1 Performance	164
8.5 Conclusions.....	167
8.6 References.....	168

CHAPTER 9: DESIGN AND DEVELOPMENT OF A DRYING GAS CHAMBER FOR PREPARING LIAD FOILS	171
9.1 Introduction	171
9.2 Design and Construction of the Drying Gas Chamber.....	172
9.3 Conclusions	179
9.4 References	180
VITA.....	182

LIST OF TABLES

Table	Page
2.1 Important properties of the metal foils that have been evaluated as substrates for LIAD	43
3.1 Approximated average relative molar abundances of the primary products of fast pyrolysis of cellobiose normalized to the most abundant product (with standard deviations based on three experiments)	68
4.1 Molecular weight distributions (MWD) and average molecular weights (AVG MW) determined for molecules in coal and petroleum asphaltenes, as well as the estimated minimum total number of carbon atoms in all side chains, estimated core sizes, and relative abundances of the ions produced by neutral hydrogen sulfide loss, given for ions with selected m/z values. The differences between the petroleum and coal samples (petroleum – coal) are given in the last column.....	91
5.1 A list of the asphaltenes samples examined.....	105
6.1 Molecular weight distributions (MWD) and average molecular weights (AVG MW) determined for molecules in FDAs and HPAs, as well as the estimated minimum total number of carbon atoms in all side chains and relative abundances of the ions produced by neutral hydrogen sulfide loss, given for ions with selected m/z values. The differences between the FDAs and HPAs (FDAs – HPAs) are given in the last column.....	125

LIST OF FIGURES

Figure	Page
2.1 Diagram depicting the ESI process (positive mode). The zoom on the spray shows how gas-phase ions are formed from a droplet explosion due to Columbic forces.....	11
2.2 Schematic of the Thermo Scientific LTQ mass spectrometer (top view) with typical operating pressures. Ions were introduced from the atmospheric pressure ionization (API) source into the heated transfer capillary.....	13
2.3 The linear quadrupole ion trap mass analyzer of the Thermo Scientific LTQ instrument (reproduced from Reference 2).....	14
2.4 Most well defined region of the Mathieu stability diagram. Ions with a_u and q_u that fall within the region with the dotted lines will have stable trajectories inside of a quadrupole ion trap.....	17
2.5 Potential diagrams depicting DC voltages applied to the front lens, back lens and three sections of the LQIT during (a) ion injection, (b) ion trapping, and (c) mass analysis. The (b) to (c) transition involves the increase of DC potentials on the front and back sections of the trap. This is done to better center the ions for ion ejection.....	19
2.6 Illustrations of different forms of ion ejection in LQIT. (a) Ions trapped in the LQIT. (b) Ion ejected at the stability limit by using the mass selective axial instability scan and the resulting mass spectrum measured in a traditional LQIT. (c) Ion ejected via resonance ejection by using the mass selective axial instability scan and the resulting mass spectrum measured by a LQIT. By ejecting ions at a lower q value, the resolution and mass range of the trap are increased.....	21
2.7 Illustration of radial ejection and detection of ions in a Thermo Scientific LTQ.....	22

Figure	Page
2.8	Illustration of ion isolation and activation in the LQIT. (a) Ions trapped in the LQIT. (b) The q value of the ion of interest (orange) is set to 0.83, resulting in lower mass ions to become unstable and get ejected from the trap. (c) An isolation waveform is applied to eject the remaining unwanted ions. (d) The q value of the desired ion is set to 0.25 in order to induce efficient fragmentation upon collision-activated dissociation while maintaining high trapping efficiency for low mass fragment ions (purple)24
2.9	Schematic of the Thermo Scientific LTQ-FT-ICR mass spectrometer28
2.10	Diagram of the cylindrical cell present in the FT-ICR of a Thermo Scientific LTQ-FT-ICR29
2.11	Frontal view of the center segments of a cylindrical ICR cell, showing how it is sectioned into four plates29
2.12	Illustration of the cyclotron motion of a positive ion in a magnetic field. The balance of the Lorentz force and centrifugal force acts to bend the ion motion into a circle perpendicular to the magnetic field in the x-y plane31
2.13	Diagram of three main motions of an ion within an ICR cell. The cyclotron orbit of the ion (green) confines it in the x and y directions as a result of the Lorentz and centrifugal forces. The trapping motion causes this orbit to oscillate back and forth (blue) in the z direction. Both motions are part of the ion motion on the larger magnetron orbit (red) as a result of the combination of the magnetic and electric fields. Note that the magnetron motion is greatly exaggerated in this figure for visual clarity34
2.14	Diagram illustrating ion excitation and detection in the ICR cell. (a) Ions are trapped in the ICR cell and have random direction and too small of cyclotron radii to be detected. (b) Application of a broadband frequency sweep to the excitation plates excites ions to larger cyclotron orbits and makes ions of same m/z -values to move coherently as packets. (c) The ions pass by the detection plates and induce an image current that is recorded as a time domain transient. The time domain transient is then converted to a frequency spectrum by Fourier transformation, which in turn is converted to a mass spectrum38
2.15	Diagram of the LIAD process41

Figure	Page
2.16	Front and back sides of a titanium foil with asphaltenes deposited onto it after it was used in a LIAD experiment. The circle on the back of the titanium foil indicates where the laser beam hit the foil and caused desorption to occur on the front of the foil where bare foil can be seen.....42
2.17	Illustration of two LIAD sample deposition methods, (a) dried-drop method and (b) electrospray deposition method.....45
2.18	Schematic for the inner mirror assembly inside the tip of the fiberless LIAD probe.....47
2.19	Illustration of the setup for coupling fiberless LIAD with a Thermo Scientific LTQ47
3.1	A cut away diagram of the ionization chamber in front of the LQIT. The pyroprobe (in blue) is shown in both the direct pyrolysis (left) orientation and within the flow tube (right). The direction of gas flow is indicated by the dashed arrow60
3.2	An APCI/ammonium hydroxide positive ion mass spectrum of an equimolar mixture of six model compounds introduced via direct injection (the molar ratio of glycolaldehyde is estimated to be between 0-2 due to the unknown extent of glycolaldehyde dimer breakdown). All model compounds were ionized but not equally efficiently63
3.3	An APCI/chloroform negative ion mass spectrum of an equimolar mixture of six model compounds introduced via the heated pyroprobe (the molar ratio of glycolaldehyde is estimated to be between 0-2 due to the unknown extent of glycolaldehyde dimer breakdown). Three model compounds were not ionized.....64

Figure	Page
3.4	Mass spectra of the primary products of fast pyrolysis of cellobiose ($C_{12}H_{22}O_{11}$) ionized using ammonium attachment in positive ion mode (top) and chloride attachment in negative ion mode (bottom). All elemental compositions were determined using high resolution data collected in a LQIT/FT-ICR. Ionized levoglucosan has m/z values of 163 and 180 in the top spectrum and m/z values of 161 and 197 in the bottom spectrum. All ions with m/z values lower than 170 correspond to protonated molecules in the top spectrum and deprotonated molecules in the bottom spectrum, and hence have m/z values that differ by two units. Protonated $C_4H_4O_2$ molecule (m/z 85) is only seen in the top spectrum, while deprotonated $C_5H_6O_3$ molecule (m/z 113) is only seen in the bottom spectrum. Otherwise, the spectra show the same ionized molecules. The most abundant product's ($C_8H_{14}O_7$) proposed structure is shown in the top spectrum.....66
3.5	Mass spectra collected after the primary products of fast pyrolysis of cellobiose were allowed to undergo reactions for 2 s at 300 °C (top), 2s at 400 °C (middle) and 11 s at 400 °C (bottom) and ionized using ammonium attachment in positive ion mode. All elemental compositions were determined using high resolution data collected in an LQIT/FT-ICR. All ions with m/z values lower than 170 correspond to protonated molecules70
3.6	CAD mass spectra measured for authentic cellotriosan ionized via chloride attachment in negative ion mode and the unknown trimer (ionized in the same manner) formed upon pyrolysis of cellobiose in the flow tube. The chloride attached cellotriosan and trimer (m/z 521) were isolated and subjected to CAD which resulted in HCl loss, forming fragment ions of m/z 485, corresponding to the deprotonated molecules of cellotriosan and the unknown trimer. These deprotonated molecules were subjected to CAD to obtain the mass spectra shown top left and bottom left, respectively. Both ions produced an abundant fragment ion corresponding to the loss of a molecule with MW 162 Da to yield an ion of m/z 323. The fragment ions of m/z 323 were isolated and subjected to CAD to produce the mass spectra shown top right and bottom right, respectively71

Figure	Page
4.1 CAD mass spectrum measured for 1-butyl-3-propylnaphthalene molecular ion of m/z 226 generated by APCI/ CS_2 . An approximation of the minimum total number of carbons in all alkyl chains and the core size is obtained from the smallest fragment ion of m/z 141 (resulting from the loss of propene from the ion of m/z 183 formed by the loss of a propyl radical from the molecular ion), revealing the presence of at least six carbon atoms in all alkyl chains and two fused rings in the core (with an attached methylene group).....	83
4.2 APCI/ CS_2 mass spectra of coal asphaltenes (top) and petroleum asphaltenes (bottom).....	84
4.3 The top two mass spectra show the isolation of ions of m/z 515 from petroleum asphaltenes by using a 2 Da (top) and a 0.3 Da (bottom) isolation window. The bottom two mass spectra show CAD products measured in the LQIT for the isolated ions using a 2 Da (top) and a 0.3 Da (bottom) isolation window.....	86
4.4 CAD mass spectra measured for ions of m/z 677 ± 1 derived from coal asphaltenes (top) and petroleum asphaltenes (bottom). The total number of carbons in the side chains and likely core sizes were estimated as described in text.....	87
4.5 A high-resolution CAD mass spectrum measured for ions of m/z 606.20 ± 0.15 derived from petroleum asphaltenes.....	87
4.6 CAD mass spectra of ions of m/z 418 ± 1 derived from coal asphaltenes (top) and ions of m/z 704 ± 1 derived from petroleum asphaltenes (bottom) with a zoom window on the fragment ions formed upon loss of hydrogen sulfide, with their relative abundance compared to the most abundant fragment ion.....	90
4.7 Graph illustrating the differences (petroleum – coal) between the coal asphaltenes and the petroleum asphaltenes as a function of their molecular size: relative abundances of ions produced from hydrogen sulfide loss, the estimated minimum total number of carbons in all side chains, and the approximate core size.....	94
5.1 Example structures of an island-type asphaltene molecule (left) and an archipelago-type molecule (right).....	102

Figure	Page	
5.2	Mass spectra showing the MWD for the six samples in the first set of samples. The red dashed line indicates the center of the MWD (the most abundant compounds in the distribution). Comparing the mass spectra of the untreated samples (<u>1U1</u> and <u>1U2</u>) to those that were hydrocracked under different intensities (<u>1M1</u> = <u>1M2</u> < <u>1H1</u> = <u>1H2</u>) the center of the MWD shifts from 750 Da for <u>1U1</u> and <u>1U2</u> to 650 Da for <u>1M1</u> and <u>1M2</u> and to 550 Da for <u>1H1</u> and <u>1H2</u> . The m/z values of ions with elevated relative abundances that are marked with a star are due to polyethylene glycol contamination.....	107
5.3	Mass spectra showing the MWD for four samples in the second set of samples. The red dashed line indicates the center of each MWD. Comparing the mass spectra measured for the hydrocracked feedstocks (<u>2M1</u> and <u>2M2</u>) to those of the corresponding untreated feedstocks (<u>2U1</u> and <u>2U2</u>) shows that hydrocracking shifts the centers of the MWDs to lower mass values, the same trend that was observed for the first set of samples.....	108
5.4	CAD mass spectra of ions of m/z 704 isolated from ionized asphaltene samples <u>1U1</u> , <u>1M1</u> , and <u>1H1</u> . Comparing the mass spectra of the untreated sample (<u>1U1</u>) to those that were hydrocracked under different intensities (<u>1M1</u> < <u>1H1</u>), the number of alkyl carbons that brake off of the core is reduced and the relative abundance of the ions produced by hydrogen sulfide loss is reduced for hydrocracked samples.....	110
5.5	CAD mass spectra of ions of m/z 704 isolated from ionized asphaltene samples <u>1U2</u> , <u>1M2</u> , and <u>1H2</u> . Comparing the mass spectra of the untreated sample (<u>1U2</u>) to those that were hydrocracked under different intensities (<u>1M2</u> < <u>1H2</u>) the number of alkyl carbons that brake off of the core is reduced and the relative abundance of the ions produced by hydrogen sulfide loss is reduced for hydrocracked samples.....	111
5.6	CAD mass spectra of ions of m/z 704 isolated from ionized asphaltene samples <u>2U1</u> and <u>2M1</u> . Comparing the mass spectrum measured for the hydrocracked feedstock (<u>2M1</u>) to the mass spectrum of the corresponding untreated feedstocks (<u>2U1</u>) the number of alkyl carbons that brake off of the core is reduced and the relative abundance of the ions produced by hydrogen sulfide loss is reduced.....	112

Figure	Page	
5.7	CAD mass spectra of ions of m/z 704 isolated from ionized asphaltene samples <u>2U2</u> and <u>2M2</u> . Comparing the mass spectrum measured for the hydrocracked feedstock (<u>2M2</u>) to the mass spectrum of the corresponding untreated feedstocks (<u>2U2</u>) the number of alkyl carbons that brake off of the core is reduced and the relative abundance of the ions produced by hydrogen sulfide loss is reduced.....	112
5.8	CAD mass spectra of ions of m/z 460 isolated from ionized asphaltene samples <u>2U2</u> and <u>2M2</u> . Comparing the mass spectrum measured for the hydrocracked feedstock (<u>2M2</u>) to the mass spectrum of the corresponding untreated feedstocks (<u>2U2</u>) the number of alkyl carbons that brake off of the core is reduced and the relative abundance of the ions produced by hydrogen sulfide loss is reduced.....	113
6.1	APCI/CS ₂ mass spectra of HPAs (top) and FDAs (bottom).....	122
6.2	CAD mass spectra measured for ions of m/z 422 ± 1 derived from HPAs (top) and FDAs (bottom). The total number of carbons in the side chains and the relative abundance of the fragment ion produced due to the loss of hydrogen sulfide are labeled in the mass spectra.....	124
6.3	Graph illustrating the differences (FDAs – HPAs) between the FDAs and the HPAs as a function of their molecular size: relative abundances of ions produced from hydrogen sulfide loss and the estimated minimum total number of carbons in all side chains.....	127
7.1	High resolution mass spectrum of an isolated asphaltene ion cluster of m/z ranging from 528.0 up to 528.5 Da. Nine peaks have greater than twenty five percent relative abundance, indicated by the red dashed line, illustrating the extreme complexity of asphaltenes.....	134
7.2	Structures and masses of the model compounds that were studied	136
7.3	Mass spectrum of compound <u>A</u> when carbon disulfide is the solvent/ionization reagent for APCI. Stable molecular ion is the only type of ion produced (the additional peaks at m/z 539.5 and 540.5 are due to C ¹³ isotopes).....	137
7.4	Mass spectrum of compound <u>A</u> when chloroform was the solvent/ionization reagent during APCI. Stable molecular ion along with many adduct ions formed from chloroform were detected (indicated with blue arrows)	138

Figure	Page
7.5	Mass spectrum of compound <u>A</u> when dichloromethane was used as the solvent/ionization reagent during APCI. Stable molecular ion, protonated molecule, and many additional adduct ions formed from dichloromethane during APCI (indicated with blue arrows) were formed138
7.6	Mass spectrum of compound <u>A</u> when toluene was used as the solvent/ionization reagent during APCI. Stable molecular ion, protonated molecule, and two additional adduct ions (indicated by blue arrows) were formed139
7.7	Mass spectrum of compound <u>A</u> when tetrahydrofuran was used as the solvent/ionization reagent during APCI. Stable protonated molecule is the only type of ion produced (the additional peak at m/z 540.4 is due to C^{13} isotopes)139
7.8	CAD mass spectra of three adduct ions formed upon APCI of <u>A</u> when chloroform was the solvent/ionization reagent141
7.9	CAD mass spectra of two adduct ions formed upon APCI of <u>A</u> when DCM was the solvent/ionization reagent141
7.10	CAD mass spectra of two adduct ions formed upon APCI of <u>A</u> when toluene was the solvent/ionization reagent142
7.11	CAD mass spectra of the protonated molecules (left) and the molecular ions (right) formed upon APCI of <u>A</u> when toluene was the solvent/ionization reagent143
7.12	Mass spectra of the asphaltene sample dissolved in carbon disulfide (top), chloroform (middle left), dichloromethane (middle right), tetrahydrofuran (bottom left), and toluene (bottom right)144
7.13	CAD mass spectrum collected for ions of m/z values of 600 ± 1 when chloroform was used as the solvent (red) overlaid with the CAD mass spectrum collected for the same ions when CS_2 was used as the solvent (black). Two new fragment ion clusters are observed in the CAD mass spectrum with chloroform as the solvent. These new fragment ions are due to adducts145

Figure	Page
7.14 CAD mass spectrum collected for ions of m/z values of 600 ± 1 when DCM was used as the solvent (red) overlaid with the CAD mass spectrum collected for the same ions when CS_2 was used as the solvent (black). Two new fragment ion clusters are observed in the CAD spectrum with DCM as the solvent. These new fragment ions are due to adducts	145
7.15 CAD mass spectrum collected for ions of m/z 600 ± 1 when toluene was used as the solvent (red) overlaid with the CAD mass spectrum collected for the same ions when CS_2 was used as the solvent (black). Two new fragment ion clusters are observed in the CAD spectrum with toluene as the solvent. These new fragment ions are due to adducts.....	146
7.16 CAD mass spectrum collected for ions of m/z 600 ± 1 when THF was used as the solvent (red) overlaid with the CAD mass spectrum collected for the same ions when CS_2 was used as the solvent (black). No new fragment ion clusters are observed in the CAD spectrum with THF as the solvent.....	146
8.1 Depiction of the novel high-throughput LIAD probe. The lens holders that are threaded into the spacer tubes are not shown in this diagram (reproduced from Reference 23).....	158
8.2 Image of the novel high-throughput LIAD probe. The probe is held by the raster assembly on the left and a custom holder on the right. The new probe can easily be removed to change sample without disturbing any of the kinematic mirrors shown on the right side of the image (picture reproduced from Reference 23)	159
8.3 Mass spectrum of Khafji asphaltenes measured using high vacuum LIAD/EI (70 eV) in a 3T FT-ICR (top) and a mass spectrum of the same asphaltene sample ionized via LIAD/APCI using nitrogen as the chemical ionization reagent in a LQIT. The MWDs measured using both methods are in good agreement with one another (reproduced from Reference 23)	161
8.4 CAD drawing of the rastering assembly (left) and a photo of the Thermo Scientific LQIT ionization chamber with the front access door open (right). The rastering assembly replaces the front door while using the original hardware for attachment (reproduced from Reference 23)	163
8.5 Images of the raster LIAD assembly (reproduced from Reference 23).....	163
8.6 Image comparing a foil used in the raster LIAD assembly to a foil used in the conventional LIAD probe (reproduced from Reference 23).....	164

Figure	Page
8.7	Total ion current as a function of time for a raster LIAD experiment (top). The mass spectrum, on bottom, was produced by averaging all of the ~922 mass spectra collected between t = 0.50 min to t = 3.75 min and subtracting the background (t = 0 min to t = 0.50 min). The desorbed octaethyl porphyrin molecules (MW = 600 Da) were ionized using APCI with carbon disulfide as the chemical ionization reagent (reproduced from Reference 23).....166
9.1	The parts of the LIAD foil sample preparation chamber. Each part is labeled for easy referencing in the description of the chamber above. <u>A</u> is the base and contains the primary cavity, <u>B</u> the foil holder, <u>C1/C2</u> are the forming mandrels, and <u>D</u> is the lid. <u>C1</u> and <u>C2</u> are interchangeable mandrels with <u>C1</u> allowing only one analyte to be deposited on the foil surface and <u>C2</u> allowing two analytes to be deposited on the foil surface (reproduced from Reference 10).....175
9.2	Computer aided design of the components of the LIAD foil drying gas chamber, dimensions given in inches (reproduced from Reference 10).....176
9.3	Comparison of a LIAD foil with asphaltenes deposited on it by using the dry drop method (left) and a LIAD foil with asphaltenes deposited on it by using the drying gas chamber (right). A visual comparison of the two samples indicates that the sample is deposited much more uniformly using the drying gas chamber (reproduced from Reference 10)177
9.4	The total ion chromatogram generated upon LIAD rastering a foil prepared using the dry drop method (top) compared to a total ion chromatogram generated upon LIAD rastering a foil prepared using the drying gas chamber (bottom). The laser began firing at 0.5 minutes for both experiments; the sporadic signal is a result of variations in the sample layer uniformity. The signal in the bottom chromatogram is more consistent than in the top chromatogram, indicating that a much more uniform layer of analyte was deposited onto the foil when using the drying gas chamber (reproduced from Reference 10).....178
9.5	A LIAD foil prepared using forming mandrels <u>C2</u> in the drying gas chamber. Brilliant green was deposited on the left side of the foil and octaethyl porphyrin was deposited on the right side (reproduced from Reference 10).....179

ABSTRACT

Hurt, Matthew R. Ph. D., Purdue University, December 2013. Mass Spectrometric Studies on the Primary Products of Fast Pyrolysis of Carbohydrates and the Molecular Structures of Asphaltenes, and the Development of a Rastering Probe for Laser-Induced Acoustic Desorption into an Atmospheric Pressure Chemical Ionization Source. Major Professor: Hilkka I. Kenttämäa.

Mass spectrometry (MS) has proven invaluable in the field of mixture analysis and structural elucidation. Tandem mass spectrometry (MS/MS) utilizing collision-activated dissociation (CAD) has become the technique of choice for structural elucidation of unknown analytes in mixtures. When coupled with gas chromatography (GC) or high performance liquid chromatography (HPLC), it allows for trace level analysis of mixture components. In spite of the utility of mass spectrometry in complex mixture analysis, it does have limitations. Traditional GC/MS methods used for the analysis of fast pyrolysis products cannot be used to analyze the primary products, thus limiting the knowledge that can be obtained regarding the true mechanisms of fast pyrolysis, ultimately restricting the level of control over what final products are formed. Analysis of mixtures of hydrocarbons, such as crude oil, is also still a problematic area for mass spectrometry due to the lack of suitable evaporation/ionization methods for the heavier components. Consequently, very little is known about the structures of molecules in asphaltenes, the heaviest fraction of crude oil and one of the most complex mixtures in

nature. Elucidating the structures of the compounds present in these mixtures is important for the rational design of methods to prevent the problems the cause.

Experiments described in this thesis employed tandem mass spectrometry to achieve a better understanding of the primary products of fast pyrolysis of carbohydrates and structures of molecules in asphaltenes. Chapter 2 briefly describes the instrumentation used for the research presented in this dissertation. Chapter 3 discusses the development of on-line mass spectrometric methods for the determination of the primary products of fast pyrolysis of carbohydrates and their gas- phase reactivity, demonstrating that there are many primary products that cannot be analyzed using traditional methods. Chapter 4 examines the differences in the molecular structures of petroleum and coal asphaltenes. Chapter 5 focuses on changes to asphaltenes' molecular structures when they are subjected to the hydrocracking process, a common practice in crude oil refinement. Chapter 6 compares field deposit asphaltenes, removed from a pipeline, to heptane precipitated asphaltenes from crude oil in a laboratory. Chapter 7 contrasts the effects of using different solvents in atmospheric pressure chemical ionization (APCI) of asphaltenes.

Chapters 8 and 9 focus on advances for laser-induced acoustic desorption (LIAD). Chapter 8 discusses improvements LIAD/APCI, including the development of a high-power laser probe for more reproducible evaporation of high-mass compounds into the gas phase, and the development of a rastering assembly that greatly increases the surface area of the LIAD foil that can be sampled. Chapter 9 discusses a novel chamber for preparing sample foils for LIAD by using a drying gas to prepare foils. The new

chamber that helps in the production of foils with a more uniform sample layer than previously possible for nonpolar analytes to improve the reproducibility of LIAD.

LIST OF PUBLICATIONS

LIST OF PUBLICATIONS

1. Borton, D.; Pinkston, D.; Hurt, M.; Tan, X.; Azyat, K.; Scherer, A.; Tykwinski, R.; Gray, M.; Qian, K.; Kenttämäa, H. “Molecular Structures of Asphaltenes Based on the Dissociation Reactions of Their Ions in Mass Spectrometry.” *Energy Fuels*, **2010**, *24*, 5548-5559.
2. Gao, J.; Borton, D.; Owen, B.; Jin, Z.; Hurt, M.; Amundson, L.; Madden, J.; Qian, K.; Kenttämäa, H. “Laser-Induced Acoustic Desorption/Atmospheric Pressure Chemical Ionization Mass Spectrometry.” *J. Am. Soc. Mass Spectrom.*, **2011**, *22*, 531-538.
3. Loegel, T.; Danielson, N.; Borton, D.; Hurt, M.; Kenttämäa, H. “Separation of Asphaltenes by Reversed-Phase Liquid Chromatography with Fraction Characterization.” *Energy Fuels*, **2012**, *26*, 2850-2857.
4. Borton, D.; Amundson, L.; Hurt, M.; Dow, A.; Madden, J.; Simpson, G.; Kenttämäa, H. “Development of a High-Throughput Laser-Induced Acoustic Desorption Probe and Raster Sampling for Laser-Induced Acoustic Desorption/Atmospheric Pressure Chemical Ionization.” *Anal. Chem.*, **2013**, *85*, 5720-5726.
5. Hurt, M.; Borton, D.; Choi, H.; Kenttämäa, H. “Comparison of the Structures of Molecules in Coal and Petroleum Asphaltenes by Using Mass Spectrometry.” *Energy Fuels*, **2013**, *27*, 3653-3658.

Molecular Structures of Asphaltenes Based on the Dissociation Reactions of Their Ions in Mass Spectrometry

David Borton II,[†] David S. Pinkston,[†] Matthew R. Hurt,[†] Xiaoji Tan,[‡] Khalid Azyat,[‡] Alexander Scherer,[‡] Rik Tykwinski,[‡] Murray Gray,[§] Kuangnan Qian,^{||} and Hilka I. Kenttämaa*[†][†]Department of Chemistry, Purdue University, 560 Oval Drive, West Lafayette, Indiana 47906, [‡]Department of Chemistry, and [§]Department of Chemical and Materials Engineering, University of Alberta, Edmonton, Alberta T6G 2G6, Canada, and ^{||}ExxonMobil Research and Engineering Company, 1545 Route 22 East, Annandale, New Jersey 08801

Received June 23, 2010. Revised Manuscript Received August 9, 2010

We report here an examination of the mass spectrometric fragmentation behavior of molecular ions generated (and excited) by electron ionization (EI) from several asphaltene model compounds simulating both the island and archipelago structural models. This behavior is compared to that of protonated molecules generated from the same compounds by atmospheric pressure chemical ionization (APCI) and excited by collision-activated dissociation (CAD). The fragmentation behavior of the protonated molecules and molecular ions is surprisingly similar. Both types of ions yielded distinct fragmentation patterns for both types of model compounds. Ions derived from the island-type model compounds fragment predominantly by losing their alkyl chains (with either all carbons or all but one), one after another, which allows for the identification of the chain lengths and counting the number of chains. Increasing the length of the alkyl chains reduces the extent of spontaneous fragmentation occurring upon EI, likely because of more efficient cooling of the fragmenting ions via emission of infrared (IR) light made possible by the reduced fragmentation rates of the longer chains. Ions derived from the archipelago model compounds with ethylene bridges connecting two or three aromatic cores (without alkyl side chains) readily undergo cleavages in these bridges. Increasing the length of the alkyl chain between the aromatic cores reduces the extent of fragmentation caused by EI. Similarly, the addition of long external alkyl chains to archipelago model compounds with an ethylene bridging two aromatic cores greatly hinders fragmentation upon EI. When these molecules are protonated and subjected to high-energy CAD, they appear to fragment almost randomly but, nevertheless, indicating some preference for cleavages of the bonds in the chain connecting the aromatic cores. A comparison of these findings to the fragmentation patterns observed for protonated asphaltenes indicates that the asphaltene molecules studied are likely composed of many isomeric and isobaric molecules. Each may contain several aromatic rings and a distribution of mostly aliphatic alkyl chains (and possibly naphthenic rings) ranging in size from 1 to at least 14 carbons, several containing methyl branching at the α carbons. The results do not allow for the unambiguous differentiation between island- and archipelago-type structures, although they are in a better agreement with the island model.

Introduction

Asphaltenes, the heaviest fraction of crude oil, are defined as being soluble in toluene and insoluble in *n*-heptane.¹ Asphaltenes are of growing importance in the oil industry as the light crude reserves begin to deplete, leading to a shift toward heavier reserves containing higher percentages of asphaltenes.¹ Asphaltenes are problematic because they precipitate out in pipelines

and foul catalysts during crude oil processing, leading to increased maintenance costs.^{1–5} To more efficiently use these heavier crude reserves, an increased knowledge of asphaltenes is necessary. This may also lead to novel uses of asphaltenes. Most recent work has been devoted to examining the molecular-weight (MW) distributions of asphaltenes, while less attention has been paid to determining their molecular structures.¹ Two structural models are currently debated: the island (one aromatic core with external alkyl chains) and the archipelago [several aromatic cores (with external alkyl chains) that are connected by alkyl chains] models.⁶ The most recent review on the field provides stronger support for the island model.^{6f}

Asphaltenes have proven difficult to analyze via mass spectrometry (MS).⁷ They are difficult to bring into the gas phase without unwanted aggregation and degradation. Furthermore, they are extremely complex mixtures, containing multiple aromatic

*To whom correspondence should be addressed. Telephone: (765) 494-0882. Fax: (765) 494-0239. E-mail: hilka@purdue.edu.

(1) Mullins, O. C.; Sheu, E. Y.; Hammami, A.; Marshall, A. G. *Asphaltenes, Heavy Oils, and Petrochemicals*; Springer: New York, 2007.

(2) Ancheyta, J.; Betancourt, G.; Centeno, G.; Marroquin, G.; Alonso, F.; Garciafigueroa, E. Catalyst deactivation during hydroprocessing of Maya heavy crude oil. 1. Evaluation at constant operating conditions. *Energy Fuels* **2002**, *16*, 1438–1443.

(3) Ancheyta, J.; Betancourt, G.; Marroquin, G.; Centeno, G.; Castaneda, L. C.; Alonso, F.; Munoz, J. A.; Gomez, M. T.; Rayo, P. Hydroprocessing of Maya heavy crude oil in two reaction stages. *Appl. Catal., A* **2002**, *233*, 159–170.

(4) Ancheyta, J.; Betancourt-Rivera, G.; Marroquin-Sanchez, G.; Perez-Arellano, A. M.; Maity, S. K.; Cortez, T.; del Rio-Soto, R. An exploratory study for obtaining synthetic crudes from heavy crude oils via hydrotreating. *Energy Fuels* **2001**, *15*, 120–127.

(5) Trejo, F.; Centeno, G.; Ancheyta, J. Precipitation, fractionation and characterization of asphaltenes from heavy and light crude oils. *Fuel* **2004**, *83*, 2169–2175.

rings and usually heteroatoms, such as nitrogen, oxygen, and sulfur, and metals, such as vanadium and nickel.¹

Laser-induced acoustic desorption (LIAD) involves desorption of the analyte molecules via an acoustic wave as neutral molecules into the gas phase.^{8–11} This method has been demonstrated to allow for the desorption of various asphaltene model compounds (including a polyphenylated vanadyl porphyrin) as intact neutral molecules into the mass spectrometer.¹² This finding indicates that this method allows for the evaporation of most if not all components of asphaltenes into mass spectrometers for further characterization.

LIAD allows for the desorption event to be decoupled from ionization. The analyte can be ionized by using a variety of methods, including electron ionization (EI) or chemical ionization (CI) inside the mass spectrometer.^{13–18} Electron ionization

(6) (a) Groenzin, H.; Mullins, O. C. Molecular size and structure of asphaltenes. *Pet. Sci. Technol.* **2001**, *19*, 219–230. (b) Groenzin, H.; Mullins, O. C. Asphaltene molecular size and structure. *J. Phys. Chem. A* **1999**, *103*, 11237–11245. (c) Groenzin, H.; Mullins, O. C. Molecular size and structure of asphaltenes from various sources. *Energy Fuels* **2000**, *14*, 677–684. (d) Ruiz-Morales, Y.; Mullins, O. C. Polycyclic aromatic hydrocarbons of asphaltenes analyzed by molecular orbital calculations with optical spectroscopy. *Energy Fuels* **2007**, *21*, 256–265. (e) Rodgers, R. P.; Lazar, A. C.; Reilly, P. T. A.; Whitten, W. B.; Ramsey, J. M. Direct determination of soil surface bound polycyclic aromatic hydrocarbons in petroleum-contaminated soils by real time aerosol mass spectrometry. *Anal. Chem.* **2000**, *72*, 5040–5046. (f) Mullins, O. C. The modified Yen model. *Energy Fuels* **2010**, *24*, 2179–2207.

(7) Mullins, O. C.; Martinez-Haya, B.; Marshall, A. G. Contrasting perspective on asphaltene molecular weight. This comment vs the overview of A. A. Herod, K. D. Bartle, and R. Kandiyoti. *Energy Fuels* **2008**, *22*, 1765–1773.

(8) Golovlev, V. V.; Allman, S. L.; Garrett, W. R.; Taranenko, N. I.; Chen, C. H. Laser-induced acoustic desorption. *Int. J. Mass Spectrom. Ion Processes* **1997**, *169*, 69–78.

(9) Lindner, B. On the desorption of electrosprayed organic compounds from supporting metal foils by laser-induced pressure waves. *Int. J. Mass Spectrom. Ion Processes* **1991**, *103*, 203–218.

(10) Perez, J.; Petzold, C. J.; Watkins, M. A.; Vaughn, W. E.; Kenttämaa, H. I. Laser desorption in transmission geometry inside a Fourier transform ion cyclotron resonance mass spectrometer. *J. Am. Soc. Mass Spectrom.* **1999**, *10*, 1105–1110.

(11) Perez, J.; Ramirez-Arizmendi, L. E.; Petzold, C. J.; Guler, L. P.; Nelson, E. D.; Kenttämaa, H. I. Laser-induced acoustic desorption/chemical ionization in Fourier transform ion cyclotron resonance mass spectrometry. *Int. J. Mass Spectrom.* **2000**, *198*, 173–188.

(12) Pinkston, D. S.; Duan, P.; Gallardo, V. A.; Habicht, S. C.; Tan, X.; Qian, K.; Gray, M.; Müllen, K.; Kenttämaa, H. I. Laser-induced acoustic desorption/Fourier transform ion cyclotron resonance mass spectrometry of asphaltenes and asphaltene model compounds. *Energy Fuels* **2009**, *23*, 5564–5570.

(13) Campbell, J. L.; Crawford, K. E.; Kenttämaa, H. I. Analysis of saturated hydrocarbons by using chemical ionization combined with laser-induced acoustic desorption/Fourier transform ion cyclotron resonance mass spectrometry. *Anal. Chem.* **2004**, *76*, 959–963.

(14) Crawford, K. E.; Campbell, J. L.; Fiddler, M. N.; Duan, P.; Qian, K.; Gorbaty, M. L.; Kenttämaa, H. I. Laser-induced acoustic desorption/Fourier transform ion cyclotron resonance mass spectrometry for petroleum distillate analysis. *Anal. Chem.* **2005**, *77*, 7916–7923.

(15) Campbell, J. L.; Fiddler, M. N.; Crawford, K. E.; Gqamana, P. P.; Kenttämaa, H. I. Analysis of polyethylene by using cyclopentadienyl cobalt chemical ionization combined with laser-induced acoustic desorption/Fourier transform ion cyclotron resonance mass spectrometry. *Anal. Chem.* **2005**, *77*, 4020–4026.

(16) Perez, J.; Petzold, C. J.; Watkins, M. A.; Vaughn, W. E.; Kenttämaa, H. I. Laser desorption in transmission geometry inside a Fourier transform ion cyclotron resonance mass spectrometer. *J. Am. Soc. Mass Spectrom.* **1999**, *10*, 1105–1110.

(17) Duan, P. G.; Fu, M. K.; Pinkston, D. S.; Habicht, S. C.; Kenttämaa, H. I. Gas-phase reactions of $\text{ClMn}(\text{H}_2\text{O})^+$ with polar and nonpolar hydrocarbons in a mass spectrometer. *J. Am. Chem. Soc.* **2007**, *129*, 9266–9267.

(18) Duan, P.; Qian, K.; Habicht, S. C.; Pinkston, D. S.; Fu, M.; Kenttämaa, H. I. Analysis of base oil fractions by $\text{ClMn}(\text{H}_2\text{O})^+$ chemical ionization combined with laser-induced acoustic desorption/Fourier transform ion cyclotron resonance mass spectrometry. *Anal. Chem.* **2008**, 1847–1853.

Table 1. Structures and MW of Asphaltene Model Compounds and the Ions Produced upon APCI and LIAD/EI

and LIAD/EI	Structure	APCI (toluene)	LIAD/EI
TDP 762.7 Da		MH ⁺ M ⁺	M ⁺
DDP 482.4 Da		MH ⁺ M ⁺	M ⁺
KS-100 535.2 Da		MH ⁺ minor M ⁺	M ⁺
PBP 612.3 Da		MH ⁺	M ⁺
KS-115 540.2 Da		MH ⁺ M ⁺ fragment ions	M ⁺ minor fragment ions
KS-136 622.2 Da		MH ⁺ fragment ions	Fragment ions only no M ⁺
KS-P4P 458.2 Da		MH ⁺ Minor M ⁺	M ⁺
KS-140 678.3 Da		MH ⁺ fragment ions	M ⁺
KS-152 534.2 Da		MH ⁺ M ⁺	M ⁺
MG-1 597.4 Da		MH ⁺	Not examined
EM-1 n = 1–6 590.5, 898.8, 1207.2, 1516.5, 1824.9, 2133.2 Da		MH ⁺	M ⁺

is a universal ionization method that ionizes all organic compounds. Although this method often leads to extensive fragmentation of the molecular ions generated, it has been found to yield stable molecular ions for most asphaltene model compounds studied in the past, and does not appear to cause dissociation of asphaltene molecular ions.¹² This method was used previously to study the MW distribution of asphaltenes.¹²

Atmospheric pressure chemical ionization (APCI) is also suitable for the analysis of asphaltenes and asphaltene model

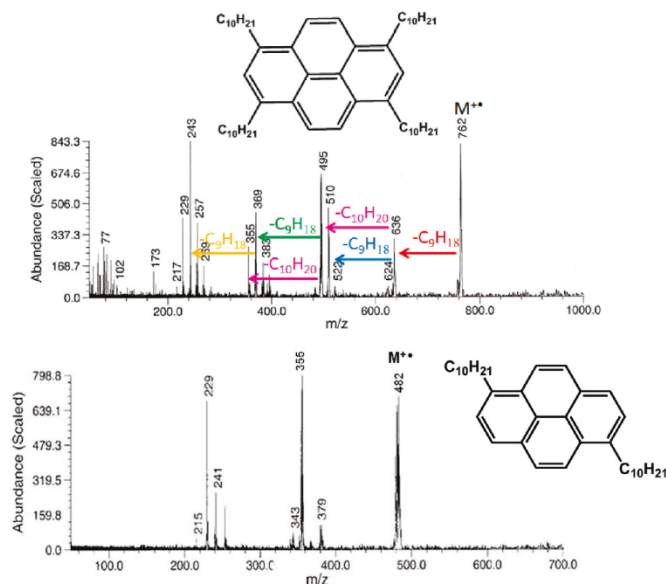


Figure 1. LIAD (12 mJ)/EI (60 eV) mass spectra of two island-type asphaltene model compounds. Both ions fragment predominantly by α cleavages at the benzylic carbons but also by cleaving benzene–alkyl bonds, losing the alkyl chains, one after each other.

compounds. For petroleum samples, APCI using toluene as a solvent/CI reagent has been shown to yield higher sensitivity than standard solvents, such as methanol, or solvent blends, such as toluene/methanol or toluene/acetonitrile.¹⁹ For this study, both LIAD/EI and APCI, using toluene as a solvent, were used to evaporate and ionize asphaltene model compounds in mass spectrometers. APCI using toluene [in a linear quadrupole ion trap (LQIT) mass spectrometer] produced predominantly MH^+ ions for the model compounds, while LIAD/EI [in a Fourier transform ion cyclotron resonance (FT-ICR) mass spectrometer] yielded M^{++} ions. The ions generated upon APCI were isolated and subjected to consecutive collision-activated dissociation (CAD) experiments to explore their fragmentation behavior. Same experiments were carried out for a sample of Maya asphaltene to gain insight into the structures of the asphaltene molecules.

Experimental Section

Chemicals. The asphaltene model compounds (with the exception of one) and the asphaltene sample were provided by Professor Murray Gray (University of Alberta, Edmonton, Alberta, Canada). One model compound mixture with the archipelago structure and varying numbers of long external alkyl groups was provided by ExxonMobil. The solvents used, toluene (100%), CS_2 (>99.9%), and methanol (99.9%), were purchased from Sigma-Aldrich (St. Louis, MO) and used without purification. A 12.7 μm thick titanium foil for LIAD was purchased from Alfa Aesar (Ward Hill, MA).

(19) Kim, Y. H.; Kim, S. Improved abundance sensitivity of molecular ions in positive-ion APCI MS analysis of petroleum in toluene. *J. Am. Soc. Mass Spectrom.* **2010**, *21*, 386–392.

Instrumentation. *FT-ICR Mass Spectrometry.* The LIAD/EI experiments were performed on a dual-cell 3 T Nicolet model FTMS-2000 FT-ICR mass spectrometer described previously.^{12–18} The three trapping plates were kept at 2 V. Asphaltene solutions were prepared by dissolving ~1 mg of the sample in ~10 mL of CS_2 . A drop of the CS_2 solution was placed onto a Ti foil on a hot plate (~50 °C). The solvent was allowed to evaporate. Each Ti foil with the sample was mounted onto a LIAD probe²⁰ and inserted into the FT-ICR mass spectrometer. Model compounds were prepared for analysis using the CS_2 technique described above. Each LIAD experiment involved desorption of molecules by using 10 laser shots (Continuum Minilite Nd:YAG laser, 532 nm wavelength light, 3 ns pulse width, and 10 Hz repetition rate) applied in a circular pattern on the backside of a Ti foil (the side opposite to where the sample was deposited). The input laser energy was set from 18 to 26 mJ, which correlates to from ~9 to 13 mJ at the backside of the foil. The desorbed neutral molecules were then ionized by EI at an energy between 40 and 70 eV. Excitation of the ions for detection was achieved by a fast broadband radio frequency (rf) sweep (from ~2 kHz to 3 MHz, 121 V_{p-p} , and 3200 Hz/ μs or from ~15 kHz to 924 kHz, 121 V_{p-p} , and 800 Hz/ μs). The transients, recorded as 64 000 data points (data system limit), were subjected to Hanning apodization, followed by augmentation of the data by one zero fill prior to Fourier transformation. All of the spectra were corrected by subtracting background spectra from them. Background spectra were recorded by performing exactly the same experiment, except not firing the laser. The experiments were performed, and data acquisition was carried out under the control of a Sun workstation running the Odyssey software, version 4.0.

(20) Shea, R. C.; Habicht, S. C.; Vaughn, W. E.; Kenttämää, H. I. Design and characterization of a high-power laser-induced acoustic desorption probe coupled with a Fourier transform ion cyclotron resonance mass spectrometer. *Anal. Chem.* **2007**, *79*, 2688–2694.

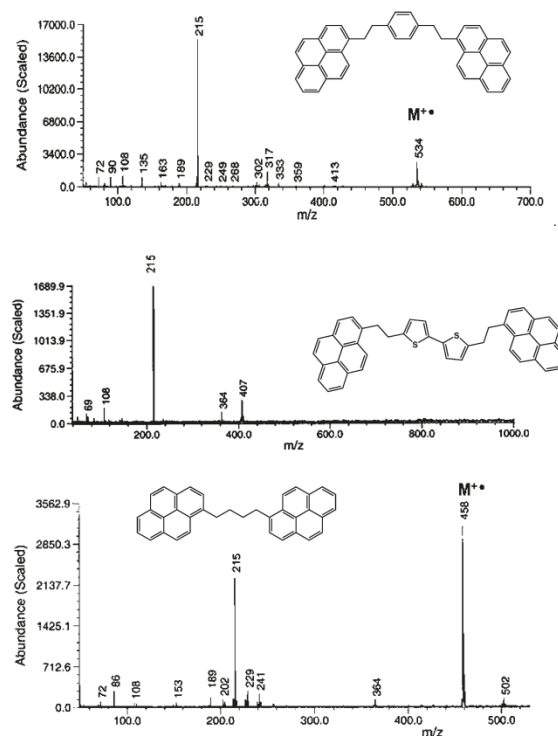


Figure 2. LIAD (18 mJ)/EI (40 eV) mass spectra of three archipelago-type asphaltene model compounds. The top two spectra indicate extensive fragmentation, mostly at the doubly benzylic C–C bonds in the middle of the carbon chains to yield an ion of m/z 215. The molecular ion is indicated in the top spectrum (m/z 534) but is absent in the middle spectrum (m/z 622). The bottom spectrum shows substantially less extensive fragmentation because of the absence of the fragile doubly benzylic C–C bond between the aromatic cores (MW 458; ion of m/z 502 corresponds to a CO_2 adduct).

LQIT Mass Spectrometry. For APCI experiments carried out using a Finnigan LTQ LQIT mass spectrometer, model compounds and the asphaltene sample were dissolved in toluene and then introduced into the ion source via direct infusion from a Hamilton 500 μL syringe through the syringe pump of the instrument. The protonated molecules were isolated and subjected to CAD at varying energies. Isolation windows for ions derived from model compounds were between 1.5 and 1.8 Da, depending upon signal strength (from ± 0.75 to ± 0.9 Da). For ions derived from asphaltenes, the isolation window was 2 Da (± 1 Da). The collision energy (not well-defined) was controlled by a parameter called “collision energy” in the LTQ software. When this value was set from 6 to 10, fragmentation was observed for ionized archipelago model compounds. For the more stable ions derived from island model compounds, such as DDP, this value had to be set to 9–17 for significant fragmentation.

Results and Discussion

The model compounds studied (Table 1) represent both island- and archipelago-type structures. Each contains several aromatic rings, and some of them also have long alkyl chains, as expected for petroleum molecules. The model compounds

were introduced into the FT ICR mass spectrometer by LIAD and ionized (and fragmented) by EI at 40–70 eV electron energy. They were also subjected to simultaneous evaporation/ionization in the LQIT mass spectrometer by APCI using toluene solvent. Both approaches successfully evaporated and ionized all of the model compounds (Table 1). These findings are in sharp contrast to results obtained when attempting to use the common electrospray ionization (ESI) technique to evaporate and ionize the model compounds in the LQIT. Only one analyte (KS-100) yielded detectable ions upon ESI.

In the above experiments, EI yielded a stable molecular ion and varying degrees of fragmentation for most of the model compounds in the FT ICR (a few yielded no stable molecular ions) (see Figures 2 and 3 for examples), while APCI in LQIT produced a stable protonated molecule with minimal or no fragmentation for all of them (Table 1). These protonated molecules were then isolated and subjected to CAD. The fragmentations observed in these two different experiments were surprisingly similar (Figures 4–6), which indicates that the resulting fragment ions must be particularly stable because the mechanisms of fragmentation are usually quite different

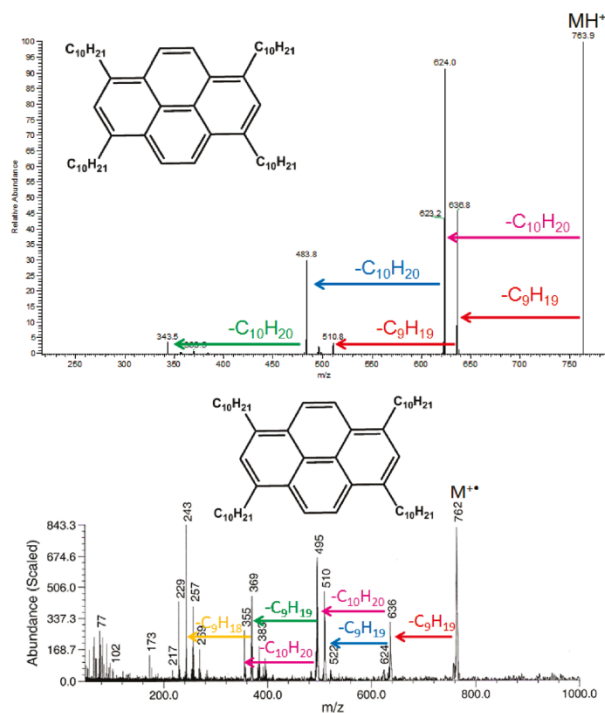


Figure 3. Different mass spectra of the model compound TDP. (Top) APCI (toluene), isolation of the protonated molecule, and CAD (collision energy of 14); loss of three alkyl chains via phenyl–alkyl cleavages is visible. (Bottom) LIAD/EI (70 eV, 10 laser pulses); loss of all four alkyl chains via α cleavages is visible.

for molecular ions (radical cations) that favor radical-induced direct bond cleavages and for protonated molecules that tend to undergo rearrangement reactions. These different mechanisms usually result in different fragment ions for protonated molecules and molecular ions (see Scheme 1 for the only model compound that follows this general trend).

As reported previously,¹² the LIAD/EI mass spectra of almost all of the model compounds studied show a predominant molecular ion (Table 1). When first discovered, this was somewhat surprising because the long alkyl chains of these compounds were expected to be relatively fragile, as is the case, for example, for the molecular ion of butylbenzene.²¹ The reason for the lack of extensive fragmentation for the ionized model compounds in these high-energy electron bombardment experiments is likely due to the many internal degrees of freedom of the long alkyl chains, which slow down unimolecular fragmentation and, hence, allow for cooling via infrared (IR) light emission by the aromatic rings.¹²

Figure 1 shows the LIAD/EI mass spectra for two island model compounds, DDP and TDP, that only differ by the

presence of two alkyl chains in one and four identical alkyl chains in the other, respectively. The extent of fragmentation is significantly less in the spectrum of the compound with the four alkyl chains, illustrating the stabilizing effect two additional alkyl chains have on these molecular ions. Both ions fragment predominantly by α cleavages at the benzylic carbons but also by cleaving phenyl–carbon bonds, thus losing the alkyl chains, one after each other, as either C₉H₁₉ or C₁₀H₂₀. These fragmentations allow for the determination of the number and length of the alkyl chains in each compound.

Figure 2 shows EI mass spectra of three archipelago-type model compounds. The two top spectra indicate extensive fragmentation, mostly at the doubly benzylic C–C bonds in the middle of the ethylene carbon chains connecting the aromatic cores to yield ions of m/z 215. The molecular ion is apparent in the top spectrum (m/z 534) but is absent in the middle spectrum (m/z 622) recorded for the sulfur-containing model compound. The bottom spectrum shows substantially less extensive fragmentation because of the absence of the fragile doubly benzylic C–C bond between the aromatic cores (MW 458; ion of m/z 502 corresponds to a CO₂ adduct). Hence, for archipelago-type model compounds with more than two carbon atoms connecting the aromatic cores, fragmentation is not excessive.

(21) Plomley, J. B.; Londry, F. A.; March, R. E. The consecutive fragmentation of *n*-butylbenzene in a quadrupole ion trap. *Rapid Commun. Mass Spectrom.* **1996**, *10*, 200–203.

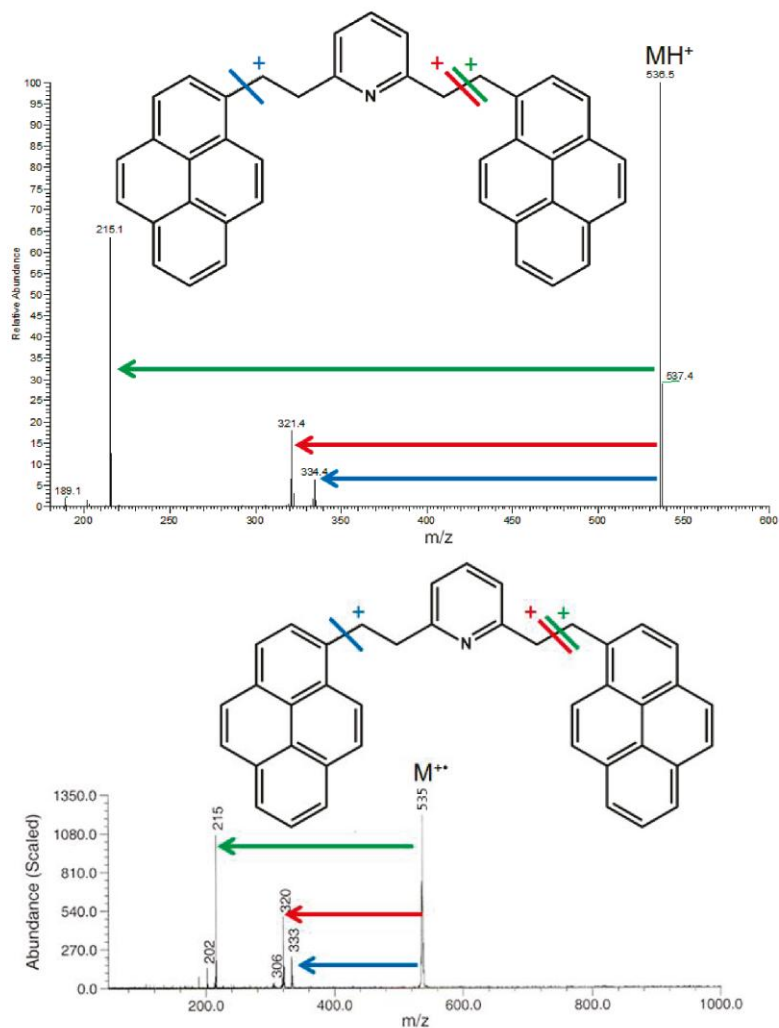


Figure 4. Different mass spectra of the model compound KS-100. (Top) APCI (toluene), isolation of the protonated molecule, and CAD (collision energy of 12). (Bottom) LIAD/EI (70 eV, 10 laser pulses). The same bond cleavages dominate.

Figure 3 shows the comparison of the EI mass spectrum and the APCI/CAD spectrum of TDP. The fragmentation of the molecular ion in the EI experiment is more extensive than the fragmentation of the protonated molecule in the CAD experiment. However, both spectra show exclusively alkyl chain losses, either loss of the whole chain without a hydrogen atom or loss of the chain without a methylene group (caused by an α cleavage in the case of the molecular ion). Hence, both experiments yield information on the number and length of

the alkyl chains. To count all chains in the protonated molecule, a MS³ experiment is needed, wherein a fragment ion formed in the MS/MS experiment (Figure 3) is isolated and subjected to CAD (spectrum not shown). The LIAD/EI mass spectrum reveals the presence of all four alkyl groups.

A similar comparison for an archipelago model compound is shown in Figure 4. In this case, the fragmentation pathways of the molecular ion and protonated molecule are remarkably similar. For both ions, fragmentation occurs predominantly

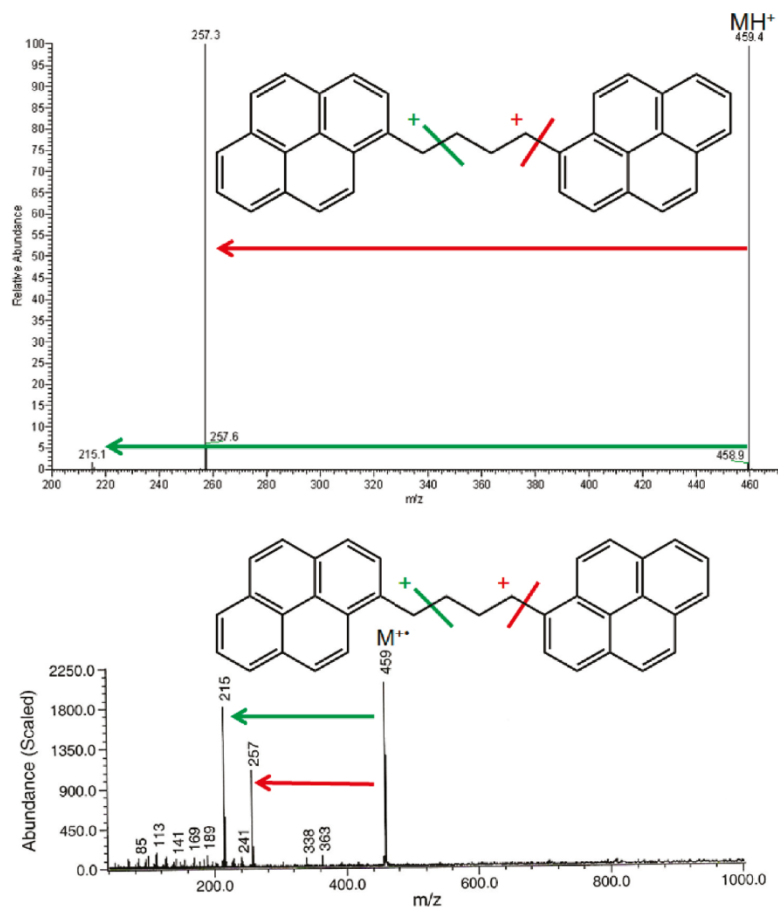


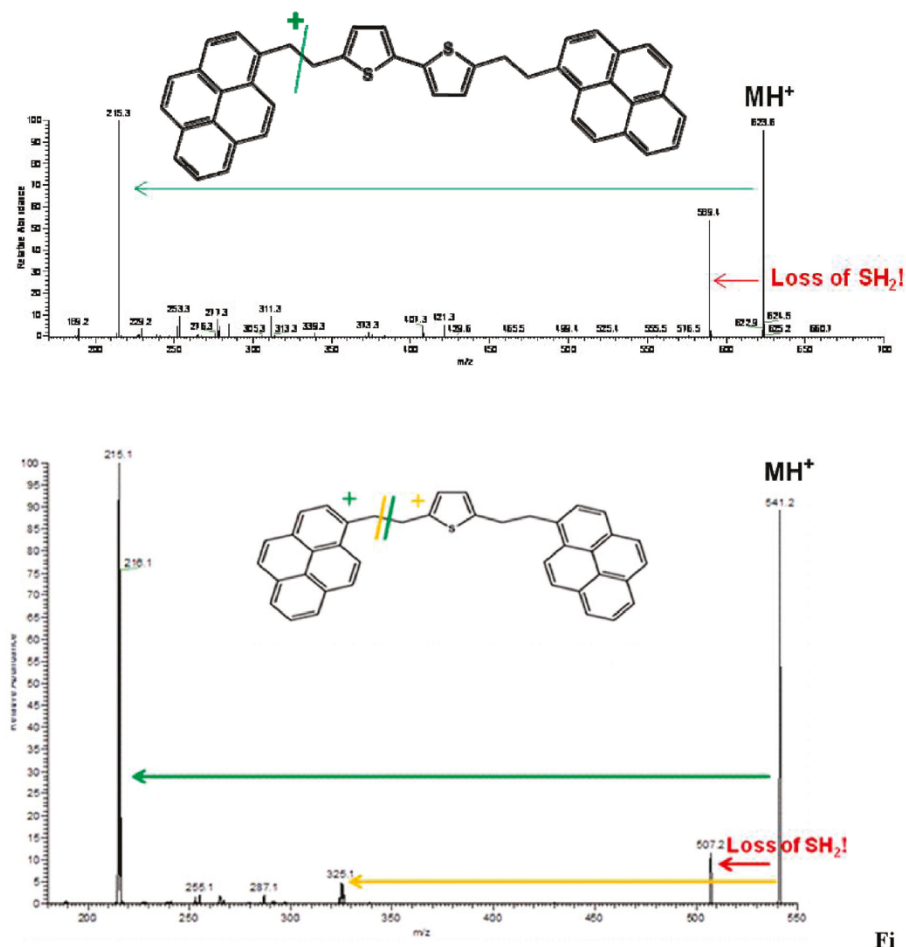
Figure 5. Different mass spectra of model compound KS-P4P. (Top) APCI (toluene), isolation of the protonated molecule, and CAD (collision energy of 8). (Bottom) LIAD/EI (70 eV, 1 laser pulse). The phenyl–alkyl bond cleavage dominates for the protonated molecule, while the α cleavage dominates for the molecular ion.

at the doubly benzylic C–C bonds in the middle of the chain that connects the aromatic cores, thus yielding information on each half of the molecule. For most of the archipelago model compounds, α cleavages were found to dominate for the molecular ion and cleavages at the same C–C bond for the protonated molecules (for example, see Figure 2). For example, protonated model compound KS-140 yields a major fragment ion by cleaving the C–C bond in the middle of the ethylene chain connecting the aromatic cores. It also yields an abundant fragment ion via the phenyl–carbon cleavage, eliminating pyrene. No ethylene losses were observed from the external ethyl groups. The only exception to this behavior is protonated model compound KS-P4P (Figure 5), which shows dominant cleavage at a pyrenyl carbon instead of benzylic carbon. M⁺⁺ shows α cleavages, similar to the other

archipelago model compounds. Possible mechanisms for these fragmentations are shown in Scheme 1. In summary, ions derived from archipelago compounds with either ethylene or butylene chains connecting the aromatic cores appear to fragment by losing half or nearly half of the molecule, yielding information on each of the aromatic cores.

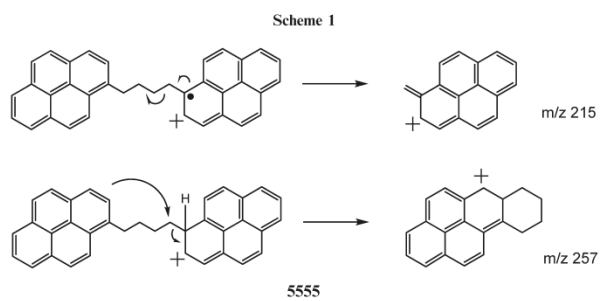
Fragmentation of the two S-containing protonated archipelago model compounds (Figure 6) upon CAD reveals the presence of a sulfur atom with the loss of H₂S. This finding may allow for the screening of asphaltenes for S-containing components.

A model compound containing a cholestane ring system attached to an aromatic core was studied next (MG-1). This protonated compound required especially harsh conditions (“collision energy” of 50) to fragment. This is likely due to the



Fi

Figure 6. APCI (toluene) CAD (collision energy of 11) mass spectra of model compounds KS-136 (MW 623.6) and KS-115 (MW 540.2). Both protonated molecules show the loss of H_2S : top spectrum, m/z 589.4; bottom spectrum, m/z 507.2.



5555

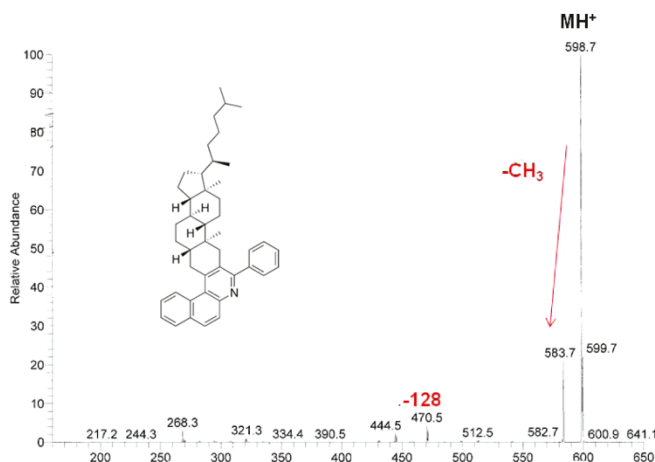


Figure 7. APCI (toluene)/CAD (collision energy of 50) mass spectrum of a model compound (MW 597.4). The loss of a methyl group dominates (ion of m/z 583.7). The loss of the 1,5-dimethylhexyl chain together with a methyl group likely yields the fragment ion of m/z 470.5.

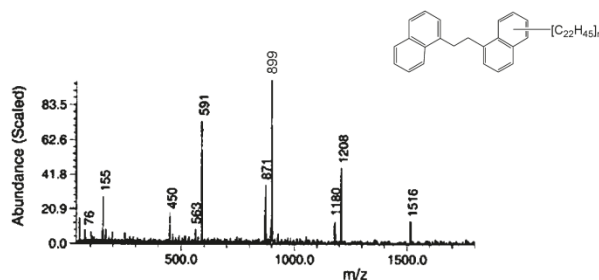


Figure 8. LIAD (22 mJ, 5 shots)/EI (60 eV) mass spectrum of a mixture of archipelago-type model compounds (EM-1) with a varying number ($n = 1-4$) of very long external alkyl chains (MW 590.5, 898.8, 1207.2, and 1516.5 Da) show minimal fragmentation (ions of m/z 155, 450, 871, and 1180). The presence of the long alkyl chains reduces the extent of fragmentation for even the fragile archipelago-type model compounds.

large cholestane ring system, containing a total of 25 carbons, much more than the alkyl chains in the other model compounds discussed here. Even so, the fact that this compound does not readily dissociate at one of its several branches, wherein the loss of an alkyl chain would produce especially stable tertiary carbocations, is surprising. The major fragmentation observed was the loss of a methyl group (Figure 7), presumably the methyl group near the aromatic core, likely followed by a 1,2-hydride shift to generate a resonance-stabilized carbocation. A fragmentation most likely involving the loss of the cholestane alkyl chain, accompanied by a loss of a methyl group, was also observed. Other fragmentations yielded only minor ions.

Finally, a mixture of archipelago model compounds with a varying number (from one to four) of long aliphatic alkyl chains (22 carbon atoms) was examined (EM-1). The LIAD/EI mass spectrum measured for this mixture (Figure 8) indicates only minor fragmentation, thus suggesting that the presence of the long alkyl chains reduces the extent of fragmentation for even

the fragile archipelago-type model compounds. When this mixture was ionized by APCI and protonated molecules were isolated and subjected to highly energetic CAD, extensive and mostly random fragmentation was observed (Figure 9). However, fragmentation to yield especially abundant fragment ions with about half of the mass of the isolated ions was observed. Hence, archipelago-type ions with even these long alkyl chains appear to form especially stable fragment ions via cleavage of the chain connecting the aromatic cores, at least when the chain is only two carbons long.

Figure 10 shows the APCI (toluene) mass spectrum measured for a Maya asphaltene sample. Some of the protonated molecules in this spectrum were isolated and subjected to CAD (Figure 11). The loss of multiple alkyl chains with up to 13 carbons can be seen, possibly indicating the presence of alkyl chains with at least 14 carbon atoms. The loss of methyl dominates the spectrum, followed by the loss of ethyl, propyl, butyl, etc. When some of the fragment ions were isolated and

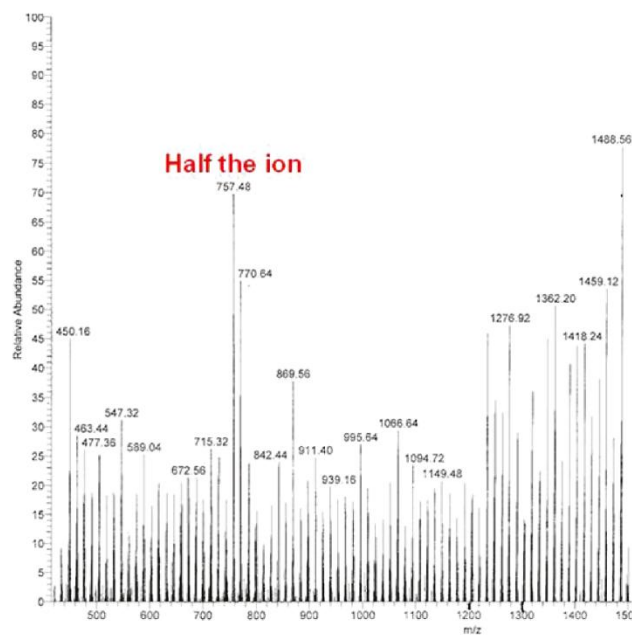


Figure 9. EM-1 sample was ionized by APCI (toluene), and the protonated molecule of m/z 1517 ($n = 4$) was isolated and subjected to CAD (collision energy of 21). The loss of an ethyl group leads to the most abundant fragment ion of m/z 1488. Another ethyl loss yields the ion of m/z 1459. The second largest peak in the spectrum corresponds to half of the ion (m/z 757). The loss of an alkyl chain ($C_{22}H_{43}$) from this ion leads to the ion of m/z 450.

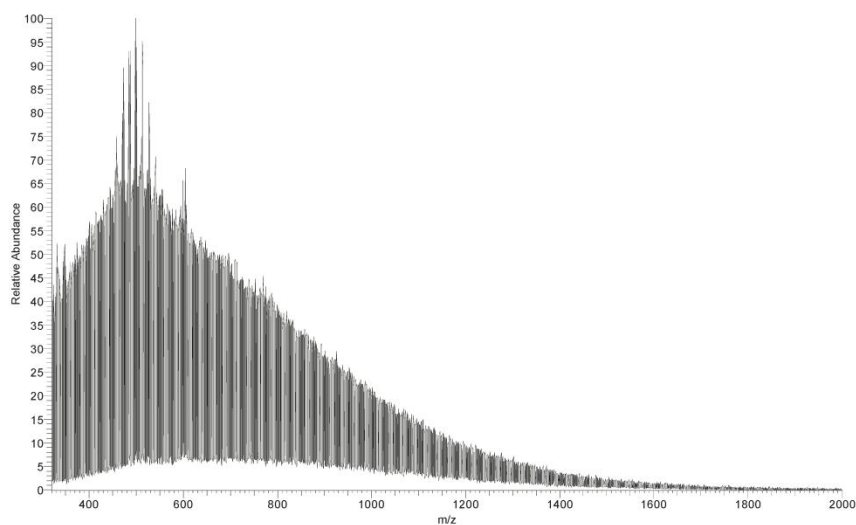


Figure 10. APCI (toluene) mass spectrum of Maya asphaltenes (350 °C). The abundant peaks at the top of the distribution are due to impurity polyethylene glyco.

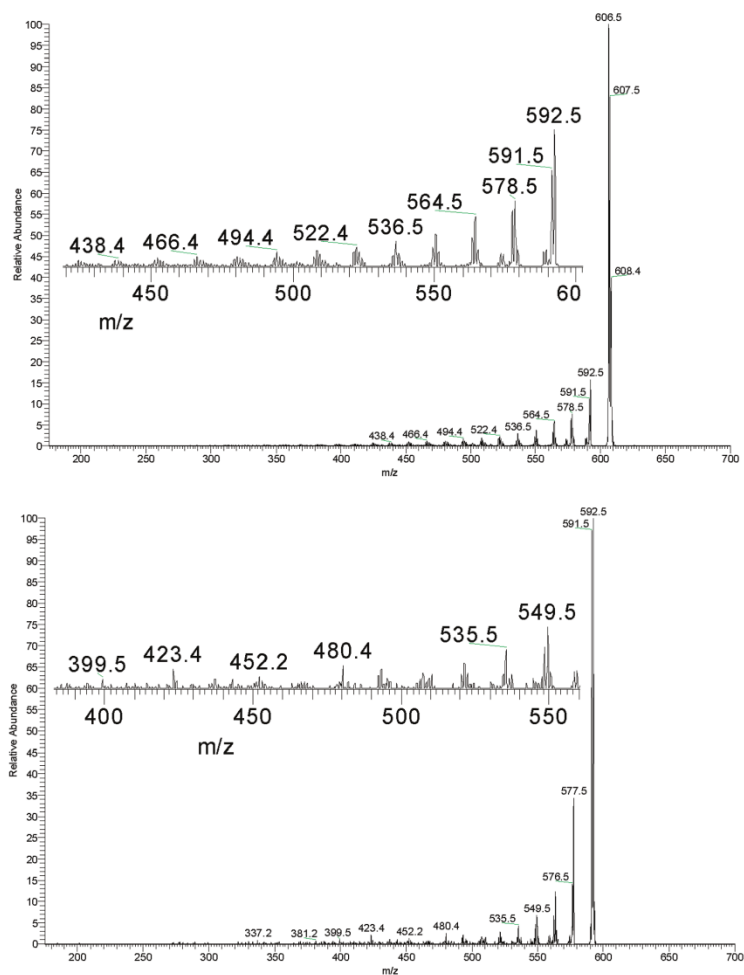


Figure 11. (Top) Ions of $m/z 607 \pm 1$ were isolated from the ion mixture generated by APCI (toluene) from Maya asphaltenes (Figure 10) and subjected to CAD (collision energy of 24). The loss of at least 13 homologous alkyl chains is visible [from CH_3 (peak at $m/z 592.5$) up to $\text{C}_{13}\text{H}_{27}$ for the parent ion of $m/z 608$; the parent ion of $m/z 607$ shows an analogous series]. The loss of a water molecule is indicated, for example, by the small peaks on the left from $m/z 591.5$. The loss of SH_2 is indicated by the peak of $m/z 573$ left of the bigger peak of $m/z 578$. (Bottom) Ions of $m/z 592 \pm 1$ were isolated from the ion mixture shown in the top spectrum and subjected to CAD (collision energy of 24). The loss of at least 10 homologous alkyl chains is visible [from CH_3 (peak at $m/z 577.5$) for the parent ion of $m/z 592.5$]. Note that the mass values of the major ions in the bottom spectrum differ from those shown in the top spectrum, thus indicating that the smaller fragment ions in the top spectrum are not the result of fragmentation of the fragment ions of $m/z 592 \pm 1$. These results indicate that the chain lengths in the asphaltene molecules of MW 607 ± 1 Da vary from 1 (not observed) to at least 13 carbons. The loss of SH_2 is indicated by a peak at $m/z 558$.

subjected to further CAD (Figure 11), the mass values of their fragment ions were found to differ from those of their precursor ions (protonated asphaltene molecules), thus indicating that the fragmentation observed for the protonated asphaltene molecules is not the result of further fragmentation of the larger fragment ions. Hence, each alkyl loss observed

for a protonated asphaltene molecule should indicate the length of an alkyl chain in that molecule, or an alkyl chain + CH_2 . These findings suggest that these asphaltene molecules contain a large number of ethyl groups or longer alkyl groups with branching at the α carbon, possibly also naphthenic rings with methyl groups at tertiary positions. The longer the alkyl

chain, the fewer are present. Minor losses of H₂O and H₂S were also observed, indicating the presence of O- and S-containing heterocycles (observed in sulfur-containing model compound studies) or side chains. Although the presence of archipelago-type structures cannot be completely ruled out, these results are in better agreement with the island-type structures. Because one asphaltene molecule cannot contain all of the chains whose losses were observed without being unreasonably large, each asphaltene ion studied here is probably composed of a set of isomeric (with exactly the same MW) and/or isobaric (with the same nominal MW) molecules. Isomers containing several aromatic rings and alkyl chains of different lengths, with the number of chains of a given length decreasing with the length, and some methyl groups at the α carbons, would explain the fragmentation behavior observed here.

Conclusions

Protonated asphaltene model compounds and the analogous molecular ions (radical cations) were found to fragment remarkably similarly, thus suggesting that the fragmentations are driven by the formation of especially stable fragment ions rather than specific fragmentation mechanisms. Ions derived from model compounds with the island structure were generally found to be more resistant to fragmentation than ions derived from model compounds with the archipelago structure, although the presence of long alkyl chains in the latter structures significantly reduces the extent of fragmentation.

Ions derived from asphaltene model compounds with the island structure and long alkyl chains showed distinctive fragmentation that allows for the number of alkyl chains and chain lengths to be determined. However, this was not true for one model compound, the large compound containing the cholestane ring system, whose ions proved to be resistant to fragmentation and, even upon highly energetic conditions, mainly fragmented just by a loss of a methyl group. The cholestane ring system contains 25 carbons and, hence, is the largest saturated hydrocarbon moiety in the model compounds studied thus far. The many internal degrees of freedom in this hydrocarbon moiety likely slow the dissociation rate enough for cooling via IR emission to dominate over dissociation of the ions.

Ions derived from model compounds with the archipelago structure predominantly show cleavages in the chain connecting the aromatic cores, thus yielding information on each core. Although the ionized model compound containing a butylene chain instead of an ethylene chain between the cores was more stable toward fragmentation, it still underwent substantial fragmentation that cleaved the ion roughly into two halves. Finally, ions derived from archipelago model compounds

with very long external alkyl chains still showed preferential fragmentation at the connecting alkyl chain, although otherwise, their fragmentation appears to be random.

Ions derived from asphaltenes were earlier found to be resistant to fragmentation upon EI.¹² This finding suggests that the asphaltene molecules contain fairly long alkyl chains. When the protonated asphaltene molecules produced by APCI were isolated and subjected to CAD, they were found to fragment via the loss of multiple alkyl chains of varying lengths, ranging from 1 to 12 carbons. These fragmentations were demonstrated to originate from the protonated asphaltene molecule and not to represent further fragmentation of fragment ions. On the basis of these observations, the chain lengths in these asphaltene molecules range from 2 to at least 13 carbons. The dominant fragmentation was the loss of a methyl group, followed by ethyl, propyl, butyl, etc., with the loss of a larger alkyl group always being less favorable than the loss of a shorter alkyl group. The dominant loss of a methyl group suggests the presence of numerous ethyl groups or alkyl chains branched at the α carbon or possibly methyl groups on naphthenic rings. The presence of archipelago-type structures is not supported by these findings because fragmentation of the ions to roughly two halves was not observed. Minor losses of H₂O and H₂S were observed for the asphaltene ions studied, indicating either the presence of heteroatom-containing side chains or bridges or O- and S-containing heterocycles. S-Containing protonated archipelago model compounds were found to fragment upon CAD via the loss of H₂S. Because a single asphaltene molecule cannot contain all of the chains whose losses were observed without being unreasonably large, each asphaltene ion studied here is probably composed of a set of isomeric (with exactly the same MW) and/or isobaric (with the same nominal MW) molecules. The fragmentation behavior reported here could be explained by the presence of a large number of isomeric asphaltene molecules, each containing several aromatic rings (and possibly a sulfur, oxygen, or nitrogen atom) and alkyl chains of different lengths, with the number of chains of a given length decreasing with the length, and some chains (possibly naphthenic) containing a methyl group at the α carbon.

Acknowledgment. The authors gratefully acknowledge Exxon-Mobil Research and Engineering Co. for providing financial support for this work.

Note Added after ASAP Publication. There were errors in the version published ASAP September 20, 2010. Several figures and captions were revised, an additional author was added, and several text changes were made. The corrected version was published on October 6, 2010.



RESEARCH ARTICLE

Laser-Induced Acoustic Desorption/ Atmospheric Pressure Chemical Ionization Mass Spectrometry

Jinshan Gao,¹ David J. Borton II,¹ Benjamin C. Owen,¹ Zhicheng Jin,¹ Matt Hurt,¹
Lucas M. Amundson,¹ Jeremy T. Madden,¹ Kuangnan Qian,² Hilikka I. Kenttämäa¹

¹Department of Chemistry, Purdue University, 560 Oval Drive, West Lafayette, IN 47906, USA

²ExxonMobil Research and Engineering Company, Annandale, NJ, USA

Abstract

Laser-induced acoustic desorption (LIAD) was successfully coupled to a conventional atmospheric pressure chemical ionization (APCI) source in a commercial linear quadrupole ion trap mass spectrometer (LQIT). Model compounds representing a wide variety of different types, including basic nitrogen and oxygen compounds, aromatic and aliphatic compounds, as well as unsaturated and saturated hydrocarbons, were tested separately and as a mixture. These model compounds were successfully evaporated into the gas phase by using LIAD and then ionized by using APCI with different reagents. From the four APCI reagent systems tested, neat carbon disulfide provided the best results. The mixture of methanol and water produced primarily protonated molecules, as expected. However, only the most basic compounds yielded ions under these conditions. In sharp contrast, using APCI with either neat benzene or neat carbon disulfide as the reagent resulted in the ionization of all the analytes studied to predominantly yield stable molecular ions. Benzene yielded a larger fraction of protonated molecules than carbon disulfide, which is a disadvantage. A similar but minor amount of fragmentation was observed for these two reagents. When the experiment was performed without a liquid reagent (nitrogen gas was the reagent), more fragmentation was observed. Analysis of a known mixture as well as a petroleum cut was also carried out. In summary, the new experiment presented here allows the evaporation of thermally labile compounds, both polar and nonpolar, without dissociation or aggregation, and their ionization to predominantly form stable molecular ions.

Key words: LIAD, APCI, APCI reagents, Petroleum, Nonpolar hydrocarbons

Introduction

Mass spectrometry has long been recognized as a powerful analytical technique for volatile analytes [1, 2]. The development of two soft evaporation/ionization

methods, electrospray ionization (ESI) [3] and matrix-assisted laser desorption ionization (MALDI) [4], made it possible to evaporate and ionize (nearly simultaneously) large, thermally labile molecules, thus enabling a broader application of mass spectrometry for uses in biology and other life sciences. The ionization of analytes in ESI and MALDI is limited to protonation, deprotonation, or cation attachment (often involving ions preformed in solution for ESI). ESI suffers from severe ion suppression in the presence of impurities with higher proton affinity (PA) than

Electronic supplementary material The online version of this article (doi:10.1007/s13361-010-0048-x) contains supplementary material, which is available to authorized users.

Correspondence to: Hilikka Kenttämäa; e-mail: hilikka@purdue.edu

Received: 18 October 2010
Revised: 9 December 2010
Accepted: 9 December 2010
Published online: 15 January 2011

the analyte [5, 6]. Neither method can ionize analytes without easily ionizable functional groups, such as saturated and unsaturated hydrocarbons, in the presence of basic or acidic analytes [7, 8]. In order to enable the analysis of polycyclic aromatic analytes, some investigators have derivatized them prior to ESI/mass spectrometry [9]. Other methods used to facilitate the analysis of polyaromatic hydrocarbons include using silver cationization or adding CHCl_3 into the ESI solvent. However, both approaches are limited to aromatic hydrocarbons and are not applicable to other nonpolar hydrocarbons [10].

Laser-induced acoustic desorption (LIAD) enables the evaporation of nonvolatile and thermally labile compounds as intact neutral molecules into the gas phase [11, 12]. This makes it possible to decouple the desorption and ionization processes, thus allowing the use of a variety of methods to ionize analytes, such as electron bombardment [13, 14] and chemical ionization (CI) [8, 15–17]. LIAD has been implemented with a Fourier-transform ion cyclotron resonance mass spectrometer [18, 19], a quadrupole ion trap [20], a linear quadrupole ion trap (LQIT) [21], and a quadrupole/time-of-flight mass spectrometer [22]. In these studies, the analyte was deposited onto either a thin titanium or aluminum foil or silicon wafer. LIAD was accomplished by irradiating the backside of the foil or wafer with high-intensity laser pulses. A laser-induced shock wave propagated through the foil or wafer and evaporated only neutral molecules from the other side of the foil into the gas phase. Because the laser pulses did not interact with the analytes directly, ions were not formed. The desorbed neutral molecules have been found to have low kinetic and internal energies [18]. LIAD/CI using $\text{CIMn}(\text{water})$ reagent ions has been demonstrated to allow the characterization of both polar and nonpolar organic compounds simultaneously without causing fragmentation at either the evaporation or ionization stage in an FT-ICR cell [15]. Furthermore, it appears to be the only mass spectrometric method that can be used to analyze large branched saturated hydrocarbons without fragmentation, including those present in petroleum [14]. Unfortunately, all these experiments were performed in high vacuum. Effective ionization of saturated hydrocarbons in atmospheric pressure is highly desired for practical analytical applications.

Recently, polar neutral compounds desorbed by LIAD were ionized by electrospray ionization (ESI) under ambient conditions before analysis by a quadrupole/time-of-flight (Q-TOF) mass spectrometer [22]. A sample droplet was first deposited onto an aluminum foil. After drying, the analyte was desorbed by LIAD into the ESI plume, resulting in singly and/or multiply charged ions. However, as the ionization step involves ESI, this method suffers from all the same limitations as ESI alone, which are discussed above.

Initially called atmospheric pressure ionization (API), APCI was developed in the 1970s [23, 24]. The chemical ionization process of APCI was initiated by a nickel-63 radiation source in the early applications; this was later replaced by a corona discharge electrode. The potential of

APCI was not realized until another API method, ESI, was developed and gained popularity for its ability to gently ionize large proteins [25]. In an APCI source, a corona discharge needle is used as the electron source to ionize gas molecules, such as N_2 (commonly used as a sheath gas for the inlet) and methanol/water (commonly used as a solvent mixture for the analyte), forming radical cations in the positive ion mode [23, 26, 27]. These ions collide with the vaporized solvent molecules to form secondary reactant ions, usually protonated methanol and cluster ions of the type $\text{H}^+(\text{H}_2\text{O})_n$ and $\text{H}^+(\text{CH}_3\text{OH})_n$ [23]. Protonation of the analyte molecules is usually observed in positive-mode APCI, although molecular ions and their fragments (including $\text{M}-\text{H}^+$) can also be formed [27, 28].

In this study, LIAD was coupled with APCI in a commercial linear quadrupole ion trap mass spectrometer to test whether this method allows for the analysis of analytes that are not amenable to LIAD/ESI experiments. Since APCI can be used to ionize compounds with low to medium polarity, this approach may be applicable to the analysis of hydrocarbon mixtures, such as petroleum. In order to facilitate ionization of hydrocarbons, and avoid fragmentation of ionized analytes, different ionization reagents were tested for APCI.

Experimental

All experiments were carried out using a linear quadrupole ion trap mass spectrometer (LQIT; specifically, LTQ of Thermo Fisher Scientific, Inc., San Jose, CA, USA), which was equipped with an APCI source. The APCI conditions were as follows: vaporizer temperature, about 375°C, nitrogen sheath gas, 40–50 (arbitrary units); nitrogen auxiliary gas, 5 (arbitrary units); capillary temperature, 275°C; the MS scan range, m/z 50–500. The flow rate of APCI reagents (liquid) was 15–25 $\mu\text{L}/\text{min}$ for all solvents. The nitrogen gas was obtained from boil-off of a liquid nitrogen cylinder.

5 α -Cholestane (purity 97%), squalene (98%), androsterone (97%), coronene (97%), bathophenanthroline (97%), and carbon disulfide (99.9%) were purchased from Sigma-Aldrich (St. Louis, MO, USA) and used as received. To prepare a sample foil, 5 α -cholestane, squalene, coronene, and bathophenanthroline were dissolved in 100% tetrahydrofuran, and coronene in 90:20 acetonitrile/methanol. A mixture of model compounds was prepared by dissolving equimolar amounts of the aforementioned compounds in 1:6 dichloromethane/methanol. By using electrospray deposition [29], a volume of 60–80 μL of each solution (~1 mM) was deposited on thin Titanium foils (12.5 μm). The solvent evaporated nearly instantaneously and the foil was placed onto the sample support stage of the LIAD probe. The back side of the foil was rested on a thin (200 μm) glass support. The petroleum cut sample was dissolved in toluene/methanol (75:25) and electrospray deposited onto the titanium foil for subsequent desorption by LIAD and ionization by APCI.

The LIAD probe employed in this study has been previously described [19]. The only difference between the

probe used here (10 in. length) and the one described in the literature is that the literature probe is longer. The glass window in the front of the source was removed so that the LIAD probe could be inserted into the APCI source. About 5 in. of the probe (from the front of a Cajon fitting adaptor) was inserted into the source, which placed the probe tip 5/8 in. away from the corona discharge needle and just underneath the back edge of the APCI probe. The side of the foil coated with sample was exposed to the ion transfer capillary entrance of the LQIT mass spectrometer. In the probe, the laser pulse generated by an Nd:YAG laser (Minilite II; Continuum Lasers, Santa Clara, CA, USA; 532 nm; 3 ns pulse width; 10 Hz) was directed by using silver mirrors (ThorLabs, Newton, NJ, USA) to an area of about 10^{-3} cm² on the back side of the foil surface. The output energy was 20 mJ/pulse, as measured by a pyroelectric meter (PE25-SH; OPHIR Laser Measurement, Logan, UT, USA). The outer cylinder of the LIAD probe, containing the sample foil, was rotated so that analytes were desorbed from multiple sites. Typically, one-fourth of a foil (90° area) was rotated during each experiment when 180 shots of the laser were fired. To prevent heating of the LIAD probe and analytes deposited on the Ti foil, the LIAD probe was inserted into the APCI source just before firing the laser and removed immediately after each experiment. Earlier studies have demonstrated that LIAD is the cause of evaporation of the analytes in these experiments, rather than thermal heating [18].

Results and Discussion

A schematic representation of a LIAD/APCI source is shown in Figure 1. To evaluate the performance of the

LIAD/APCI source, model compounds of different types (Table 1) were analyzed. These compounds are structurally similar to components commonly present in petroleum, ranging from saturated hydrocarbons to polar compounds. All analytes were successfully evaporated into the APCI source by using LIAD. Three different liquid APCI reagent systems were employed to ionize the analytes, a mixture of methanol and water (1:1, vol/vol), neat benzene, and neat carbon disulfide. APCI with no liquid reagent (hence, using nitrogen gas as the ionizing reagent) was also employed. The mass spectra measured for each analyte under the different ionization conditions are discussed below. After that, results obtained upon analysis of a mixture of these model compounds, as well as a petroleum cut, are discussed.

Bathophenanthroline

When a mixture of methanol and water (1:1, vol/vol) was introduced into the APCI source, only protonated methanol and its cluster ion, $\text{CH}_3\text{OH}_2^+(\text{CH}_3\text{OH})$, were observed. This ion mixture is the reagent mixture that will ionize any introduced analyte. Hence, it is not surprising that the production of only stable protonated molecules was observed for the nitrogen heteroaromatic analyte, bathophenanthroline (Supplemental Figure S1, top). However, when benzene was used as the reagent, the dominant reagent ions generated upon APCI were the benzene molecular ions (radical cations). These conditions lead to the initial formation of analyte molecular ions if the ionization energy (IE) of the analyte is lower than that of benzene (9.24 eV) [30]. For bathophenanthroline, both protonated molecules (branching ratio: 80%) and molecular ions (branching ratio: 20%) were observed. The protonated molecules are likely

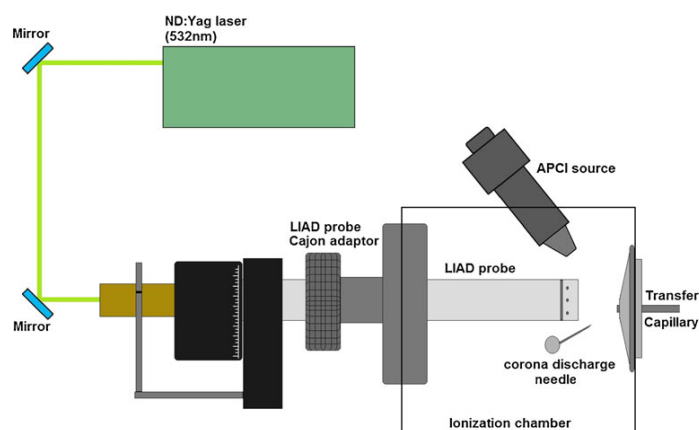
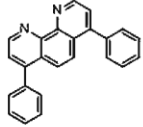
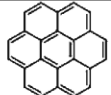
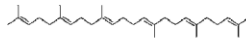
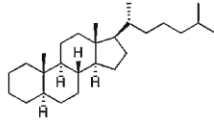
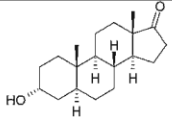


Figure 1. Schematic view of the LIAD/APCI source

Table 1. Ions (with their branching ratios, corrected for ^{13}C isotope; only ions with branching ratios $\geq 5\%$ are listed) formed upon LIAD/APCI of model compounds

Analyte \ Reagent	$\text{CH}_3\text{OH}/\text{H}_2\text{O}$ IE = 10.84 eV PA = 754.3 kJ/mol (methanol)	Benzene IE = 9.24 eV PA = 750.4 kJ/mol	CS_2 IE = 10.07 eV PA = 681.9 kJ/mol
 Bathophenanthroline (MW 332)	M+H ⁺ 100%	M+H ⁺ 80% M ⁺⁺ 20%	M+H ⁺ 30% M ⁺⁺ 70%
 Coronene (MW 300)	M+H ⁺ 100%	M+H ⁺ 48% M ⁺⁺ 52%	M+H ⁺ 9% M ⁺⁺ 91%
 Squalene (MW 410)	M+H ⁺ 95% m/z 329 5%	M+H ⁺ 7% M ⁺⁺ 76% m/z 341 17% (-(CH ₃) ₂ C=CH-CH ₂)	M+H ⁺ 8% M ⁺⁺ 92%
 5 α -Cholestane (MW 372)	No ions detected	M ⁺⁺ 80% m/z 218 20%	M ⁺⁺ 81% M-H ⁺ 8% m/z 218 11%
 Androsterone (MW 290)	M+H ⁺ 46% M+H ⁺ -H ₂ O 45% M+H ⁺ -2H ₂ O 9%	M+H ⁺ 4% M ⁺⁺ 87% M+H ⁺ -H ₂ O 9%	M ⁺⁺ 73% M+H ⁺ -H ₂ O 19% M+H ⁺ -2H ₂ O 8%

formed in secondary reactions of the benzene or bathophenanthroline molecular ions either with bathophenanthroline or with adventitious water. These results are similar to those of a previous study on APCI of polycyclic aromatic compounds where both molecular ions and protonated

molecules were observed when using toluene as the APCI reagent [27]. APCI with no liquid reagent (i.e., N₂ molecular ions as the most likely ionization reagent ions) of this analyte yielded a mass spectrum similar to that obtained using benzene reagent (Supplemental Figure S1, bottom).

Carbon disulfide was tested as an APCI reagent to avoid proton transfer reactions and to make the method less energetic than when using nitrogen gas as the reagent but more widely applicable than when using benzene, as this reagent has a higher ionization energy (IE=10.07 eV) than benzene (IE=9.24 eV) but lower than nitrogen (IE=15.6 eV) [30]. This reagent was expected to lead to more efficient electron transfer, but possibly more fragmentation of the molecular ions, than APCI with benzene reagent. However, no fragmentation was observed for bathophenanthroline. As expected, the branching ratio for molecular ions was substantially greater than that for protonated molecules (70:30; Table 1).

Coronene

Upon methanol/water APCI, coronene, a polyaromatic analyte with no heteroatoms, only generated protonated molecules, as expected (Table 1). APCI with either benzene or carbon disulfide reagent, or no liquid reagent, resulted in the formation of both the protonated molecules and molecular ions. The relative abundance of the protonated molecules was less than for bathophenanthroline, a substantially more basic compound. Out of these three conditions, APCI with carbon disulfide yielded the most desirable mass spectrum for coronene, with the molecular ion dominating. This is likely due to the lack of hydrogens in carbon disulfide, as opposed to benzene.

Squalene

Squalene, a linear polyene hydrocarbon, yields predominantly protonated molecules upon LIAD/APCI when a mixture of methanol and water is used as the reagent system (Table 1). Only a small amount of fragmentation was observed. When benzene was used as the reagent, the molecular ions dominate the spectrum. Fragmentation was also observed and it occurred via the cleavage of the weakest, doubly allylic C-C bond. Again, APCI with carbon disulfide yielded the most desirable mass spectrum, with molecular ions dominating and no obvious fragmentation.

5 α -Cholestane

5 α -Cholestane, a saturated hydrocarbon containing three six-membered rings and one five-membered ring, yielded no detectable ions when a mixture of methanol and water were used as the APCI reagent. However, molecular ions dominated (branching ratio: 80% 81%) the APCI mass spectra obtained by using benzene or carbon disulfide (Supplemental Figure S2, top) as the reagent. About an equal amount of fragment ions were also observed in these experiments.

Interestingly, APCI with benzene resulted in a cleavage of the alkyl chain and most of the five-membered ring in 5 α -cholestane, while carbon disulfide also showed loss of a

hydrogen atom from the molecular ion (Table 1). APCI with no liquid reagent yielded a mass spectrum (Supplemental Figure S2, bottom) indicating more fragmentation than those obtained by using benzene or carbon disulfide as liquid reagents in APCI. Hence, detection of this hydrocarbon cannot be achieved using proton transfer APCI, and the carbon disulfide APCI method again yields the best results.

Androsterone

Androsterone is an interesting analyte since it is known, after protonation, to readily fragment by loss of water. Androsterone yields some stable protonated molecules (46%) upon LIAD/APCI using methanol/water, but fragmentation by losses of one and two water molecules also occurs readily (Table 1). In sharp contrast, when benzene was used as the reagent, the molecular ions dominate the spectrum. Only minor fragmentation took place. APCI with CS₂ also yielded an abundant molecular ion but more fragmentation than APCI with benzene (Figure 2). Hence, for this analyte, APCI with benzene reagent yielded the best results.

Mixture of Model Compounds

A mixture of all five model compounds (all in equimolar ratios) was analyzed by LIAD/APCI using CS₂ reagent. The mass spectrum (Figure 3) shows molecular ions for all five analytes, as well as their most abundant fragment ions (Table 1). While the relative abundances of the molecular ions do not exactly match the relative molar concentrations, all analytes were successfully detected in a single experiment, in spite of their widely varying ionization energies, compositions, structures, and volatilities. The same mixture was also analyzed using water/methanol as the APCI reagent mixture, as well as with no liquid reagent at all. Similar molecular ion branching ratios were observed when no liquid APCI reagent was used and

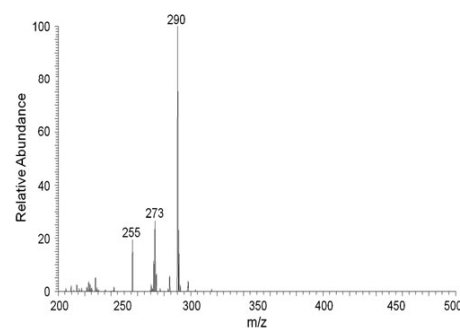


Figure 2. LIAD/APCI mass spectrum of androsterone in positive ion mode. The solvent was CS₂.

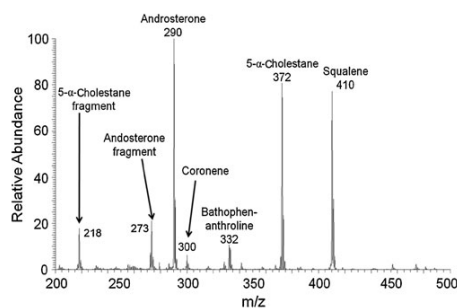


Figure 3. A mixture of 5- α -cholestane (MW 372), coronene (MW 300), squalene (MW 410), androsterone (MW 290), and bathophenanthroline (MW 332) (all in equimolar ratios) analyzed by LIAD/APCI using CS₂ as the reagent

when the CS₂ reagent was used. APCI using the water/methanol reagent mixture yielded protonated molecules for the analytes, with the exception of 5 α -cholestane, which cannot be detected under these conditions. Future research will focus on

improving the relative sensitivity of APCI using CS₂ reagent toward the aromatic analytes.

Petroleum Cut 800

Petroleum cut 800, a petroleum distillate provided by ExxonMobil, was analyzed by LIAD/APCI using nitrogen gas as the reagent (no liquid reagent). The mass spectrum (Figure 4, top) shows a bimodal distribution where the ions with the greater m/z ratios (m/z 400–950) appear to be comprised mostly of even mass ions. Hence, these ions are most likely hydrocarbon molecular ions formed by electron transfer. Some of them may also be protonated nitrogen compounds. Their true identities need to be resolved by ultra-high resolution mass spectrometry. The lower mass distribution has ions with mostly odd mass values, indicating that the lower mass distribution mostly consists of fragment ions formed from the molecular ions. This is as expected because ionization occurred via the high-energy process of electron abstraction by N₂⁺⁺ and this method caused fragmentation also for the model compounds discussed above. The high mass distribution correlates well with

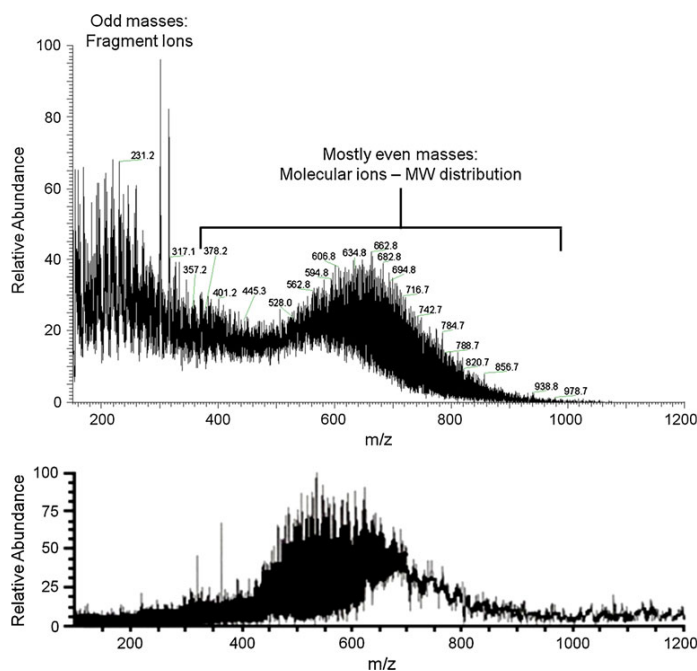


Figure 4. Top: LIAD/APCI (no liquid reagent) mass spectrum of petroleum cut 800 (MW~400–950). Bottom: LIAD/EI mass spectrum of the same sample measured in a 3 T FT-ICR spectrometer. The mass ranges for the molecular ions in the two spectra are similar

the MW distribution measured for the same sample (Figure 4, bottom) in an experiment wherein the sample was evaporated by high-power LIAD into high vacuum (10^{-9} Torr) and ionized by 30 eV electron impact (EI) in a 3 Tesla Fourier-transform ion cyclotron (FT-ICR) mass spectrometer [14].

Detection Limit

Finally, the detection limit for LIAD/APCI analysis of bathophenanthroline (MW 332 Da) by using methanol/water reagent system was determined to be 2.3 ng by depositing a known amount of the analyte on the foil, and estimating the amount of molecules evaporated when rotating the foil 90 degrees (if the foil is rotated the full 360 degrees, this number reduces to 0.6 ng). This value corresponds to a detectable solution concentration of about 100 pmol/mL (1×10^{-7} M) when the foil is rotated 360° (100 μ L spray volume). This value compares well with literature values. For example, 10^{-6} to 10^{-7} M solution was reported as the detection limit for LIAD/ESI mass spectrometric analysis of hemoglobin [22]. The LIAD/APCI detection limit for squalene with no liquid APCI reagent was determined to be 2.9 ng.

Conclusions

LIAD was successfully combined with the APCI source of a commercial linear quadrupole ion trap mass spectrometer. By changing (or omitting) the liquid reagent used in APCI, different mass spectra were obtained. A mixture of methanol and water was found to produce protonated molecules for polar compounds while saturated hydrocarbons produced no detectable ions. Both molecular ions and protonated molecules (likely formed in secondary reactions) were observed for polar compounds when benzene or carbon disulfide were used as the reagent, but carbon disulfide forms mostly molecular ions. Both of these reagents led to ionization of the nonpolar analytes studied, including saturated hydrocarbons. Carbon disulfide appears to be the best reagent among those studied since it forms predominantly molecular ions for both polar and nonpolar analytes. Only minor fragmentation of the molecular ions was observed, and this was found to be comparable in the carbon disulfide and benzene experiments, in spite of the different ionization energies of these two reagents. However, APCI with no liquid reagent led to more extensive fragmentation. The detection limit was determined to be about 7×10^{-7} M for bathophenanthroline. Finally, a known mixture containing all the model compounds, and a petroleum cut sample, were examined by LIAD/APCI using APCI with carbon disulfide or nitrogen as the reagent, respectively. All five analytes were successfully detected in a single experiment, in spite of their widely varying ionization energies, compositions, structures, and volatilities. On the other hand, the molecular weight distribution determined for the petroleum cut agrees

well with that determined by using another method, LIAD coupled with EI in a Fourier-transform ion cyclotron resonance mass spectrometer.

The LIAD/APCI experiment described here benefits from several advantages. As opposed to LIAD/ESI and other ESI- and MALDI-based methods, both polar and nonpolar compounds (including saturated hydrocarbons) can be analyzed simultaneously by using the carbon disulfide reagent. Only minimal fragmentation is observed, and predominantly stable molecular ions are formed for all analytes. The results presented here suggest no strong bias toward basic or acidic analytes. Further, any solvent can be used to deposit the analyte on the surface, as opposed to ESI. In fact, this can be performed without using a solvent at all [13]. Further, the analysis can be done on any mass spectrometer equipped with an APCI source. Finally, rastering the LIAD foil will be much more straightforward than using the traditional LIAD set-up due to the atmospheric pressure conditions, thus enabling rapid analysis of a large number of different samples deposited onto one LIAD foil and using LIAD as a novel imaging tool.

Acknowledgments

The authors thank ExxonMobil Research and Development Co., the National Institutes of Health, and the National Science Foundation for financial support of this work.

References

1. Reemtsma, T.: Liquid chromatography-mass spectrometry and strategies for trace-level analysis of polar organic pollutants. *J. Chromatogr. A* **1000**, 477–501 (2003)
2. Hogenboom, A.C., Niessen, W.M.A., Brinkman, U.A.T.: The role of column liquid chromatography-mass spectrometry in environmental trace-level analysis. Determination and identification of pesticides in water. *J. Sep. Sci.* **24**, 331–354 (2001)
3. Fenn, J.B., Mann, M., Meng, C.K., Wong, S.F., Whitehouse, C.M.: Electrospray ionization—principles and practice. *Mass Spectrom. Rev.* **9**, 37–70 (1990)
4. Tanaka, K., Waki, H., Ido, Y., Akita, S., Yoshida, Y., Yoshida, T.: Protein and polymer analyses up to m/z 100 000 by laser ionization time-of-flight mass spectrometry. *Rapid Commun. Mass Spectrom.* **2**, 151–153 (1988)
5. Souverain, S., Rudaz, S., Veuthey, J.L.: Matrix effect in LC-ESI-MS and LC-APCI-MS with off-line and on-line extraction procedures. *J. Chromatogr. A* **1058**, 61–66 (2004)
6. Ismaiel, O.A., Halquist, M.S., Elmamly, M.Y., Shalaby, A., Karnes, H. T.: GC-MS analysis of breath odor compounds in live patients. *J. Chromatogr. B* **875**, 333–343 (2008)
7. Marshall, A.G., Rodgers, R.P.: Petroleomics: chemistry of the underworld. *Proc. Natl. Acad. Sci. U.S.A.* **105**, 18090–18095 (2008)
8. Duan, P., Fu, M., Pinkston, D.S., Habicht, S.C., Kenttämaa, H.I.: Gas-phase reactions of $\text{ClMn}(\text{H}_2\text{O})^+$ with polar and nonpolar hydrocarbons in a mass spectrometer. *J. Am. Chem. Soc.* **129**, 9266–9267 (2007)
9. (a) Airiau, C. Y., Breton, R. G., Crosby, J.: High-performance liquid chromatography/electrospray tandem mass spectrometry of polycyclic aromatic hydrocarbons. *Rapid Commun. Mass Spectrom.* **15**, 135–140 (2001) (b) Van Berkel, G. J., Asano, K. G.: Chemical derivitization for electrospray ionization mass spectrometry. 2. Aromatic and highly conjugated molecules. *Anal. Chem.* **66**, 2096–2102 (1994)
10. (a) Miyabayashi, K., Naito, Y., Tsujimoto, K., Miyake, M.: Structure characterization of polyaromatic hydrocarbons in arabian mix vacuum residue by electrospray ionization fourier transform ion cyclotron resonance mass spectrometry. *Int. J. Mass Spectrom.* **235**, 49–57 (2004) (b) Ng, K.

- M., Ma, M. L., Twang, C. W.: Differentiation of isomeric polyaromatic hydrocarbons by electrospray Ag(I) cationization mass spectrometry. *Rapid Commun. Mass Spectrom.* **17**, 2082–2088 (2003)
- (a) Lindner, B., Seydel, U.: Laser desorption mass spectrometry of nonvolatiles under shock wave conditions. *Anal. Chem.* **57**, 895–899 (1985) (b) Lindner, B.: On the desorption of electrosprayed organic compounds from supporting metal foils by laser induced pressure waves. *Int. J. Mass Spectrom.* **103**, 203–218 (1991)
 - Golovlev, V.V., Allman, S.L., Garrett, W.R., Taranenko, N.I., Chen, C.H.: Laser-induced acoustic desorption. *Int. J. Mass Spectrom.* **169**, 69–78 (1997)
 - Pinkston, D.S., Duan, P., Gallardo, V.A., Habicht, S.C., Tan, X., Qian, K., Gray, M., Mullen, K., Kenttämää, H.I.: Analysis of asphaltenes and asphaltene model compounds by laser-induced acoustic desorption/fourier transform ion cyclotron resonance mass spectrometry. *Energy Fuels* **23**, 5564–5570 (2009)
 - Crawford, K.E., Campbell, J.L., Fiddler, M.N., Duan, P., Qian, K., Gorbaty, M.L., Kenttämää, H.I.: Laser-induced acoustic desorption/fourier transform ion cyclotron resonance mass spectrometry for petroleum distillate analysis. *Anal. Chem.* **77**, 7916–7923 (2005)
 - Duan, P., Qian, K., Habicht, S.C., Pinkston, D.S., Fu, M., Kenttämää, H.I.: Analysis of base oil fractions by $\text{ClMn}(\text{H}_2\text{O})^+$ chemical ionization combined with laser-induced acoustic desorption/fourier transform ion cyclotron resonance mass spectrometry. *Anal. Chem.* **80**, 1847–1853 (2008)
 - Campbell, J.L., Crawford, K.E., Kenttämää, H.I.: Analysis of saturated hydrocarbons by using chemical ionization combined with laser-induced acoustic desorption/fourier transform ion cyclotron resonance mass spectrometry. *Anal. Chem.* **76**, 959–963 (2004)
 - Campbell, J.L., Fiddler, M.N., Crawford, K.E., Gqamana, P.P., Kenttämää, H.I.: Analysis of polyethylene by using cyclopentadienyl cobalt chemical ionization combined with laser-induced acoustic desorption/fourier transform ion cyclotron resonance mass spectrometry. *Anal. Chem.* **77**, 4020–4026 (2005)
 - Shea, R.C., Petzold, C.J., Campbell, J.L., Li, S., Aaserud, D.J., Kenttämää, H.I.: Characterization of laser-induced acoustic desorption coupled with a fourier transform ion cyclotron resonance mass spectrometer. *Anal. Chem.* **78**, 6133–6139 (2006)
 - Shea, R.C., Habicht, S.C., Vaughn, W.E., Kenttämää, H.I.: Design and characterization of a high-power laser-induced acoustic desorption probe coupled with a fourier transform ion cyclotron resonance mass spectrometer. *Anal. Chem.* **79**, 2688–2694 (2007)
 - Peng, W.P., Yang, Y.C., Kang, M.W., Tzeng, Y.K., Nie, Z.X., Chang, H.C., Chang, W., Chen, C.H.: Laser-induced acoustic desorption mass spectrometry of single bioparticles. *Angew. Chem. Int. Ed.* **45**, 1423–1426 (2006)
 - Habicht, S.C., Amundson, L.M., Duan, P.G., Vinueza, N.R., Kenttämää, H.I.: Laser-induced acoustic desorption coupled with a linear quadrupole ion trap mass spectrometer. *Anal. Chem.* **82**, 608–614 (2010)
 - Cheng, S.C., Cheng, T.L., Chang, H.C., Shiea, J.: Using laser-induced acoustic desorption/electrospray ionization mass spectrometry to characterize small organic and large biological compounds in the solid state and in solution under ambient conditions. *Anal. Chem.* **81**, 868–874 (2009)
 - Horning, E.C., Horning, M.G., Carroll, D.I., Dzidic, I., Stillwell, R.N.: New picogram detection system based on a mass spectrometer with an external ionization source at atmospheric pressure. *Anal. Chem.* **45**, 936–943 (1973)
 - Dzidic, I., Carroll, D.I., Stillwell, R.N., Horning, E.C.: Comparison of positive ions formed in nickel-63 and corona discharge ion sources using nitrogen, argon, isobutane, ammonia and nitric oxide as reagents in atmospheric pressure ionization mass spectrometry. *Anal. Chem.* **48**, 1763–1768 (1976)
 - Byrdwell, W.C.: Atmospheric pressure chemical ionization mass spectrometry for analysis of lipids. *Lipids* **36**, 327–346 (2001)
 - Sunner, J., Nicol, G., Kebarle, P.: Factors determining relative sensitivity of analytes in positive mode atmospheric pressure ionization mass spectrometry. *Anal. Chem.* **60**, 1300–1307 (1988)
 - Herrera, L.C., Grossert, J.S., Ramaley, L.: Quantitative aspects of and ionization mechanisms in positive-ion atmospheric pressure chemical ionization mass spectrometry. *J. Am. Soc. Mass Spectrom.* **19**, 1926–1941 (2008)
 - Kim, H.Y., Kim, S.: Improved abundance sensitivity of molecular ions in positive-ion APCI MS analysis of petroleum in toluene. *J. Am. Soc. Mass Spectrom.* **21**, 386–392 (2010)
 - Meneal, C.J., Macfarlane, R.D., Thurston, E.L.: Thin film deposition by the electrospray method for californium-252 plasma desorption studied of involatile molecules. *Anal. Chem.* **51**, 2036–2039 (1979)
 - Lias, S. G., Levin, R. D., Kafafi, S. A.: Ion energetics data. In: Lindstrom, P. J., Mallard, W. G. (eds.) NIST Chemistry WebBook, NIST Standard Reference Database Number 69. National Institute of Standards and Technology, Gaithersburg, MD, 20899, <http://webbook.nist.gov> (accessed April 27, 2010)

Separation of Asphaltenes by Reversed-Phase Liquid Chromatography with Fraction Characterization

Thomas N. Loegel,[†] Neil D. Danielson,^{*,†} David J. Borton,[‡] Matthew R. Hurt,[‡] and Hilka I. Kenttämä^{*,‡}

[†]Department of Chemistry and Biochemistry, Miami University, Oxford, Ohio 45056, United States

[‡]Department of Chemistry, Purdue University, West Lafayette, Indiana 47907, United States

Supporting Information

ABSTRACT: The use of a 4.6 × 250 mm, 5 μm cyanopropyl column is effective for the liquid chromatography (LC) separation of asphaltenes with sequential ultraviolet (UV) and fluorescence detection. The mobile-phase composition is an optimized gradient from acetonitrile (MeCN) and water to *N*-methyl-2-pyrrolidone (NMP) and tetrahydrofuran (THF). A low flow rate of 0.5 mL min⁻¹ is used to maintain lower operating pressure to minimize aggregate formation. Using a 0.02 g L⁻¹ asphaltene sample for preliminary optimization, three peaks, with two partially resolved, are evident in the fluorescence chromatogram. The UV chromatogram revealed an extra weakly retained peak, suggesting aggregates that quench fluorescence. Aggregation of asphaltenes increases with time up to about 10 h and is dependent upon the choice of sample solvent. On the basis of the reversed-phase mobile-phase gradient, the relative polarity of the peaks from least to most retained can be estimated over the polarity index (*P'*) range from about 6.3–4.3 on a scale of 0.1 for hexane (least polar) to 10.6 for water (most polar). The sample concentration is increased to 1 g L⁻¹ for separation and collection of 12 fractions. Selected fractions are subjected to characterization using atmospheric pressure chemical ionization mass spectrometry (APCI–MS) using a linear quadrupole ion trap (LQIT). The variation of the molecular-weight distribution of the asphaltenes for the 12 fractions is fairly constant, indicating that the retention mechanism is not controlled by size exclusion but likely a partitioning/adsorption mechanism.

INTRODUCTION

Because of limited resource availability, light crude oil is slowly being replaced by heavier crude oil and oil sands as feedstocks for petroleum refineries.¹ As heavier crude oils are used, a number of problems arise, including plugging of oil wells, residue deposition in pipelines, and increasing amounts of distillation residue and coke production. One of the major contributing factors to many of these problems is the least volatile fraction of crude oil, petroleum asphaltenes. Asphaltenes are known to aggregate and cause precipitation problems during many stages of petroleum production. They are also known to foul crude oil catalysts, increasing refining cost.^{2–6} To better understand how asphaltenes interact with one another, with geological formations, and/or with industrial surfaces, more information about the molecular structures is required. Asphaltenes do not form a monolayer on a mineral surface, such as mica, but form an irregular or meandering layer on the order of 10 nm thick.⁷ Because of the sensitivity of the phase behavior of asphaltenes to the suspending or solvating fluid, uncertainties remain regarding many aspects of the molecular structures. However, asphaltenes have been demonstrated to possess a high degree of aromaticity and also to contain alkyl chains extending from the aromatic core(s), in addition to the presence of heteroatoms, such as nitrogen, sulfur, and oxygen.⁸ The molecular-weight distribution (MWD) of asphaltenes is still contested but is considered to be roughly 300–2000 Da.^{8–11} The Yen–Mullins model describes the formation of nanoaggregates of about six asphaltene molecules, which can then cluster with aggregation numbers of about eight nanoaggregates.¹²

Asphaltenes are extremely complex mixtures, with upward of tens of thousands of species present.^{13,14} Therefore, one particularly suitable analytical method that can be used to characterize asphaltenes at the molecular level is mass spectrometry (MS) because of its ability to discriminate between individual components from a polydispersed sample. To obtain structural information, tandem mass spectrometry (MS/MS) experiments are needed.¹⁵ During such an experiment, asphaltene molecules are ionized, the ions of interest are isolated and then subjected to collisions with an inert gas to induce fragmentation [collision-activated dissociation (CAD)], and the fragment ions are detected. On the basis of the fragment ions produced, the structure of the original ion can be deduced. MS/MS experiments have been shown previously to provide insights into the molecular architecture of asphaltenes.¹⁵ However, the complexity of asphaltenes presents a problem for these studies^{16–18} because asphaltenes can contain up to 244 molecules with the same nominal molecular weight (MW).¹⁶ After ionization, ion isolation cannot be performed at high enough resolution to select only one or a few of the isobaric ions for analysis. Hence, during a MS/MS experiment, multiple ions of the same nominal *m/z* value are isolated and fragmented, complicating the spectrum. Furthermore, sufficient signal intensities for the ions of interest can be difficult to generate without space charging the mass analyzer because of the numerous species present in asphaltenes.

Received: December 6, 2011

Revised: April 23, 2012

Published: April 23, 2012



Chromatography potentially offers a solution to the above problem. The separation of the asphaltenes into simpler mixtures based on polarity or structural differences prior to MS/MS analysis would greatly simplify the data. Typically, for petroleum samples, gas chromatography (GC) has been the technique of choice because of its high separation efficiency and the relatively low boiling points of most crude oil components. However, the temperatures required to bring asphaltenes into the gas phase are too high for most GC columns, and at those temperatures, the asphaltenes begin to degrade, thus limiting GC analysis to compounds with MWs below about 450 Da.^{9,19–21}

Although ion-exchange fractionation of asphaltenes into acid, base, and neutral fractions has been reported,^{22–24} size-exclusion chromatography (SEC) has been more commonly used, particularly in recent years. Coal-derived materials separated by SEC using a poly(divinylbenzene) column with *N*-methyl-2-pyrrolidone (NMP) as the mobile phase has been reported,²⁵ and this topic has been reviewed.²⁶ Molecular mass calibration for SEC of coal derivatives can be challenging^{27–29} and has been performed by matrix-assisted laser desorption/ionization (MALDI)–MS.³⁰ Laser desorption MS was investigated to improve the mass ranges for complex hydrocarbons, such as creosote and anthracene oils, after fractionation by thin-layer chromatography (TLC).³¹ Coal pitch was fractionated using a combination of solvent solubility, ultrafiltration, TLC, and SEC; laser desorption MS of the fractions then showed a wide MW range from 800 to greater than 10 000 Da.³²

MW ranges of asphaltenes after SEC fractionation have been estimated using laser desorption MS^{33–35} and MALDI–MS³⁶ to be 200–4000 Da. Morgan et al. have separated asphaltenes using a combination of TLC and SEC using both ultraviolet (UV) and fluorescence detection.³⁶ Proper standards are difficult to obtain for asphaltenes, and SEC tends to overestimate the breadth of the MW range.³⁷ Phthalocyanines have been proposed as more realistic SEC standards for petroleum fractions, including asphaltenes.³⁷ In general, the separation efficiency of SEC is low, generally only two peaks (sometimes one),³⁶ which limits characterization of asphaltenes.

To structurally characterize asphaltene samples, other types of separation science have been explored. An “asphaltene determinator” for crude oil samples uses a 250 mm long × 7 mm inner diameter (ID) column packed with 350–420 μm Teflon [polytetrafluoroethylene (PTFE)] particles with a series of stepwise mobile-phase solvents and various detection approaches.^{38–41} However, because the separation is based on the solvent changes and partitioning of the sample components with the very low surface area Teflon particles is negligible, this cannot be considered a chromatographic method. Recently, asphaltenes were separated by non-aqueous capillary electrophoresis into a neutral fraction and a nanoaggregate cluster peak with a MWD from 3000 to 4000 Da and a net charge of +1.⁴²

Although not typically used for petroleum samples, high-performance liquid chromatography (HPLC) represents the best approach to separate mixtures of large molecules with polar heteroatoms, such as asphaltenes that are not amenable to GC because of nonvolatility. HPLC involves a partitioning of the analyte from the liquid mobile phase to a chemically bonded stationary phase or adsorption to a polar stationary phase, such as silica. Individual analytes interact with the

stationary phase to different degrees, leading to more or less retention. To date, little has been published on the use of adsorption or partitioning HPLC for the separation of asphaltenes. This is most likely due to the adverse effects of traditional HPLC solvents, such as weak solvents hexane (normal phase) or water (reversed phase), with asphaltene solubility. Even strong solvents, such as acetonitrile (MeCN) or methanol, do not dissolve asphaltenes well. In contrast, there have been numerous publications of HPLC separations of condensed polyaromatic hydrocarbons (PAHs), such as naphthalene, pyrene, benzo[*a*]pyrene, and indeno[123-*cd*]pyrene, using a wide variety of C18 silica-based columns.⁴³ Fractionation of PAHs by number of rings first using normal-phase HPLC on an aminosilica column and then separation of these fractions by reversed-phase C18 HPLC has been effective for environmental samples.^{44,45} The cyanopropyl- and amino-bonded silica phases have been compared and shown to be similar in resolution and analysis time for PAHs.⁴⁶ Large PAHs ranging from 4- to 10-ring compounds have been separated by a C18 silica-packed capillary column.⁴⁷ PAHs ranging from coronene (7 rings) to decacyclene (13 rings) have been separated using a polymeric C18 column with a methanol to tetrahydrofuran (THF) mobile-phase gradient with particle-beam MS detection.⁴⁸

However, common HPLC column chemistries used for these PAH separations, such as C18 or bare silica columns, will likely prove ineffective or problematic with petroleum asphaltenes. It is well-known that adsorption of asphaltenes from toluene onto silica involves aggregate formation and is considered an irreversible process.^{49,50} However, NMP at relatively low concentrations (2–10%) in toluene was found to be effective in desorption of asphaltenes from silica.⁵¹ Adsorption of asphaltenes on silica wafers modified through silylation chemistry with alkyltrichlorosilanes ranging in chain length from *n*-butyl to octadecyl was found to be minimal.⁵² Shielding of the underlying silica surface by the alkyl substituents was deemed important, as shown by a decreased asphaltene adsorption with an increased thickness of the alkyl silane layer. This study was expanded to include aromatic trichlorosilanes,⁵³ but the nature of the silane substituent was less important than the masking of the silica surface. Recently, it has been shown that the polymer ethyl cellulose dissolved in toluene can displace asphaltenes adsorbed to silica or alumina surfaces, as shown by a decreased surface hydrophobicity.⁵⁴ These studies have provided evidence that high-quality uniformly silanized (end-capped) silica particles, found in modern HPLC columns, along with optimization of the mobile-phase gradient with a strong solvent, such as NMP, should be effective for the fractionation of asphaltenes. Our early scouting studies showed that the use of C18 silica- or Hypercarb carbon-based columns cause excessive retention with little if any elution of asphaltenes. Because of the nonpolar nature of asphaltenes but also the presence of polar heteroatoms, we propose the use of a mixed mode (polar and nonpolar) stationary phase for their separation.

In this paper, we will demonstrate reverse-phase HPLC separation of asphaltenes using a solvent gradient of water and MeCN to a mixture of NMP and THF on a cyanopropyl silica column. The cyanopropyl column was chosen for this work based on reports of cyano and amino stationary phases to separate PAHs in crude oil with high resolution and selectivity.^{45,46} We used online fluorescence and ultraviolet–visible (UV–vis) detection to monitor possible aggregate

formation as well as the overall separation. Using a fraction collector, volume segments over the entire chromatogram were collected and analyzed using atmospheric pressure chemical ionization mass spectrometry (APCI-MS). We believe that this is possibly the first HPLC report of a more partitioning and less adsorption or sizing retention mode being applied for the separation of asphaltenes.

EXPERIMENTAL SECTION

HPLC. An Agilent 1100 microdegasser and Hewlett-Packard 1050 quaternary pumps were used to supply tetrahydrofuran (THF, from Fischer Scientific, HPLC grade), water (18.2 MΩ Millipore Milli-Q Biocell), acetonitrile (MeCN, from Acros Organics, HPLC grade), and N-methyl-2-pyrrolidone (NMP, from Sigma Aldrich, Chromasolv) to a 250 × 4.6 mm Phenomenex Luna cyanopropyl-phase column containing 5 μm particles with 100 Å pore size with a Phenomenex SecurityGuard 3 mm amino guard column. After weighing, the Mayan asphaltene (Mexican origin) were dissolved in 100% THF, unless otherwise noted. The samples (from 2 to 50 μL) were injected using a Thermo Scientific AS3500 autosampler. The autosampler tray temperature was kept at 20 °C, and the column compartment was at room temperature (21–22 °C). Detection was accomplished using a Hewlett-Packard 1050 VWD UV detector and a Shimadzu RF-10AXL fluorescence detector. Signals were collected using a Dionex UCI-100 analog to digital converter. Fractions were collected in 30 s intervals using an ISCO Foxy fraction collector and combined according to the elution of the peaks in the chromatogram. Data collection and instrument control was accomplished using Dionex Chromeleon 6.8 SR10c software. Fractions were combined on the basis of peak elution times. Solvent was removed from the fractions using a vacuum oven (mTorr; 30–50 °C) as soon as possible to minimize oxygen exposure, and special effort was taken to minimize light exposure (amber vials).

MS. A Finnigan LTQ linear quadrupole ion trap (LQIT) with an APCI source was used for all mass spectrometric studies. Dried asphaltene fractions were dissolved in chloroform (Mallinckrodt Chemicals, ChromAR HPLC) and introduced into the APCI source via direct infusion via a Hamilton 500 μL syringe at a flow rate of 20 μL min⁻¹ using the integral syringe pump of the instrument. The instrument was in positive-ion mode. MS/MS studies were conducted by isolating ions of several *m/z* values for each fraction and fragmenting the isolated ions using CAD to provide structural information. Data was processed using ThermoScientific Xcalibur software.

RESULTS AND DISCUSSION

After testing isocratic mobile phases, such as various MeCN-THF combinations, with no success (either too short or excessive peak retention), it was apparent that a gradient mobile-phase composition would be required for this separation. The initial conditions tried for the gradient separation involved the combination of the mobile phases used previously for HPLC of PAHs (MeCN-water) and SEC of asphaltene (NMP-THF). The beginning of the gradient was found to play an important role in the separation of asphaltene. Small variations (±5%) away from 75:25 MeCN/H₂O determined how well the two main peaks are resolved, as shown in runs 1–5 of Figure S1 and Table S1 of the Supporting Information. For a reversed-phase gradient separations as is this, the polarity of the mobile phase is ramped from high to low. A measure of the strength of the mobile phase is the polarity index (*P'*), as calculated as $P' = \phi_A P'_A + \phi_B P'_B + \phi_C P'_C + \phi_D P'_D$, where ϕ is the fraction of the solvent and *P'* is the polarity parameter for that solvent.⁵⁵ The *P'* scale ranges from close to 0 for hexane to 10.6 for water. The *P'* trends in Table S1 of the Supporting Information show a decrease in polarity over the course of the run. Lowering the

polarity of the mobile phase was accomplished using a steady increase of the percentage of THF and maintaining a modest amount of NMP. Run 9 of Figure S1 of the Supporting Information is the final analytical chromatogram that was the basis for the preparative runs that were used to collect fractions. The mobile-phase gradient for run 9 was 75% MeCN–25% H₂O at 0 min, 5% THF–20% NMP–60% MeCN–15% water at 5 min, 20% THF–30% NMP–40% MeCN–10% water at 10 min, 70% THF–30% NMP at 12.5 min, 80% THF–20% NMP at 15 min, and 90% THF–10% NMP at 25 min, until 30 min. The corresponding change in *P'* was 6.90, 6.55, 6.15, 4.81, 4.54, and 4.27.

Both UV and fluorescence detectors were used to obtain a more complete picture of the separation because some of the components may lack conjugation or the rigid structure required for a strong fluorescence signal. Additionally, once asphaltene aggregate, the fluorescence is self-quenched but the UV signal is strong. On the basis of the polarity of the mobile phase, the molecules producing the peak at 7 min should be more polar compounds, possessing more heteroatoms than the molecules producing the peaks starting at 14 min (Figure 1).

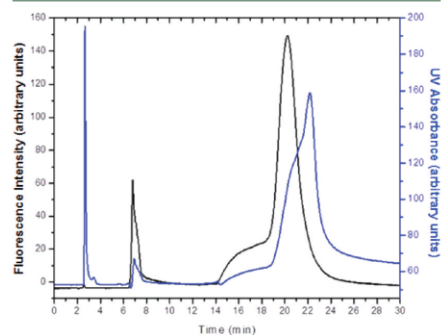


Figure 1. Overlay of UV absorption and fluorescence analytical-scale chromatograms of a single 20 μL injection of 0.02 g L⁻¹ solution of asphaltene at 0.5 mL/min. Fluorescence: excitation wavelength, 340 nm; emission wavelength, 450 nm. UV absorbance at 340 nm. The first larger peak at 3 min and the smaller two peaks at 7 and 22 min correspond to the UV chromatogram. The mobile-phase gradient was that indicated in the first paragraph of the Results and Discussion.

Controlling how fast THF and NMP are added into the mobile phase determines how sharp the second main peak will be. With the initial 75:25 MeCN/H₂O mobile phase, THF is immediately and steadily added to maintain solubility of the sample. Asphaltene is not soluble in 75:25 MeCN/H₂O, and this combined with the difference in polarity between the sample solvent, THF, causes the injection plug to tighten and concentrate at the precolumn. Despite the high water content, the column pressure was constant and did not spike upon sample injection. The first peak at 2.5 min is believed to be due to asphaltene aggregates that are likely large enough to not effectively enter the pores of the silica particles and undergo retention. This is supported by the presence of a very small negative peak at 2.2 min (Figure 1) on the fluorescence trace, which corresponds to the unretained sample solvent peak, caused by a refractive index effect.

Figure 2 shows two preparative chromatograms using UV detection taken at two different flow rates, 0.5 and 1.0 mL/min.

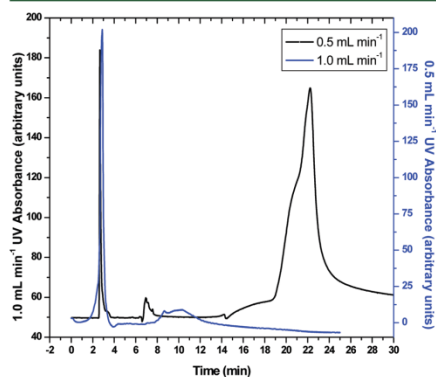


Figure 2. Comparison of preparative chromatograms using the optimized gradient (see first paragraph of the Results and Discussion) as a function of the flow rate. The chromatogram with the peak at 22 min was taken at 0.5 mL/min. These analytical chromatograms were taken together in sequence using a 20 μL injection of the 0.1 g L^{-1} sample. UV absorbance detection at 340 nm. Sensitivity of the scale changed from Figure 1 to keep peaks on scale.

The chromatogram at 0.5 mL/min is similar to the analytical chromatogram in Figure 1 but just with a less sensitive signal output, as expected. Surprisingly, for the chromatogram at 1.0 mL/min, the large peak at 22 min is now much smaller at 11 min and the first aggregate peak is broader. A flow rate of 0.5 mL min^{-1} was determined to be the best compromise between analysis time and the amount of aggregation observed. Figure 3 shows a series of blank chromatograms (100% THF injections)

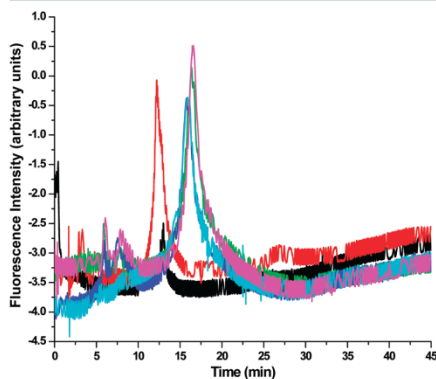


Figure 3. Six blank (100% THF injected) chromatograms, each taken after every 30 preparative sample (0.1 g L^{-1}) injection. Fluorescence detection is the same as in Figure 1. Note that the y axis encompasses only 5.5 units.

taken after every 30 preparative injections. Considering that the y axis is highly magnified, the blank peaks are very small, indicating insignificant carryover from injection to injection. However, some adsorption of asphaltenes at the head of the column but not the tail of the column was visually noted and will be discussed later.

Asphaltene aggregation was found to increase over time in solution in the sample vial. This is revealed by an increase in the aggregate peak over the span of 30 injections of a freshly prepared sample, as shown in the preparative chromatograms of Figure 4. The reason for the slight shift in peak retention time

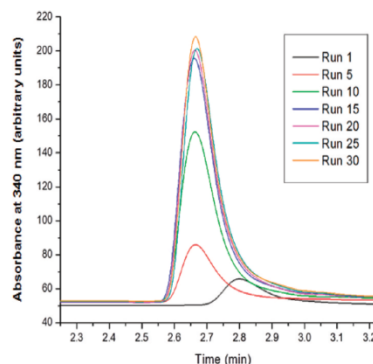


Figure 4. Preparative chromatograms of aggregate peaks measured over 22.5 h (30 injections) of the same 0.1 g L^{-1} asphaltene solution. Run 1 shows a peak maximum at 2.8 min. Runs 5–30 show increasing height at 2.65 min.

after the first run is unclear at this time. Aggregation seems to increase rapidly and then level off after roughly 10 h with a sample concentration of 0.1 g L^{-1} asphaltenes in 100% THF (Figure 5). If the sample solvent is changed to a 50:50 mixture of THF/NMP, aggregation levels off more rapidly in about 4.5 h (Figure 5). Carryover between injections was minimal unless the column was overloaded, which occurred when injecting 80 μL of 0.1 g L^{-1} solution of asphaltenes.

Because of mass balance, it would seem the other peaks in the chromatogram must decrease in area while the aggregate peak increases. In Figure 6, the UV trace shows no major changes in peak areas [percent relative standard deviation (% RSD) range is 3.8–6.7] for the two main peaks (UV 1 and 2); we are unsure as to why. If the same trend lines (% RSD range is 0.7–6.6) for the three peaks in the fluorescence (FL) chromatogram are compared, there might be a very slight decreasing trend for FL peak 3 (Figure 6). However, further study is definitely required to understand from what possible asphaltene fraction(s) the aggregate peak may be forming.

The fractions that were collected are shown in Figure 7. These fractions were collected by using an asphaltene concentration of 0.1 g L^{-1} , instead of 0.02 g L^{-1} , despite an increase in aggregation, to reduce the time needed to collect enough of each fraction to enable analysis by MS. The fractions collected from each peak had different colors. Peaks that do not show up in the fluorescence trace but do show up in the UV trace correspond to fractions P4.3 and V4. The reproducibility

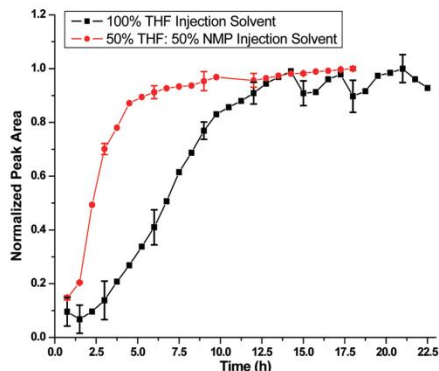


Figure 5. Comparison of the influence of 100% THF (black ■) and 50:50 THF/NMP (red ●) sample solvents on the peak area of the aggregate peak over a 22.5 h (30 injections) preparative run, with a 50 μ L injection size of 0.1 g L⁻¹ asphaltenes solution.

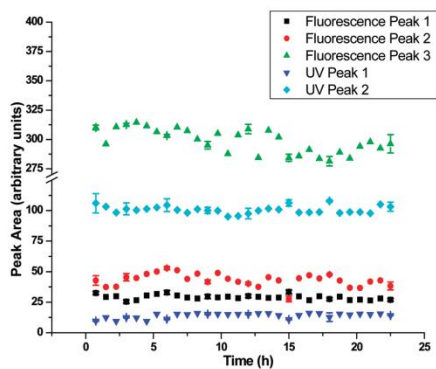


Figure 6. Comparison of UV absorbance peak areas for the three main peaks in the chromatograms measured over 22.5 h (30 injections) time span, with a 50 μ L injection size of 0.1 g L⁻¹ asphaltenes solution. A comparison of the FL peak areas of the three main peaks in chromatograms measured over 22.5 h (30 injections) time span, with a 50 μ L injection size. From the top trace to the bottom trace: FL peak 3, UV peak 2, FL peak 2, FL peak 1, and UV peak 1.

of the peak retention times for these fraction collections was 2.2% RSD for P1, 2.6% RSD for P2.1, and 0.25% RSD for P4.1 ($n = 10$). A visual comparison of the column packing at the two column ends shows a black discoloration at the front of the column, while the end of the column is white. The length of discoloration in the column head was short, about 10 mm. Electron micrographs of the column packing (Figure 8) indicate some dark channels spread throughout the pores for the front of the column, as compared to a more typical discrete pore structure at the end of the column. However, the column pressure did not increase significantly over the course of this study.

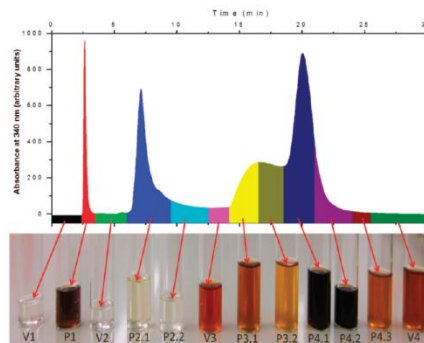


Figure 7. Sectioned off chromatogram showing each collected fraction. It is possible to visually see differences in colors of each fraction in THF.

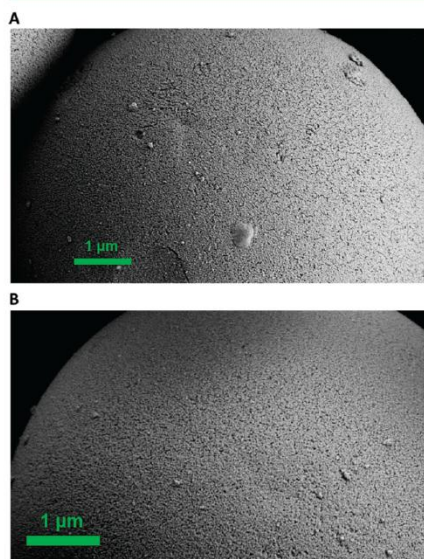


Figure 8. (A) Electron micrograph of the sample of column packing (black in color) taken from the front of the column. (B) Electron micrograph of the sample of column packing (white in color) taken from the end of the column.

Each of the dried fractions collected during the HPLC run was dissolved in chloroform and ionized using (+)APCI, with the solvent chloroform acting as the chemical ionization reagent. This ionization method produces $[M + H]^+$ pseudo-molecular ions, through proton transfer.⁵⁶ The full spectrum for each fraction was used to determine the low and high ends of the MWD, as well as the center of the distribution (Figure 9).

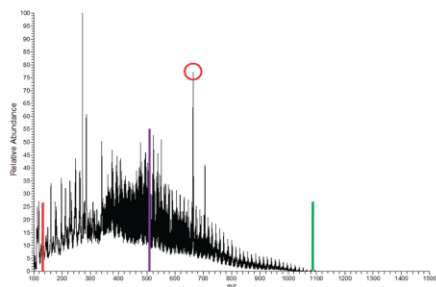


Figure 9. Shown above is the positive-mode APCI mass spectrum for fraction P1 from Figure 7. The broad red line near m/z 140 indicates the lower end of the MWD. The broad purple line near m/z 510 denotes the center of the MWD. The broad green line near m/z 1090 marks the heavy end of the MWD. The red circle denotes contamination from the degradation of the stationary phase of the column.

The MWD for each fraction was plotted as shown in Figure 10, where the red line denotes the low end, the green line indicates

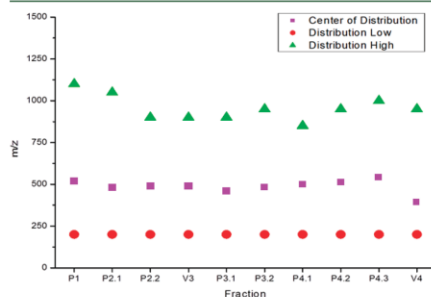


Figure 10. Plot outlining the MWD for each fraction, as seen in Figure 7. The center of maximum intensity of each distribution is also indicated.

the high end, and the purple line shows the center of the distribution. The high end of the MWD varies slightly for each fraction but falls between m/z 800 and 1100 for all of the fractions. More importantly, there is no obvious trend toward the higher end of the MWD for fractions that eluted later, indicating that the asphaltene were not mainly separated by size but separated more based on polarity. The m/z values in the spectra display numerous impurities because of NMP, which forms adducts with the asphaltene (Figure 9). Despite rigorous attempts to dry the asphaltene fractions and remove the solvents used for HPLC, NMP remained a problem because of its high boiling point (200 °C), leading to impurities in the mass spectra, such as for example the peak highlighted by a red circle at m/z 662 in Figure 9. However, some m/z values show more NMP adducts than others, perhaps two or even three NMP adducts per m/z . Also, there are still some NMP-adduct-free asphaltene in the spectra, but they are masked by impurities. Finding solvents that are more suitable for both

HPLC separation and MS analysis of asphaltene is the next step in this research.

MS/MS experiments, intended to provide structural information for each fraction, were not successful because of NMP contamination. An example of this can be seen in Figure 11 for fraction P3.1. This figure shows the mass spectrum

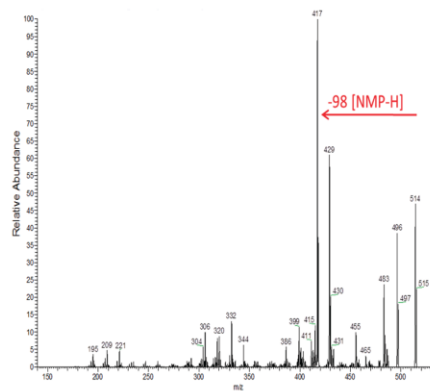


Figure 11. (+)APCI-MS/MS CAD spectrum of the ion of m/z 515 from P3.1. The dominant neutral molecule lost has a MW of 98, which corresponds to the NMP-H molecule (one of the solvents used during HPLC runs).

obtained when ions of m/z 515 were isolated and subjected to CAD. The dominant neutral molecule lost has a MW of 98 Da, which corresponds to NMP-H, which corresponds to the NMP-H molecule (one of the solvents used during HPLC runs). Losses of other neutral molecules indicating the presence of NMP in the isolated ions include water. Apparently, NMP rapidly adds to asphaltene molecules prior to MS or asphaltene ions generated in the ion source. The facile fragmentation of the NMP moiety in the ions masks the fragmentation patterns of the asphaltene molecules themselves. Previous mass spectrometric analysis of asphaltene dissolved in NMP involved only a single stage of MS.^{32,57,58} Thus, the problem posed by NMP adducts and contamination was not readily apparent in these experiments like it is for multiple stages of MS used to elucidate the molecular structure.

CONCLUSION

Liquid chromatographic separation of asphaltene using a cyanopropyl column with an optimized gradient from MeCN and water to NMP and THF with UV and fluorescence as well as MS detection has been demonstrated. Using a 0.02 g L⁻¹ asphaltene solution for preliminary optimization and fraction collection of multiple injections of 0.1 g L⁻¹ asphaltene solution, three definitive peaks are evident in the fluorescence chromatogram. Aggregation of asphaltene, indicated by the presence of a weakly retained peak in the UV chromatogram but no such corresponding peak in the fluorescence chromatogram, was found to increase with time up to about 10 h and to be dependent upon the choice of the solvent. On the basis of the reversed-phase nature of the mobile-phase gradient, the relative polarity of the compounds based on P' of the mobile phase is decreasing significantly and separation between polar and nonpolar molecules seems likely. For the last 10 of 12

fractions, the MWD determined by MS is fairly constant, indicating that the retention mechanism is not a size-exclusion mechanism but more likely a partitioning/adsorption mechanism. Although NMP has been used as a mobile-phase solvent previously for SEC with spectroscopic detection, we cannot recommend it as a good choice for APCI-MS/MS analysis because of facile adduct formation of asphaltenes.

■ ASSOCIATED CONTENT

Supporting Information

Data obtained during gradient development for the separation of 0.02 g L⁻¹ asphaltenes (Table S1) and progression of mobile-phase gradient development for the analytical-scale separation of 0.02 g L⁻¹ asphaltenes (Figure S1). This material is available free of charge via the Internet at <http://pubs.acs.org>.

■ AUTHOR INFORMATION

Corresponding Author

*E-mail: danielnd@muohio.edu (N.D.D.); hilkka@purdue.edu (H.I.K.).

Notes

The authors declare no competing financial interest.

■ ACKNOWLEDGMENTS

The National Science Foundation (NSF) is acknowledged for funding of this research to Hilkka I. Kenttämä.

■ REFERENCES

- Williams, B. *Oil Gas J.* **2003**, *29*, 20–36.
- Aldoubwarej, H.; Beck, J.; Svrcek, W. Y.; Yarranton, H. W. *Energy Fuels* **2002**, *16*, 462–469.
- Asphaltene and Asphalts*; Yen, T. F., Chillingarian, G. V., Eds.; Elsevier: Amsterdam, The Netherlands, 1994.
- Guisnet, M.; Magnoux, P. *Appl. Catal.* **1989**, *54*, 1–27.
- Qian, K.; Tomczak, D. C.; Rakiewicz, E. F.; Harding, R. H.; Yalun, G.; Cheng, W. C.; Zhao, X.; Peters, A. W. *Energy Fuels* **1997**, *11*, 596–601.
- Harding, R. H.; Zhao, X.; Qian, K.; Rajagopalan, K.; Cheng, W. C. *Ind. Eng. Chem. Res.* **1996**, *35*, 2561–2569.
- Cadena-Nava, R. D.; Cosultchi, A.; Ruiz-Garcia, J. *Energy Fuels* **2007**, *21*, 2129–2137.
- Asphaltenes, Heavy Oils, and Petrochemicals*; Mullins, O. C., Sheu, E. Y., Hammami, A., Marchall, A. G., Eds.; Springer: New York, 2007.
- Herod, A. A.; Bartle, K. D.; Kandiyoti, R. *Energy Fuels* **2007**, *21*, 2176–2203.
- Mullins, O. C.; Martinez-Haya, B.; Marshall, A. G. *Energy Fuels* **2008**, *22*, 1765–1773.
- Herod, A. A.; Bartle, K. D.; Kandiyoti, R. *Energy Fuels* **2008**, *22*, 4312–4317.
- Mullins, O. C. *Annu. Rev. Anal. Chem.* **2011**, *4*, 393–418.
- Hsu, C. S.; Hendrickson, C. L.; Rodgers, R. P.; McKenna, A. M.; Marshall, A. G. *J. Mass Spectrom.* **2011**, *46*, 337–343.
- Qian, K. *Energy Fuels* **2001**, *15*, 492–498.
- Borton, D., II; Pinkston, D. S.; Hurt, M. R.; Xiaol, T.; Azza, K.; Scherer, A.; Tykwinski, R.; Gray, M.; Qian, K.; Kenttämä, H. I. *Energy Fuels* **2010**, *24*, 5548–5559.
- Hortal, R. A.; Hurtado, P.; Martinez-Haya, B.; Mullins, O. C. *Energy Fuels* **2007**, *21*, 2863–2868.
- Smith, D. F.; Schaub, T. M.; Sunghwan, K.; Rodgers, R. P.; Rahimi, P.; Teclamarium, A.; Marshall, A. G. *Energy Fuels* **2008**, *22*, 2372–2378.
- Klein, G. C.; Sunghwan, K.; Rodgers, R. P.; Marshall, A. G. *Energy Fuels* **2006**, *20*, 1973–1979.
- Buenrostro-Gonzalez, E.; Lira-Galeana, C.; Gil-Villegas, A.; Wu, J. *AIChE J.* **2004**, *50*, 2552–2570.
- Gonzalez, D. L.; Hirasaki, G. J.; Creek, J.; Chapman, W. G. *Energy Fuels* **2007**, *21*, 1231–1242.
- Zhang, L. L.; Yang, G. H.; Que, G. H.; Zhang, Q. X.; Yang, P. J. *Energy Fuels* **2006**, *20*, 2008–2012.
- Boduszynski, M.; Raj Chadha, R.; Szkuta-Pochopien, T. *Fuel* **1977**, *56*, 432–436.
- Selucky, M. L.; Kim, S. S.; Skinner, F.; Strausz, O. P. *Chemistry of Asphaltene*; American Chemical Society (ACS): Washington, D.C., 1982; Advances in Chemistry Series, Vol. 195, Chapter 6, pp 83–118.
- Green, J. B.; Hoff, R. J.; Woodward, P. W.; Stevens, L. L. *Fuel* **1984**, *63*, 1290–1301.
- Lafleur, A. L.; Nakagawa, Y. *Fuel* **1989**, *68*, 741–752.
- Johnson, B. R.; Bartle, K. D.; Herod, A. A.; Kandiyoti, R. *J. Chromatogr. A* **1997**, *758*, 65–74.
- Bartle, K. D.; Mulligan, M. J.; Taylor, N.; Martin, T. G.; Snape, C. E. *Fuel* **1984**, *63*, 1556–1560.
- Herod, A. A.; Zhang, S.; Johnson, B. R.; Bartle, K. D.; Kandiyoti, R. *Energy Fuels* **1996**, *10*, 743–750.
- Bartle, K. D.; Mills, D. G.; Mulligan, M. J.; Amaechina, I. O.; Taylor, N. *Anal. Chem.* **1986**, *58*, 2403–2408.
- Johnson, B. R.; Bartle, K. D.; Domin, M.; Herod, A. A.; Kandiyoti, R. *Fuel* **1998**, *77*, 933–945.
- Morgan, T. J.; George, A.; Alvarez, P.; Millan, M.; Herod, A. A.; Kandiyoti, R. *Energy Fuels* **2008**, *22*, 3275–3292.
- George, A.; Morgan, T. J.; Alvarez, P.; Millan, M.; Herod, A. A.; Kandiyoti, R. *Fuel* **2010**, *89*, 2953–2970.
- Morgan, T. J.; George, A.; Alvarez, P.; Herod, A. A.; Millan, M.; Kandiyoti, R. *Energy Fuels* **2009**, *23*, 6003–6014.
- Trejo, F.; Ancheyta, J.; Morgan, T. J.; Herod, A. A.; Kandiyoti, R. *Energy Fuels* **2007**, *21*, 2121–2128.
- Karaca, F.; Morgan, T. J.; George, A.; Bull, I. D.; Herod, A. A.; Millan, M.; Kandiyoti, R. *Rapid Commun. Mass Spectrom.* **2009**, *23*, 2087–2098.
- Morgan, T. J.; George, A.; Alvarez-Rodriguez, P.; Millan, M.; Herod, A. A.; Kandiyoti, R. *J. Chromatogr. A* **2010**, *1217*, 3804–3818.
- Guzman, A.; Bueno, A.; Carboognani, L. *Pet. Sci. Technol.* **2009**, *27*, 801–816.
- Schabron, J. F.; Rovani, J. F. *Fuel* **2008**, *87*, 165–176.
- Rogel, E.; Ovalles, C.; Moir, M. E. *Energy Fuels* **2009**, *23*, 4515–4521.
- Rogel, E.; Ovalles, C.; Moir, M. *Energy Fuels* **2010**, *24*, 4369–4374.
- Schabron, J. F.; Rovani, J. F.; Sanderson, M. M. *Energy Fuels* **2010**, *24*, 5984–5996.
- Kok, W. T.; Tüdös, A. J.; Grutters, M.; Shepherd, A. G. *Energy Fuels* **2011**, *25*, 208–214.
- Wise, S. A.; Sander, L. C.; May, W. E. *J. Chromatogr.* **1993**, *642*, 329–349.
- Wise, S. A.; Chesler, S. N.; Hertz, H. S.; Hillpert, L. R.; May, W. E. *Anal. Chem.* **1977**, *49*, 2306–2310.
- Wise, S. A.; May, W. E. *Anal. Chem.* **1984**, *56*, 225–232.
- Lafleur, A. L.; Monchamp, P. A.; Chang, N. T.; Plummer, E. F.; Wormmat, M. J. *J. Chromatogr. Sci.* **1988**, *26*, 337–344.
- Novotny, M.; Hirose, A.; Wiesler, D. *Anal. Chem.* **1984**, *56*, 1243–1248.
- Pace, C. M.; Betowski, L. D. *J. Am. Soc. Mass Spectrom.* **1995**, *6*, 597–607.
- Acevedo, S.; Ranaudo, M. A.; Garcia, C.; Castillo, J.; Fernández, A.; Goncalvez, S. *Colloids Surf., A* **2000**, *166*, 145–152.
- Acevedo, S.; Ranaudo, M. A.; Garcia, C.; Castillo, J.; Fernández, A. *Energy Fuels* **2003**, *17*, 257–261.
- Pernyeszi, T.; Dekany, I. *Colloids Surf., A* **2001**, *194*, 25–39.
- Turgman-Cohen, S.; Fischer, D. A.; Kilpatrick, P. K.; Genzer, J. *ACS Appl. Mater. Interfaces* **2009**, *1*, 1347–1357.
- Turgman-Cohen, S.; Smith, M. B.; Fischer, D. A.; Kilpatrick, P. K.; Genzer, J. *Langmuir* **2009**, *25*, 6260–6269.
- Wang, S.; Segin, N.; Wang, K.; Maslyah, J. H.; Xu, Z. *J. Phys. Chem. C* **2011**, *115*, 10576–10587.

- (55) Skoog, D. A.; Holler, F. J.; Crouch, S. R. *Principles of Instrumental Analysis*, 6th ed.; Thomson Brooks/Cole: Tampa, FL, 2007; pp 831–833.
- (56) Horning, E. C.; Horning, M. G.; Carroll, D. L.; Dzidic, L.; Stillwell, R. N. *Anal. Chem.* **1973**, *45*, 936–943.
- (57) Al-Muhareb, E.; Morgan, T. J.; Herod, A. A.; Kandiyoti, R. *Pet. Sci. Technol.* **2007**, *25*, 81–91.
- (58) Millan, M.; Behrouzi, M.; Karaca, F.; Morgan, T. J.; Herod, A. A.; Kandiyoti, R. *Catal. Today* **2005**, *109*, 154–161.

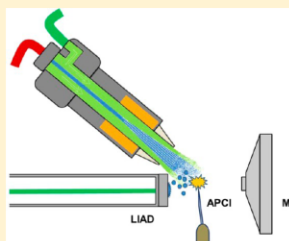
Development of a High-Throughput Laser-Induced Acoustic Desorption Probe and Raster Sampling For Laser-Induced Acoustic Desorption/Atmospheric Pressure Chemical Ionization

David J. Borton,[†] Lucas M. Amundson,[†] Matthew R. Hurt,[†] Alex Dow,[†] Jeremy T. Madden,[†] Garth J. Simpson,[†] and Hilkka I. Kenttämä^{*,†}

[†]Department of Chemistry, Purdue University, 560 Oval drive, West Lafayette, Indiana 47907, United States

Supporting Information

ABSTRACT: Laser-induced acoustic desorption (LIAD) was recently coupled to atmospheric pressure chemical ionization (APCI) and shown to be of great utility for the analysis of a variety of thermally labile nonpolar analytes that are not amenable to ionization via electrospray ionization, such as nonvolatile hydrocarbons. Despite these advancements, LIAD still suffered from several limitations, including only being able to sample a small fraction of the analyte molecules deposited on a Ti foil for desorption, poor reproducibility, as well as limited laser power throughput to the backside of the foil. These limitations severely hinder the analysis of especially challenging analytes, such as asphaltenes. To address these issues, a novel high-throughput LIAD probe and an assembly for raster sampling of a LIAD foil were designed, constructed, and tested. The new probe design allows 98% of the initial laser power to be realized at the backside of the foil over the 25% achieved previously, thus improving reproducibility and allowing for the analysis of large nonvolatile analytes, including asphaltenes. The raster assembly provided a 5.7 fold increase in the surface area of a LIAD foil that could be sampled and improved reproducibility and sensitivity for LIAD experiments. The raster assembly can also improve throughput as foils containing multiple analytes can be prepared and analyzed.



Soft ionization techniques, such as electrospray ionization (ESI) and matrix-assisted laser desorption ionization (MALDI), have greatly improved the analysis of thermally labile and nonvolatile analytes by mass spectrometry.^{1–5} However, both ESI and MALDI are limited to ionization via protonation, deprotonation, or the attachment of a cation or an anion (for ESI, this often relies on ions preformed in solution). Furthermore, ESI preferentially ionizes the most polar components present, which can lead to suppression of the analyte ions' signal, or the signals of the less polar molecules in mixtures. Neither method can ionize compounds that do not contain easily ionizable groups, such as hydrocarbons, and thus have limited applicability toward nonpolar analytes.^{6,7}

Laser-induced acoustic desorption (LIAD) involves firing laser pulses at the backside of a thin metal foil to generate acoustic waves that propagate through the foil and evaporate the intact neutral analyte molecules from the front side of the foil.^{8–11} LIAD is typically coupled with a postionization method, such as electron ionization (EI) or chemical ionization (CI).^{12–15} A combination of LIAD with these ionization methods has been demonstrated to be useful for mass spectrometric analysis of biomolecules, such as nucleotides and peptides, as well as petroleum samples, such as saturated hydrocarbons, base oil fractions, and asphaltenes.^{12,14–17} Conventionally, LIAD has been used in high vacuum in mass spectrometers, such as Fourier-transform ion cyclotron resonance (FT-ICR) instruments.^{12–15,18} However, recently,

LIAD was successfully coupled to atmospheric pressure ionization sources, such as ESI and atmospheric pressure chemical ionization (APCI).^{7,19,20} LIAD/ESI still suffers from the same limitations as ESI itself, such as a strong bias in ionization efficiency toward the most polar compounds. LIAD/APCI does not suffer from this drawback and has been used to successfully examine a variety of analytes, ranging from polar molecules to nonpolar hydrocarbons, including petroleum distillate cuts.^{7,20} However, LIAD/APCI is not without its limitations, such as poor reproducibility, being able to sample only a small portion of the analyte molecules deposited on the foil surface, and the inability to desorb large thermally labile molecules such as asphaltenes.

Previous work demonstrated that higher laser power densities produce more powerful acoustic waves, which might desorb larger analytes.²¹ This was demonstrated to be true when a high power LIAD probe was developed for high-vacuum experiments.²² The same probe was used in the first implementation of LIAD on an APCI source. While this setup allowed for the analysis of heavier analytes than previously possible,⁷ reproducibility from shot to shot was poor, especially for large compounds such as asphaltenes. A key contributor to

Received: January 27, 2013

Accepted: May 16, 2013

Published: May 16, 2013

this issue was the long laser beam path. Although the probe developed for LIAD/APCI was shorter than the previous probe, the laser and external optics (mirrors) were set up some distance from the linear quadrupole ion trap's ion source to allow the instrument to be easily used without LIAD when necessary, which caused beam divergence and hence a large loss in laser power density. Further, the mirrors inside the probe had to be manually aligned without the ability for fine adjustments, which made alignment cumbersome. Finally, the alignment drifted due to vibrations or when switching foils in the probe. These factors led to suboptimal alignment of the optics inside the probe, which was a contributor to the loss of power density and poor reproducibility. To address these issues, a high-power LIAD probe was developed.

Another drawback in the previous practice of LIAD was that a circular area of only roughly 26.5 mm² of the foil's total surface area of 227 mm² was exposed to laser irradiation. Thus, most of the sample deposited on the foil was not utilized. To address this issue, an assembly that allows the foil to be rastered by the laser beam was developed.

The uniformity of the layer of the deposited analyte on the foil is also an important factor that influences the reproducibility of LIAD. Previously, the sample has been deposited on the foil via two methods. The first method, electro-spray deposition, creates a relatively uniform layer of analyte on the foil, but this method is only amenable to polar molecules.²³ Nonpolar analytes, such as petroleum distillate cuts or asphaltene, cannot be deposited using electro-spray because they are nonpolar. Thus, nonpolar analytes have been deposited onto the foils by using the dry-drop technique.¹⁵ While this technique can be used for nonpolar compounds, unlike electro-spray deposition, it deposits nonuniform layers of analyte on the foils. During deposition of the analyte, the solvent tends to move toward the edges of the foil due to cohesion between solvent molecules being greater than the adhesive forces between the solvent and the foil surface, creating areas of high analyte concentration, as well as spots of low analyte concentration on the foil. To overcome this issue, the foil can be gently spun to redistribute the analyte solution over the foil. However, this is a tedious and difficult process, as spinning too slowly will not redistribute the analyte solution and spinning too vigorously will cause the solution to spill off of the foil. Another limitation stems from the fact that some analytes may undergo thermal degradation during this process, as the foil is gently heated to facilitate evaporation of solvent from the foil's surface.

Moreover, electro-spray deposition and dry-drop methods were developed for conventional LIAD that used circular foils. The switch to larger rectangular foils needed for rastering makes it even more difficult to generate evenly coated foils as the new foils are larger than the spray cone area for electro-spray deposition. Further, rotating the rectangular foils without the sample spilling off the foil or pulling back to the edges is challenging for the dry-drop technique. Thus, a need exists for a technique to produce uniform sample layers for many different types of analytes on rectangular LIAD foils. A chamber using drying gas to evaporate solvent and deposit analyte on rectangular LIAD foils was developed to address this need.

EXPERIMENTAL SECTION

All experiments were performed using a linear quadrupole ion trap (LQIT) from Finnigan. The instrument was operated in the positive ion mode and was equipped with an APCI source

operated at 300 °C, with a sheath gas flow rate of 40–50 (arbitrary units) and an auxiliary gas rate of 5 (arbitrary units). The transfer capillary into the instrument was held at 275 °C. For LIAD/APCI, either carbon disulfide was used as a chemical ionization reagent and was flown into the source at a rate of 20 μL/min, or no solvent was used and the nitrogen nebulizer gas (sheath and auxiliary gas) served as the chemical ionization reagent. Both carbon disulfide and nitrogen reagent ions yielded molecular ions for analyte molecules desorbed via LIAD.

A Continuum Minilite Nd:YAG laser (Model Continuum Minilite I, model ML 1) of 532 nm wavelength, 12 mJ (@ 532 nm) nominal power, 10 Hz repetition rate, 1 cm⁻¹ line width, < 3 mrad divergence, and beam diameter of 3 mm, was used to perform LIAD. The laser described previously, equipped with kinematically mounted high-power reflective mirrors for beam path alignment, was used in the new LIAD setup.⁷ Deposition of a sample on a foil was done in the new drying gas sample preparation chamber. The samples were dissolved in carbon disulfide and pipetted into the chamber. The process is described in detail in Results and Discussion.

RESULTS AND DISCUSSION

Novel High Throughput LIAD Probe. When LIAD is coupled to a linear quadrupole ion trap with an atmospheric pressure chemical ionization (APCI) source, many of the considerations (such as desorbing neutral molecules on axis with the magnetic field for the FT-ICR) that required the use of a mirror assembly internal to the conventional LIAD probe are no longer a factor.²² Hence, the internal mirror assembly, which guided the laser beam off axis onto the foil, was removed, thus eliminating the problems related to the alignment of the mirror assembly.

To overcome the issue of poor reproducibility and loss of laser power density in previous LIAD/APCI experiments performed on a LQIT,⁷ a new LIAD probe was designed that focuses and recollimates the laser beam as it travels from the laser head to the backside of the foil, by use of a pair of telecentric lenses, with a third lens used to focus the laser beam onto the backside of the foil (laser spot diameter at foil was roughly 0.3 mm). The probe consists of two brass tubes and three lens holders. Each lens holder contains a telecentric lens (Figure 1). By focusing and recollimating the laser beam, beam

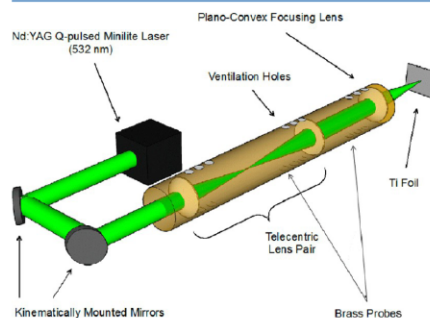


Figure 1. Illustration of the novel high throughput LIAD probe. The lens holders threaded into the spacer tubes are not shown.

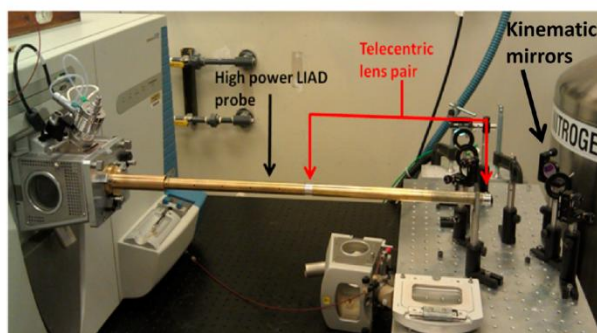


Figure 2. Image of the novel high throughput LIAD probe. The tip is held by the raster assembly on the left side of the picture. The high power probe can readily be removed for changing of sample foils without disturbing the kinematic mirrors seen on the far right of the image.

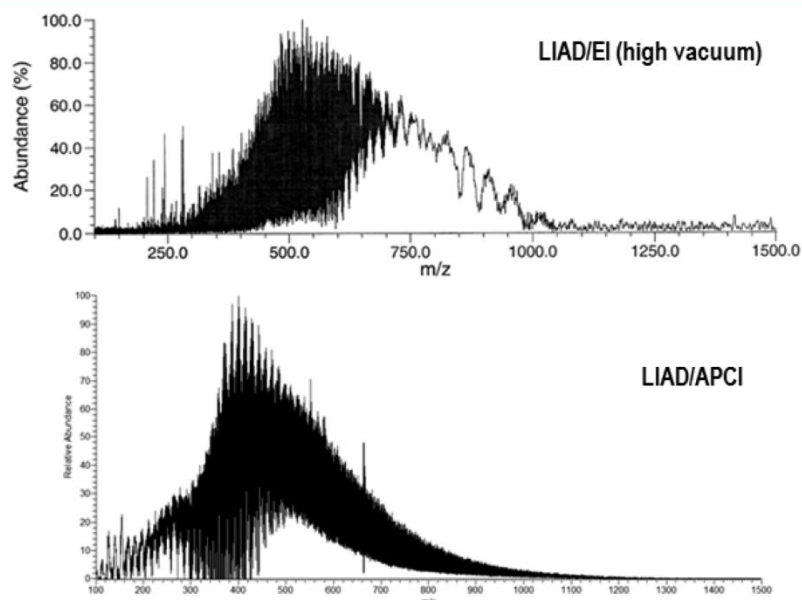


Figure 3. (top) High vacuum LIAD/EI (70 eV) mass spectrum of an asphaltene sample measured using a 3 T FTICR. (bottom) LIAD/APCI mass spectrum of the same asphaltene sample measured, using nitrogen as the chemical ionization reagent, in a LQIT. The molecular weight distributions shown in the two mass spectra are in good agreement.

divergence can be minimized to avoid losses in laser power density over the approximately three foot beam path. Details of the probe are provided in the Supporting Information.

The above probe fits into an adapter built into the raster assembly (discussed below), which bolts onto the atmospheric pressure ionization chamber of the LQIT. The other end is held by a custom holder affixed to a stand secured to the breadboard

table top the setup sits on. The distance between the ionization chamber and external kinematically mounted mirrors is such that the probe can easily be removed without moving the external optics, which is important when changing samples in order to avoid the need to realign the optics with each new sample. Once the flange with new sample is in place, the probe is simply reinserted into the adapter the proper distance from

the foil (marked on the probe) without the need for realignment of any of the optics. A photograph of the high throughput probe is provided in Figure 2.

Performance of the New High-Throughput LIAD Probe. The new high-throughput LIAD probe with a telecentric lens pair makes alignment of the laser beam to the backside of the foil much easier than for the old setup.^{7,22} Furthermore, since the lens pair focuses and recollimates the laser beam, the power lost over the path of the beam is greatly reduced. The previous LIAD setup²² suffered from a 75% loss of power over its beam path. Thus, when using the Continuum Minilite II laser, a maximum power density of only 2000 MW/cm² at the backside of the foil was achieved when the power density at the laser head was 8000 MW/cm². The new probe design results in the loss of only 2% of the initial laser power. A maximum power density of 8200 MW/cm² at the backside of the foil was measured when a power density of 8300 MW/cm² was measured at the head of the same laser used in the earlier experiments. This is over a 4-fold increase in laser power at the foil compared to the previous setup, allowing for the use of a majority of the maximum laser power output. Power densities for both setups were measured using an Ophir power meter (model no. 7Z0287), placed where a foil would be fixed for a LIAD-APCI experiment. The power density at the position of the foil was divided by the power density measure at the head of the laser to find the percent of power density lost over the beam path of the laser beam.

An example of the performance of the new high-throughput probe can be seen in Figure 3, which shows a LIAD/APCI mass spectrum measured for an asphaltene sample (crude oil fraction that dissolves in toluene but not *n*-heptane) dissolved in carbon disulfide (approximately 1 mg/mL) and deposited on a Ti foil by using the dry drop method, as described previously.¹⁵ The foil was attached to the sample stage of a raster assembly (described below), and the analyte was desorbed using LIAD. The gaseous analyte was ionized using APCI with nitrogen as the reagent gas wherein N₂⁺ generated by Corona discharge abstracts an electron from an analyte molecule, thus generating a radical cation of the analyte. The resulting mass spectrum shows a distribution of ions starting at *m/z* 200 and ending at *m/z* 1050. This distribution is in good agreement with that previously determined,¹⁵ by using LIAD/EI (70 eV), as seen in Figure 3. Asphaltenes did not yield a detectable signal when using the previous⁷ LIAD/APCI setup but with the higher power that is achieved at the backside of the foil by using the high-throughput probe, asphaltenes can be desorbed into the gas phase and detected after ionization (Figure 3).

Novel LIAD Rastering Assembly. As discussed in the introduction, much of the analyte deposited on the foil is not sampled during a traditional LIAD experiment. To address this issue, a rastering assembly was built to allow for a greater portion of the foil to be sampled, which in turn will increase the total ion signal and enable multiple experiments with more than one analyte per foil. When designing the rastering assembly, a few important criteria had to be met. The assembly had to allow for the movement of the foil in the *x* and *y* directions (by using a fixed laser beam path geometry) to be able to sample the entire foil surface. Further, the setup needed to allow the position of the new high throughput LIAD probe to be adjustable in the *z* direction (desorption axis) to be able to change the focal volume and power density of the laser beam at the backside of the foil. Finally, the setup had to allow for foils

to be changed without disturbing the optical components of the LIAD setup.

The LIAD rastering assembly is shown in Figure 4. The assembly has a movable brass holder (inner diameter of 0.74", outer diameter of 1.03") for the high throughput LIAD probe

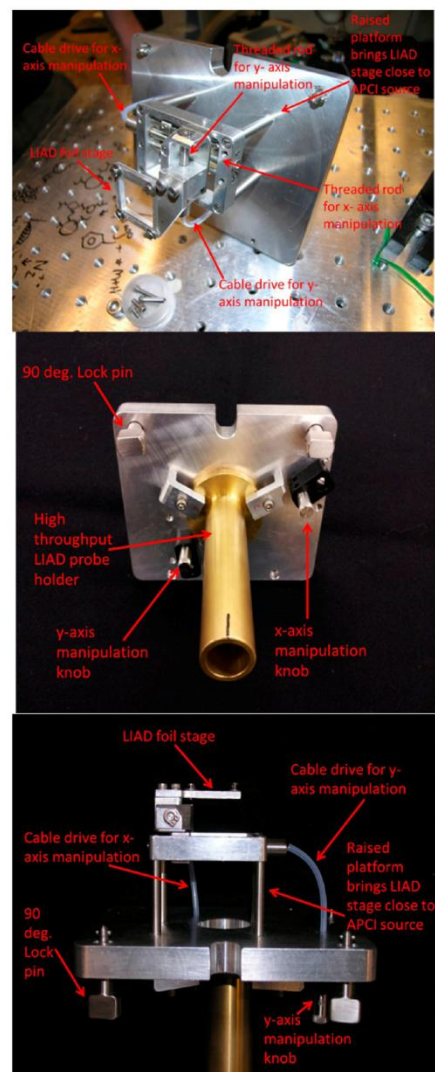


Figure 4. Images of the raster LIAD assembly.

that houses the final 3.75" of the tip of the probe. This allows the location of the probe tip to be optimized in the x - y plane for efficient ionization, which requires that the beam path overlaps with the tip of the corona discharge needle. Furthermore, this holder allows the high throughput probe to be moved along the z axis to change the focal volume and power density of the laser beam at the backside of the foil. The LIAD foil itself is held in place by tightening four screws with washers on the foil stage. The stage is attached to two perpendicular threaded rods (1/32" thread), which move the stage in the x and y directions, allowing the entire foil to be sampled. The threaded rods are attached to two cable drives, which are connected to two knobs mounted on the outside of the raster assembly base. Manually turning one knob will move the stage in the y direction (vertically), while the other knob controls movement in the x direction (horizontally). The assembly bolts directly onto the commercial ionization chamber (Ion Max box) of the Finnigan LQIT in place of its original front access door, as illustrated in Figure S1 of the Supporting Information. The assembly uses the same bolts (#4/40) and 90° lock pins as the original door.

Performance of the Raster Assembly. The rastering LIAD assembly greatly increases the surface area of the LIAD foil that can be sampled. Figure 5 shows a used raster LIAD foil

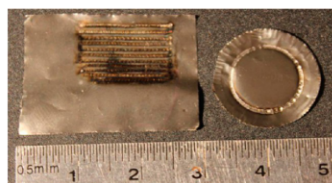


Figure 5. Image comparing a raster LIAD foil (left; about 500 laser shots) to a conventional LIAD foil (right; about 85 laser shots).

compared to a conventional LIAD foil. The raster assembly sampled roughly 133 mm² of the foil covered by analyte compared to 26.5 mm² for the conventional setup. This is a 5-fold increase in the utilized foil surface area.

On the basis of previous LIAD/APCI work, molecules on 1/4 of the sample area of the foil had to be evaporated by using LIAD to produce acceptable signal-to-noise ratio with the conventional LIAD/APCI setup, allowing for a maximum of four experiments per foil.⁷ This corresponds to desorbing analyte from an area of roughly 6.63 mm² of the foil's surface. The raster assembly allows for 133 mm² of the foil surface to be sampled, but half of this surface area is unused to allow a space in between the rows where the laser irradiates the back of the foil. This prevents overlap for consecutive shots so that a maximum amount of analyte molecules is desorbed with each shot. This means that at least 10 experiments can be performed per foil, a nearly 3-fold increase over the conventional setup. Depositing multiple analytes per foil in specific sections would allow for the analysis of multiple samples per foil, thus greatly improving throughput.

The raster assembly also provides several other benefits, such as improved sensitivity and reproducibility. With the ability to sample a large surface area, multiple spectra measured during a lengthy LIAD experiment can be averaged to account for uneven sample deposition on the foil surface or a low

concentration of sample. An example of this is provided in Figure S2 of the Supporting Information.

Design and Development of a Drying Gas Chamber for Sample Foil Preparation. To address the issues hindering the production of more uniform sample layers on foils, a foil preparation chamber was designed that uses an inert drying gas to evaporate the solvent from the analyte solution. The chamber consists of four main parts: (A) stainless steel block, (B) Teflon foil holder, (C) stainless steel forming mandrel, and (D) lid, shown in Figure 6. A milled out cavity is

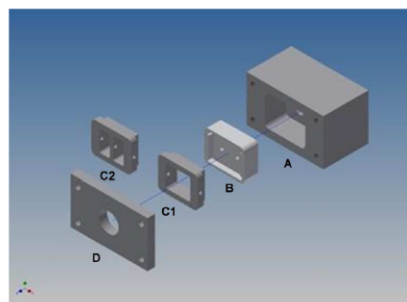


Figure 6. The components of the LIAD foil preparation chamber. Each part is labeled for easy referencing in the description of the chamber. A is the primary cavity, B the foil holder, C1 the forming mandrel, and D is the lid. C2 is an interchangeable mandrel that can replace C1, allowing for the preparation of a foil with two different analytes on separate regions of the foil.

centered on the stainless steel block A. Within this cavity are two wells that are milled out further to collect any solvent that may leak from the foil. The foil holder, B, was made of Teflon and designed to be inserted into the cavity of part A. Part C (either C1 or C2) is a forming mandrel made from stainless steel (similar to A) and has a mushroom shape when viewed from the side. A cutout centered horizontally and vertically creates a rectangular hole in the center of C1. Once the foil is inserted into B, C1 is inserted, so that its lower half slides into the cavity of B. This forms a seal between the foil and B, so that the foil is exposed in the cutout of C1. This region of exposed foil is where the analyte solution is deposited. Alternatively, C1 can be exchanged for C2 with a bridge down the center, thus containing two separate regions for sample deposition, which allows for two different samples to be deposited on a single foil for higher sample throughput. Finally, to complete the assembly, a lid, D, is set atop A. When the bolts are tightened, an O ring forms a seal between parts A and D so that the drying gas does not leak excessively from the chamber during foil preparation. Also centered on the lid is a clearance hole. This hole is filled with a rubber septum during foil preparation. Two needles are inserted into the septum. One needle has a 90 degree bend in the shaft so that the tip, after piercing the septum, will be parallel with the titanium foil. This needle is hooked up to a compressed gas cylinder of an inert dry gas, such as argon or nitrogen, which is used to evaporate the solvent. The needle needs to be bent so that the drying gas does not flow directly onto the foil surface, which would create a pocket where the sample solution is blown away, exposing

bare foil. The other needle, which exhausts drying gas from the chamber to avoid pressure build up, is unmodified. A detailed description of the chamber is provided in the Supporting Information.

To prepare a foil, it is inserted into B and into the chamber. Once the chamber is assembled with the foil inside and before the septum is inserted, the chamber is filled with the analyte solution by using a pipet until the solvent completely covers the titanium foil as a thin layer. Volatile solvents are best suited for this technique as they evaporate quickly. The septum with the two needles is then inserted to gently flow drying gas over the sample. The flow rate for the drying gas is very low (just a few bubbles per second when the needle is inserted into a vial of water). For samples dissolved in CS_2 , 10 min is often more than enough time to evaporate the solvent. The septum is then removed to check the condition of the foil. The previous steps are repeated if a more concentrated sample layer is desired.

Performance of the Drying Gas Sample Preparation Chamber. Use of the drying gas chamber produces a sample foil with a more uniform sample layer than the dry-drop method, as shown in Figure 7. The relative standard deviation



Figure 7. (Left) A LIAD foil with asphaltene deposited on it by using the dry-drop technique, showing that the analyte layer is very uneven, with spots of heavy sample amounts and areas of little to no sample. (Right) A LIAD foil with asphaltene deposited on it by using the drying gas chamber, showing that the surface is more uniform than for the dry-drop method.

determined for the rastering and round foils are 60% and 22.5%, respectively. The foils shown in Figure 7 have asphaltene deposited on them, which could not be done using electrospray deposition that is only suitable for polar compounds because asphaltene is comprised of nonpolar hydrocarbons.

Figure S4 of the Supporting Information shows the total ion current as a function of time produced by the mass spectrometer, while LIAD was rastering over a foil to which a sample was deposited using the dry-drop method and one to which the sample was deposited using the drying gas chamber. The foil prepared using the drying gas chamber shows a much more stable total ion current than the foil prepared using the dry-drop method, indicating that a more uniform layer of analyte was deposited using the drying gas chamber. The chamber also greatly simplifies producing rectangular foils for raster sampling. Furthermore, using the forming mandrel C2, foils with two different analytes deposited to them can be prepared, as seen in Figure S5 of the Supporting Information. This will help increase the throughput.

CONCLUSIONS

A novel high throughput LIAD probe using a telecentric lens pair was developed for LIAD/APCI, which increases the maximum laser power density at the backside of the LIAD foil by minimizing beam divergence. The new probe design allows

98% of the initial laser power to reach the backside of the foil, as opposed to a mere 25% for the previous setup.²² The higher laser power throughput allows for more efficient evaporation of heavy analytes into the gas phase, as evidenced by the LIAD/APCI mass spectrum of asphaltene obtained using the new probe and the novel rastering assembly. A mass spectrum could not be measured for asphaltene using the previous LIAD/APCI setup.⁷

A raster assembly was constructed to allow for a greater area of the LIAD foil to be sampled. The assembly is fastened to the commercial ionization chamber of a Thermo Scientific LTQ. The rastering setup has a stage mounted on two perpendicular threaded rods that move in the x - y plane, allowing much more surface area of a foil to be sampled. Currently, the stage is manipulated manually by two external knobs, but automating the setup by using electric motors and computer control should be achievable with minimal changes to the current design. The raster assembly improves sensitivity and reproducibility by allowing for multiple scans to be averaged. Alternatively, more LIAD experiments can be performed per foil than for the conventional setup, as the raster setup samples up to 150 mm² of foil compared to 26.5 mm² for the previous setup. The raster assembly also can be used to analyze multiple analytes deposited on separate sections of a foil, thus greatly improving the throughput of LIAD/APCI.

Finally, a chamber was designed and constructed that uses an inert drying gas to prepare square sample foils for LIAD. The chamber can be used to prepare foils with either polar or nonpolar analytes, thus overcoming the inability of electrospray deposition to spray nonpolar compounds. Furthermore, the chamber produces a more uniform layer of analyte on the foil surface than the dry-drop method. The chamber also has interchangeable forming mandrels, which allow for one or two different analytes to be deposited on the foil surface. This will improve the throughput as multiple analytes per foil can be studied.

ASSOCIATED CONTENT

Supporting Information

Additional information as noted in text. This material is available free of charge via the Internet at <http://pubs.acs.org>.

AUTHOR INFORMATION

Corresponding Author

*E-mail: hilkka@purdue.edu. Tel: (765) 494-0882. Fax: (765) 494-0239.

Notes

The authors declare no competing financial interest.

ACKNOWLEDGMENTS

This work was supported as part of the Center for Direct Catalytic Conversion of Biomass to Biofuels (C3Bio), an Energy Frontier Research Center funded by the U.S. Department of Energy, Office of Science, Office of Basic Energy Sciences under Award Number DE-SC0000997.

REFERENCES

- (1) Whitehouse, C. M.; Dreyer, R. N.; Yamashita, M.; Fenn, J. B. *Anal. Chem.* **1985**, *57* (3), 675–679.
- (2) Yamashita, M.; Fenn, J. B. *J. Phys. Chem.* **1984**, *88* (20), 4451–4459.
- (3) Karas, M.; Bahr, U.; Gießmann, U. *Mass Spectrom. Rev.* **1991**, *10* (5), 335–357.

- (4) Fenn, J.; Mann, M.; Meng, C.; Wong, S.; Whitehouse, C. *Science* **1989**, *246* (4926), 64–71.
- (5) Tanaka, K.; Waki, H.; Ido, Y.; Akita, S.; Yoshida, Y.; Yoshida, T.; Matsuo, T. *Rapid Commun. Mass Spectrom.* **1988**, *2* (8), 151–153.
- (6) Marshall, A. G.; Rodgers, R. P. *Acc. Chem. Res.* **2004**, *37*, 53–59.
- (7) Gao, J.; Borton, D.; Owen, B.; Jin, Z.; Hurt, M.; Amundson, L.; Madden, J.; Qian, K.; Kenttämää, H. *J. Am. Soc. Mass Spectrom.* **2011**, *22* (3), 531–538.
- (8) Golovlev, V. V.; Allman, S. L.; Garrett, W. R.; Taranenko, N. L.; Chen, C. H. *Int. J. Mass Spectrom. Ion Processes* **1997**, *169–170* (0), 69–78.
- (9) Lindner, B. *Int. J. Mass Spectrom. Ion Processes* **1991**, *103* (2–3), 203–218.
- (10) Pérez, J.; Petzold, C.; Watkins, M.; Vaughn, W.; Kenttämää, H. *J. Am. Soc. Mass Spectrom.* **1999**, *10* (11), 1105–1110.
- (11) Pérez, J.; Ramírez-Arizmendi, L. E.; Petzold, C. J.; Guler, L. P.; Nelson, E. D.; Kenttämää, H. *Int. J. Mass Spectrom.* **2000**, *198* (3), 173–188.
- (12) Duan, P.; Qian, K.; Habicht, S. C.; Pinkston, D. S.; Fu, M.; Kenttämää, H. *Anal. Chem.* **2008**, *80* (6), 1847–1853.
- (13) Crawford, K. E.; Campbell, J. L.; Fiddler, M. N.; Duan, P.; Qian, K.; Gorbaty, M. L.; Kenttämää, H. *Anal. Chem.* **2005**, *77* (24), 7916–7923.
- (14) Campbell, J. L.; Crawford, K. E.; Kenttämää, H. *Anal. Chem.* **2004**, *76* (4), 959–963.
- (15) Pinkston, D. S.; Duan, P.; Gallardo, V. A.; Habicht, S. C.; Tan, X.; Qian, K.; Gray, M.; Müllen, K.; Kenttämää, H. *Energy Fuels* **2009**, *23* (11), 5564–5570.
- (16) Somuramasami, J.; Kenttämää, H. *J. Am. Soc. Mass Spectrom.* **2007**, *18* (3), 525–540.
- (17) Petzold, C. J.; Ramírez-Arizmendi, L. E.; Heidbrink, J. L.; Pérez, J.; Kenttämää, H. *J. Am. Soc. Mass Spectrom.* **2002**, *13* (2), 192–194.
- (18) Duan, P.; Fu, M.; Pinkston, D. S.; Habicht, S. C.; Kenttämää, H. *J. Am. Chem. Soc.* **2007**, *129* (30), 9266–9267.
- (19) Cheng, S.-C.; Cheng, T.-L.; Chang, H.-C.; Shiea, J. *Anal. Chem.* **2009**, *81* (3), 868–874.
- (20) Nyadong, L.; McKenna, A. M.; Hendrickson, C. L.; Rodgers, R. P.; Marshall, A. G. *Anal. Chem.* **2011**, *83* (5), 1616–1623.
- (21) Shea, R. C.; Petzold, C. J.; Campbell, J. L.; Li, S.; Aaserud, D. J.; Kenttämää, H. *Anal. Chem.* **2006**, *78* (17), 6133–6139.
- (22) Shea, R. C.; Habicht, S. C.; Vaughn, W. E.; Kenttämää, H. *Anal. Chem.* **2007**, *79* (7), 2688–2694.
- (23) McNeal, C. J.; Macfarlane, R. D.; Thurston, E. L. *Anal. Chem.* **1979**, *51* (12), 2036–2039.

Comparison of the Structures of Molecules in Coal and Petroleum Asphaltenes by Using Mass Spectrometry

Matthew R. Hurt, David J. Borton, Heewon J. Choi, and Hilkka I. Kenttämä*

Department of Chemistry, Purdue University, 560 Oval Dr., West Lafayette, Indiana 47906, United States

ABSTRACT: Asphaltenes are a complex mixture of aromatic compounds that are present in petroleum and liquefied coal and have unknown molecular structures. Determination of the molecular structures of asphaltenes is greatly hindered by the extreme complexity of the mixtures. The average molecular weight of coal asphaltenes is known to be roughly half that of petroleum asphaltenes. In this study, tandem mass spectrometry experiments were used to compare the fragmentation patterns of molecular ions of the same mass-to-charge (m/z) value derived from coal and petroleum asphaltenes. The fragmentation pathways of the asphaltene ions were used to determine structural differences between the two types of asphaltenes. This type of analysis is new to the field of asphaltenes research and has not yet been utilized to compare coal and petroleum asphaltenes. Thus, this study was performed to both confirm its viability as well as further corroborate previous data gathered using different techniques. The results reported here demonstrate that the molecules in coal asphaltenes have shorter alkyl chains and larger aromatic cores than their petroleum-derived counterparts with the same molecular weight (MW). Furthermore, they have a higher aromatic-to-alkane carbon ratio, independent of the MW. However, the typical petroleum and coal asphaltenes (when considering the most abundant molecules in each) have a similarly sized aromatic core (~ 8 rings), but very different total lengths of the alkyl side chains (~ 4 for coal asphaltenes, ~ 22 for petroleum asphaltenes).

■ INTRODUCTION

Crude oil is a highly complex mixture of compounds that is divided into different fractions based on the compounds boiling points and solubility.^{1,2} Asphaltenes are defined as the fraction of crude oil that is soluble in toluene and insoluble in *n*-heptane.³ This fraction contains many of the least-volatile compounds of crude oil. Most of the compounds are thought to be aromatic but their structures are unknown. Asphaltenes are problematic for the petroleum industry, because they precipitate in pipes, which results in restricted flow and clogs. Furthermore, they contain metals that foul catalysts during oil processing. Both of these behaviors increase production costs.^{3,5} The recent shift to the utilization of heavier crude oils that contain greater amounts of asphaltenes due to a depletion of oil reserves with a low asphaltene content further emphasizes the need to acquire a better understanding of the molecular structures of asphaltenes. If even the general features of the molecular structures of asphaltenes can be determined, methods for reducing or eliminating the problems they cause might be devised, along with increasing the potential of converting them to useful compounds.⁶

One approach that has been taken to address this issue is the comparison of the physical and chemical properties of coal and petroleum asphaltenes, since these properties are dictated by the structures of the molecules. The molecular weight distribution (MWD) for coal asphaltenes has been determined to be about half that of petroleum asphaltenes.^{6,7} The lower molecular weights of coal asphaltenes should make it easier to determine their molecular structures, which may facilitate the determination of the molecular structures for petroleum asphaltenes.⁸

Two structure classes are currently debated for asphaltenes: the island model and the archipelago model.¹ The island model consists of molecules with a single aromatic core containing several fused aromatic rings with alkyl chains branching off the core.¹

The archipelago model consists of molecules with several aromatic cores connected by alkyl bridges.¹ Experiments using time-resolved fluorescence depolarization suggest that asphaltenes mainly consist of molecules fitting the island model.^{9,10} Other methods, such as Taylor dispersion diffusion and NMR pulsed field gradient measurements, along with others, have revealed similar results.^{3,8,11} Studies using NMR and average structural parameter calculations have found that a small amount of archipelago-type molecules can be present in asphaltenes.¹² Recently, we published a study comparing the fragmentation patterns of ionized model compounds of asphaltenes with ions derived from asphaltenes by using mass spectrometry. The results suggest that molecules with structures corresponding to the island model dominate.¹³

Asphaltenes have proven to be a challenge to analyze by using mass spectrometry.⁶ Asphaltenes tend to degrade or aggregate when they are introduced into the gas phase.¹⁴ Ionization bias is also a problem when attempting to ionize mixtures of this complexity by using ionization methods such as electrospray ionization (ESI) and matrix-assisted laser desorption/ionization (MALDI).¹⁵ Both ESI and MALDI predominantly ionize the most polar molecules present, thus often giving no signal for a large portion of the compounds present. Atmospheric pressure chemical ionization (APCI) was used here for the analysis of asphaltenes because it exhibits less bias than ESI and MALDI and has previously been shown to be suitable for the analysis of petroleum.¹⁶ Toluene is a solvent commonly used to dissolve asphaltenes, but our recent research using APCI with toluene as a solvent for evaporation and ionization of asphaltene model

Received: December 9, 2012

Revised: May 22, 2013

Published: May 29, 2013

compounds showed that toluene produces both protonated molecules ($M+H^+$) and molecular ions ($M^{+\bullet}$).¹³ The possible production of two different ions for each compound is problematic, since it further convolutes the mass spectrum measured for a complex mixture, such as asphaltenes. To address this problem, carbon disulfide was used as the solvent for asphaltenes instead of toluene. This approach produces only stable molecular ions for the model compounds of asphaltenes.¹⁷

In this study, tandem mass spectrometry experiments were carried out using a Thermo Scientific linear quadrupole ion trap (LQIT), as well as a LQIT coupled with a Fourier transform-ion cyclotron resonance (FT-ICR) system. Several molecular ions with varying m/z values derived from the coal and petroleum asphaltenes were isolated and subjected to collisionally activated dissociation (CAD). Comparison of their fragmentation pathways yielded information about the differences in the molecular structures of coal and petroleum asphaltenes.

EXPERIMENTAL SECTION

Chemicals. The petroleum asphaltenes samples originated from a Russian oil field and were obtained by heptane precipitation. The coal asphaltenes were generously donated by Dr. Oliver Mullins. They had been extracted from coal that originated from Tanito Harum, Indonesia. The coal liquefaction and asphaltene extraction method has been previously described in the literature.¹⁰ Carbon disulfide

(>99.9%) and heptanes (99+%) were purchased from Sigma-Aldrich (St. Louis, MO) and used without further purification. Both asphaltene samples were sonicated for 1 h in *n*-heptanes and centrifuged to remove the maltene content.

Instrumentation. A Thermo Scientific LTQ linear quadrupole ion trap (LQIT) and a LQIT coupled to a FT-ICR mass spectrometer were used for mass spectrometric analyses. The asphaltenes were dissolved in carbon disulfide at a concentration of 0.5 g/mL and then introduced into the APCI source via direct infusion from a Hamilton 500 μ L syringe through the instrument's syringe pump at a rate of 20 μ L per minute. The APCI source was set at 300 °C. Several ions were isolated and subjected to CAD. The isolation window used was either 0.3 or 2 Da (selected m/z value ± 1) and a CAD energy of 35 arbitrary units was used. Both were controlled by the LTQ software. The LQIT-FT-ICR instrument was used to determine the elemental compositions of interesting ions, because of the accurate mass measurement capability of the FT-ICR system.

RESULTS AND DISCUSSION

For this study, asphaltenes derived from liquefied coal were compared to the petroleum asphaltenes samples. Asphaltenes were dissolved in carbon disulfide and ionized via positive-mode APCI since this approach is known to form stable molecular ions ($M^{+\bullet}$) for the model compounds of asphaltenes.¹⁷ The mass spectra measured for these ions yielded the MWDs, while the average molecular weight (AVG MW) values were derived from the MWDs using eq 1 (see Table 1).

Table 1. Molecular Weight Distributions (MWD) and Average Molecular Weights (AVG MW) Determined for Molecules in Coal and Petroleum Asphaltenes, as Well as the Estimated Minimum Total Number of Carbon Atoms in All Side Chains and Estimated Core Sizes, Given for Ions with Selected m/z Values

	coal	petroleum	difference ^a		coal	petroleum	difference ^a
MWD	200–800 Da	275–1450 Da			Ion of m/z 606		
AVG MW	443 \pm 33 Da	708 \pm 14 Da	265 Da	carbons in side chains	5	17	12
	Ion of m/z 220			estimated core size	10	7	–3
carbons in side chains	3			Ion of m/z 647			
estimated core size	3			carbons in side chains	5	17	12
	Ion of m/z 285			estimated core size	11	8	–3
carbons in side chains	4			Ion of m/z 677			
estimated core size	4			carbons in side chains	5	19	14
	Ion of m/z 325			estimated core size	12	8	–4
carbons in side chains	4			Ion of m/z 688			
estimated core size	5			carbons in side chains	6	22	16
	Ion of m/z 360			estimated core size	12	7	–5
carbons in side chains	5	5	0	Ion of m/z 704			
estimated core size	6	6	0	carbons in side chains	6	22	16
	Ion of m/z 418			estimated core size	12	8	–4
carbons in side chains	4	6	2	Ion of m/z 736			
estimated core size	7	6	–1	carbons in side chains	5	17	12
	Ion of m/z 456			estimated core size	13	10	–3
carbons in side chains	4	8	4	Ion of m/z 780			
estimated core size	8	7	–1	carbons in side chains		25	
	Ion of m/z 490			estimated core size		8	
carbons in side chains	5	11	6	Ion of m/z 810			
estimated core size	8	6	–2	carbons in side chains		26	
	Ion of m/z 515			estimated core size		9	
carbons in side chains	5	10	5	Ion of m/z 850			
estimated core size	9	7	–2	carbons in side chains		27	
	Ion of m/z 530			estimated core size		9	
carbons in side chains	5	12	7	Ion of m/z 875			
estimated core size	9	7	–2	carbons in side chains		35	
				estimated core size		7	

^aDifference = MW petroleum – MW coke.

$$\text{AVG MW} = \frac{\sum (m/z) \times \text{area}(\text{all peaks})}{\sum \text{area}(\text{all peaks})} \quad (1)$$

Tandem mass spectrometry experiments were performed to estimate the minimum combined length of the alkyl chains branching from the core. This was achieved by subjecting several isolated molecular ions of different m/z values to CAD and by counting the methylenes in the observed consecutive alkyl losses until the abundance of the corresponding fragment ions was <2%, relative to the abundance of the most abundant ion, as described previously.¹³ The same fragment ions were used to determine the molecule's core sizes by estimating the number of fused rings required to reach the masses of those fragment ions (methylene functional groups possibly left onto the core after benzylic cleavages of the alkyl chains were included in this estimate). An example of both procedures is shown in Figure 1 for a model compound. The determination of the number of fused rings is a rough estimate, since it does not take into account the presence of heteroatoms, but this should not change the values significantly. The accuracy of these determinations is still under investigation and they are being used here for comparison only due to the lack of suitable model compounds that adequately simulate the CAD mass spectra of ions derived from asphaltenes.

Figure 2 displays a comparison of the MWD measured for the coal and petroleum asphaltenes. The observed MWD for coal asphaltenes ranges from 200 Da to 800 Da, with a weighted MW average of 443 ± 33 Da, while the MWD for the petroleum asphaltenes ranges from 275 Da to 1500 Da, with a

weighted MW average of 708 ± 14 Da. These data agree with previous studies that were conducted on coal and petroleum asphaltenes by using different methods.⁶

Based on the hydrogen to carbon (H/C) ratios measured previously using other experimental methods (87–91 wt % carbon, 5–7 wt % hydrogen in coal asphaltenes and 79–82 wt % carbon, 7–8 wt % hydrogen in petroleum asphaltenes), it has been concluded that coal asphaltenes have a higher (aromatic carbon):(alkane carbon) ratio than petroleum asphaltenes.^{8,18} To determine the extent of aromaticity of the molecules in the samples studied here, CAD was conducted on selected molecular ions derived from each sample. Because of the low ion signal that is generated by these complex mixtures, a relatively wide (2 Da) window was used for isolating ions for CAD in most experiments. From high-resolution data collected in our laboratories and in others, it has been determined that this m/z range may contain 5–15 abundant isobaric ions.¹⁹ All these ions may contribute to the CAD mass spectrum. Hence, a narrower isolation window of 0.3 was also used in a few cases (Figure 3). However, the main fragment ions and fragmentation patterns were found to be independent of the size of the ion isolation window (Figure 3).

Figure 4 displays typical CAD mass spectra measured for ions of $m/z 677 \pm 1$ Da derived from coal and petroleum asphaltenes. These CAD mass spectra are similar to those measured earlier for petroleum asphaltenes, showing systematically decreasing abundances for fragment ions formed via the loss of larger alkyl radicals.^{13,14} The identity of the

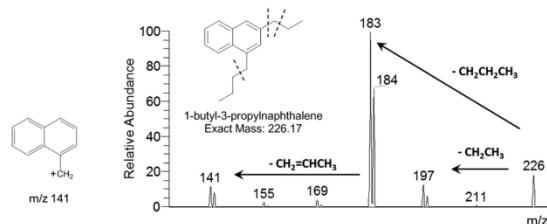


Figure 1. CAD mass spectrum measured for 1-butyl-3-propylnaphthalene molecular ion of $m/z 226$ generated by APCI/CS₂. An approximation of the minimum total number of carbons in all alkyl chains and the core size is obtained from the smallest fragment ion of $m/z 141$ (resulting from the loss of propene from the ion of $m/z 183$ formed by the loss of a propyl radical from the molecular ion), revealing the presence of at least six C atoms in all alkyl chains and two fused rings (with an attached methylene group).

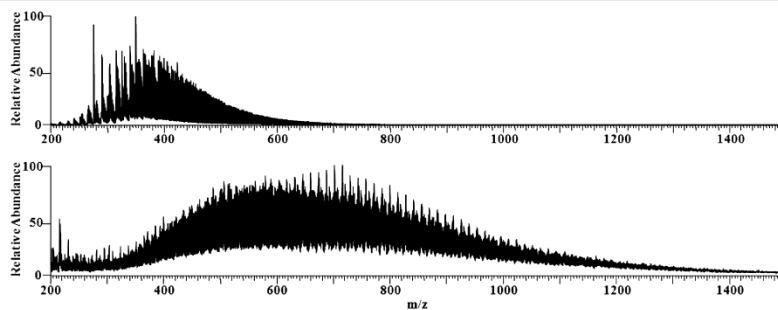


Figure 2. APCI/CS₂ mass spectra of coal asphaltenes (top) and petroleum asphaltenes (bottom).

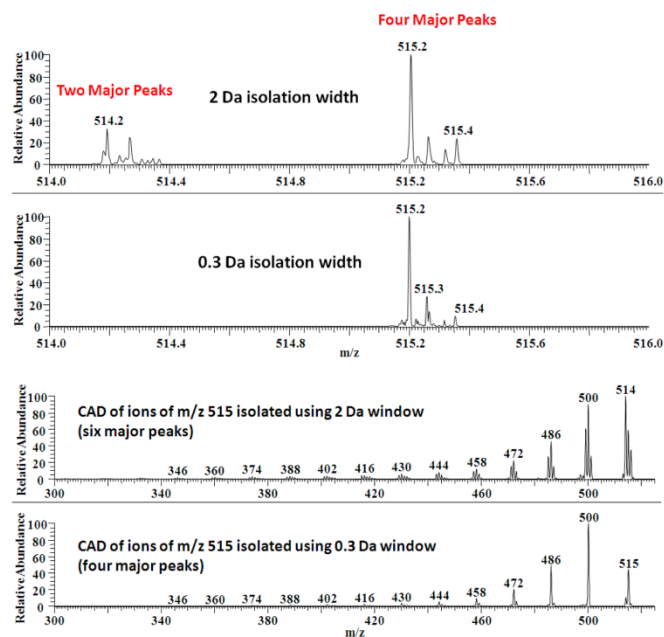


Figure 3. Mass spectra obtained from asphaltenes; the top two mass spectra show isolation of ions of m/z 515 from petroleum asphaltenes by using 2 and 0.3 Da isolation windows, and the bottom two spectra are CAD mass spectra measured for the ions isolated by using 2 and 0.3 Da isolation windows.

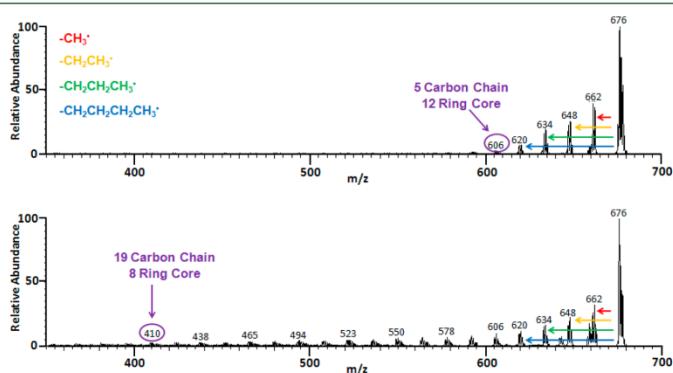


Figure 4. CAD mass spectra measured for ions of m/z 677 ± 1 derived from coal asphaltenes (top) and petroleum asphaltenes (bottom). The total number of carbons in the side chains and likely core size were estimated as described in the text.

fragmentations was determined by using high-resolution measurements such as those depicted in Figure 5.

The fragmentation patterns seen in Figure 4 are believed to correspond to island-type ionized molecules, because of the lack of facile losses of apparently random large highly aromatic

neutral molecules that would be expected for archipelago-type molecules, based on previous studies on asphaltene model compounds.¹³ As indicated in Figure 4, the most favored lost neutral fragments correspond to a series of alkyl radicals ranging from methyl up to an alkyl radical with 19 carbons,

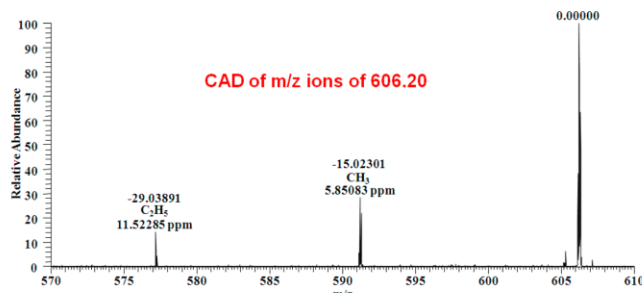


Figure 5. High-resolution CAD mass spectrum measured for ions of m/z 606.20 \pm 0.15 derived from petroleum asphaltenes.

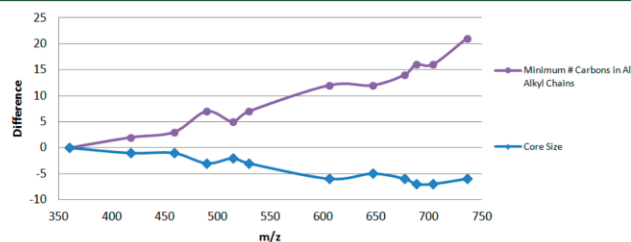


Figure 6. Graph illustrating the differences (petroleum – coal) between the coal asphaltenes and the petroleum asphaltenes as a function of their molecular size: the estimated minimum total number of carbons in all side chains and the approximate core size.

indicating the presence of a complex mixture of isomers (and possibly isobars) with alkyl chains of varying lengths. The larger the lost alkyl radical, the smaller the abundance of the corresponding fragment ion, which suggests that shorter alkyl groups are much more prominent in the asphaltenes molecules than longer ones. The ions of m/z 677 \pm 1 (Figure 4) derived from coal asphaltenes appear to have a total number of at least 5 carbons in side chains and a core of roughly 12 fused aromatic rings, while those from petroleum asphaltenes have a total of at least 19 carbons in side chains and a core of roughly 8 aromatic rings. The core sizes are larger than have been reported previously. The exact reason for this is still under investigation and will be resolved once adequate model compounds have been found. These results, along with those shown in Table 1, indicate that coal asphaltenes have a substantially higher aromatic carbon to alkane carbon ratio than petroleum asphaltenes. CAD mass spectra measured for ions with various m/z values (Table 1) suggest that the total number of carbons in all side chains in coal and petroleum asphaltenes range from at least 3 carbons up to 6 carbons and at least 6 carbons up to 35 carbons, respectively.

While the above results are true for ionized asphaltenes of each type with a similar m/z value, results in Table 1 show that this is not true when the most abundant species of each type are considered (roughly, ions of m/z 440 for coal and ions of m/z 710 for petroleum asphaltenes). The comparison of the tabulated data for ions of m/z 456 for coal and m/z 704 for petroleum asphaltenes (Table 1) indicates that the typical petroleum and coal asphaltenes have a similar polyaromatic core (eight rings). However, the coal asphaltenes have only

~4 carbons making up their alkyl chains, while the petroleum asphaltenes have up to 20 two carbons in their alkyl chains.

The differences between the coal and petroleum asphaltenes samples shown in Table 1 are graphed as a function of the mass of the ions in Figure 6. Figure 6 shows that petroleum and coal asphaltenes are quite similar in chain length and core size at low MW and that the differences gradually increase with MW. While bulk analysis methods can also measure these differences, they are unable to track how they change for molecules with different MWs like this method can.

■ CONCLUSIONS

The results obtained upon mass spectrometric determination of the molecular weight distributions (MWDs) were found to be in good agreement with a previous study using laser desorption/ionization coupled to a time-of-flight mass spectrometer.⁶ For this study, the observed MWD for coal and petroleum asphaltenes ranges from 200 Da up to 800 Da and from 275 Da up to 1500 Da, respectively, with average MWs of 443 \pm 33 Da and 708 \pm 14 Da, respectively. The CAD mass spectra collected for molecular ions of varied m/z values reveal a dramatic decrease in alkane carbon content relative to aromatic carbon content from petroleum (a total of ~35 carbons maximum in all side chains) to coal asphaltenes (a total of ~6 carbons maximum in all side chains). The core size of coal asphaltenes was found to range from 3 rings up to 13 rings and for petroleum asphaltenes from 6 rings up to 10 rings. These core sizes are greater than measured by other techniques, possibly due to a lack of adequate model compounds, but the trends between the samples are expected to be correct. From these results, it is

concluded that the ratio of aromatic carbons to alkane carbons in coal asphaltenes is much higher than that of petroleum asphaltenes, independent of the molecular weight (MW). However, the typical petroleum and coal asphaltenes (when considering the most abundant molecules in each) have a similarly sized aromatic core (~8 rings), although very different total lengths of the alkyl side chains (~4 for coal asphaltenes, ~22 for petroleum asphaltenes). The lower alkane content agrees with the bulk elemental compositions previously determined: 87–91 wt % carbon, 5–7 wt % hydrogen in coal asphaltenes and 79–82 wt % carbon, 7–8 wt % hydrogen in petroleum asphaltenes.^{8,18} The agreement of these results with previous results collected using different techniques helps to validate this technique.

■ AUTHOR INFORMATION

Corresponding Author

*E-mail: hilkka@purdue.edu.

Notes

The authors declare no competing financial interest.

■ ACKNOWLEDGMENTS

Nadine Njoya is acknowledged for providing mass spectrometric data for 1-propyl-3-butylphthalene.

■ REFERENCES

- (1) Mullins, O.; Sheu, E. *Structure and Dynamics of Asphaltenes*; Plenum Press: New York, 1998.
- (2) Buenrostro-Gonzalez, E.; Groenzin, H.; Lira-Galeana, C.; Mullins, O. The Overriding Chemical Principles that Define Asphaltenes. *Energy Fuels* **2001**, *12*, 972–978.
- (3) Mullins, O.; Sheu, E.; Hammami, A.; Marshall, A. *Asphaltenes, Heavy Oils, and Petroleomics*; Springer: New York, 2007.
- (4) Yen, T.; Chilingarian, G. *Asphaltenes and Asphalts*; Elsevier: Amsterdam, 1994.
- (5) Anচেyта, J.; Betancourt, G.; Centeno, G.; Marroquín, G.; Alonso, F.; Garciafigueroa, E. Catalyst Deactivation during Hydroprocessing of Maya Heavy Crude Oil. I. Evaluation at Constant Operating Conditions. *Energy Fuels* **2002**, *16*, 1438–1443.
- (6) Hortal, A.; Hurtado, P.; Martínez-Haya, B.; Mullins, O. Molecular-Weight Distributions of Coal and Petroleum Asphaltenes from Laser Desorption/Ionization Experiments. *Energy Fuels* **2007**, *21*, 2863–2868.
- (7) (a) Andrews, A.; Shih, W.; Mullins, O.; Norinaga, K. Molecular Size Determination of Coal-Derived Asphaltene by Fluorescence Correlation Spectroscopy. *Appl. Spectrosc.* **2011**, *65*, 1348–1356. (b) Wargadalam, V.; Norinaga, K.; Lino, M. Size and shape of a coal asphaltene studied by viscosity and diffusion coefficient measurements. *Fuel* **2002**, *81*, 1403–1407.
- (8) Andrews, A.; Edwards, J.; Pomerantz, A.; Mullins, O.; Nordlund, D.; Norinaga, K. Comparison of Coal-Derived and Petroleum Asphaltenes by ¹³C Nuclear Magnetic Resonance, DEPT, and XRS. *Energy Fuels* **2011**, *25*, 3068–3076.
- (9) Badre, S.; Goncalves, C.; Norinaga, K.; Gustavson, G.; Mullins, O. Molecular size and weight of asphaltene and asphaltene solubility fractions from coals, crude oils and bitumen. *Fuel* **2006**, *85*, 1–11.
- (10) Groenzin, H.; Mullins, O. Molecular Size and Structure of Asphaltenes from Various Sources. *Energy Fuels* **2000**, *14*, 677.
- (11) Mullins, O.; Sabbah, H.; Eyssautier, J.; Pomerantz, A.; Barre, L.; Andrews, A.; Ruiz-Morales, Y.; Mostowfi, F.; McFarlane, R.; Goual, L.; Lepkowitz, R.; Cooper, T.; Orbulescu, J.; Leblanc, R.; Edwards, J.; Zare, R. Advances in Asphaltene Science and the Yen–Mullins Model. *Energy Fuels* **2012**, *26*, 3986–4003.
- (12) Morgan, T.; Alvarez-Rodriguez, P.; George, A.; Herod, A.; Kandiyoti, R. Characterization of Maya Crude Oil Maltenes and Asphaltenes in Terms of Structural Parameters Calculated from Nuclear Magnetic Resonance (NMR) Spectroscopy and Laser Desorption–Mass Spectrometry (LD-MS). *Energy Fuels* **2010**, *24*, 3977–3989.
- (13) Borton, D.; Pinkston, D.; Hurt, M.; Tan, X.; Azyat, K.; Scherer, A.; Tykwinski, R.; Gray, M.; Qian, K.; Kenttämää, H. Molecular Structures of Asphaltenes Based on the Dissociation Reactions of Their Ions in Mass Spectrometry. *Energy Fuels* **2010**, *24*, 5548–5559.
- (14) Pinkston, D.; Duan, P.; Gallardo, V.; Habicht, S.; Tan, X.; Qian, K.; Gray, M.; Mullen, K.; Kenttämää, H. Analysis of Asphaltenes and Asphaltene Model Compounds by Laser-Induced Acoustic Desorption/Fourier Transform Ion Cyclotron Resonance Mass Spectrometry. *Energy Fuels* **2009**, *23*, 5564–5570.
- (15) de Hoffmann, E.; Stroobant, V. *Mass Spectrometry: Principles and Applications*, 3rd Edition; Wiley–Interscience: West Sussex, England, 2007.
- (16) Kim, Y.; Kim, S. Improved Abundance Sensitivity of Molecular Ions in Positive-Ion APCI MS Analysis of Petroleum in Toluene. *J. Am. Soc. Mass Spectrom.* **2010**, *21*, 386–392.
- (17) Owen, B.; Gao, J.; Amundson, L.; Archibold, E.; Tan, X.; Azyat, K.; Tykwinski, R.; Gray, M.; Kenttämää, H. Carbon disulfide reagent allows the characterization of nonpolar analytes by atmospheric pressure chemical ionization mass spectrometry. *Rapid Commun. Mass Spectrom.* **2011**, *25*, 1924–1928.
- (18) Long, R. The Concept of Asphaltenes. In *Chemistry of Asphaltenes*; Bunger, J., Norman, L., Eds.; American Chemical Society: Washington, DC, 1981; Vol. 195.
- (19) Klein, G.; Kim, S.; Rodgers, R.; Marshall, A.; Yen, A. Mass spectral analysis of asphaltenes. II. Detailed compositional comparison of asphaltenes deposit to its crude oil counterpart for two geographically different crude oils by ESI FT-ICR MS. *Energy Fuels* **2006**, *20*, 1973–1979.

CHAPTER 1: INTRODUCTION AND OVERVIEW

1.1 Introduction

Since the construction of the first mass spectrometer in 1913 by J.J. Thomson,¹ mass spectrometry (MS) has developed into an extremely popular technique for solving complex scientific problems due to its special capabilities, including high sensitivity, specificity, speed, and experimental versatility.² This development was foreshadowed by Thomson when he stated:¹ “I feel sure that there are many problems in chemistry which could be solved with far greater ease by this than any other methods.”

Mass spectrometric experiments consist of four principle components: evaporation, ionization, separation and detection.³ For an analyte to be studied via mass spectrometry, it must first be evaporated into the gas phase and ionized. Ionization can either occur before (pre-ionized), during, or after evaporation. Generally, ionization and evaporation occur nearly simultaneously in modern ionization sources. An evaporation technique that will be discussed throughout this thesis, called laser-induced acoustic desorption (LIAD), is decoupled from ionization, making it a very powerful technique.⁴⁻⁶ Further, various mass analyzers have been developed that separate ions by mass as a function of some fundamental parameter, e.g., momentum, flight time, or frequency of motion, among others.³ Most mass analyzers utilize some combination of electric and magnetic fields under various levels of vacuum to manipulate ions. After the ions have

been adequately separated, they need to be detected, their abundance measured and the results transformed into usable information. The usual mass spectrum will display the mass-to-charge (m/z) ratios of the ions on the x-axis and their abundances (either relative or absolute) on the y-axis.

Compositional and structural elucidation of unknown analytes is among the various applications of MS. Many different approaches have been employed for this task that vary depending on the type of information desired. A single stage MS experiment can provide molecular weight information.⁷ If an accurate enough mass can be measured, the elemental composition of an analyte ion can be determined.⁸

To obtain additional information that cannot be obtained from the first MS stage, multiple-stage tandem mass spectrometry⁹ (MS^n) experiments can be conducted. The additional stage of analysis can involve collisional activation of the analyte ion.¹⁰ Collisional activation can provide structurally informative fragment ions which allow the structure of the analyte ion to be determined. Ion-molecule reactions can also be used to obtain useful structural information.^{11,12} The neutral reagents that are allowed to react with the analyte ions may be chosen to identify specific functional groups or compound classes¹³ or to distinguish isomers,¹⁴ tasks that are often difficult or impossible via collisionally-activated dissociation (CAD) alone.

Tandem mass spectrometry has been found to be very useful for mixture analysis. MS^n and the various types of scan modes available with this technique provide many useful options for problem solving.¹⁵ For analytes in complex matrices, such as those found in the pharmaceutical industry, the coupling of a chromatographic technique with MS is often desired.¹⁶ In addition to the separation of the analytes and matrix,

chromatography also allows for purification and concentration of the analyte prior to MS analysis, thus improving sensitivity.

1.2 Overview

This dissertation focuses on the development of on-line tandem mass spectrometric methods for the determination of the primary products of fast pyrolysis of carbohydrates and their gas-phase manipulation, as well as on tandem mass spectrometry experiments conducted to characterize different asphaltene samples and probe their molecular structures. Further, instrumentation development was carried out to couple LIAD to an atmospheric pressure ionization source of a commercial mass spectrometer with rastering capabilities. Chapter 2 describes the experimental aspects and principles of the instrumentation employed in the studies described in this thesis. The projects presented in this thesis required the use of two different types of mass spectrometers, linear quadrupole ion traps (LQIT) and Fourier-transform ion cyclotron resonance (FT-ICRs), which are described in this chapter. The basics of LIAD are also introduced in Chapter 2.

Chapter 3 focuses on the development of methods for the determination of the primary products of fast pyrolysis of carbohydrates and for their gas-phase manipulation. The next four chapters discuss the analysis of various petroleum samples, with Chapter 4 focusing on the comparison of the structures of the molecules present in coal and petroleum asphaltenes. Chapter 5 discusses the differences in the structures of asphaltene molecules that have been subjected to different levels of hydrocracking treatment. Chapter 6 compares the structures of the molecules present in field deposit asphaltenes to

those in heptane precipitated asphaltenes. Chapter 7 examines the effects of different solvents on atmospheric pressure chemical ionization (APCI) of asphaltene molecules in an LQIT. The last two chapters focus on instrumentation developments involving the coupling of LIAD to a commercial APCI source. Chapter 8 details LIAD/APCI instrumentation development that produced an assembly for the rastering of sample foils for increased throughput and sensitivity. Lastly, Chapter 9 discusses the development of a sample deposition chamber with the ability to form semi-uniform sample layers onto LIAD foils for all samples regardless of type of analyte or solvent.

1.3 References

1. Thomson, J., *Rays of Positive Electricity and Their Application to Chemical Analysis*. Longmans Green: London, 1913.
2. McLuckey, S.; Wells, J., Mass Analysis at the Advent of the 21st Century. *Chem. Rev.* **2001**, 101, 571-606.
3. de Hoffmann, E.; Stroobant, V., *Mass Spectrometry Principles and Applications*. 3rd ed.; John Wiley & Sons, Ltd: West Sussex, England, 2007.
4. Shea, R.; Petzold, C.; Campbell, J.; Li, S.; Aaserud, D.; Kenttämaa, H., Characterization of Laser-Induced Acoustic Desorption Coupled with a Fourier Transform Ion Cyclotron Resonance Mass Spectrometer. *Anal. Chem.* **2006**, 78, 6133-6139.
5. Gao, J.; Borton, D.; Owen, B.; Jin, Z.; Hurt, M.; Amundson, L.; Madden, J.; Qian, K.; Kenttämaa, H., Laser-Induced Acoustic Desorption/Atmospheric Pressure Chemical Ionization Mass Spectrometry. *J. Am. Soc. Mass Spectrom.* **2011**, 22, 531-538.
6. Borton, D.; Amundson, L.; Hurt, M.; Dow, A.; Madden, J.; Simpson, G.; Kenttämaa, H., Development of a High-Throughput Laser-Induced Acoustic Desorption Probe and Raster Sampling For Laser-Induced Acoustic Desorption/Atmospheric Pressure Chemical Ionization. *Anal. Chem.* **2013**, 85, 5720-5726.
7. McLafferty, F. W., *Interpretation of Mass Spectra*. 4th ed.; University Science Books: Sausalito, CA, 1993.
8. Zubarev, R.; Hakansson, P.; Sundqvist, B., Accuracy Requirements for Peptide Characterization by Monoisotopic Molecular Mass Measurements. *Anal. Chem.* **1996**, 68, 4060-4063.
9. Busch, K.; Glish, G.; McLuckey, S., *Mass Spectrometry/Mass Spectrometry: Techniques and Applications of Tandem Mass Spectrometry*. VCH Publishers: New York, 1988.
10. McLuckey, S., Principles of Collisional Activation in Analytical Mass Spectrometry. *J. Am. Soc. Mass Spectrom.* **1992**, 3, 599-614.
11. Brodbelt, J., Analytical Applications of Ion-Molecule Reactions. *Mass Spectrom. Rev.* **1997**, 16, 91-110.

12. Habicht, S.; Vinueza, N.; Archibold, E.; Duan, P.; Kenttämäa, H., Identification of the Carboxylic Acid Functionality by Using Ion-Molecule Reactions in a Modified Linear Ion Trap Mass Spectrometer. *Anal. Chem.* **2008**, 80, 3416-3421.
13. Eberlin, M., Structurally Diagnostic Ion/Molecule Reactions: Class and Functional-Group Identification by Mass Spectrometry. *J. Mass Spectrom.* **2006**, 41, 141-156.
14. Stirk, K.; Kiminkinen, M.; Kenttämäa, H., Ion-Molecule Reactions of Distonic Radical Cations. *Chem. Rev.* **1992**, 92, 1649-1685.
15. Schwartz, J.; Wade, A.; Enke, C.; Cooks, R., Systematic Delineation of Scan Modes in Multidimensional Mass Spectrometry. *Anal. Chem.* **1990**, 62, 1809-1818.
16. Ermer, J.; Vogel, M., Applications of Hyphenated LC-MS Techniques in Pharmaceutical Analysis. *Biomed. Chromatogr.* **2000**, 14, 373-383.

CHAPTER 2:
FOURIER-TRANSFORM ION CYCLOTRON RESONANCE AND LINEAR
QUADRUPOLE ION TRAP MASS SPECTROMETRY: INSTRUMENTAL AND
EXPERIMENTAL CONSIDERATIONS

2.1 Introduction

Since the invention of mass spectrometry, the diversity of mass analyzers has consistently increased, with each analyzer having its own unique role within the mass spectrometric community based on its distinctive advantages and disadvantages.¹ Mass analyzers can be classified into one of two categories: trapping and scanning. Trapping mass analyzers confine ions into a particular area where all ion manipulations are conducted at different points in time.¹ Common types of ion trapping analyzers include linear quadrupole ion traps (LQIT), Fourier transform ion cyclotron resonance (FT-ICR) instruments, 3D quadrupole ion traps, and orbitrap mass spectrometers. Scanning mass analyzers are quite different from trapping mass analyzers because they allow the flow of a preselected beam of ions through the analyzer while others are deflected. The ion beam is then manipulated in different parts of the instrument.¹ Scanning analyzers include time-of-flight (TOF), sector, and quadrupole mass analyzers.

Two different types of ion-trapping instruments were used in the experiments described in this thesis: LQIT and FT-ICR mass spectrometers. Two Thermo Scientific LQIT instruments were utilized during this research.^{2,3} In addition to a standalone LQIT,

a LQIT coupled to a 7 T FT-ICR was employed.⁴ The FT-ICR was used solely as a high resolution detector, all other ion manipulation were conducted in the LQIT. Both instruments were utilized to study molecular structures of various coal, petroleum, and biomass pyrolysis samples by using fragment ions produced upon collisionally activated dissociation (CAD).⁵ The development and utilization of methods for the analysis of petroleum and coal samples was accomplished using an unmodified Thermo Scientific LTQ equipped with an HPLC system. The same Thermo Scientific LTQ, with the exception of an ionization chamber modified to allow for the insertion of various pyrolysis adaptors, was used for the analysis of biomass fast pyrolysis products along with their gas phase reactivity. Important fundamental aspects of these instruments and the specific experimental setups employed for this research are discussed in the following sections. It needs to be noted that all equations and parameters are based on S.I. units, unless otherwise noted.

2.2 Ionization Methods

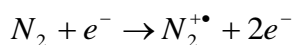
Many different ionization methods are utilized to produce ions in mass spectrometry. These methods include atmospheric pressure chemical ionization (APCI),^{6,7} atmospheric pressure photoionization (APPI),⁸ electrospray ionization (ESI),^{9,10} desorption electrospray ionization (DESI),¹¹ direct analysis in real time (DART),¹² matrix-assisted laser desorption/ionization (MALDI),¹³ inductively coupled plasma (ICP),¹⁴ fast atom bombardment (FAB),¹⁵ field desorption/field ionization (FD/FI),^{16,17} laser desorption/ionization (LDI),¹⁸ electron ionization (EI),¹⁹ and chemical ionization (CI).²⁰ Each of the ionization methods mentioned has its own unique

advantages and disadvantages. Only the methods utilized during the course of this research will be discussed further.

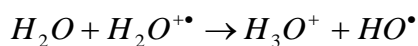
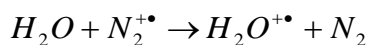
2.2.1 Atmospheric Pressure Chemical Ionization (APCI)

APCI is considered a “soft” ionization technique since analytes seldom fragment during ionization. APCI relies on a series of gas-phase ion-molecule reactions similar to those occurring upon CI but at atmospheric pressure instead of in a vacuum.^{6,7,21} An APCI source works by heating a dissolved analyte, that is infused into the source, to 300 °C - 500 °C with a nebulizer gas, often nitrogen. The heat combined with the nebulizer gas causes the solution to nebulize i.e., to create a mist of fine droplets. When the mist passes over the corona discharge needle, the needle ionizes the nebulizer gas (the most abundant molecules present). The ionized nebulizer gas usually then ionizes solvent molecules that ionize the analyte via ion-molecule reactions. A typical APCI reaction cascade may proceed as follows when using water as the solvent:²²

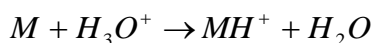
- (1) Corona Discharge Ionization of Nebulizer Gas:



- (2) Ionization of Solvent Molecules:



- (3) Ionization of Analyte Molecules:



2.2.2 Electrospray Ionization (ESI)

ESI is considered a “soft” ionization technique but it does not require heating, like APCI.²³ Hence, ESI can be used to ionize thermally labile molecules. ESI often readily forms multiply charged analyte ions, which enables the analysis of very large molecules, such as biopolymers.⁹ Multiple charges per molecule reduces its mass-to-charge ratio, allowing for it to be analyzed in mass analyzers with limited mass range such as LQITs. Upon ESI, preformed ions are transferred from solution into the gas phase through a stepwise process that starts when the analyte solution passes through a needle with a high voltage (several kV) applied to it.²⁴ As the solution passes through the needle, a fine spray of droplets is formed, with each droplet containing multiple charges within it.²³ As the droplet moves towards the inlet of the mass spectrometer, the solvent within the droplet keeps evaporating, causing the charges to move towards each other.²³ Once the charges are concentrated to the point that the electrostatic repulsion is stronger than the surface tension of the droplet, known as the Rayleigh stability limit, the droplet explodes producing smaller droplets. This repeats until gas-phase ions are released and analyzed in the mass spectrometer.²³ A diagram of this process is shown in Figure 2.1.

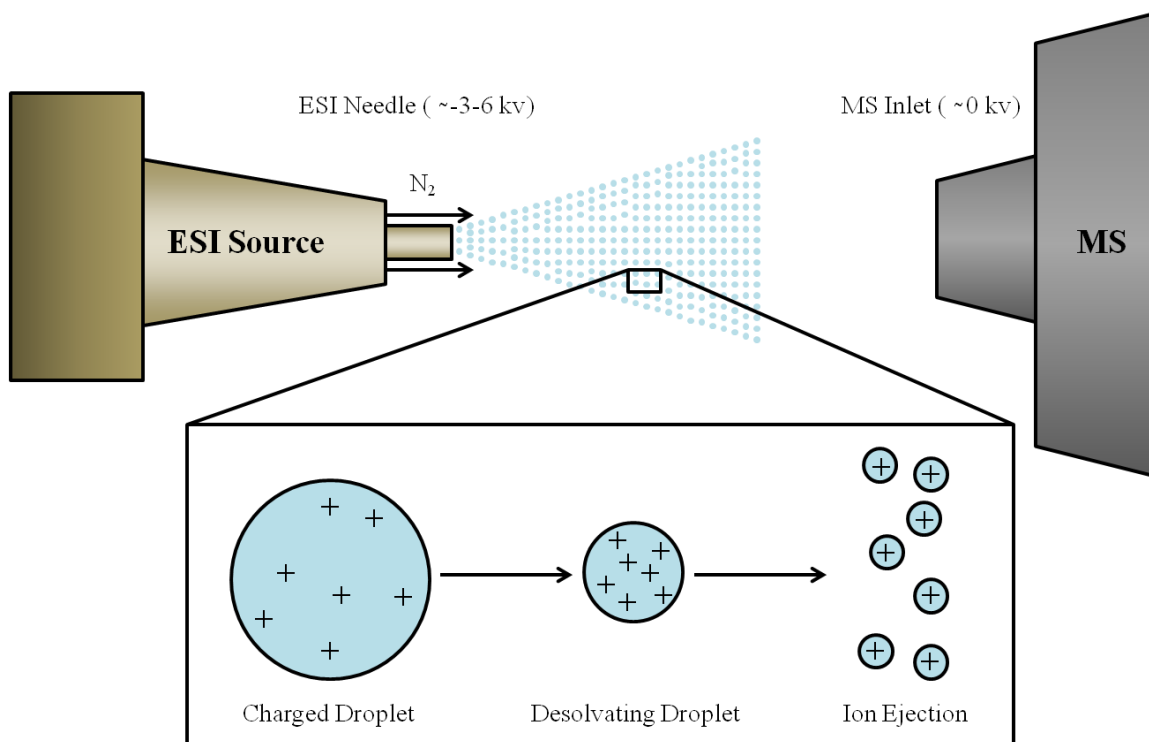


Figure 2.1 Diagram depicting the ESI process (positive mode). The zoom on the spray shows how gas-phase ions are formed from a droplet explosion due to Coulombic forces.

2.3 Linear Quadrupole Ion Trap (LQIT) Mass Spectrometry

The first reports of LQIT mass spectrometers appeared in 2002.^{2,3} Since then, their popularity in academia and industry has increased rapidly.²⁵ Many of the fundamental principles of operation of LQITs are the same as for the well-known 3-D quadrupole ion traps^{26,27} (QIT), but there are several distinct advantages of LQITs over QITs. The trapping capacity and trapping efficiency of the LQITs are sixteen times and six times higher, respectively, than that of QITs.² These improvements in ion trapping parameters result in an increased sensitivity, lowering the detection limit of LQITs as much as fivefold when compared to similar QITs. The increased sensitivity also result in

an enhancement in the resolution of mass spectra since ion scanning can be performed lower (thus enhancing resolution) without as much sensitivity loss as in a QIT.² The improvements in ion trapping in LQITs have led to the creation of several hybrid instruments, such as LQIT-Orbitrap,²⁸ LQIT-TOF,²⁹ and LQIT-FT-ICR,⁴ of which the last one was used for high resolution experiments discussed in this thesis.

2.3.1 Instrumentation Overview

LQIT experiments were performed using a Thermo Scientific LTQ linear quadrupole ion trap mass spectrometer (Figure 2.2) equipped with one of two atmospheric pressure ionization sources, ESI or APCI.³⁰ The mass analyzer chamber was maintained at approximately $0.5 - 1.0 \times 10^{-5}$ Torr by one inlet (400 L/s) of a Leybold TW220/150/15S triple-inlet turbomolecular pump. The two additional inlets, with pumping efficiencies of 25 L/s and 300 L/s, of this turbo pump served to evacuate the initial and intermediate sections of the vacuum chamber down to 500 mTorr and 1 mTorr, respectively. The turbo pump was backed by two Edwards E2M30 rotary-vane mechanical pumps (10.8 L/s each), which also served to evacuate the capillary-skimmer region of the instrument down to approximately 1 Torr.

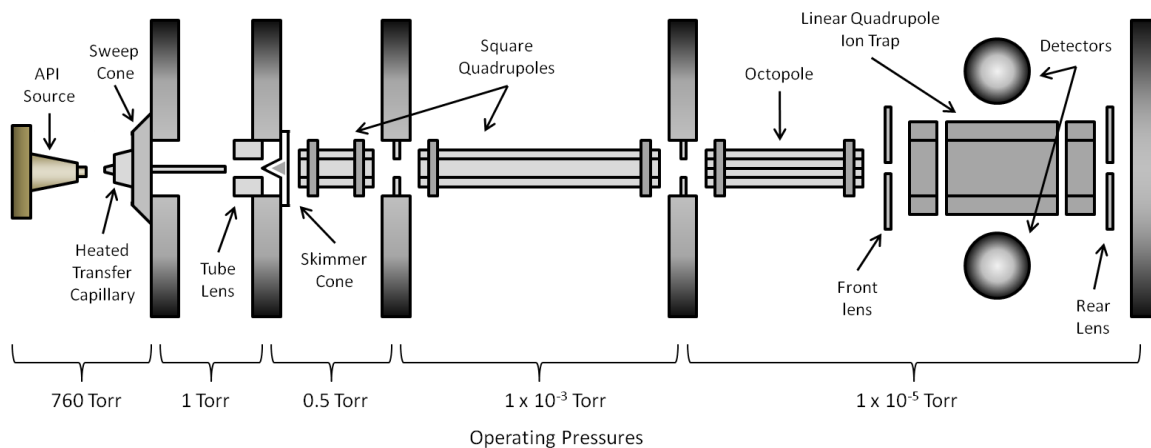


Figure 2.2 Schematic of the Thermo Scientific LTQ mass spectrometer (top view) with typical operating pressures. Ions were introduced from the atmospheric pressure ionization (API) source into the heated transfer capillary.

A schematic of the Thermo Scientific LTQ mass spectrometer is shown above in Figure 2.2. Once ions were created in the API source, they were directed through the heated transfer capillary, followed by a series of ion optics and a lens before being injected into the mass analyzer. The mass analyzer consisted of four parallel hyperbolic rods divided into three sections. A schematic of the mass analyzer can be seen in Figure 2.3. The front and rear sections of the mass analyzer were 12 mm long and the center section 37 mm long. Two phases of a main radio frequency (RF) voltage (± 5 kV, 1 MHz) were applied to the rod pairs (x pair and y pair) for radial trapping. Two phases of a supplementary RF voltage (± 80 V, 5-500 kHz) were applied to the x rods of the mass analyzer for resonant ejection/excitation. Additionally, a direct current (DC) voltage (± 100 V) was applied to the three sections of the mass analyzer for axial trapping. The x rods contained a 0.25 mm high and 30 mm wide slit in the center section so that ions

could be ejected radially into two detection systems, both consisting of a conversion dynode and electron multiplier.

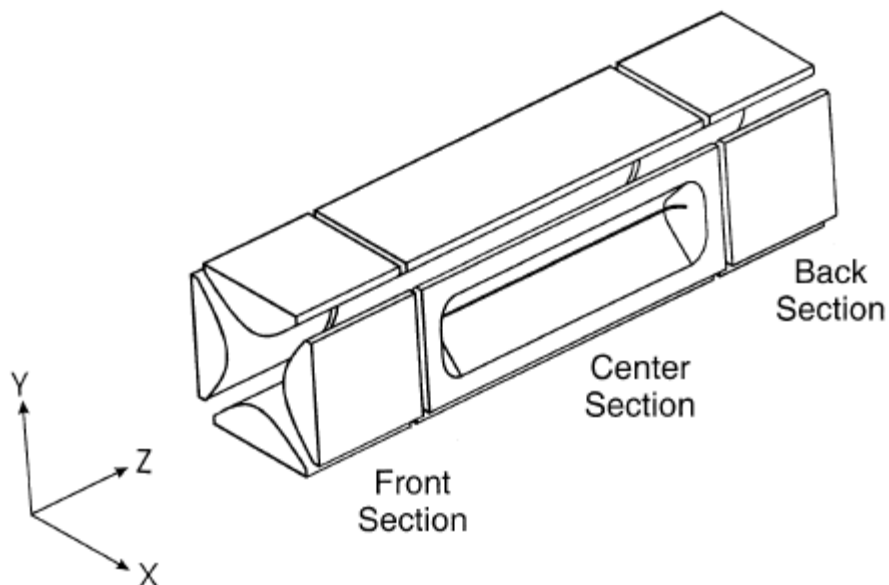


Figure 2.3 The linear quadrupole ion trap mass analyzer of the Thermo Scientific LTQ instrument (reproduced from Reference 2).

Sample solutions were introduced into the API source of the LQIT by either direct infusion by using an integrated syringe drive or in the eluent of an HPLC system. A Dell Optiplex workstation (Microsoft Windows XP operating system) running Xcalibur 2.1 software was used for instrumental control, data acquisition and data processing.

2.3.2 Ion Motion

Ions were trapped in the LQIT by the use of RF potentials in the radial direction and DC potentials in the axial direction. The ions' motions resulting from these potentials are discussed below.^{2,27,30,31}

2.3.2.1 Radial Motion

In the LQIT, the forces that confine an ion in the radial (x - y plane) direction are equivalent to those used in the quadrupole mass filter.²⁷ A combination of RF and DC voltages were applied to the four hyperbolic rods to produce the following potentials (Φ_0):

$$\pm \Phi_0 = \pm(U - V \cos \Omega t) \quad (2.1)$$

where U is the DC voltage, V is the zero-to-peak amplitude of the RF voltage, Ω is the angular frequency of the main RF field, and t is time. These potentials create a quadrupolar electric field in the space between the four rods. When ions were injected into the LQIT on the z-axis, they were subjected to the following forces in the x and y directions as a result of the quadrupolar field:

$$F_x = m \frac{d^2 x}{dt^2} = -ze \frac{d\Phi}{dx} \quad (2.2)$$

$$F_y = m \frac{d^2 y}{dt^2} = -ze \frac{d\Phi}{dy} \quad (2.3)$$

in which

$$\Phi_{(x,y)} = \frac{\Phi_0(x^2 - y^2)}{r_0^2} = \frac{(U - V \cos \Omega t)(x^2 - y^2)}{r_0^2} \quad (2.4)$$

and m is the mass of the ion, e is an elementary charge, z is the number of charges of the ion, and r_0 is the radius of a circle inscribed within the quadrupole rods. Rearrangement of these equations leads to the following equations of ion motion:

$$\frac{d^2x}{dt^2} + \frac{2ze}{mr_0^2}(U - V \cos \Omega t)x = 0 \quad (2.5)$$

$$\frac{d^2y}{dt^2} - \frac{2ze}{mr_0^2}(U - V \cos \Omega t)y = 0 \quad (2.6)$$

These equations are similar to the general form of the Mathieu equation,

$$\frac{d^2u}{d\xi^2} + (a_u - 2q_u \cos 2\xi)u = 0 \quad (2.7)$$

Thus, by performing a change of variables where

$$\xi = \frac{\Omega t}{2} \quad (2.8)$$

the equations of motion can be expressed in terms of the Mathieu equation:

$$a_u = \frac{8zeU}{mr_0^2\Omega^2} \quad (2.9)$$

$$q_u = \frac{4zeV}{mr_0^2\Omega^2} \quad (2.10)$$

in which

$$a_u = a_x = -a_y \quad (2.11)$$

$$q_u = q_x = -q_y \quad (2.12)$$

The variables a_u and q_u are known as the Mathieu stability parameters. For a given ion to have a stable trajectory within the trap, the ions' a and q values must fall within a stability region of the Mathieu stability diagram (the most well-defined overlap region is shown in

Figure 2.4). The LQIT is usually operated with $a_u = 0$ so that a broad range of ions can be simultaneously trapped.

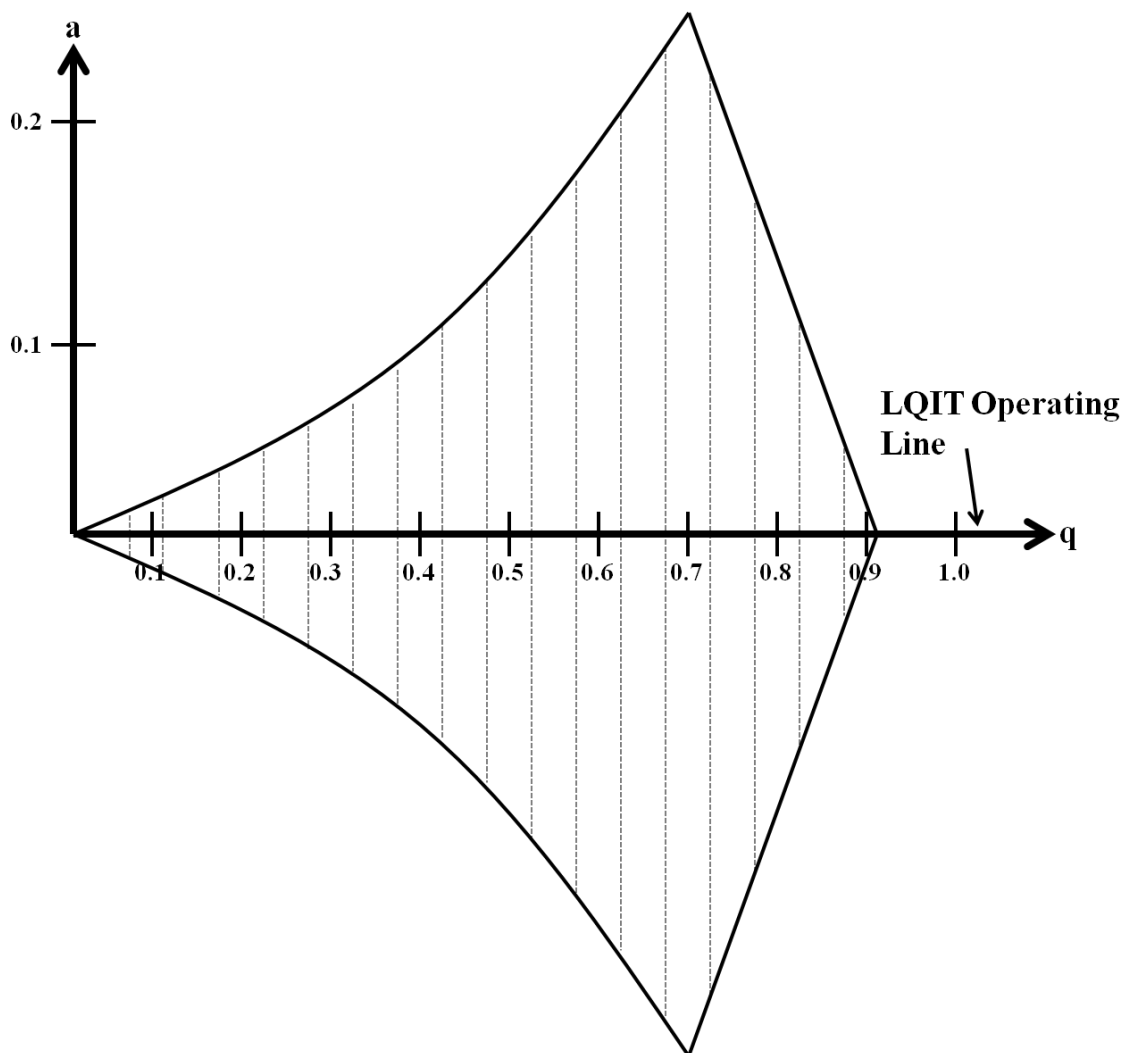


Figure 2.4 Most well defined region of the Mathieu stability diagram. Ions with a_u and q_u that fall within the region with the dotted lines will have stable trajectories inside of a quadrupole ion trap.

The secular frequency of ion motion, ω_u , within the LQIT can be calculated by using the following equation:

$$\omega_u = \frac{1}{2} \beta_u \Omega \quad (2.13)$$

in which

$$\beta_u = \sqrt{\left(a_u + \frac{1}{2} q_u^2 \right)} \quad (2.14)$$

for $q_u < 0.4$. The term β_u is known as the Dehmelt approximation,²⁷ and when $0 < \beta_u < 1$ for an ion, the ion will have a stable motion in the trap. Equation 2.14 shows that the secular frequency of an ion will be equal to half of the RF angular frequency.

Each individual ion within the trapping field of the LQIT is in a pseudo-potential well with a depth, D_u , that can be described by

$$D_u = \frac{q_u V}{4} \quad (2.15)$$

D_u is known as the Dehmelt pseudo potential well.²⁷ Lower mass ions will have larger q values and will exist in deeper pseudo-potential wells.³¹ Calculation of the depth of the pseudo-potential well of an ion is important when determining a proper q value (RF voltage) for resonant excitation or ejection of that ion.

2.3.2.2 Axial Motion

In the LQIT, ion motion is confined axially (in the z direction) by the application of repulsive dc potentials to the front and back lenses and the front and back sections of the mass analyzer,³⁰ as shown in Figure 2.5. The DC voltages that are applied to the front and back sections of the trap centralize the ions in the mass analyzer, effectively reducing

fringe field effects that are created by the front and rear lenses.² The centering of the ions also allows for more efficient ion ejection through the slits in x rods of the mass analyzer during mass analysis.²

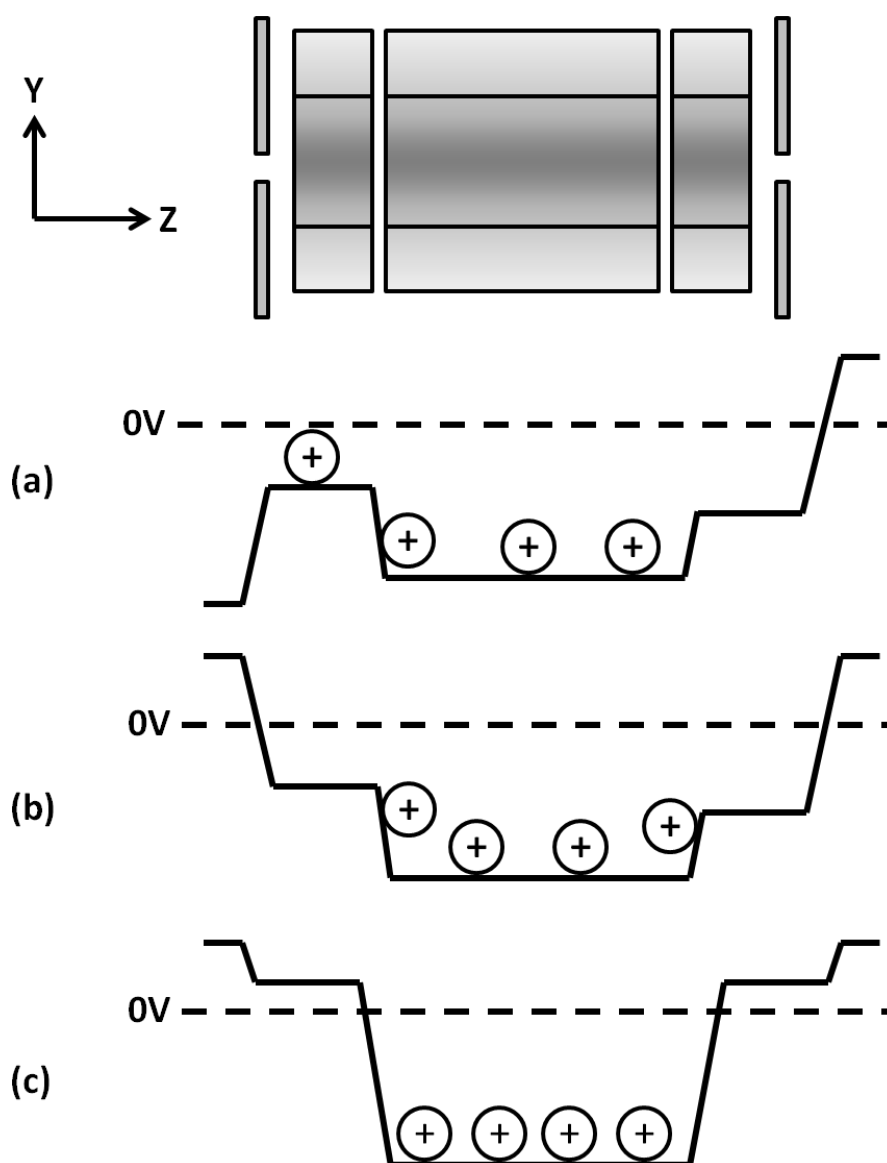


Figure 2.5 Potential diagrams depicting DC voltages applied to the front lens, back lens and three sections of the LQIT during (a) ion injection, (b) ion trapping, and (c) mass analysis. The (b) to (c) transition involves the increase of DC potentials on the front and back sections of the trap. This is done to better center the ions for ion ejection.

Buffer gas plays a significant role in the efficient trapping of ions in a LQIT (helium is the buffer gas used in Thermo Scientific LTQ's).³² The buffer gas is required to lower the kinetic energies of ions through collisions as they enter the trap because the ions gain a large amount of kinetic energy as they are transported into the trap. Ions with low kinetic energies can then be trapped by the RF and DC fields and travel to the center of the trap.² The Thermo Scientific LTQ uses approximately 3 mTorr of helium within the trapping region.² This pressure is a compromise between a better ion trapping efficiency and more efficient collision-activated dissociation (CAD) at higher helium pressures and a better resolution at lower helium pressures.

2.3.3 Ion Ejection and Detection

As stated above, the LQIT is usually operated with $a = 0$; thus, mass analysis can be achieved by ramping the RF voltage. Based on Eq. 2.10, as the RF voltage is increased, ions of increasing m/z value will become unstable and be ejected from the trap in the direction of instability as depicted in Figure 2.6. This is called mass selective axial instability scan. In the original QITs this scan was performed by ejecting ions at the stability limit where $a = 0$ and $q = 0.908$.³² To increase mass range, sensitivity and resolution, LQITs use resonant ejection to eject ions at a lower q value.³³ Resonant ejection is achieved by applying a supplementary RF voltage to the x rods of the mass analyzer. As the amplitude of the main RF voltage is increased during the scan, the secular frequency of ions starts to resonate with the supplementary RF voltage. During resonance, the ions gain energy from the supplementary RF field, which increases the amplitude of their motion and eventually causes their ejection from the trap in the x

direction. The Thermo Scientific LTQ mass spectrometer utilizes the mass selective instability scan with resonant ejection at $q = 0.880$.² Using mass selective instability with resonant ejection also affords higher scan speeds while maintaining unit mass resolution. This phenomenon also allows for an increase in resolution at lower scan rates.³⁴

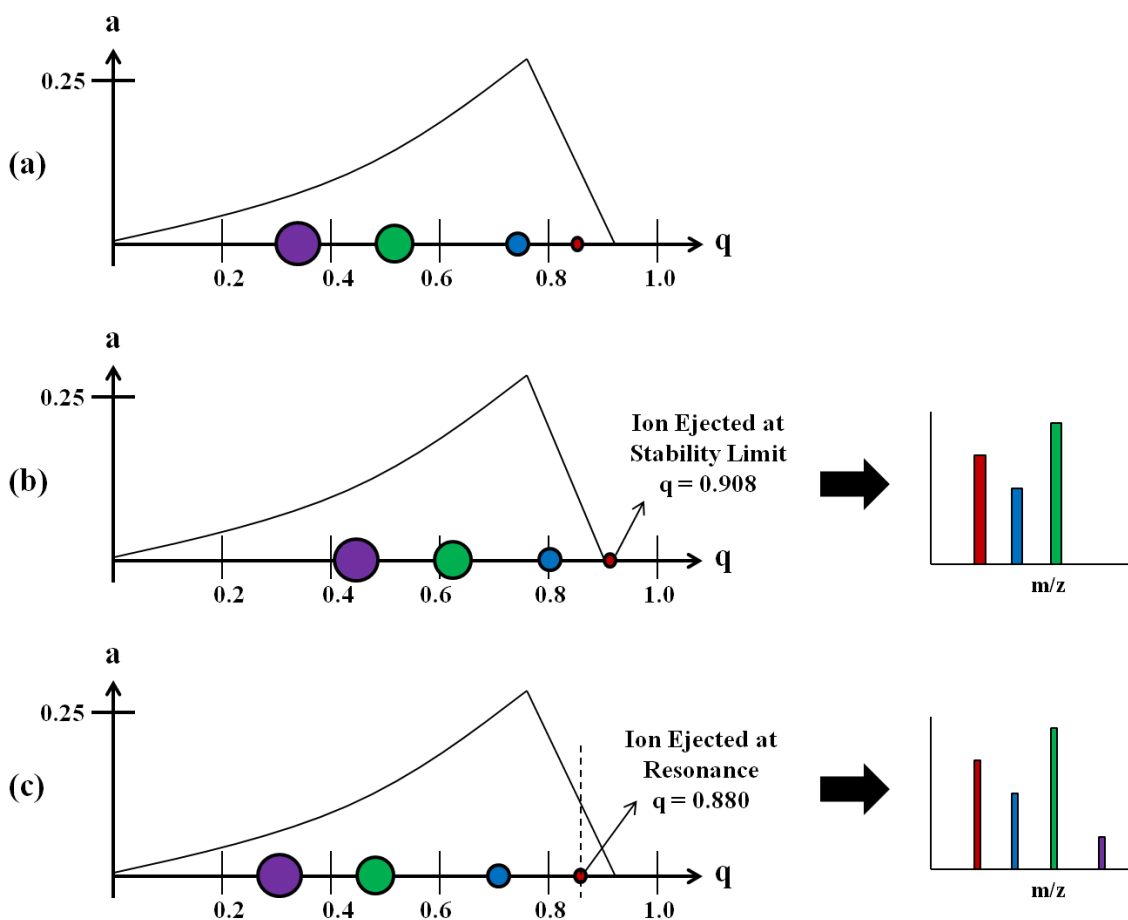


Figure 2.6 Illustrations of different forms of ion ejection in LQIT. (a) Ions trapped in the LQIT. (b) Ion ejected at the stability limit by using the mass selective axial instability scan and the resulting mass spectrum measured in a traditional LQIT. (c) Ion ejected via resonance ejection by using the mass selective axial instability scan and the resulting mass spectrum measured by a LQIT. By ejecting ions at a lower q value, the resolution and mass range of the trap are increased.

During the mass analysis scan, ions are ejected from the trap for detection. In the Thermo Scientific LTQ, ions are ejected radially through slits in the x rods. The ions are directed towards a conversion dynode that is held at -15 kV (for positive ions). As the ions strike the conversion dynode, multiple secondary particles are generated that are then sent into the electron multiplier for detection. Each particle from the conversion dynode will strike the inside of the electron multiplier, which in turn generates a cascade of secondary particles that, upon collision with the surface, generate even more particles. This cascade greatly increases the signal for each ion. A great advantage of this type of a detection scheme is that theoretically 100% of the ejected ions are detected, in contrast to 50% for a QIT,^{2,31} resulting in an instrument with twice the sensitivity. Figure 2.7 provides an illustration of the ion ejection and detection event for the Thermo Scientific LTQ mass spectrometer.

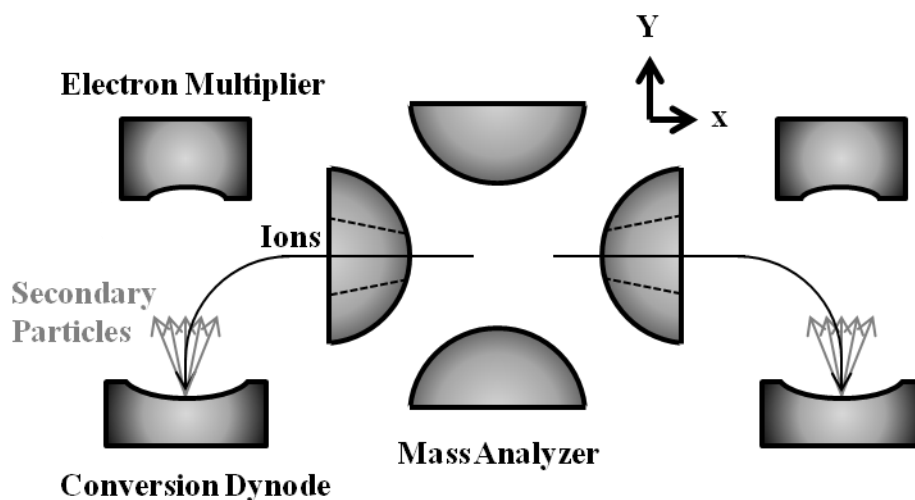


Figure 2.7 Illustration of radial ejection and detection of ions in a Thermo Scientific LTQ.

2.3.4 Tandem Mass Spectrometry in LQIT

Multiple-stage tandem mass spectrometry (MS^n) capabilities of the LQIT are one of the features that make these instruments so powerful.³⁵ Tandem mass spectrometry in the LQIT is a tandem-in-time experiment, meaning that all events of the experiment occur within the same space and are separated by time.³⁶ For the research presented in this thesis, collision-activated dissociation (CAD) was used for all MS^n experiments.

2.3.4.1 Ion Isolation

During ion isolation, the ion of interest is first placed at the proper q value by ramping the RF voltage. The ramping of the RF voltage also ejects ions of lower mass than the desired ion. A broadband waveform is then used to excite all remaining unwanted ions. In the Thermo Scientific LTQ, resonant ejection is accomplished via the application of a 5 – 500 kHz multi-frequency waveform with sine components spaced every 0.5 kHz, with a notch at $q = 0.83$ (where the ion of interest resides).² Under these conditions, unit mass resolution for isolated ions can be achieved up to roughly m/z 1500. Once the ion is isolated, the q value is usually reduced to 0.25 (this can be adjusted in the Xcalibur software) for MS/MS experiments.

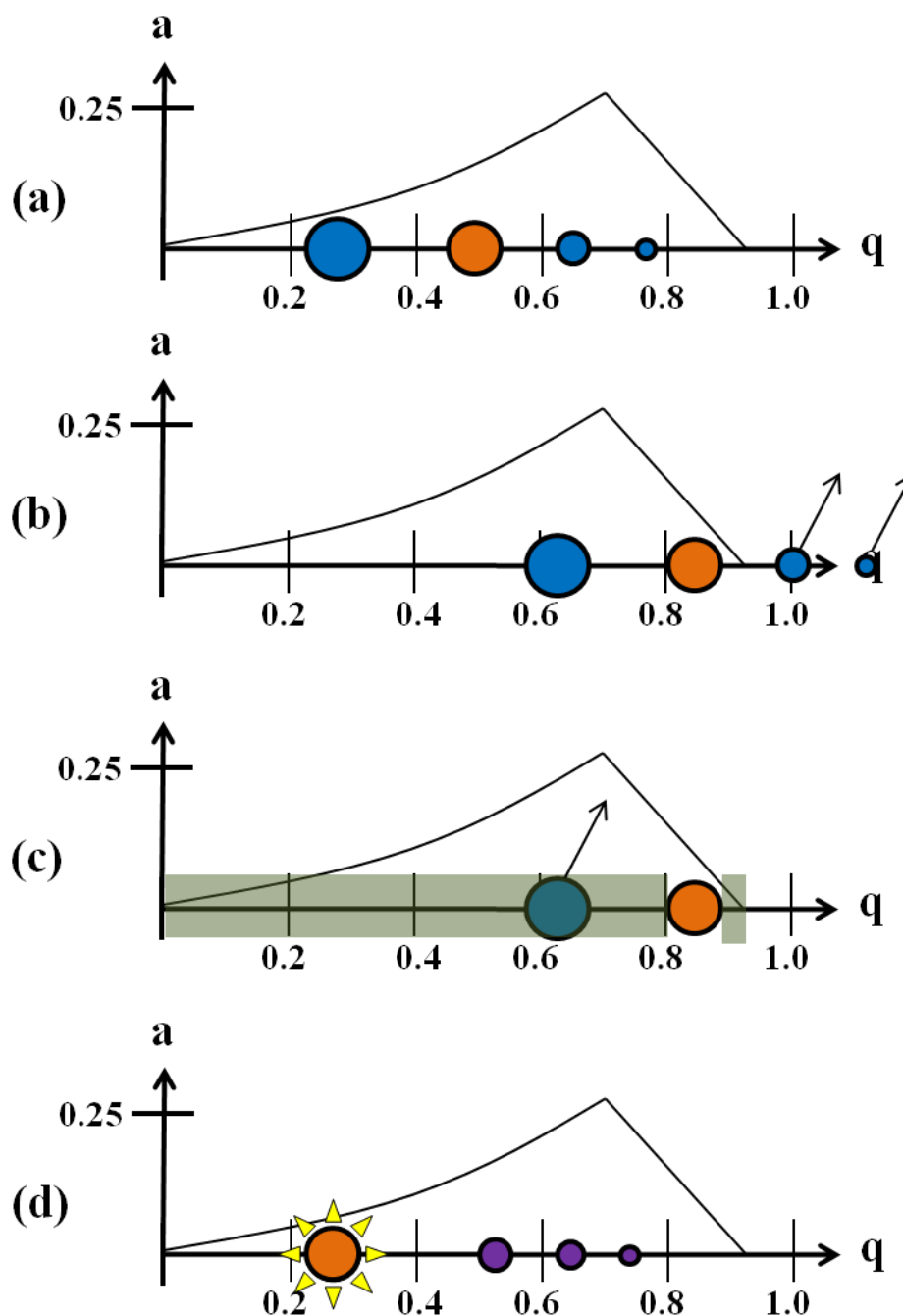


Figure 2.8 Illustration of ion isolation and activation in the LQIT. (a) Ions trapped in the LQIT. (b) The q value of the ion of interest (orange) is set to 0.83, resulting in lower mass ions to become unstable and get ejected from the trap. (c) An isolation waveform is applied to eject the remaining unwanted ions. (d) The q value of the desired ion is set to 0.25 in order to induce efficient fragmentation upon collision-activated dissociation while maintaining high trapping efficiency for low mass fragment ions (purple).

2.3.4.2 Collision-Activated Dissociation (CAD)

CAD within a LQIT is a slow heating process, wherein ions are subjected to many low-energy collisions with the helium buffer gas over relatively long activation times.³⁵ Once ions are isolated and stored, typically with a q value of 0.25 as described in section 2.3.4, the ions' kinetic energy is increased using resonant excitation.³⁷ This is achieved using a supplementary RF voltage (generally with an amplitude $< 1 V_{p-p}$) applied to the x rods at the secular frequency of the ion for approximately 10 – 100 ms. This voltage is referred to as a “tickle” voltage.

As the ion gains kinetic energy, it undergoes energetic collisions with the helium buffer gas present in the trap. The collisions convert the ion's kinetic energy to internal energy, and once enough collisions have occurred and enough energy is built up within the ion, the ion will dissociate. An important characteristic of resonant excitation in a Thermo Scientific LQIT is that only the parent ion is excited, generally preventing the further fragmentation of the fragment ions.

The q value used during CAD is a compromise between efficient activation of the parent ion and efficient confinement of product ions. For efficient activation, the q value should be chosen such that the ion gains maximum kinetic energy without being ejected from the trap. However, higher q values prevent the trapping of low mass fragment ions. The result of performing CAD at a q value of 0.25 is that activation is reasonably efficient while only being able to trap fragment ions with a m/z value of approximately 25% or greater than that of the precursor ion. Thus, the CAD experiments in an LQIT have a low mass cut-off for detection of fragment ions.

Lately, new collision-activated dissociation methods have been developed to avoid the low mass cut-off during CAD in a LQIT such as pulsed q collision-activated dissociation (PqCAD).³⁸ This method utilizes a shorter activation time (100 μ s), a larger than normal q value (normally $q > 0.6$), and a higher amplitude RF voltage (roughly 1 - 2 V) than conventional CAD. Immediately after activation and before dissociation of the precursor ion has occurred, the main RF supply voltage is quickly dropped to a low value, lowering the q value as well, which allows lower mass fragment ions to be trapped. The down side of using this fast excitation CAD method is a reduction in the fragmentation efficiency, which is likely from the precursor ion being accidentally ejected because of the large tickle voltages used to excite the ion.³⁹

2.4 Liquid Chromatography-Mass Spectrometry (LC-MS)

Even though MS^n experiments are powerful for mixture analysis, chromatographic coupling is still often warranted to provide sample purification and/or concentration, in addition to separation of components in very complex mixtures. With the invention of atmospheric pressure ionization methods, such as ESI and APCI discussed above, high-performance liquid chromatography (HPLC) coupled with MS has become an important tool for structural elucidation of unknown analytes in complex mixtures.^{40,41} Chromatographic separation using HPLC allows the separation and concentration of mixture components much more efficiently and cost-effectively than many conventional wet chemistry techniques. The coupling of HPLC with a highly sensitive mass spectrometer, such as an LQIT, allows for the analysis of trace level analytes in complex mixtures with no sample preparation.

A Finnigan Surveyor HPLC system, consisting of an autosampler, thermostatted column compartment, quaternary pump and photodiode array (PDA) detector was used for chromatographic separation in this research. The analytes were separated by using a reversed phase HPLC column (typically with C₁₈ or phenyl mobile phase) with a slightly elevated column temperature (30 – 40 °C). The most commonly used mobile phases consisted of an aqueous solvent (pure water or a buffer solution) and an organic solvent (CH₃CN or CH₃OH). For each run, 25 µL of sample solution was loaded onto the column. Separation was accomplished by using an HPLC flow rate of 300 - 500 µL/min with various mobile phase gradients.

2.5 Fourier-Transform Ion Cyclotron Resonance (FT-ICR) Mass Spectrometry

Marshall and Comisarow first experimented with the concept of combining FT with ICR in 1974, which led to the realization of the FT-ICR mass spectrometer as a powerful analytical instrument.⁴² The FT-ICR mass spectrometer is known for its ultrahigh resolution and high mass accuracy,^{43,44} making this instrument ideal for analyzing very complex mixtures without chromatographic separation. To achieve the highest performance of the FT-ICR, ultrahigh vacuum and a high magnetic field are essential.⁴⁵

2.5.1 Instrumentation Overview

FT-ICR experiments were performed in a Thermo Scientific 7-T LTQ-FT-ICR⁴ mass spectrometer equipped cylindrical cell mass analyzer. A schematic of the LTQ-FT-ICR instrument is shown in Figure 2.9. The cell of the instrument was pumped by a

Pfeiffer TMU 262 turbo pump (210 L/s) to achieve a nominal baseline pressure of 2×10^{-10} Torr. The Pfeiffer TMU 262 turbo pump was backed by an intermediate state of a Pfeiffer TMH 262 turbo pump which in turn was backed by a Pfeiffer DUO 2.5 rotary-vane mechanical pump. A Dell optiplex workstation (Microsoft Windows XP operating system) running Xcalibur software was used to control the instrument as well as to acquire and process data.

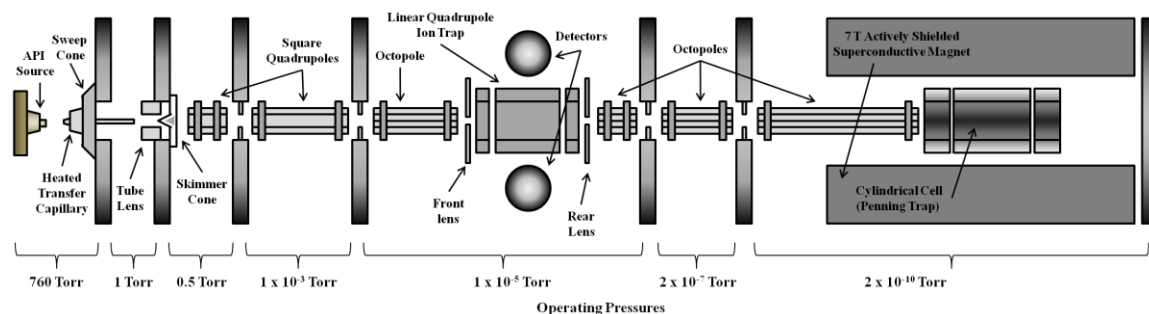


Figure 2.9 Schematic of the Thermo Scientific LTQ-FT-ICR mass spectrometer.

The cell of the instrument comprised of a segmented cylindrical cell illustrated in Figure 2.10. The cell was used solely for the purpose of high resolution data collection, all ion manipulation was conducted in the LQIT as described in Section 2.3. The three segments of the cylindrical cell function like the three segments of the LQIT, with the outer segments constraining the ions inside the middle section once they have entered. The middle segment was split into four pieces, two for excitation and two for detection, as shown in Figure 2.11.

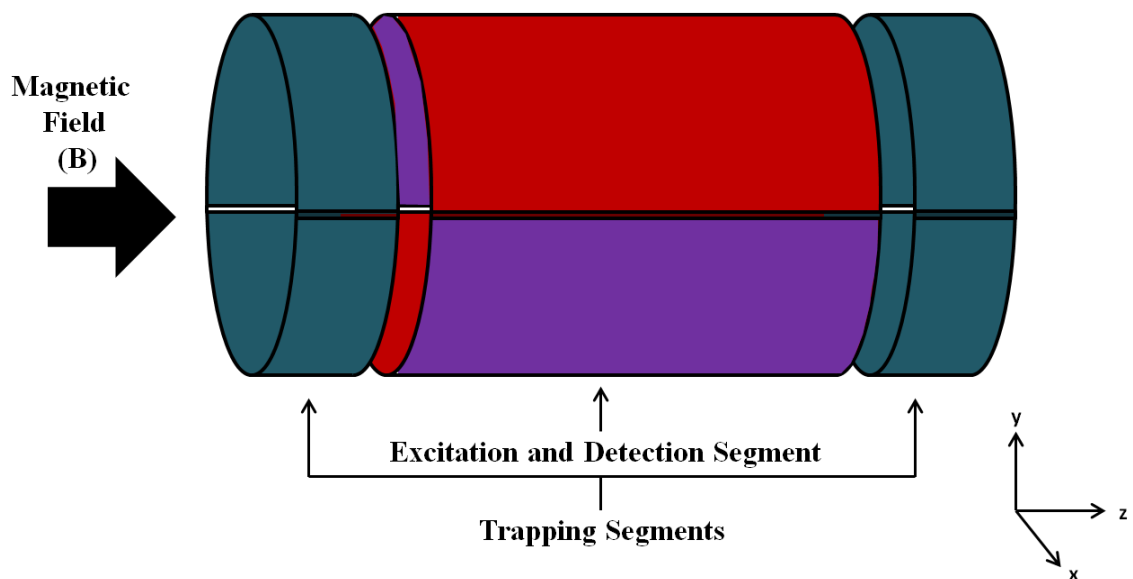


Figure 2.10 Diagram of the cylindrical cell present in the FT-ICR of a Thermo Scientific LTQ-FT-ICR.

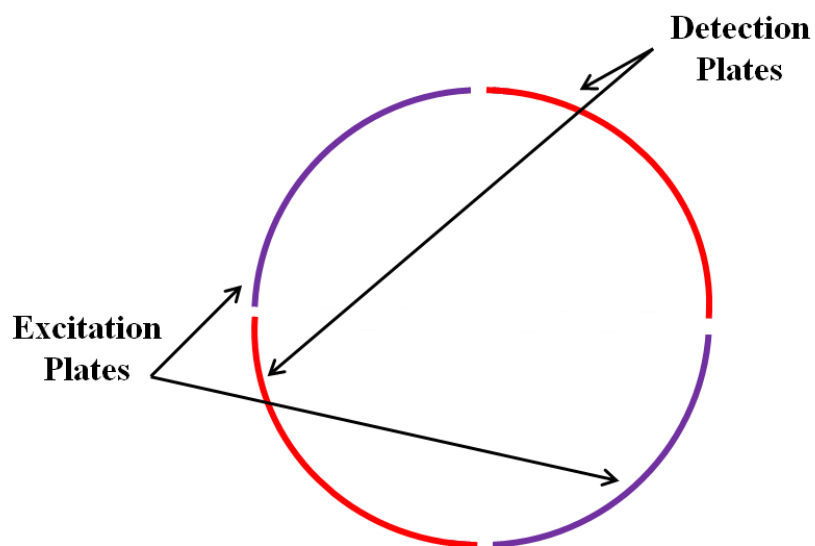


Figure 2.11 Frontal view of the center segments of a cylindrical ICR cell, showing how it is sectioned into four plates.

2.5.2 Ion Motion

Ions confined in the cell of an FT-ICR mass spectrometer are subject to three characteristic motions: cyclotron motion, trapping motion and magnetron motion. These motions are discussed below.

2.5.2.1 Cyclotron Motion

An ion moving in a uniform magnetic field is subjected to a Lorentz force, $F_{Lorentz}$,

$$F_{Lorentz} = qv_{xy}B \quad (2.16)$$

where q is the charge of the ion, v_{xy} is its velocity in the x-y plane perpendicular to the magnetic field, and B is the magnetic field strength. In addition to the Lorentz force, the ion also is subjected to a centrifugal force, $F_{centrifugal}$, that is directed outward due to the ion's momentum,

$$F_{centrifugal} = \frac{mv_{xy}^2}{r} \quad (2.17)$$

where m is the mass of the ion and r is the orbital radius of the ion. The balance of these two forces, as shown in Figure 2.12, produces a stable ion trajectory,⁴⁴

$$qv_{xy}B = \frac{mv_{xy}^2}{r} \quad (2.18)$$

Since frequency (ω) can be described as

$$\omega = \frac{v_{xy}}{r} \quad (2.19)$$

equation 2.18 can be rearranged so that cyclotron frequency (ω_c) can be defined as follows,⁴⁴

$$\omega_c = \frac{qB}{m} \quad (2.20)$$

Thus, the cyclotron frequency of the ion is dependent on only the charge of the ion, the magnetic field strength, and the mass of the ion. For the 7 T instrument used in this research, ICR frequencies range from a few kHz to a few MHz. Rearrangement of Equation 2.18 also allows the calculation of the ion cyclotron radius, r_c ,⁴⁴

$$r_c = \frac{mv_{xy}}{qB} \quad (2.21)$$

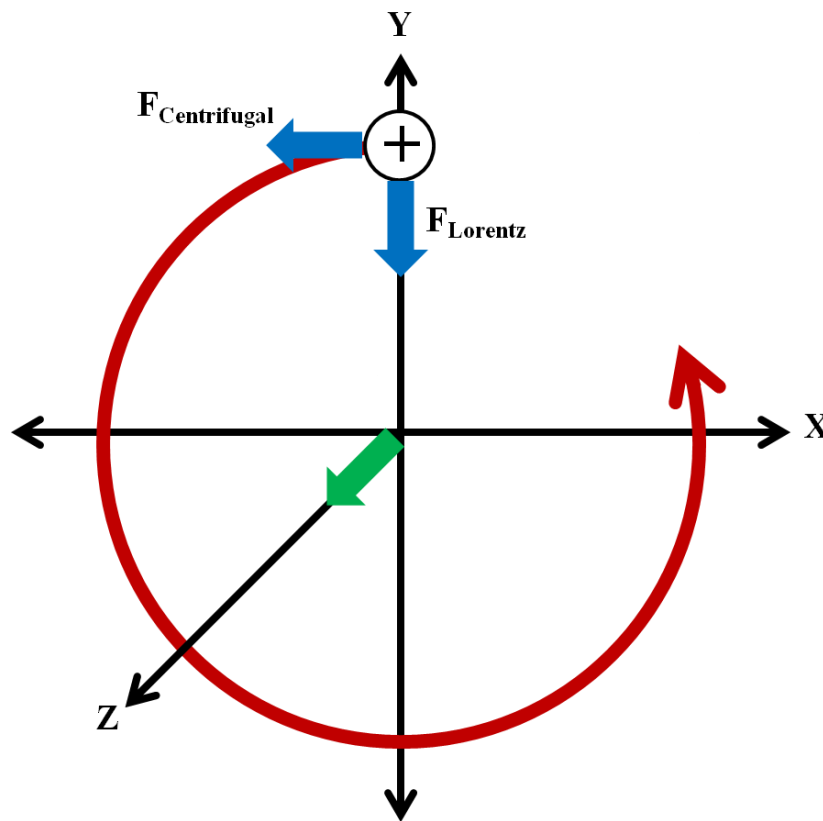


Figure 2.12 Illustration of the cyclotron motion of a positive ion in a magnetic field. The balance of the Lorentz force and centrifugal force acts to bend the ion motion into a circle perpendicular to the magnetic field in the x-y plane.

2.5.2.2 Trapping Motion

While the cyclotron motion of an ion confines it in the x and y directions, it is still able to move freely in the z direction. In order to confine the ion in the z direction, a small DC voltage (V_T) of the same polarity as the ion is applied to the trapping segments.⁴⁶ The center segment is held at ground. This set-up creates a potential well in the center segment similar to that of the LQIT that prevents the ion from drifting out of it. As a result of the voltages applied to the trapping segments, ions oscillate back and forth within the center segment in a mass dependent fashion. The frequency of this trapping motion, ω_T , is given by:

$$\omega_T = \sqrt{\frac{2qV_T\alpha}{md^2}} \quad (2.22)$$

where V_T is the trapping voltage, d is the distance between the trapping segments and α is the cell geometry constant. The trapping frequencies are typically much lower than the cyclotron frequencies, in the range of 10 - 10^3 Hz.

2.5.2.3 Magnetron Motion

A result of the DC potential used to trap ions in the z-direction is that a radial (in the x-y plane) electric field is also generated that acts on the ions. The DC potential in the x-y plane may be viewed as an inverted parabola with its maximum at the center of the cell. This field generates an outward electric force that directly opposes the inward Lorentz force produced by the magnetic field. This outward force causes the cyclotron orbit of the ions to shift off the z axis and the ions to orbit within the cell with a larger radius, called magnetron motion. The frequency of magnetron motion, ω_m , is given⁴⁷ by

$$\omega_m = \frac{2\alpha V_T}{d^2 B} \quad (2.23)$$

The magnetron frequency is independent of the mass of an ion, thus causing it not to be useful for mass measurement.⁴⁷ The magnetron frequency is much lower than the cyclotron frequency, and does not cause interference with the signal detection and processing. A diagram of an ion's trajectory as a result of all three motions cyclotron, trapping, and magnetron, is shown in Figure 2.13.

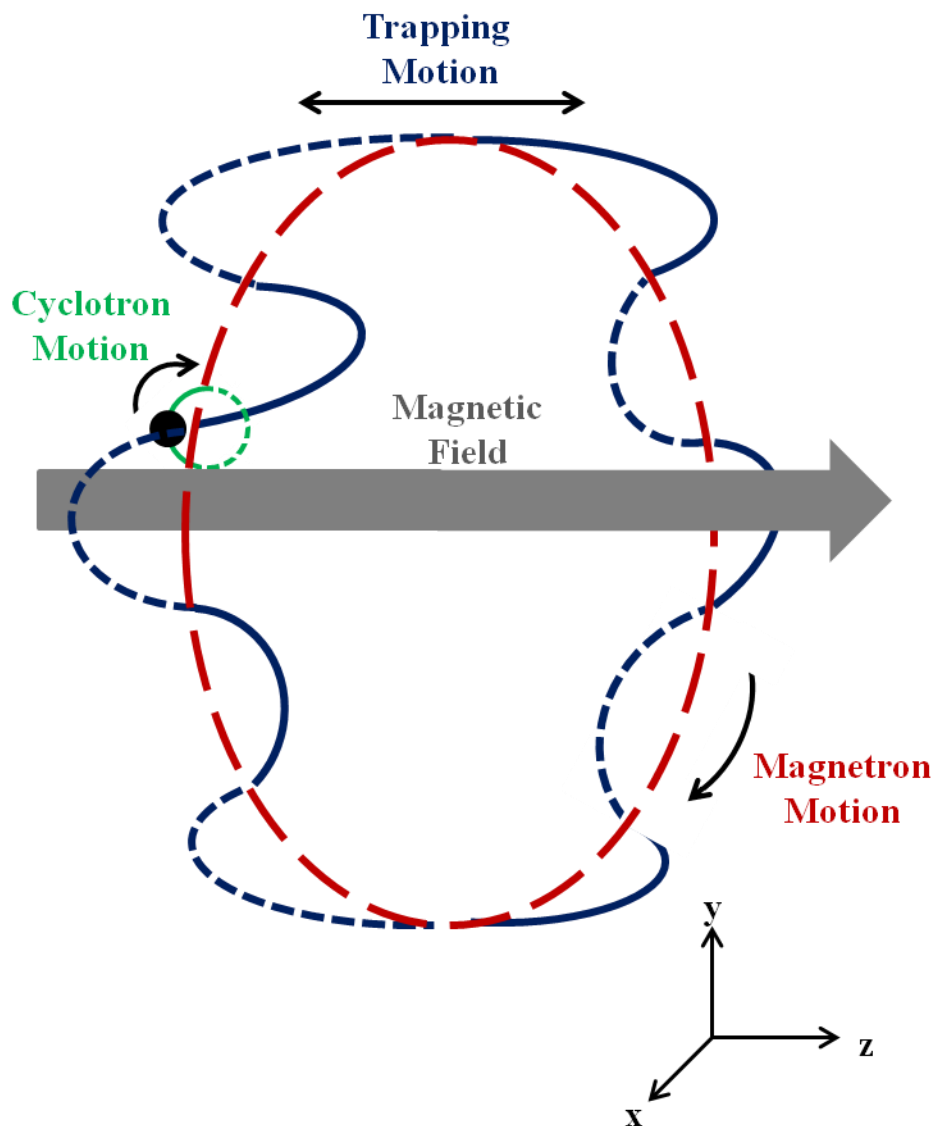


Figure 2.13 Diagram of three main motions of an ion within an ICR cell. The cyclotron orbit of the ion (green) confines it in the x and y directions as a result of the Lorentz and centrifugal forces. The trapping motion causes this orbit to oscillate back and forth (blue) in the z direction. Both motions are part of the ion motion on the larger magnetron orbit (red) as a result of the combination of the magnetic and electric fields. Note that the magnetron motion is greatly exaggerated in this figure for visual clarity.

2.5.3 Ion Excitation For Detection and Ejection

Ions in a FT-ICR are detected based on the image current they produce due to their coherent cyclotron motion near the detection plates. Without exciting the ions to a larger cyclotron radius, they are too far from the detection plates to be detected. Additionally, ions of the same m/z value do not move coherently as a packet. If the ions do not orbit coherently their phases are random and hence their signal will average to zero. By applying a dipolar RF excitation voltage sweep to the excitation plates in the center segment of the cell, both requirements are met.⁴⁴ All ions whose cyclotron frequencies fall within the range of the frequencies of the excitation voltage sweep are excited to a larger cyclotron orbit, r_{ex} , given by

$$r_{ex} = \frac{\beta V_{ex} \sqrt{\frac{1}{\text{Sweep Rate}}}}{2dB} \quad (2.24)$$

where β is the azimuthal dipolar excitation scale factor for the ICR cell and V_{ex} is the peak-to-peak dipolar excitation voltage.⁴⁸ The radius of the ions' motions after excitation is independent of the ions' m/z value, thus all ions are excited to the same cyclotron radius for detection. Continued excitation will excite ions to larger and larger cyclotron orbits. If the excitation duration is too long, ions will collide with the plates and become neutralized by the cell walls. For detection, ions are excited to move close to the plates of the cell.

The ion packet generates an alternating current as it passes between the detection plates, which is referred to as the image current.⁴⁹ An illustration of ion excitation and detection is shown in Figure 2.14. The frequency of the image current is the same as the

ions' cyclotron frequency, and the amplitude of the current is proportional to the number of ions within the packet.⁴⁹ The image current can be converted into a voltage difference between the detection plates and detected as a function of time to generate a transient. Using Fourier transformation, a frequency domain spectrum can be created from this transient. Using equation 2.20, a mass spectrum can be generated from the frequency domain spectrum.

For the experiments described in this thesis, a stored-waveform inverse Fourier transform (SWIFT) pulse was used to both excite and eject ions from the cell. SWIFT is an ion excitation method in which the excitation profile is determined in the frequency domain, and then subjected to inverse Fourier transformation to create the time domain waveform.^{50,51} This results in a well-defined excitation profile with good selectivity helping with both ion isolation for MS/MS⁵² and ion ejection to enhance dynamic range and reduce space charge.⁵³ SWIFT technique was primarily used for ion excitation for ejection to clean the cell in the research.

The ability to accurately measure the cyclotron frequency of ions gives FT-ICR mass spectrometers the ability to obtain very high resolution.⁵⁴ To increase the resolving power of an FT-ICR, longer transients may be recorded or more cycles of the cyclotron motion can be measured per a unit time. In order to record longer transients, high vacuum is needed because ions collapse back towards the center of the cell when they collide with neutral molecules or atoms. To measure more cycles of cyclotron motion, a higher magnetic field is needed since cyclotron frequency increases linearly with magnetic field strength.

The detection method utilized by FT-ICR instruments is unique compared to other detection methods used in mass spectrometry. The detection plates measure the image current produced by the ion packets, allowing ions of a wide mass range to be detected simultaneously.⁴⁴ Furthermore, since the detection of image current is non-destructive, ions can be continually excited and relaxed to remeasure the same sample multiple times to improve the signal to noise ratio.^{55,56}

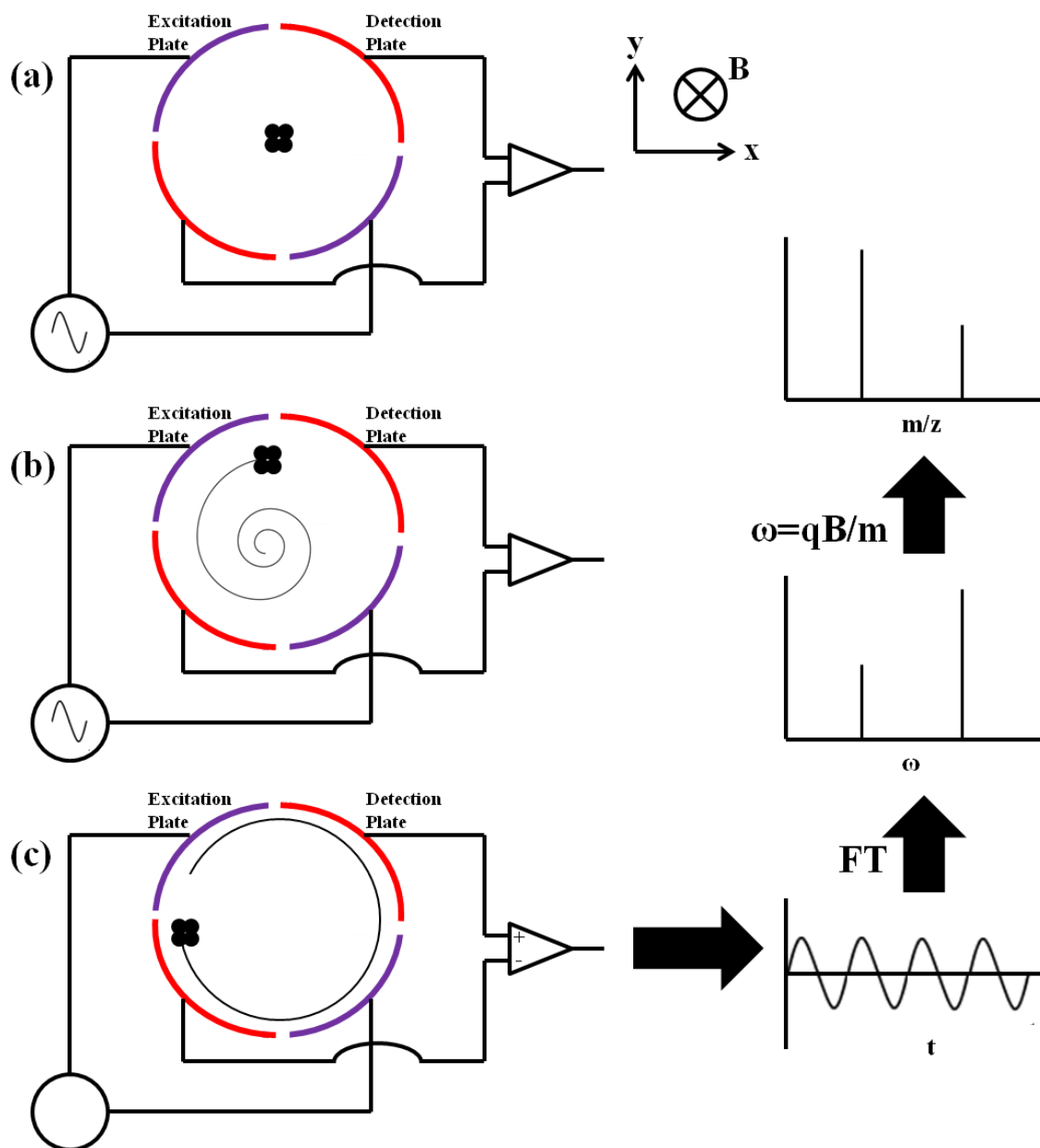


Figure 2.14 Diagram illustrating ion excitation and detection in the ICR cell. (a) Ions are trapped in the ICR cell and have random direction and too small of cyclotron radii to be detected. (b) Application of a broadband frequency sweep to the excitation plates excites ions to larger cyclotron orbits and makes ions of same m/z -values to move coherently as packets. (c) The ions pass by the detection plates and induce an image current that is recorded as a time domain transient. The time domain transient is then converted to a frequency spectrum by Fourier transformation, which in turn is converted to a mass spectrum.

2.6 Laser-Induced Acoustic Desorption (LIAD)

Seydel and Lindner in 1985 demonstrated that laser-induced acoustic waves could be used as a desorption technique for mass spectrometry.⁵⁷ They explored LIAD as a desorption/ionization technique but found it to suffer from poor ionization efficiency. Desorption of neutral molecules instead of ions was observed.⁵⁸⁻⁶⁰ Hence, these studies showed that the acoustic waves were adequate for desorption of the surface molecules but not for ionization. This discovery led our laboratories to investigate using LIAD solely as a desorption technique coupled to various post ionization methods.⁶¹ The decoupling of desorption and ionization is advantageous since both steps of the experiment can be optimized independently. Many commonly used desorption/ionization techniques, like ESI and MALDI, suffer from the lack of control over the type of ions that can be formed, that has led to a bias towards polar species for ESI and MALDI.²³ Since LIAD is decoupled from ionization, the ionization method can be tailored toward the analyte, which has been demonstrated through these different combinations: LIAD-EI,^{61,62} LIAD-CI,⁶³⁻⁶⁵ LIAD-PI,⁶⁶ and LIAD-ESI.⁶⁷ These different methods have proven useful for the analysis of various petroleum samples,⁶² biopolymers,⁶⁸⁻⁷⁰ as well as performing particle counting.^{71,72}

2.6.1 Generation of Acoustic Waves

LIAD uses the propagation of laser-induced shockwaves through a thin metal foil to evaporate neutral molecules deposited on the other side of the foil. For the studies presented in this thesis, LIAD was accomplished by firing frequency doubled (532 nm) laser pulses (3 ns pulse width) with a Continuum Minilite II Nd:YAG laser onto the back

side of the foil. The laser beam was focused onto the backside of the foil using a focusing lens so that the surface area irradiated is approximately 10^{-3} cm^2 . The irradiation of the backside of the foil generates acoustic waves that propagate through the foil to desorb the analyte as shown in Figure 2.15. While the mechanism of the desorption is not fully understood, the method has been shown to desorb neutral molecules with low internal and kinetic energy.^{73,74} The laser beam causes ablation of the titanium foil, resulting in the need for a sacrificial piece of glass to protect the high-vacuum fused silica window attached to the LIAD probe. The glass is replaced after each experiment due to the buildup of ablated metal on its surface. A digital picture showing the front and back sides of a sample foil following the LIAD experiment is shown in Figure 2.16. The current design allows for about 5% of the total surface of the foil to be used per experiment.

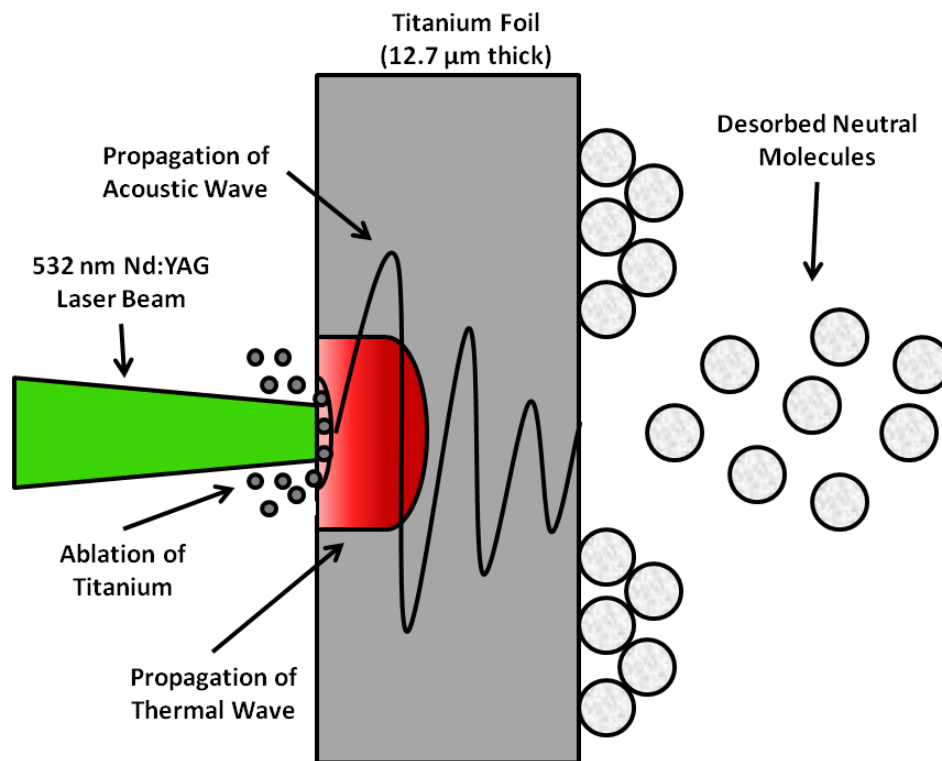


Figure 2.15 Diagram of the LIAD process.

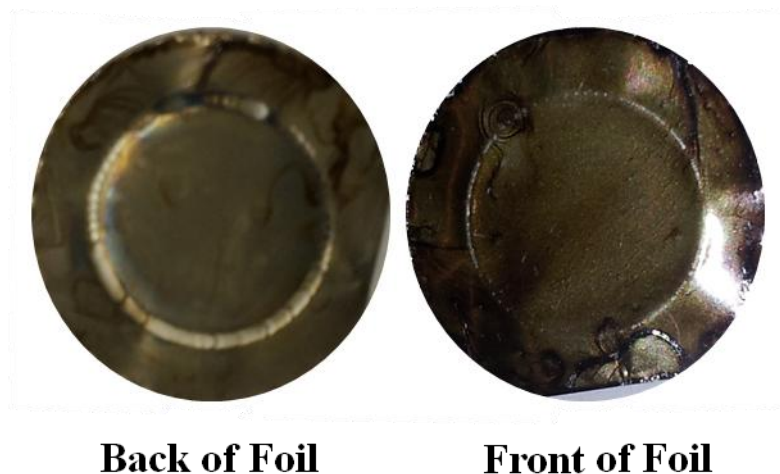


Figure 2.16 Front and back sides of a titanium foil with asphaltenes deposited onto it after it was used in a LIAD experiment. The circle on the back of the titanium foil indicates where the laser beam hit the foil and caused desorption to occur on the front of the foil where bare foil can be seen.

2.6.2 Metal Substrate

Work conducted early on utilizing LIAD found that acoustic wave generation during the experiment depended highly on the thickness and type of foil used.^{57,58,61} Low reflectivity, low thermal conductivity, and a high thermal expansion coefficient were found to be the ideal characteristics for efficient production of the thermal wave in the metal foil.⁷⁵ Low reflectivity allows more of the laser energy to be absorbed, low thermal conductivity prevents thermal degradation of the sample, and higher thermal expansion coefficient will produce a stronger acoustic wave. Metals were determined to be the best material in which to generate acoustic waves. Experiments showed that foils thicker than 20 μm were too thick for the acoustic wave to penetrate through the foil, resulting in poor desorption, but foils thinner than 5 μm resulted in thermal degradation of the sample.^{58,61}

Foils of approximately 10 μm thick were found to have the best desorption properties while preventing thermal degradation of the sample.

Many different metals, including Ti, were examined in a characterization study to determine which was best suited for LIAD experiments.^{66,76} Table 2.1 lists the different metal experimented with. Of the many different metals, titanium was determined to be the best substrate. All experiments utilizing LIAD described in this thesis were performed with 12.7 μm thick titanium foils.

Table 2.1 Important properties⁷⁷ of the metal foils that have been evaluated as substrates for LIAD.

<i>Metal</i>	<i>Thickness (μm)</i>	<i>Thermal Expansion Coefficient ($\times 10^{-6} \text{K}^{-1}$)</i>	<i>Thermal Conductivity ($\text{W cm}^{-1} \text{K}^{-1}$)</i>	<i>Reflectivity (at 532 nm)</i>
Ag ¹	12.5	18.8	4.29	0.81
Al ¹	10.0	23.1	2.37	0.91
Au ^{1,2}	10.0	14.2	3.17	0.81
Cu ¹	12.5	16.5	4.01	0.62
Fe ¹	12.5	11.8	0.802	0.57
Mo ²	12.5	4.8	1.38	0.58
Ni ²	12.5	13.4	0.907	0.61
Ta ²	12.5	6.3	0.575	0.37
Ti¹	12.7	8.6	0.219	0.50

¹ Ref. 77

² Ref. 68

2.6.3 Sample Preparation

Each LIAD experiment requires the analyte of interest to be deposited onto the surface of a titanium foil. This was accomplished using either electrospray deposition (ESD) or the dry drop method. An illustration of both ESD and the dry drop method is shown in Figure 2.17. ESD uses many of the same principles as ESI in its function, resulting in it requiring polar solvents and polar analytes to function properly.^{78,79} The solution was infused through a high voltage needle using a syringe pump at flow rates between 1 – 10 $\mu\text{L}/\text{min}$ onto the foil. The needle was held at a high potential, around 6 – 8 kV, with a high voltage power supply. The titanium foil was placed directly beneath the needle on a stage set to ground. To optimize sample coverage, the distance between the needle and the stage was adjusted between 2 to 5 cm. The ESD method reproducibly produces a uniform sample layer onto the titanium foil. Much of the research described in this thesis was performed on nonpolar compounds; hence, the dry drop method had to be used for sample deposition.

The dry drop method used for nonpolar analytes dissolved in nonpolar volatile solvents is heat-assisted. Hence, the titanium foil was usually placed onto a hot plate, a variant of a commonly used method for MALDI sample preparation.¹³ In the studies presented in this thesis, carbon disulfide (CS_2) was used to dissolve the analyte. A pipette was used to deposit drops of the solution onto the titanium foil until the surface was completely covered. During the sample deposition process, the foil was placed on a hot plate heated at ~ 40 $^\circ\text{C}$, causing the solvent to quickly evaporate and leaving a thin film of the analyte deposited on the surface of the foil. Additional drops were added until a sufficient amount of analyte was on the surface.

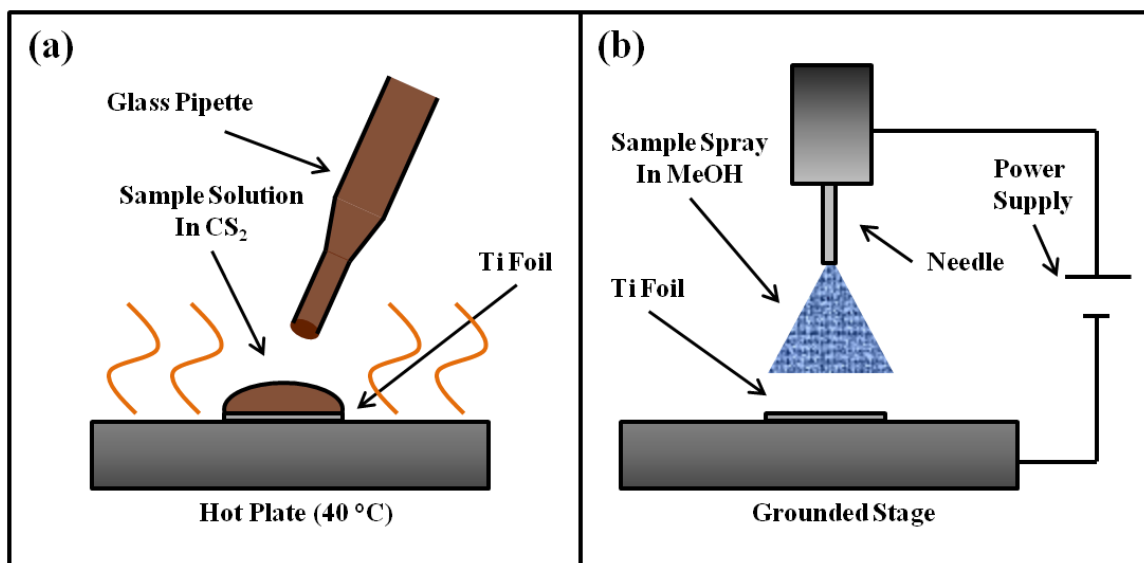


Figure 2.17 Illustration of two LIAD sample deposition methods, (a) dried-drop method and (b) electro spray deposition method.

2.6.4 LIAD Probes

Two different types of LIAD probes have been utilized to conduct LIAD experiments in the Kenttämä laboratories, the conventional, fiber LIAD probe that utilizes a fiber optic to transport the laser light to the titanium foil and a high power, fiberless probe using mirrors to reflect laser light that is to intense to use the fiber optic to the back side of the foil. Both probes are described further below.

2.6.4.1 Fiber LIAD Probe

For the fiber LIAD probe, the light from a Nd:YAG laser (532 nm) is focused onto a fiber optic cable that transports the beam through the probe to a set of 1:1 imaging optics. These optics focus the laser beam onto the backside of the foil that is positioned

at the end of the LIAD probe, resulting in the evaporation of the neutral analyte molecules when the laser is fired.⁶¹ The fiber LIAD probe can use power densities from $5 \times 10^8 \text{ W cm}^{-2}$ up to $9 \times 10^8 \text{ W cm}^{-2}$ at the back of the titanium foil. If the power exceeds $9 \times 10^8 \text{ W cm}^{-2}$, the fiber optic becomes damaged and requires replacement. The power densities able to be used with the fiber LIAD probe are insufficient to desorb heavy petroleum samples which was to focus for the work presented in this thesis requiring the use of the fiberless LIAD setup instead. Additional details on this setup can be found in the literature.^{61,80}

2.6.4.2 Fiberless LIAD Probe

To allow for the use of higher power densities than are allowed using fiber LIAD, a fiberless LIAD probe was developed.⁸¹ Fiberless LIAD uses high energy reflective kinematic mirrors to guide the laser beam through the LIAD probe onto the back of the foil. To guide the beam off axis there is a pair of internal mirrors placed at the tip of the probe. Once off axis, the beam is passed through a focusing lens onto the back of the titanium foil held at the end of the probe. An illustration of the inner mirror assembly is shown in Figure 2.18. Power densities up to $9 \times 10^9 \text{ W cm}^{-2}$ could be attained at the backside of the foil. Both the fiber LIAD and fiberless LIAD probes have been coupled to an LQIT using APCI.⁸² A diagram of fiberless LIAD coupled to an LQIT is shown in Figure 2.19. Additional details on this setup can be found in the literature.⁸¹

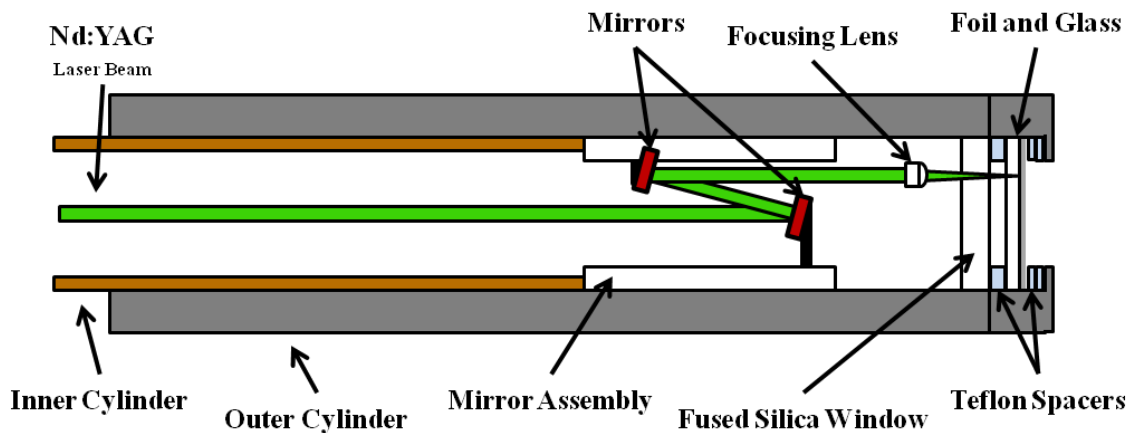


Figure 2.18 Schematic for the inner mirror assembly inside the tip of the fiberless LIAD probe.

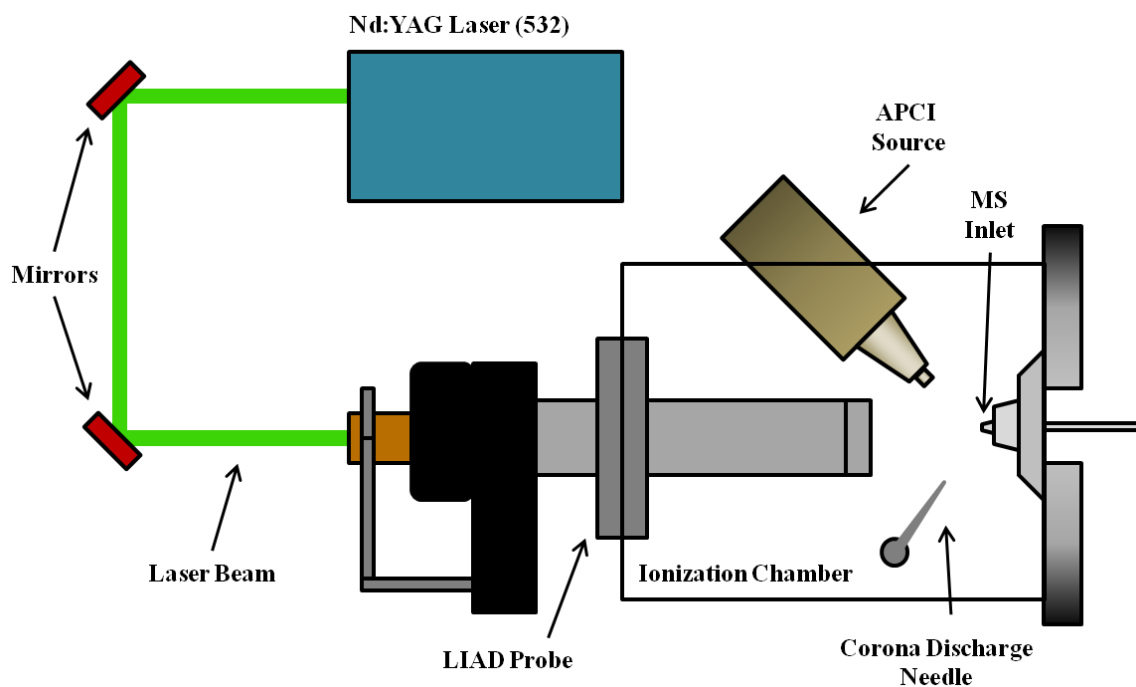


Figure 2.19 Illustration of the setup for coupling fiberless LIAD with a Thermo Scientific LTQ.

2.7 References

1. McLuckey, S.; Wells, J., Mass Analysis at the Advent of the 21st Century. *Chem. Rev.* **2001**, 101, 571-606.
2. Schwartz, J.; Senko, M.; Syka, J., A Two-Dimensional Quadrupole Ion Trap Mass Spectrometer. *J. Am. Soc. Mass Spectrom.* **2002**, 13, 659-669.
3. Hager, J., A New Linear Ion Trap Mass Spectrometer. *Rapid Commun. Mass Spectrom.* **2002**, 16, 512-526.
4. Syka, J.; Marto, J.; Bai, D.; Horning, S.; Senko, M.; Schwartz, J.; Ueberheide, B.; Garcia, B.; Busby, S.; Muratore, T.; Shabanowitz, J.; Hunt, D., Novel Linear Quadrupole Ion Trap/FT Mass Spectrometer: Performance Characterization and Use in the Comparative Analysis of Histone H3 Post-Translational Modifications. *J. Proteome Res.* **2004**, 3, 621-626.
5. Borton, D.; Pinkston, D.; Hurt, M.; Tan, X.; Azyat, K.; Scherer, A.; Tykwinski, R.; Gray, M.; Qian, K.; Kenttämä, H., Molecular Structures of Asphaltenes Based on the Dissociation Reactions of Their Ions in Mass Spectrometry. *Energy Fuels* **2010**, 24, 5548-5559.
6. Carroll, D.; Dzidic, I.; Stillwell, R.; Haegele, K.; Horning, E., Atmospheric Pressure Ionization Mass Spectrometry. Corona Discharge Ion Source for Use in a Liquid Chromatograph-Mass Spectrometer-Computer Analytical System. *Anal. Chem.* **1975**, 47, 2369-2373.
7. Carroll, D.; Dzidic, I.; Stillwell, R.; Horning, M.; Horning, E., Subpicogram Detection System for Gas Phase Analysis Based Upon Atmospheric Pressure Ionization (API) Mass Spectrometry. *Anal. Chem.* **1974**, 46, 706-710.
8. Raffaelli, A.; Saba, A., Atmospheric Pressure Photoionization Mass Spectrometry. *Mass Spectrom. Rev.* **2003**, 22, 318-331.
9. Whitehouse, C.; Dreyer, R.; Yamashita, M.; Fenn, J., Electrospray Interface for Liquid Chromatographs and Mass Spectrometers. *Anal. Chem.* **1985**, 57, 675-679.
10. Yamashita, M.; Fenn, J., Electrospray Ion Source. Another Variation on the Free Jet Theme. *J. Phys. Chem.* **1984**, 88, 4451-4459.
11. Takáts, Z.; Wiseman, J.; Gologan, B.; Cooks, R., Mass Spectrometry Sampling Under Ambient Conditions with Desorption Electrospray Ionization. *Science* **2004**, 306, 471-473.

12. Cody, R.; Laramée, J.; Durst, H., Versatile New Ion Source for the Analysis of Materials in Open Air under Ambient Conditions. *Anal. Chem.* **2005**, *77*, 2297-2302.
13. Karas, M.; Bahr, U.; Gießmann, U., Matrix Assisted Laser Desorption Ionization Mass Spectrometry. *Mass Spectrom. Rev.* **1991**, *10*, 335-357.
14. Houk, R.; Thompson, J., Inductively Coupled Plasma Mass Spectrometry. *Mass Spectrom. Rev.* **1988**, *7*, 425-461.
15. Barber, M.; Bordoli, R.; Sedgwick, R.; Tyler, A., Fast Atom Bombardment of Solids (F.A.B.): A New Ion Source for Mass Spectrometry. *J. Chem. Soc. Chem. Commun.* **1981**, (7), 325-327.
16. Bekey, H., Field Desorption Mass Spectrometry: A Technique for the Study of Thermally Unstable Substances of Low Volatility. *Int. J. Mass Spectrom. Ion Phys.* **1969**, *2*, 500-502.
17. Bekey, H., *Principles of Field Ionization and Field Desorption Mass Spectrometry*. 1st ed.; Pergamon Press: Oxford, 1977.
18. Nayak, R.; Knapp, D., Matrix-Free LDI Mass Spectrometry Platform Using Patterned Nanostructured Gold Thin Film. *Anal. Chem.* **2010**, *82*, 7772-7778.
19. Dempster, A., A New Method of Positive Ray Analysis. *Phys. Rev.* **1918**, *11*, 316-325.
20. Munson, M.; Field, F., Chemical Ionization Mass Spectrometry. I. General Introduction. *J. Am. Chem. Soc.* **1966**, *88*, 2621-2630.
21. Covey, T.; Thomson, B.; Schneider, B., Atmospheric Pressure Ion Sources. *Mass Spectrom. Rev.* **2009**, *28*, 870-897.
22. Sunner, J.; Nicol, G.; Kebarle, P., Factors Determining Relative Sensitivity of Analytes in Positive Mode Atmospheric Pressure Ionization Mass Spectrometry. *Anal. Chem.* **1988**, *60*, 1300-1307.
23. de Hoffmann, E.; Stroobant, V., *Mass Spectrometry Principles and Applications*. 3rd ed.; John Wiley & Sons, Ltd: West Sussex, England, 2007.
24. Cech, N.; Enke, C., Practical Implications of Some Recent Studies in Electrospray Ionization Fundamentals. *Mass Spectrom. Rev.* **2001**, *20*, 362-387.
25. Douglas, D.; Frank, A.; Mao, D., Linear Ion Traps in Mass Spectrometry. *Mass Spectrom. Rev.* **2005**, *24*, 1-29.

26. March, R., An Introduction to Quadrupole Ion Trap Mass Spectrometry. *J. Mass Spectrom.* **1997**, 32, 351-369.
27. March, R.; Todd, J., *Quadrupole Ion Trap Mass Spectrometry*. 2nd ed.; Wiley-Interscience: Hoboken, 2005.
28. Makarov, A.; Denisov, E.; Kholomeev, A.; Balschun, W.; Lange, O.; Strupat, K.; Horning, S., Performance Evaluation of a Hybrid Linear Ion Trap/Orbitrap Mass Spectrometer. *Anal. Chem.* **2006**, 78, 2113-2120.
29. Collings, B.; Campbell, J.; Mao, D.; Douglas, D., A Combined Linear Ion Trap Time-of-Flight System with Improved Performance and MS_n Capabilities. *Rapid Commun. Mass Spectrom.* **2001**, 15, 1777-1795.
30. Bier, M.; Syka, J. Ion Trap Mass Spectrometer System and Method. 1995.
31. Todd, J., Ion Trap Mass Spectrometer—Past, Present, and Future (?). *Mass Spectrom. Rev.* **1991**, 10, 3-52.
32. Stafford Jr, G.; Kelley, P.; Syka, J.; Reynolds, W.; Todd, J., Recent Improvements in and Analytical Applications of Advanced Ion Trap Technology. *Int. J. Mass Spectrom. Ion Process.* **1984**, 60, 85-98.
33. Kaiser Jr, R.; Cooks, G.; Stafford Jr, G.; Syka, J.; Hemberger, P., Operation of a Quadrupole Ion Trap Mass Spectrometer to Achieve High Mass/Charge Ratios. *Int. J. Mass Spectrom. Ion Process.* **1991**, 106, 79-115.
34. Schwartz, J.; Syka, J.; Jardine, I., High Resolution on a Quadrupole Ion Trap Mass Spectrometer. *J. Am. Soc. Mass Spectrom.* **1991**, 2, 198-204.
35. Busch, K.; Glish, G.; McLuckey, S., *Mass Spectrometry/Mass Spectrometry: Techniques and Applications of Tandem Mass Spectrometry*. VCH Publishers: New York, 1988.
36. Sleno, L.; Volmer, D., Ion Activation Methods for Tandem Mass Spectrometry. *J. Mass Spectrom.* **2004**, 39, 1091-1112.
37. Louris, J.; Cooks, G.; Syka, J.; Kelley, P.; Stafford, G.; Todd, J., Instrumentation, Applications, and Energy Deposition in Quadrupole Ion-Trap Tandem Mass Spectrometry. *Anal. Chem.* **1987**, 59, 1677-1685.
38. Schwartz, J.; Syka, J.; Quarmby, S., Improving the Fundamentals of MSⁿ on 2D Ion Traps: New Ion Activation and Isolation Techniques. In *53rd ASMS Conference on Mass Spectrometry and Allied Topics*, San Antonio, TX, 2005.

39. Murrell, J.; Despeyroux, D.; Lammert, S.; Stephenson Jr, J.; Goeringer, D., "Fast Excitation" CID in a Quadrupole Ion Trap Mass Spectrometer. *J. Am. Soc. Mass Spectrom.* **2003**, 14, 785-789.
40. Thomson, B., Atmospheric Pressure Ionization and Liquid Chromatography/Mass Spectrometry--Together at Last. *J. Am. Soc. Mass Spectrom.* **1998**, 9, 197-193.
41. Ermer, J.; Vogel, M., Applications of Hyphenated LC-MS Techniques in Pharmaceutical Analysis. *Biomed. Chromatogr.* **2000**, 14, 373-383.
42. Comisarow, M.; Marshall, A., Fourier Transform Ion Cyclotron Resonance Spectroscopy. *Chem. Phys. Lett.* **1974**, 25, 282-283.
43. Marshall, A.; Hendrickson, C.; Jackson, G., Fourier Transform Ion Cyclotron Resonance Mass Spectrometry. In *Encyclopedia of Analytical Chemistry*, John Wiley & Sons, Ltd: 2006.
44. Marshall, A.; Hendrickson, C.; Jackson, G., Fourier Transform Ion Cyclotron Resonance Mass Spectrometry: A Primer. *Mass Spectrom. Rev.* **1998**, 17, 1-35.
45. Marshall, A.; Guan, S., Advantages of High Magnetic Field for Fourier Transform Ion Cyclotron Resonance Mass Spectrometry. *Rapid Commun. Mass Spectrom.* **1996**, 10, 1819-1823.
46. McIver, R., A Trapped Ion Analyzer Cell for Ion Cyclotron Resonance Spectroscopy. *Rev. Sci. Instrum.* **1970**, 41, 555-558.
47. Amster, I., Fourier Transform Mass Spectrometry. *J. Mass Spectrom.* **1996**, 31, 1325-1337.
48. Wang, M.; Marshall, A., Laboratory-Frame and Rotating-Frame Ion Trajectories in Ion Cyclotron Resonance Mass Spectrometry. *Int. J. Mass Spectrom. Ion Process.* **1990**, 100, 323-346.
49. Comisarow, M., Signal Modeling for Ion Cyclotron Resonance. *J. Chem. Phys.* **1978**, 69, 4097-4104.
50. Guan, S.; Marshall, A., Stored Waveform Inverse Fourier Transform (SWIFT) Ion Excitation in Trapped-Ion Mass Spectrometry: Theory and Applications. *Int. J. Mass Spectrom. Ion Process.* **1996**, 157-158, 5-37.
51. Marshall, A.; Wang, T.; Ricca, T., Tailored Excitation for Fourier Transform Ion Cyclotron Resonance Mass Spectrometry. *J. Am. Chem. Soc.* **1985**, 107, 7893-7897.

52. Heeren, R.; Kleinnijenhuis, A.; McDonnell, L.; Mize, T., A Mini-Review of Mass Spectrometry Using High-Performance FTICR-MS Methods. *Anal. Bioanal. Chem.* **2004**, 3778, 1048-1058.
53. Guan, S.; Marshall, A. G.; Scheppele, S. E., Resolution and Chemical Formula Identification of Aromatic Hydrocarbons and Aromatic Compounds Containing Sulfur, Nitrogen, or Oxygen in Petroleum Distillates and Refinery Streams. *Anal. Chem.* **1996**, 68, 46-71.
54. Marshall, A.; Hendrickson, C., Charge Reduction Lowers Mass Resolving Power for Isotopically Resolved Electrospray Ionization Fourier Transform Ion Cyclotron Resonance Mass Spectra. *Rapid Commun. Mass Spectrom.* **2001**, 15, 232-235.
55. Williams, E.; Henry, K.; McLafferty, F., Multiple Remeasurement of Ions in Fourier-Transform Mass Spectrometry. *J. Am. Chem. Soc.* **1990**, 112, 6157-6162.
56. Speir, J.; Gorman, G.; Pitsenberger, C.; Turner, C.; Wang, P.; Amster, I., Remeasurement of Ions Using Quadrupolar Excitation Fourier Transform Ion Cyclotron Resonance Spectrometry. *Anal. Chem.* **1993**, 65, 1746-1752.
57. Lindner, B.; Seydel, U., Laser Desorption Mass Spectrometry of Nonvolatiles Under Shock Wave Conditions. *Anal. Chem.* **1985**, 57, 895-899.
58. Lindner, B., On the Desorption of Electrosprayed Organic Compounds from Supporting Metal Foils by Laser Induced Pressure Waves. *Int. J. Mass Spectrom. Ion Process.* **1991**, 103, 203-218.
59. Golovlev, V.; Allman, S.; Garrett, W.; Taranenko, N.; Chen, C., Laser-Induced Acoustic Desorption. *Int. J. Mass Spectrom. Ion Process.* **1997**, 169-170, 69-78.
60. Golovlev, V.; Allman, S.; Garrett, W.; Chen, C., Laser-Induced Acoustic Desorption of Electrons and Ions. *Applied Physics Letters* **1997**, 71, 852-854.
61. Pérez, J.; Ramírez-Arizmendi, L.; Petzold, C.; Guler, L.; Nelson, E.; Kenttämä, H., Laser-Induced Acoustic Desorption/Chemical Ionization in Fourier-Transform Ion Cyclotron Resonance Mass Spectrometry. *Int. J. Mass Spectrom.* **2000**, 198, 173-188.
62. Pinkston, D.; Duan, P.; Gallardo, V.; Habicht, S.; Tan, X.; Qian, K.; Gray, M.; Müllen, K.; Kenttämä, H., Analysis of Asphaltenes and Asphaltene Model Compounds by Laser-Induced Acoustic Desorption/Fourier Transform Ion Cyclotron Resonance Mass Spectrometry. *Energy Fuels* **2009**, 23, 5564-5570.

63. Duan, P.; Qian, K.; Habicht, S.; Pinkston, D.; Fu, M.; Kenttämäa, H., Analysis of Base Oil Fractions by $\text{ClMn}(\text{H}_2\text{O})^+$ Chemical Ionization Combined with Laser-Induced Acoustic Desorption/Fourier Transform Ion Cyclotron Resonance Mass Spectrometry. *Anal. Chem.* **2008**, *80*, 1847-1853.
64. Crawford, K.; Campbell, J.; Fiddler, M.; Duan, P.; Qian, K.; Gorbaty, M.; Kenttämäa, H., Laser-Induced Acoustic Desorption/Fourier Transform Ion Cyclotron Resonance Mass Spectrometry for Petroleum Distillate Analysis. *Anal. Chem.* **2005**, *77*, 7916-7923.
65. Campbell, J.; Crawford, K.; Kenttämäa, H., Analysis of Saturated Hydrocarbons by Using Chemical Ionization Combined with Laser-Induced Acoustic Desorption/Fourier Transform Ion Cyclotron Resonance Mass Spectrometry. *Anal. Chem.* **2004**, *76*, 959-963.
66. Zinovev, A.; Veryovkin, I.; Moore, J.; Pellin, M., Laser-Driven Acoustic Desorption of Organic Molecules from Back-Irradiated Solid Foils. *Anal. Chem.* **2007**, *79*, 8232-8241.
67. Cheng, S.; Cheng, T.; Chang, H.; Shiea, J., Using Laser-Induced Acoustic Desorption/Electrospray Ionization Mass Spectrometry to Characterize Small Organic and Large Biological Compounds in the Solid State and in Solution Under Ambient Conditions. *Anal. Chem.* **2009**, *81*, 868-874.
68. Petzold, C.; Ramirez-Arizmendi, L.; Heidbrink, J.; Perez, J.; Kenttämäa, H., Gas-Phase Reactions of Charged Phenyl Radicals with Neutral Biomolecules Evaporated by Laser-Induced Acoustic Desorption. *J. Am. Soc. Mass Spectrom.* **2002**, *13*, 192-194.
69. Liu, J.; Petzold, C.; Ramirez-Arizmendi, L.; Perez, J.; Kenttämäa, H., Phenyl Radicals React with Dinucleoside Phosphates by Addition to Purine Bases and H-Atom Abstraction from a Sugar Moiety. *J. Am. Chem. Soc.* **2005**, *127*, 12758-12759.
70. Yang, L.; Nash, J.; Yurkovich, M.; Jin, Z.; Vinueza, N.; Kenttämäa, H., Gas-Phase Reactivity of Aromatic s,s-Biradicals Toward Dinucleoside Phosphates. *Org. Lett.* **2008**, *10*, 1889-1892.
71. Peng, W.; Yang, Y.; Kang, M.; Tzeng, Y.; Nie, Z.; Chang, H.; Chang, W.; Chen, C., Laser-Induced Acoustic Desorption Mass Spectrometry of Single Bioparticles. *Angew. Chem. Int. Ed.* **2006**, *45*, 1423-1426.
72. Nie, Z.; Cui, F.; Tzeng, Y.; Chang, H.; Chu, M.; Lin, H.; Chen, C.; Lin, H.; Yu, A., High-Speed Mass Analysis of Whole Erythrocytes by Charge-Detection Quadrupole Ion Trap Mass Spectrometry. *Anal. Chem.* **2007**, *79*, 7401-7407.

73. Shea, R.; Petzold, C.; Liu, J.; Kenttämää, H., Experimental Investigations of the Internal Energy of Molecules Evaporated via Laser-Induced Acoustic Desorption into a Fourier Transform Ion Cyclotron Resonance Mass Spectrometer. *Anal. Chem.* **2007**, 79, 1825-1832.
74. Dow, A.; Wittrig, A.; Kenttämää, H., Laser-Induced Acoustic Desorption (LIAD) Mass Spectrometry. *Eur. J. Mass Spectrom.* **2012**, 18, 77-92.
75. Scruby, C.; Drain, L., *Laser Ultrasonics: Techniques and Applications*. Adam Hilger: New York, 1990.
76. Shea, R.; Petzold, C.; Campbell, J.; Li, S.; Aaserud, D.; Kenttämää, H., Characterization of Laser-Induced Acoustic Desorption Coupled with a Fourier Transform Ion Cyclotron Resonance Mass Spectrometer. *Anal. Chem.* **2006**, 78, 6133-6139.
77. Haynes, W., *CRC Handbook of Chemistry and Physics*. 93th (Internet Version 2012) ed.; CRC Press/Taylor and Francis: Boca Raton, FL, 2012/2013.
78. Hensel, R.; King, R.; Owens, K., Electrospray Sample Preparation for Improved Quantitation in Matrix-Assisted Laser Desorption/Ionization Time-of-Flight Mass Spectrometry. *Rapid Commun. Mass Spectrom.* **1997**, 11, 1785-1793.
79. Axelsson, J.; Hoberg, A.; Waterson, C.; Myatt, P.; Shield, G.; Varney, J.; Haddleton, D.; Derrick, P., Improved Reproducibility and Increased Signal Intensity in Matrix-Assisted Laser Desorption/Ionization as a Result of Electrospray Sample Preparation. *Rapid Commun. Mass Spectrom.* **1997**, 11, 209-213.
80. Pérez, J.; Petzold, C.; Watkins, M.; Vaughn, W.; Kenttämää, H., Laser Desorption in Transmission Geometry Inside a Fourier-Transform Ion Cyclotron Resonance Mass Spectrometer. *J. Am. Soc. Mass Spectrom.* **1999**, 10, 1105-1110.
81. Shea, R.; Habicht, S.; Vaughn, W.; Kenttämää, H., Design and Characterization of a High-Power Laser-Induced Acoustic Desorption Probe Coupled with a Fourier Transform Ion Cyclotron Resonance Mass Spectrometer. *Anal. Chem.* **2007**, 79, 2688-2694.
82. Gao, J.; Borton, D.; Owen, B.; Jin, Z.; Hurt, M.; Amundson, L.; Madden, J.; Qian, K.; Kenttämää, H., Laser-Induced Acoustic Desorption/Atmospheric Pressure Chemical Ionization Mass Spectrometry. *J. Am. Soc. Mass Spectrom.* **2011**, 22, 531-538.

CHAPTER 3: ON-LINE MASS SPECTROMETRIC METHODS FOR THE DETERMINATION OF THE PRIMARY PRODUCTS OF FAST PYROLYSIS OF CARBOHYDRATES AND FOR THEIR GAS-PHASE MANIPULATION.

3.1 Introduction

With the diminishing petroleum resources along with various environmental concerns regarding petroleum based energy, new sources of fuel are needed.¹⁻³ Fast pyrolysis, i.e., rapid heating of matter in the absence of oxygen, is thought to be a potentially viable approach to produce fuels and other valuable chemicals from lignocellulosic biomass.²⁻⁶ This is attributable to the ability of pyrolysis to cleave vast polymers into smaller carbon containing molecules that retain most of the energy-rich chemical bonds that were present in the polymer.^{7,8} Cellulose is the simplest and most abundant polymer in biomass, consisting of up to thousands of dehydrated glucose building blocks (molecular weight (MW) 162 Da) linked together via glycosidic bonds.^{4,9} Consequently, cellulose and related carbohydrates are a logical starting point for the study of biomass pyrolysis.

Most current fast pyrolysis reactors produce bio-oils from carbohydrates that are viscous liquids with several unfavorable properties that prevent them from being a viable precursor to fuel production, including their tendency to degrade over time.^{1,2,4,10-14} Bio-oils are very complex, oxygen-rich mixtures with roughly half the heating value of gasoline that require catalytic upgrading.^{10,12} The upgrading process is greatly hindered

by the complexity of bio-oils as well as their compositional dependence on the time and temperature that the primary pyrolysis products experience within the pyrolysis reactor.^{13,15,16} The first compounds that leave the surface of the pyroprobe ribbon (for the experiments presented in this chapter) are considered here the primary products.

To better understand the reactor parameters that control the complexity of bio-oils, the primary products of carbohydrate pyrolysis need to be determined, along with how those primary products react within a pyrolysis reactor. The fast pyrolysis reactors that have been used to study carbohydrates normally have residence times that range from hundreds of milliseconds up to several seconds.^{17,18} Due to the length of these reaction times and the process of condensing the products into a bio-oil, the final liquid pyrolysis products no longer bear a resemblance to the primary products since they have undergone secondary gas-phase and solution reactions.^{4,16,19} To help address this problem, many fast-pyrolysis experiments have been coupled with gas chromatography/mass spectrometry (GC/MS) to carry out on-line studies of primary pyrolysis products.²⁰⁻²⁶ Based on these and other similar studies, levoglucosan is widely believed to be the major primary product of cellulose fast pyrolysis although some studies suggest formation of other small molecules in tandem with the formation of levoglucosan.^{22,26-28} A serious limitation of the GC/MS approach is that it only allows the determination of relatively volatile and thermally stable compounds. Carbohydrates larger than a single monomeric unit (MW 162 Da) cannot be detected by GC/MS without derivatization.^{11,27,29} A different on-line analysis method coupled with fast-pyrolysis with is needed in order to be able to observe and study all of the primary products.

To achieve the above goal, two fast pyrolysis/tandem mass spectrometry systems were devised, one to measure the primary products of carbohydrate fast pyrolysis and another one to study how changes in temperature and residence time change the extent of secondary reactions of the primary products in order to simulate a pyrolysis reactor. The results obtained using both systems for model compounds as well as cellobiose are described below.

3.2 Experimental

Chemicals. Hydroxyacetone (technical grade, 90%), furfural (99%), 5-hydroxymethylfurfural (99%), levoglucosan (99%), chloroform (ChromasolvPlus for HPLC, $\geq 99.9\%$ with amylene stabilizer), and glycolaldehyde dimer were purchased from Sigma Aldrich. Cellobiosan ($>95\%$) and cellobiose ($\geq 98\%$) were purchased from Carbosynth, methanol (Optima LC/MS, $\geq 99.9\%$) was purchased from Fisher Scientific, ammonium hydroxide (28-30% as NH_3) was purchased from Mallinckrodt Chemicals, cellotriosan (98%) was purchased from LC Scientific, and a compressed nitrogen cylinder ($\geq 99.9\%$) was purchased from Indiana Oxygen. All chemicals except for the glycolaldehyde dimer were used without further modification. Glycolaldehyde dimer was converted to monomers via dissolving in water and heating at 65°C for 10 minutes.³⁰

Instrumentation. Detection and characterization of cellobiose fast pyrolysis products was performed using a Thermo Scientific LTQ linear quadrupole ion trap (LQIT) mass spectrometer coupled with a Finnigan Surveyor Liquid Chromatograph (LC). High resolution data to determine elemental compositions were collected using a 7 Tesla Thermo Scientific LTQ-FT-ICR. Solutions for direct injection experiments of

model compounds were made at a concentration of 10^{-5} M in 3 mL methanol : water (50 : 50 v/v) with either 200 μ L of chloroform for negative ion mode chloride attachment or 200 μ L ammonium hydroxide for positive ion mode ammonium attachment. The solutions were pumped into an APCI source via the APCI probe at a rate of 3 μ L/min with a solution of methanol : water (50 : 50 v/v) tee-infused from the LC at a rate of 100 μ L/min. During pyrolysis experiments, either chloroform : methanol (50 : 50 v/v) or ammonium hydroxide : water (50 : 50 v/v) solution was pumped into the APCI source via the APCI probe at a rate of 10 μ L/min with a solution of methanol : water (50 : 50 v/v) tee-infused from the LC at a rate of 100 μ L/min. The instrumental variables of the LQIT were set to the following values for all experiments: discharge current 5.0 μ A, vaporizer temperature 300 $^{\circ}$ C, sheath gas (N_2) flow 40 arbitrary units, auxiliary gas flow (N_2) 10 arbitrary units, sweep gas flow (N_2) 0 arbitrary units, capillary temperature 250 $^{\circ}$ C, capillary voltage -1 V, and tube lens voltage -105 V. Collisionally activated dissociation (CAD) experiments used an ion isolation window of ± 2 Daltons (Da), with the normalized collision energy ranging from 5 up to 30 arbitrary units and activation time being 30 ms. Data collection and processing was carried out using Xcalibur 2.1 software.

All pyrolysis experiments were performed using a Pyroprobe 5200 purchased from CDS Analytical. The pyroprobe uses a resistively heated platinum ribbon (2.1 mm x 35 mm x 0.1 mm) with the ability to heat at rates up to 20,000 $^{\circ}$ C s^{-1} . Based on previous work in other laboratories, platinum is not acting as a catalyst during the pyrolysis experiments.^{31,32} Roughly tens to hundreds of micrograms of sample were loaded onto the platinum ribbon and held onto the surface via electrostatic attractions. This method of loading of the ribbon resulted in a submonolayer of sample on its surface.

This was done to ensure rapid and uniform heat transfer to all particles. The ribbon was heated up to 600 °C at a rate of 1,000 °C s⁻¹ resulting in a heating time of 0.6 s. The pyroprobe was maintained at 600° for 1 s. This final temperature and rate of temperature increase were selected due to minimal char formation (optical observation) under these conditions.

The tip on the probe described above was inserted into the ionization chamber of the LQIT through a home-built adaptor that was placed into the unused atmospheric pressure photoionization (APPI) port. This adaptor positioned the platinum ribbon approximately 5 mm in front of and 5 mm below the skimmer cone/inlet of the LQIT. A diagram of this setup is shown in Figure 3.1. Once pyrolysis occurred, the evaporated products were immediately diluted via diffusion into the 2 L ionization chamber and subsequently quenched via collisions with nitrogen gas (at about 100 °C), which prevented secondary reactions. The products were ionized and characterized by high-resolution multi-stage tandem mass spectrometry experiments. For ammonium attachment in positive ion mode, the average standard deviations of the product ions' relative abundances were about 7%. For chloride attachment in negative ion mode, the average standard deviations of the product ions' relative abundances were about 5%.

To explore the secondary reactions of the primary pyrolysis products, a home-built aluminum flow tube was constructed to prevent immediate quenching of the primary products. The tip of the pyroprobe was placed in the end of the heated aluminum tube. Preheated nitrogen gas was passed through the flow tube and over the platinum ribbon to sweep the products through the flow tube and into the ionization zone of the LQIT where they were quenched and ionized. A diagram of this setup is also shown in Figure 3.1. To

adapt the instrument for the placement of the flow tube into the ionization area, the window in the front door of the ionization chamber was replaced with a piece of ceramic with a hole in the center that had the same diameter as the flow tube. The flow tube and nitrogen gas were kept at the same temperature by using a temperature control system. This configuration allowed the study of the effects of temperature and residence time on the reactions of the primary products within the flow tube. The residence times were estimated by determining the time it takes for the gas with a known flow rate to pass through the flow tube with a known internal volume.

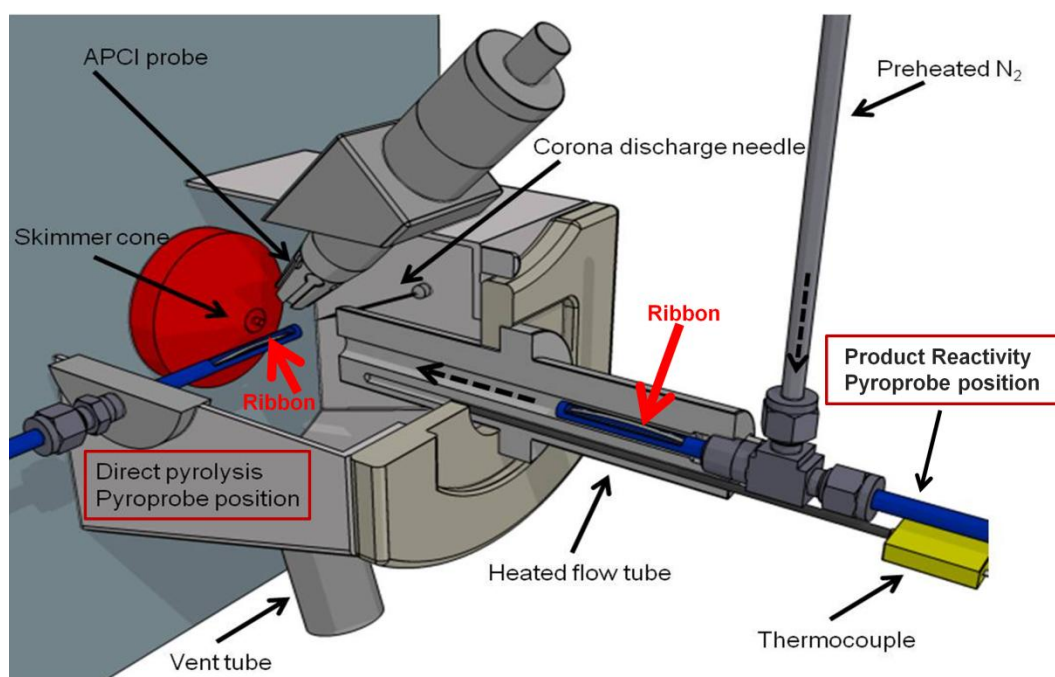


Figure 3.1. A cut away diagram of the ionization chamber in front of the LQIT. The pyroprobe (in blue) is shown in both the direct pyrolysis (left) orientation and within the flow tube (right). The direction of gas flow is indicated by the dashed arrow.

3.3 Results and Discussion

In order to develop methodology for the determination of the primary products of fast pyrolysis of carbohydrates, and to examine their secondary reactions, two pyrolysis probe setups were coupled with a LQIT. In the setup for analysis of the primary pyrolysis products, the products from the pyroprobe were quenched and ionized by APCI immediately after evaporation into the ion source, followed by analysis of the product ions in the LQIT. In the other setup, the pyrolysis products were provided time in a flow tube to undergo secondary and tertiary reactions before quenching and analysis of the products.

Six model compounds commonly formed during carbohydrate pyrolysis,^{9,33} glycolaldehyde, hydroxyacetone, furfural, 5-hydroxymethylfurfural, levoglucosan, and cellobiosan, were examined to select an appropriate APCI method for the analysis of pyrolysis products. Negative ion mode APCI doped with chloroform has been shown to create chloride anions that readily attach to carbohydrates with nearly equal efficiencies and without extensive fragmentation.³⁴⁻³⁷ Each of the six model compounds were introduced individually into the APCI source by direct injection while using chloroform dopant to test this method's ability to ionize pyrolysis products. The results obtained using direct injection show that although this method formed stable chloride anion adducts with no fragmentation for most compounds, it formed deprotonated hydroxyacetone instead of a chloride anion adduct and did not ionize glycolaldehyde and furfural.

Since negative ion mode chloride anion attachment was unable to ionize all of the model compounds, a complementary ionization technique was tested. Ammonium

hydroxide dopant in positive ion mode chemical ionization and APCI is known to form stable ammonium adducts with carbohydrate residues and to produce either protonated molecules or molecular ions from related low molecular weight molecules.³⁷⁻³⁹ Each of the six model compounds were individually introduced into the APCI source both via direct injection and by vaporizing them off the heated pyrolysis probe while using ammonium hydroxide dopant. This approach was found to ionize all six model compounds without fragmentation. However, the different analytes produced different types of ions (ammonium adducts, molecular ions and/or protonated molecules) when they were introduced via direct injection. When the compounds were evaporated from the heated pyroprobe, on the other hand, the ammonium adducts dominated for most model compounds. However, furfural, glycolaldehyde and 5-hydroxymethylfurfural still formed more than one type of ion and hydroxyacetone only produced a molecular ion. It is important to note that during heated pyroprobe introduction of glycolaldehyde, the ionized dimer was observed for both ionization methods, indicating that the method that was used to break down the glycolaldehyde dimer did not result in complete dissociation or reassociation occurred on the pyroprobe as the solvent evaporated. This may be the reason for the inability to observe glycolaldehyde in some of the experiments.

Finally, an equimolar mixture of all six model compounds (the concentration of glycolaldehyde was not exactly known due to the incomplete conversion of its dimer to glycolaldehyde) was injected into the ion source and analyzed by using both ionization methods to determine whether the detection of some of the compounds may be hindered by the presence of compounds with greater ionization efficiencies. The mass spectrum obtained using positive ion mode with ammonium hydroxide dopant (Figure 3.2) shows

that all six compounds can be observed if they are present in roughly equal proportions. Interestingly, only 5-hydroxymethylfurfural produced more than one ion (it produced two). The response factors of the compounds varied widely.

Chloride attachment APCI did not ionize glycolaldehyde, hydroxyacetone, and furfural in the mixture introduced via direct injection or by the heated pyroprobe. 5-Hydroxymethylfurfural, levoglucosan, and cellobiosan produced solely chloride anion adducts. Levoglucosan and cellobiosan were evaporated and ionized with almost equal efficiency (Figure 3.3). 5-Hydroxymethylfurfural yielded a very low signal due to its low chloride anion affinity (it contains only one hydroxyl group).

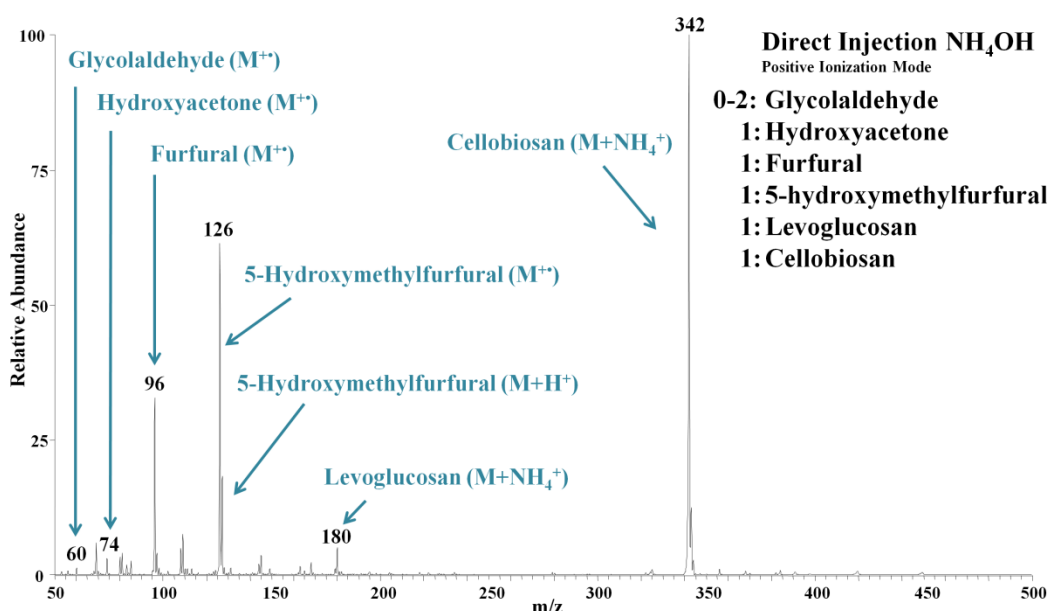


Figure 3.2 An APCI/ammonium hydroxide positive ion mass spectrum of an equimolar mixture of six model compounds introduced via direct injection (the molar ratio of glycolaldehyde is estimated to be between 0-2 due to the unknown extent of glycolaldehyde dimer breakdown). All model compounds were ionized but not equally efficiently.

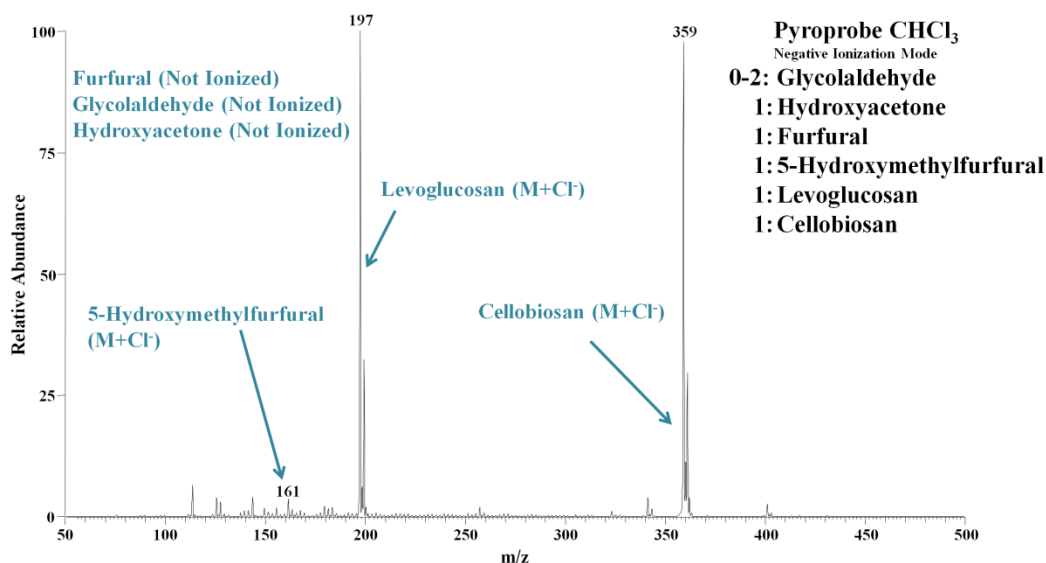


Figure 3.3 An APCI/chloroform negative ion mass spectrum of an equimolar mixture of six model compounds introduced via the heated pyroprobe (the molar ratio of glycolaldehyde is estimated to be between 0-2 due to the unknown extent of glycolaldehyde dimer breakdown). Three model compounds were not ionized.

Once it was realized that the ammonium hydroxide dopant method can be used to ionize all six model compounds but not with equal response factors and that the chloroform dopant method yields semi-quantitative information for carbohydrates but not for smaller model compounds, both ionization methods were used to examine the primary products of fast pyrolysis of cellobiose by using the direct pyrolysis setup described previously. All but a few pyrolysis products were found to ionize by both methods (Figure 3.4). All compounds larger than levoglucosan demonstrated 100% ammonium or chloride attachment. Levoglucosan showed both adducts as well as protonated (positive ion mode) and deprotonated molecules (negative ion mode). The compounds smaller than levoglucosan did not show adducts but instead were either protonated (positive ion mode) or deprotonated (negative ion mode).

Several primary products were detected for fast pyrolysis of cellobiose (Figure 3.4). Their elemental compositions were determined by using high-resolution experiments. Many of these products arise from losses of water (18 Da), formaldehyde (30 Da) and glycolaldehyde (60 Da) in various combinations. Although water, formaldehyde and glycolaldehyde were not efficiently detected in these experiments, their formation can be inferred from the reactions observed. In addition to these compounds, among the products observed, only levoglucosan (MW 162) and 5-hydroxymethylfurfural (MW 126) have been reported in the literature as major final fast pyrolysis products of cellobiose.^{22,26} This is not surprising since most previous studies have employed GC-MS analysis. For example, the largest molecules observed in such previous studies were levoglucosan and its isomers.^{22,26} Therefore, it is not unexpected that several products that had not been previously reported were observed to be present in large quantities (Table 3.1), including glucose, cellobiosan and cellobiose that has lost glycolaldehyde or an isomeric molecule. The most abundant product with an elemental composition of $C_8H_{14}O_7$ is likely to have the structure shown in Figure 3.4. This structure is proposed due to the similarity of the ionized molecule's CAD mass spectrum to that published for an authentic ion in a previous study.⁴⁰

Due to the semi-quantitative nature of the chloride attachment method,³⁵ approximate relative quantitation can be achieved for molecules with at least two hydroxyl groups by considering the relative abundances of their chloride adducts (Table 3.1). The relative molar percent for the molecules that do not form chloride anion adducts was estimated (Table 3.1) using relative ionization efficiencies for ammonium cation attachment determined for model compounds under the same conditions as in

pyrolysis experiments. Deprotonated 5-hydroxymethylfurfural (m/z 127; identified based on the identical CAD mass spectra measured for the unknown ion and the deprotonated authentic 5-hydroxymethylfurfural) is considered first.

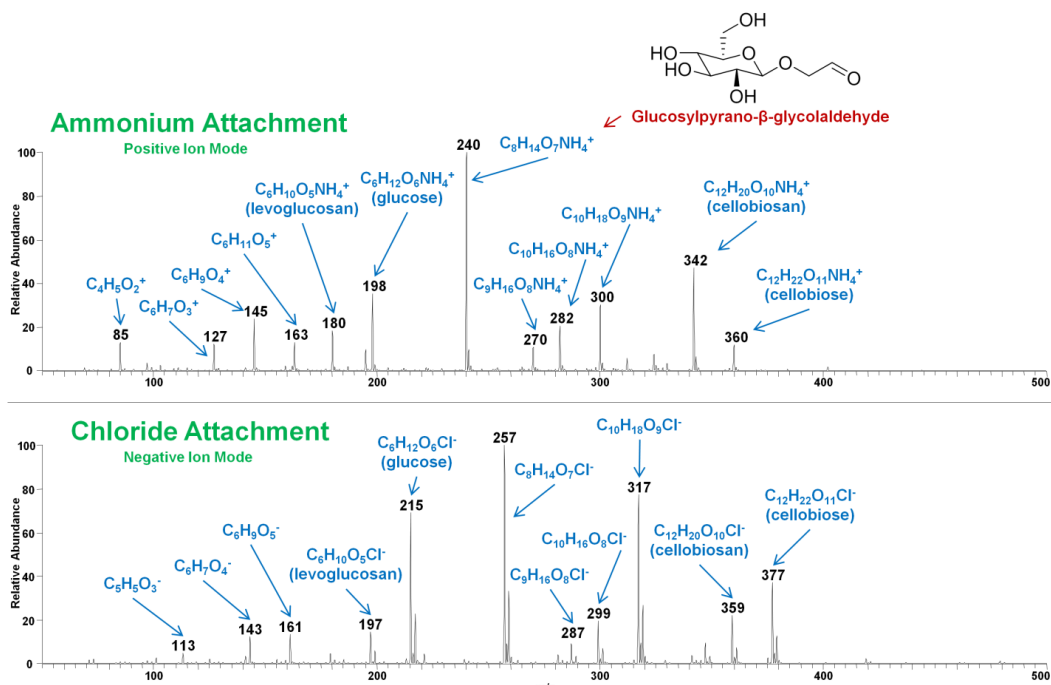


Figure 3.4 Mass spectra of the primary products of fast pyrolysis of cellobiose ($C_{12}H_{22}O_{11}$) ionized using ammonium attachment in positive ion mode (top) and chloride attachment in negative ion mode (bottom). All elemental compositions were determined using high resolution data collected in a LQIT/FT-ICR. Ionized levoglucosan has m/z values of 163 and 180 in the top spectrum and m/z values of 161 and 197 in the bottom spectrum. All ions with m/z values lower than 170 correspond to protonated molecules in the top spectrum and deprotonated molecules in the bottom spectrum, and hence have m/z values that differ by two units. Protonated $C_4H_5O_2$ molecule (m/z 85) is only seen in the top spectrum, while deprotonated $C_5H_6O_3$ molecule (m/z 113) is only seen in the bottom spectrum. Otherwise, the spectra show the same ionized molecules. The most abundant product's ($C_8H_{14}O_7$) proposed structure is shown in the top spectrum.

Based on the mass spectrum shown in Figure 3.2, the ionization efficiency of 5-hydroxymethylfurfural is 75 ± 1 % of that of cellobiosan. To correct for this bias, the relative abundance measured for 5-hydroxymethylfurfural formed in fast pyrolysis of cellobiose and ionized by protonation upon ammonium APCI (ion of m/z 127; Figure 4, top) was multiplied by 1.33, resulting in a corrected relative molar abundance of 15 ± 6 %. This corrected relative molar abundance of 5-hydroxymethylfurfural was then divided by the relative abundance measured (using the same approach) for cellobiosan formed in pyrolysis of cellobiose in order to get the molar ratio of these two pyrolysis products: 0.3 ± 0.1 moles of 5-hydroxymethylfurfural for every mole of cellobiosan. The molar ratio (0.3) was then correlated back to the molecules that could be ionized by chloride attachment by multiplying it by the relative abundance measured by using chloride attachment mass spectrometry for cellobiosan produced upon fast pyrolysis of cellobiose (26 ± 3 % when taking into account the ^{37}Cl isotope) to obtain a value 7 ± 3 %. Hence, the approximate relative molar abundance of 5-hydroxymethyl furfural was found to be 7 ± 3 % relative to the abundance of the ions of m/z 257 (most abundant ions in the bottom spectrum in Figure 3.4).

Based on their measured elemental compositions, the ions of m/z 145 and m/z 85 (Figure 3.4, top), derived from molecules formed upon fast pyrolysis of cellobiose and ionized by ammonium attachment, are furan derivatives. The ionization efficiencies of these molecules were assumed to be the same as for 5-hydroxymethylfurfural and their measured relative abundances were corrected in the same way as that of 5-hydroxymethylfurfural. The relative abundances of the deprotonated molecules of m/z 161 and 113 (negative ion mode) are not included in Table 3.1. The former is an isomer

of levoglucosan (that does not form a chloride adduct like levoglucosan), not a furan derivative, and neither one is a chloride adduct; hence, it is not possible at this time to reasonably estimate their ionization efficiencies. The approximate relative abundances of the most abundant primary products of fast pyrolysis of cellobiose are listed in Table 3.1.

Table 3.1 Approximated average relative molar abundances of the primary products of fast pyrolysis of cellobiose normalized to the most abundant product (with standard deviations based on three experiments).

MW	Elemental Composition	Average Relative Molar Abundance (%)
84	C ₄ H ₄ O ₂	8 ± 7
114	C ₅ H ₆ O ₃	Not Estimated
126	C ₆ H ₆ O ₃	7 ± 3
144	C ₆ H ₈ O ₄	13 ± 9
162 (no adduct formation)	C ₆ H ₁₀ O ₅	Not Estimated
162	C ₆ H ₁₀ O ₅	10 ± 4
180	C ₆ H ₁₂ O ₆	70 ± 9
222	C ₈ H ₁₄ O ₇	100 ± 0
252	C ₉ H ₁₆ O ₈	11 ± 3
264	C ₁₀ H ₁₆ O ₈	17 ± 4
282	C ₁₀ H ₁₈ O ₉	61 ± 19
324	C ₁₂ H ₂₀ O ₁₀	20 ± 3
342	C ₁₂ H ₂₂ O ₁₁	34 ± 6

In order to determine the types of secondary reactions that may be expected for the primary fast pyrolysis products of cellobiose, it was pyrolyzed inside the flow tube (depicted in Figure 3.1). The primary products of cellobiose were allowed to react for 2 s and 11 s at two different temperatures (300 °C and 400 °C). Similar product distributions were measured using both ionization methods. Hence, only results obtained using

positive ion mode ionization are discussed below. Figure 3.5 shows that most of the primary fast pyrolysis products of cellobiose react away, ultimately producing anhydro-oligosaccharides up to cellopentosan or an isomer under the conditions used. The ability of anhydrosugars to polymerize is not a new phenomenon.⁴¹⁻⁴⁵ The most abundant primary product of cellobiose with the elemental composition $C_8H_{14}O_7$ (its ammonium adduct has the m/z value of 240) reacts away rapidly. Hence, it is not unexpected that this product has not been reported in the literature. These findings demonstrate that a method other than GC/MS is needed to detect many of the products formed upon reactions of the primary pyrolysis products of cellobiose (and other carbohydrates). These results also suggest that the larger anhydro-oligosaccharides (cellotetrosan, cellopentosan, etc., or their isomers) that have been detected in bio-oils via HPLC analysis are likely, in part, to be formed via polymerization reactions of the primary fast pyrolysis products as opposed to incomplete breakdown of the pyrolyzed carbohydrate.²⁹ This hypothesis was confirmed by measuring CAD mass spectra for selected fragment ions of authentic cellotriosan (MW 486 Da) after ionization by chloride attachment. These CAD mass spectra were compared to those measured for the analogous fragment ions of the unknown trimer pyrolysis product formed from cellobiose within the flow tube (m/z 521; Figure 5). The MS^2 mass spectra of the chloride attached cellotriosan and unknown trimer (m/z 521) display solely HCl loss resulting in fragment ions of m/z 485. The ions of m/z 485 correspond to the deprotonated cellotriosan and unknown trimer molecules. They were isolated and subjected to further CAD to obtain the mass spectra presented in Figure 3.6, left. The deprotonated trimer produced several fragment ions of various m/z values that are not produced during the CAD of authentic deprotonated

cellotriosan (i.e., ions of m/z 467, 365, and 347) but both produced an abundant fragment ion of m/z 323 corresponding to the loss of a molecule with a MW of 162 Da. The fragment ions of m/z 323 were isolated and subjected to CAD to produce the spectra in Figure 3.6, right. Several new fragment ions were produced upon CAD of ions of m/z of 323 formed from the unknown trimer compared to those produced from authentic cellotriosan (i.e., ions of m/z 305, 275, and 203). From the CAD mass spectra presented in Figure 3.6, the unknown trimer is concluded to be a mixture of isomers, including cellotriosan.

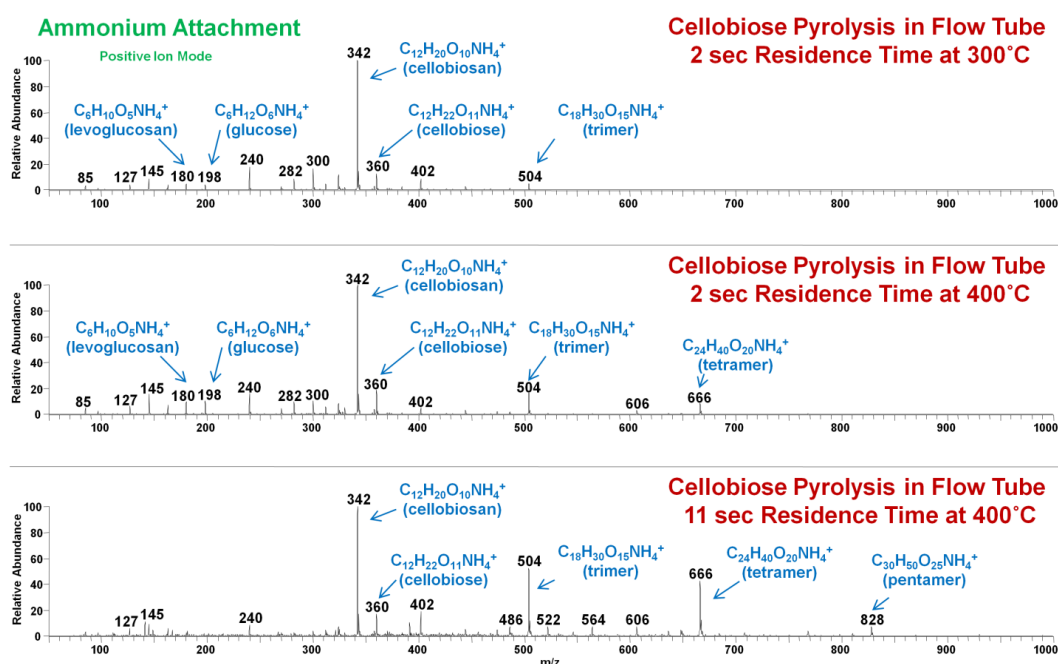


Figure 3.5 Mass spectra collected after the primary products of fast pyrolysis of cellobiose were allowed to undergo reactions for 2 s at 300 °C (top), 2s at 400 °C (middle) and 11 s at 400 °C (bottom) and ionized using ammonium attachment in positive ion mode. All elemental compositions were determined using high resolution data collected in an LQIT/FT-ICR. All ions with m/z values lower than 170 correspond to protonated molecules.

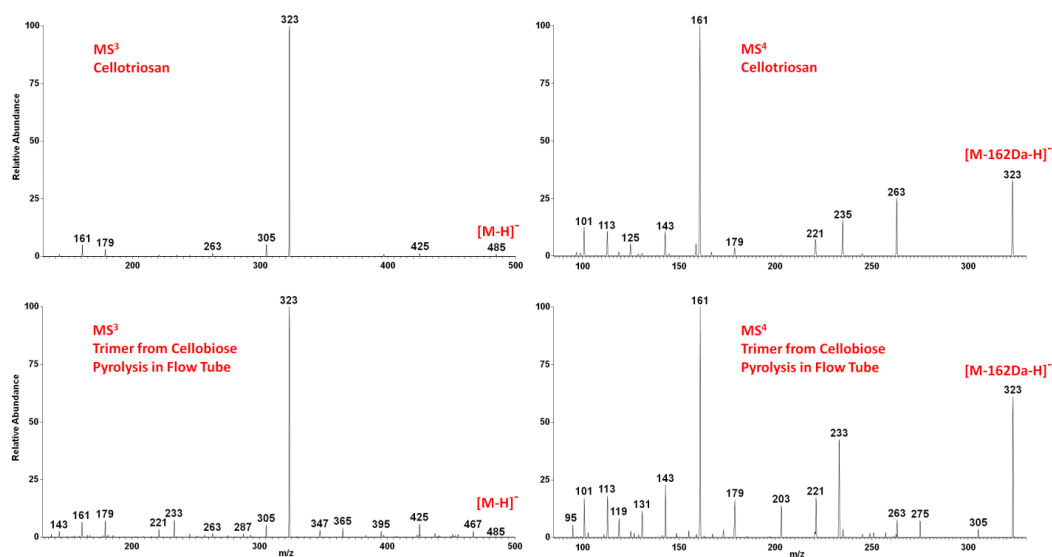


Figure 3.6 CAD mass spectra measured for authentic cellotriosan ionized via chloride attachment in negative ion mode and the unknown trimer (ionized in the same manner) formed upon pyrolysis of cellobiose in the flow tube. The chloride attached cellotriosan and trimer (m/z 521) were isolated and subjected to CAD which resulted in HCl loss, forming fragment ions of m/z 485, corresponding to the deprotonated molecules of cellotriosan and the unknown trimer. These deprotonated molecules were subjected to CAD to obtain the mass spectra shown top left and bottom left, respectively. Both ions produced an abundant fragment ion corresponding to the loss of a molecule with MW 162 Da to yield an ion of m/z 323. The fragment ions of m/z 323 were isolated and subjected to CAD to produce the mass spectra shown top right and bottom right, respectively.

3.4 Conclusions

Two fast pyrolysis/tandem mass spectrometry systems were devised, one to determine the primary products of fast pyrolysis of carbohydrates and another one to study how changes in temperature and residence time change the extent of secondary reactions of the primary products in order to simulate a pyrolysis reactor. Two complementary ionization methods were chosen to detect the pyrolysis products: APCI doped with chloroform in the negative ion mode and APCI doped with ammonium

hydroxide in the positive ion mode. Examination of an equimolar mixture of six model compounds commonly produced during carbohydrate pyrolysis (glycolaldehyde, hydroxyacetone, furfural, 5-hydroxymethylfurfural, levoglucosan, and cellobiosan) demonstrated that the positive ion mode APCI doped with ammonium hydroxide allows the detection of all these compounds but they do not have equal response factors. On the other hand, examination of the same mixture by using the negative ion mode APCI method revealed roughly equal ionization efficiency for compounds with at least two hydroxyl groups, consistent with previous studies for this method.³⁵ Hence, this ionization method allows semiquantitative analysis of carbohydrates produced during pyrolysis of oligosaccharides. However, this method cannot be used to detect pyrolysis products with fewer than two hydroxyl groups. A rough estimate of the relative molar abundances of the pyrolysis products that did not form chloride anion adducts was obtained using ionization efficiencies of model compounds determined using ammonium attachment in positive ion mode or chloride attachment in negative ion mode.

The fast pyrolysis/MS systems described above were used to examine fast pyrolysis of cellobiose. The primary fast pyrolysis products of cellobiose were determined to consist of only a handful of compounds that quickly polymerize to form anhydro-oligosaccharides when allowed to react at high temperatures for an extended period of time. The primary and secondary fast pyrolysis products of cellobiose include compounds that cannot be detected using GC/MS analysis that was employed in many previous studies.²⁶ These findings demonstrate that a method other than GC/MS is necessary to detect the primary, secondary and possibly also final products of fast pyrolysis of carbohydrates. Further, the results suggest that the complexity of bio-oils

arises, in part, from a variety of polymerization reactions of the primary pyrolysis products. Comparison of the CAD mass spectra measured for authentic deprotonated celotriosan and the deprotonated unknown trimer formed in flow tube pyrolysis of cellobiose suggests that along with the formation of celotriosan, other isomers are also formed in the flow tube, likely due to polymerization of the primary products. Hence, the use of residence times that are as short as possible should allow the generation of a bio-oil with a simple molecular composition from carbohydrates, including cellulose. Finally, the pyrolysis/MS methods developed here require only micrograms of sample and provide a fast approach for the examination of the influence of pyrolysis conditions and different feedstocks on the primary and secondary pyrolysis products of carbohydrates.

3.5 References

1. Huber, G.; Iborra, S.; Corma, A., Synthesis of Transportation Fuels from Biomass: Chemistry, Catalysts, and Engineering. *Chem. Rev.* **2006**, 106, 4044-4098.
2. Bridgwater, A., Biomass Fast Pyrolysis. *Thermal Science* **2004**, 8, 21-49.
3. Vispute, T.; Zhang, H.; Sanna, A.; Xiao, R.; Huber, G., Renewable Chemical Commodity Feedstocks from Integrated Catalytic Processing of Pyrolysis Oils. *Science* **2010**, 330, 1222-1227.
4. Mohan, D.; Pittman, C.; Steele, P., Pyrolysis of Wood/Biomass for Bio-Oil: A Critical Review. *Energy Fuels* **2006**, 20, 848-889.
5. Ragauskas, A.; Williams, C.; Davison, B.; Britovsek, G.; Cairney, J.; Eckert, C.; Frederick Jr., W.; Hallett, J.; Leak, D.; Liotta, C.; Mielenz, J.; Murphy, R.; Templer, R.; Tschaplinski, T., The Path Forward for Biofuels and Biomaterials. *Science* **2006**, 311, 484-489.
6. Lanza, R.; Nogare, D.; Canu, P., Gas Phase Chemistry in Cellulose Fast Pyrolysis. *Ind. Eng. Chem. Res.* **2009**, 48, 1391-1399.
7. Agrawal, R.; Singh, N., Solar Energy to Biofuels. *Ann. Rev. Chem. Biomol. Eng.* **2010**, 1, 343-364.
8. Bradbury, A.; Sakai, Y.; Shafizadeh, F., A Kinetic Model for Pyrolysis of Cellulose. *J. Appl. Polym. Sci.* **1979**, 23, 3271-3280.
9. Shen, D.; Xiao, R.; Gu, S.; Luo, K., The Pyrolytic Behavior of Cellulose in Lignocellulosic Biomass: A Review. *Rsc Advances* **2011**, 1, 1641-1660.
10. Czernik, S.; Bridgwater, A., Overview of Applications of Biomass Fast Pyrolysis Oil. *Energy Fuels* **2004**, 18, 590-598.
11. Oasmaa, A.; Leppämäki, E.; Koponen, P.; Levander, J.; Tapola, E., *Physical Characterization of Biomass-Based Pyrolysis Liquids*. Technical Research Centre of Finland: 1997.
12. Elliott, D., Historical Developments in Hydroprocessing Bio-Oils. *Energy Fuels* **2007**, 21, 1792-1815.
13. Furimsky, E., Catalytic Hydrodeoxygenation. *Appl. Catal. A* **2000**, 199, 147-190.
14. Evans, R.; Milne, T., Molecular Characterization of the Pyrolysis of Biomass. 2. Applications. *Energy Fuels* **1987**, 1, 311-319.

15. Overend, R.; Milne, T.; Mudge, L., *Fundamentals of Thermochemical Biomass Conversion*. Elsevier Applied Science Publishers Ltd.: London, 1985.
16. Radlein, D.; Grinshpun, A.; Piskorz, J.; Scott, D., On the Presence of Anhydro-Oligosaccharides in the Syrups from the Fast Pyrolysis of Cellulose. *J. Anal. Appl. Pyrolysis* **1987**, 12, 39-49.
17. Scott, D.; Piskorz, J.; Radlein, D., Liquid Products from the Continuous Flash Pyrolysis of Biomass. *Ind. Eng. Chem. Proc. DD* **1985**, 24, 581-588.
18. Peacocke, G.; Bridgwater, A., Ablative Plate Pyrolysis of Biomass for Liquids. *Biomass Bioenergy* **1994**, 7, 147-154.
19. Antal, M.; Hofmann, L.; Moreira, J.; Brown, C.; Steenblik, R., Design and Operation of a Solar Fired Biomass Flash Pyrolysis Reactor. *Solar Energy* **1983**, 30, 299-312.
20. Torri, C.; Reinikainen, M.; Lindfors, C.; Fabbri, D.; Oasmaa, A.; Kuoppala, E., Investigation on Catalytic Pyrolysis of Pine Sawdust: Catalyst Screening by Py-GC-MIP-AED. *J. Anal. Appl. Pyrolysis* **2010**, 88, 7-13.
21. Lu, Q.; Donga, C.; Zhanga, X.; Tiana, H.; Yanga, Y.; Zhub, X., Selective Fast Pyrolysis of Biomass Impregnated with ZnCl₂ to Produce Furfural: Analytical Py-GC/MS Study. *J. Anal. Appl. Pyrolysis* **2011**, 90, 204-212.
22. Patwardhan, P.; Satrio, J.; Brown, R.; Shanks, B., Product Distribution from Fast Pyrolysis of Glucose-Based Carbohydrates. *J. Anal. Appl. Pyrolysis* **2009**, 86, 323-330.
23. Patwardhan, P.; Satrio, J.; Brown, R.; Shanks, B., Influence of Inorganic Salts on the Primary Pyrolysis Products of Cellulose. *Bioresource Technol.* **2010**, 101, 4646-4655.
24. Patwardhan, P.; Dalluge, D.; Shanks, B.; Brown, R., Distinguishing Primary and Secondary Reactions of Cellulose Pyrolysis. *Bioresource Technol.* **2011**, 102, 5265-5269.
25. Patwardhan, P.; Brown, R.; Shanks, B., Product Distribution from the Fast Pyrolysis of Hemicellulose. *Chem. Sus. Chem.* **2011**, 4, 636-643.
26. Mettler, M.; Paulsen, A.; Vlachos, D.; Dauenhauer, P., The Chain Length Effect in Pyrolysis: Bridging the Gap Between Glucose and Cellulose. *Green Chem.* **2012**, 14, 1284-1288.
27. Lin, Y.; Cho, J.; Tompsett, G.; Westmoreland, P.; Huber, G., Kinetics and Mechanism of Cellulose Pyrolysis. *J. Phys. Chem. C* **2009**, 113, 20097-20107.

28. Zhang, X.; Li, J.; Yang, W.; Blasiak, W., Formation Mechanism of Levoglucosan and Formaldehyde During Cellulose Pyrolysis. *Energy Fuel* **2011**, *25*, 3739-3746.
29. Piskorz, J.; Majerski, P.; Radlein, D.; Vladars-Usas, A.; Scott, D., Flash Pyrolysis of Cellulose for Production of Anhydro-Oligomers. *J. Anal. Appl. Pyrolysis* **2000**, *56*, 145-166.
30. Anderson, S.; Wells, J.; Fedorowicz, A.; Butterworth, L.; Meade, B.; Munson, A., Evaluation of the Contact and Respiratory Sensitization Potential of Volatile Organic Compounds Generated by Simulated Indoor Air Chemistry. *Toxicol. Sci.* **2007**, *97*, 355-363.
31. Andersson, E.; Ericsson, I., Determination of the Temperature-Time profile of the Sample in Pyrolysis-Gas Chromatography. *J. Anal. Appl. Pyrolysis* **1979**, *1*, 27-38.
32. Andersson, E.; Ericsson, I., Thermal-Degradation of Organic Polymers using different Metals as the Pyrolysis Filament. *J. Anal. Appl. Pyrolysis* **1981**, *3*, 35-47.
33. Lede, J., Cellulose Pyrolysis Kinetics: An Historical Review on the Existence and Role of Intermediate Active Cellulose. *J. Anal. Appl. Pyrolysis* **2012**, *94*, 17-32.
34. Cmelik, R.; Chmelik, J., Structural Analysis and Differentiation of Reducing and Nonreducing Neutral Model Starch Oligosaccharides by Negative-Ion Electrospray Ionization Ion-Trap Mass Spectrometry. *Int. J. Mass Spectrom.* **2010**, *291*, 33-40.
35. Vinueza, N.; Gallardo, V.; Klimek, J.; Carpita, N.; Kenttämäa, H., Analysis of Carbohydrates by Atmospheric Pressure Chloride Anion Attachment Tandem Mass Spectrometry. *Fuel* **2013**, *105*, 235-246.
36. Zhu, J.; Cole, R., Ranking of Gas-Phase Acidities and Chloride Affinities of Monosaccharides and Linkage Specificity in Collision-Induced Decompositions of Negative Ion Electrospray-Generated Chloride Adducts of Oligosaccharides. *J. Am. Soc. Mass Spectrom.* **2001**, *12*, 1193-1204.
37. Lomax, J.; Boon, J., Characterisation of Polysaccharides by In-Source Pyrolysis Positive- and Negative-Ion Direct Chemical Ionization-Mass Spectrometry. *Carbohydrate Res.* **1991**, *221*, 219-233.
38. Madhusudanan, K., Tandem Mass Spectra of Ammonium Adducts of Monosaccharides: Differentiation of Diastereomers. *J. Mass Spectrom.* **2006**, *41*, 1096-1104.

39. Helleur, R., Initial Application of Desorption Chemical Ionization-Pyrolysis-Tandem Mass Spectrometry to Structural Analysis of Carbohydrates. *J. Anal. Appl. Pyrolysis* **1989**, 15, 85-95.
40. Fang, T.; Bendiak, B., The Stereochemical Dependence of Unimolecular Dissociation of Monosaccharide-Glycolaldehyde Anions in the Gas Phase: A Basis for Assignment of the Stereochemistry and Anomeric Configuration of Monosaccharides in Oligosaccharides by Mass Spectrometry via a Key Discriminatory Product Ion of Disaccharide Fragmentation, m/z 221. *J. Am. Chem. Soc.* **2007**, 129, 9721-9736.
41. Kawamoto, H.; Murayama, M.; Saka, S., Pyrolysis Behavior of Levoglucosan as an Intermediate in Cellulose Pyrolysis: Polymerization into Polysaccharide as a Key Reaction to Carbonized Product Formation. *J. Wood Sci.* **2003**, 49, 469-473.
42. Wolfrom, M.; Thompson, A.; Ward, R., The Composition of Pyrodextrins. II. Thermal Polymerization of Levoglucosan *J. Amer. Chem. Soc.* **1959**, 81, 4623-4625.
43. Pictet, A.; Sarasin, J., Distillation of Cellulose and Starch In Vacuo *Helv. Chim. Acta.* **1918**, 1, 87-96.
44. Carvalho, J.; Prins, W.; Schuerch, C., Addition Polymerization of Anhydro Sugar Derivatives. I. A polyanhydroglucose. *J. Am. Chem. Soc.* **1959**, 81, 4054-4058.
45. Ponder, G.; Richards, G., Polysaccharides from Thermal Polymerization of Glucosides *Carbohydr. Res.* **1990**, 208, 93-104.

CHAPTER 4: COMPARISON OF MOLECULES' STRUCTURES IN COAL AND PETROLEUM ASPHALTENES BY USING MASS SPECTROMETRY

4.1 Introduction

Asphaltenes are the heaviest fraction of crude oil and are defined as the fraction that is soluble in toluene and insoluble in n-heptane.¹⁻³ Most of the compounds present in asphaltenes are believed to be aromatic in nature but their exact structures are still unknown. Asphaltenes present major problems in crude oil transportation and refining, which are getting worse as heavier crude oil reserves are being utilized due to the world-wide depletion of the lighter crude oil reserves.³⁻¹⁰ The problems caused by asphaltenes increase the production cost of crude oil.^{4,5} A better understanding of asphaltenes is needed in order to solve these problems. To date, the molecular weight distribution of asphaltenes is still debated¹¹⁻¹⁴ and only limited work has been carried out to determine the structures of asphaltene molecules.¹⁵⁻¹⁸ Once the understanding of asphaltenes' molecular structures has been substantially improved, methods may be developed for reducing or eliminating the problems they cause and for converting them into useful compounds.¹⁹

Asphaltenes are believed to be comprised of island and/or archipelago type molecules.¹ Island type molecules consist of a single aromatic core made up of several fused aromatic rings with alkyl chains branching from that core.¹ Archipelago type

molecules contain several smaller aromatic cores that are connected by alkyl bridges, and that have alkyl chains branching from the cores.¹ Many experiments, ranging from time resolved fluorescence depolarization, Taylor dispersion diffusion, and NMR pulsed field gradient measurements, have indicated that asphaltenes mainly consist of island type molecules.^{3,20-23} However, some studies, such as using NMR with average structural parameter calculations and thermal cracking, have provided evidence in support of the presence of a small amount of archipelago type molecules in asphaltenes, as well.^{24,25} We recently published a study that compared the fragmentation patterns produced by collisionally-activated dissociation (CAD) of ionized asphaltenes with those of ionized model compounds that concluded that island like molecules dominate. No evidence was found in support of the existence of archipelago type molecules.¹⁶

One of the approaches that some research groups have attempted to address the lack of knowledge of asphaltenes' molecular structures is comparing chemical and physical properties of coal and petroleum asphaltenes. The molecular weight distribution (MWD) for coal asphaltenes has been determined to be much smaller, about half, of that of petroleum asphaltenes.^{19,26,27} Since fewer isomers and isobars are possible at lower molecular weights, the likelihood of determining molecular structures for coal asphaltenes is much higher than for petroleum asphaltenes.²²

For this study, coal and petroleum asphaltene samples were analyzed with tandem mass spectrometry experiments utilizing CAD were carried out using a Thermo Scientific linear quadrupole ion trap (LQIT) and a LQIT coupled with an FT-ICR. Several molecular ions with varying m/z values derived from the coal and petroleum asphaltenes were isolated and fragmented to probe their structural characteristics. Comparison of their

fragmentation pathways yielded information about the differences in the molecular structures of coal and petroleum asphaltenes.

Asphaltenes are very challenging to analyze using mass spectrometry.¹⁹ Asphaltenes are predisposed to degrade and aggregate when they are introduced into the gas phase.²⁸ Once in the gas phase, the ability to ionize a mixture as complex as asphaltenes is a problem when using ionization methods such as electrospray ionization (ESI) and matrix assisted laser desorption/ionization (MALDI) due to the fact that both methods preferentially ionize polar molecules.²⁹ For the study presented in this chapter, atmospheric pressure chemical ionization (APCI) was used because it has less of an ionization bias and has been shown to be an appropriate method for petroleum analysis.³⁰ Carbon disulfide was used as the solvent to dissolve and ionize the asphaltenes with APCI. This approach has been shown to produce only stable molecular ions for asphaltene model compounds.³¹

4.2 Experimental

Chemicals. The petroleum asphaltene sample originated from a Russian oil field and was obtained by heptane precipitation. The coal asphaltenes were kindly donated by Dr. Oliver Mullins. The coal asphaltenes had been extracted from coal that originated from Tanito Harum, Indonesia. The coal liquefaction and asphaltene extraction method has been previously described in the literature.²¹ Carbon disulfide (>99.9%) and heptanes (99+%) were purchased from Sigma Aldrich (St. Louis, MO) and used without further purification. Both asphaltenes samples were sonicated for one hour in n-heptanes and centrifuged to remove any remaining maltene content.

Instrumentation. A Thermo Scientific LTQ linear quadrupole ion trap (LQIT) and a LQIT coupled to a 7 Tesla Fourier transform - ion cyclotron resonance (FT-ICR) mass spectrometer were used for mass spectrometric analyses. The asphaltenes were dissolved in carbon disulfide at a concentration of 0.5 g/mL and then introduced into the APCI source via direct infusion from a Hamilton 500 μL syringe through the instrument's syringe pump at a rate of 20 μL per minute. The APCI source was set at 300°C. Several ions were isolated and subjected to collisionally activated dissociation (CAD). The isolation window used was either 0.3 or 2 m/z-units (selected m/z value ± 1) and a CAD energy of 35 arbitrary units was used. Both were controlled by the LTQ software. The LQIT-FT-ICR instrument was used to determine the elemental compositions of interesting ions, utilizing the accurate mass measurement capability of the FT-ICR.

4.3 Results and Discussion

Presented here is a study that compares asphaltenes derived from liquefied coal to those derived from petroleum. The asphaltenes were dissolved in carbon disulfide and ionized via positive mode APCI to produce stable molecular ions (M^{+}). The full (MS^1) mass spectra measured for these ions yielded information about the samples MWDs. The CAD (MS^2) mass spectra measured for the isolated ions yielded information about the molecular structures of the compounds present in the samples. The average molecular weight (MW) of both samples was derived from the MWDs by using Equation 4.1 and the values are given in Table 4.1.

$$\text{AVG MW} = \frac{\sum \frac{m}{z} * \text{area (all peaks)}}{\sum \text{area (all peaks)}} \quad (4.1)$$

One of the structural features that was examined was the approximate minimum combined length of the alkyl chains branching from the aromatic core. The minimum combined length of the alkyl chains was experimentally determined by isolating several molecular ions of different m/z values, subjecting them to CAD and determine the number of carbon atoms lost, until the corresponding fragment ions' abundance was below two percent (arbitrarily chosen) relative to the abundance of the most abundant ion, as described previously.¹⁶ The same fragment ions that were used to determine the minimum combined length of the alkyl chains were used to determine the molecule's core size (methylene functional groups possibly left onto the core after benzylic cleavages of the alkyl chains were included in this estimate). An example of both calculations is illustrated in Figure 4.1 for a model compound. The calculation of the number of fused rings that comprise the core is a rough estimate as it does not take into account the presence of heteroatoms and the exact number of methylene groups left on the core is unknown, but these factors should not change the final results to a significant degree. The accuracy of these conclusions are still being investigated and are only used here for comparison purposes because of the lack of adequate model compounds that accurately duplicate the CAD mass spectra collected for asphaltenes.

The last structural feature considered was the approximate relative heteroaromatic sulfur content in the samples. A rough estimate of the amount of heteroaromatic sulfur present in the ions was obtained from the abundance of the fragment ions formed by the loss of hydrogen sulfide (34 Da) relative to that of the most abundant fragment ion in the CAD mass spectrum. High resolution experiments confirmed this assignment (exact mass measurement: 33.96236 Da). This conclusion is also supported by preliminary

results using model compounds with sulfur containing heteroaromatic rings that showed hydrogen sulfide loss upon CAD in a LQIT.¹⁶

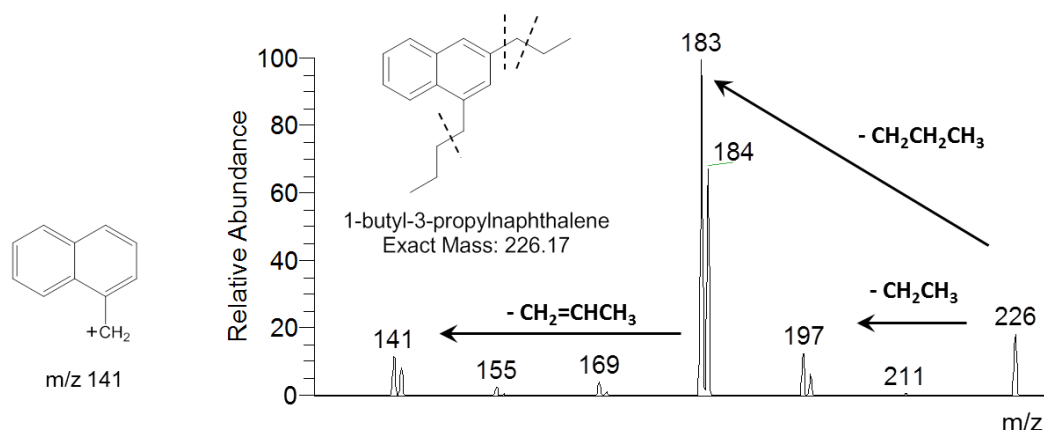


Figure 4.1 CAD mass spectrum measured for 1-butyl-3-propylnaphthalene molecular ion of m/z 226 generated by APCI/CS₂. An approximation of the minimum total number of carbons in all alkyl chains and the core size is obtained from the smallest fragment ion of m/z 141 (resulting from the loss of propene from the ion of m/z 183 formed by the loss of a propyl radical from the molecular ion), revealing the presence of at least six carbon atoms in all alkyl chains and two fused rings in the core (with an attached methylene group).

Figure 4.2, below, displays a direct comparison of the MWD measured for the coal and petroleum asphaltene samples. The observed MWD for coal asphaltenes ranges from 200 up to 800 Daltons (Da) with a weighted MW average of 443 ± 33 Da, whereas the MWD for the petroleum asphaltenes ranges from 275 up to 1500 Da with a weighted MW average of 708 ± 14 Da. These data are in good agreement with previous studies that were conducted on coal and petroleum asphaltenes by using different methods.¹⁹

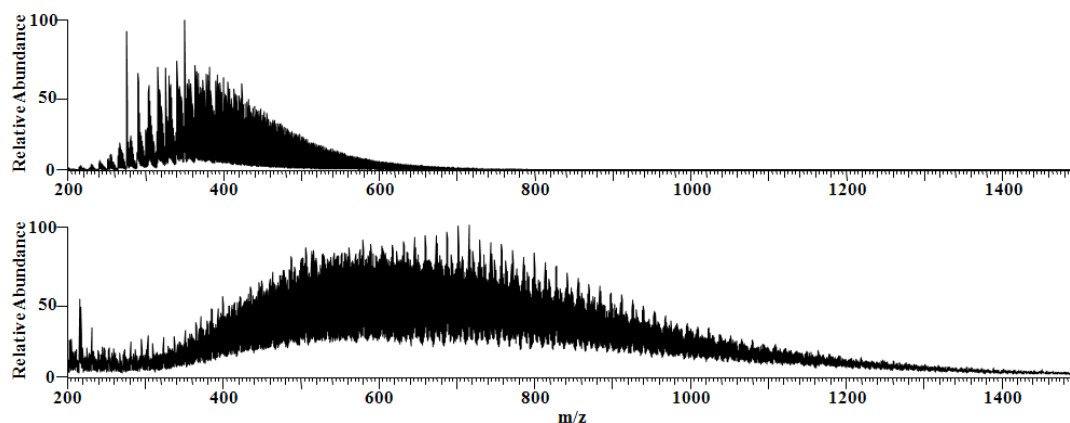


Figure 4.2 APCI/CS₂ mass spectra of coal asphaltenes (top) and petroleum asphaltenes (bottom).

The hydrogen to carbon ratios measured using other experimental methods (87-91 wt% carbon : 5-7 wt% hydrogen in coal asphaltenes and 79-82 wt% carbon : 7-8 wt% hydrogen in petroleum asphaltenes) suggest that a larger number of carbons is present in the aromatic core than in the alkyl chains in coal asphaltenes when compared to petroleum asphaltenes.^{22,32} To experimentally compare the relative aromaticity of the molecules present in the coal and petroleum asphaltenes, CAD was conducted on many molecular ions derived from both samples. A relatively wide (2 m/z-units) window was used during the isolation event for the MS/MS experiments due to poor signal intensity resulting from the extreme complexity of the mixture. High resolution data collected both in our laboratory and in others have found that this 2 m/z window may contain between five and fifteen abundant isobaric ions, all of which may contribute to the CAD mass spectrum.³³ Hence, a narrower isolation window of 0.3 Da was used in some cases to help reduce the effects of the additional ions. However, the main fragment ions and

fragmentation patterns were found to be independent of the size of the isolation window, as shown in Figure 4.3.

Typical CAD mass spectra for ions of $m/z\ 677 \pm 1$ Da derived from coal and petroleum asphaltene are shown in Figure 4.4. These CAD mass spectra are similar to ones measured previously for petroleum asphaltene, depicting steadily decreasing abundances for fragment ions formed by the loss of larger alkyl radicals from the aromatic core.^{16,24} High resolution data, like the one shown in Figure 4.5, was conducted to positively identify the fragments as alkyl radicals.

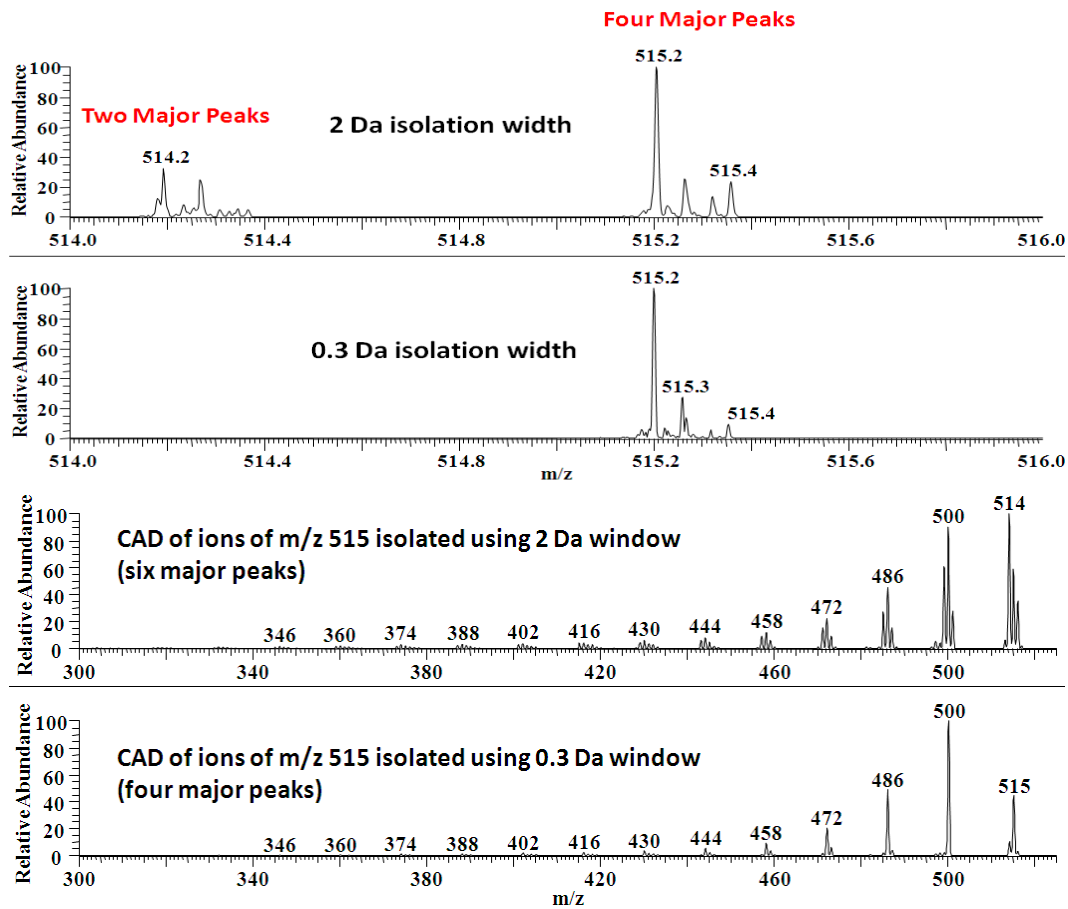


Figure 4.3 The top two mass spectra show the isolation of ions of m/z 515 from petroleum asphaltenes by using a 2 Da (top) and a 0.3 Da (bottom) isolation window. The bottom two mass spectra show CAD products measured in the LQIT for the isolated ions using a 2 Da (top) and a 0.3 Da (bottom) isolation window.

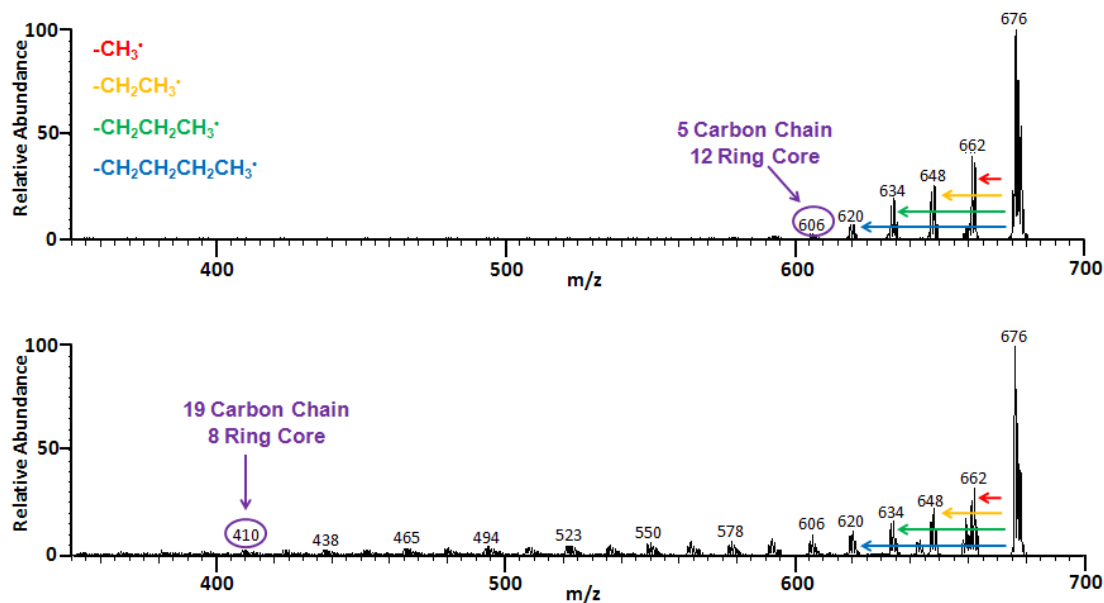


Figure 4.4 CAD mass spectra measured for ions of m/z 677 ± 1 derived from coal asphaltenes (top) and petroleum asphaltenes (bottom). The total number of carbons in the side chains and likely core sizes were estimated as described in text.

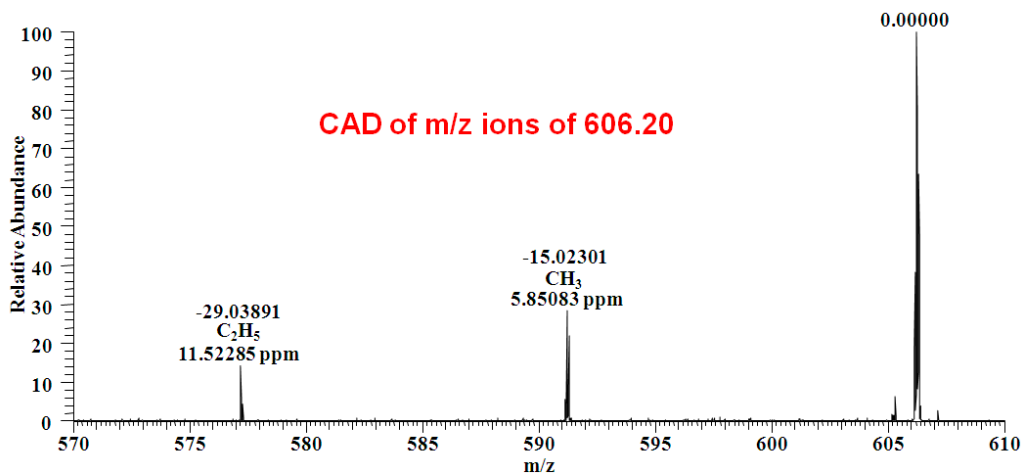


Figure 4.5 A high-resolution CAD mass spectrum measured for ions of m/z 606.20 ± 0.15 derived from petroleum asphaltenes.

The fragmentation patterns shown in Figure 4.4 are currently thought to be the result of the fragmentation of ionized island type molecules. Ionized archipelago type molecules are expected to undergo facile losses of large highly aromatic neutral molecules, based on studies conducted with asphaltene model compounds.¹⁶ When looking at Figure 4.4, it can be noted that the most favored neutral fragments correspond to a series of alkyl radicals ranging from methyl up to an alkyl radical 19 carbons in length. This series of alkyl radicals cannot be lost from an ion of m/z 677 due to its small size and hence are likely formed from a mixture of isomers and/or isobars containing alkyl chains of various lengths. The decay in the abundance of ions formed upon alkyl radical losses, with ions corresponding to short alkyl losses being higher in abundance, suggests that shorter alkyl groups are much more prominent in asphaltene molecules than longer alkyl groups. Based on Figure 4.4, the ions of m/z 677 ± 1 derived from coal asphaltene appear to contain a total number of at least 5 carbons in side chains with a core size of about 12 fused aromatic rings. On the other hand, the ions derived from petroleum asphaltene have a total of at least 19 carbons in side chains with a core of about 8 aromatic rings. These core sizes are larger than previously reported.^{22,26,34} The reason for this is still being investigated. The results for ions of m/z 677 ± 1 , along with the other ions studied, are displayed in Table 4.1. These results suggest that coal asphaltene contain a much higher aromatic carbon to alkane carbon ratio than petroleum asphaltene. The CAD mass spectra measured for ions with several m/z values suggest that the total number of carbons in all side chains in coal and petroleum asphaltene range from at least 3 up to 6 carbons and at least 6 up to 35 carbons, respectively.

While the above results are true for ionized asphaltenes of both types when comparing similar m/z values, the data presented in Table 4.1 show that this is not true when comparing the most abundant molecules of each type (roughly, ions of m/z 440 for coal and ions of m/z 710 for petroleum asphaltenes). The comparison of the data for ions of m/z 456 for coal and m/z 704 for petroleum asphaltenes indicates that the typical petroleum and coal asphaltenes have a similarly sized polyaromatic core of about eight fused rings. However, the coal asphaltenes only have about four carbons making up its alkyl chains while the petroleum asphaltenes have up to twenty two carbons in their alkyl chains.

CAD mass spectra of ions derived from asphaltenes also yield a very rough estimate for their relative heteroaromatic sulfur content. Preliminary heteroaromatic model compound data indicate that heteroaromatic sulfur atoms can be lost as neutral hydrogen sulfide (MW 34 Da) when the ionized model compounds are subjected to CAD.¹⁶ Some ions derived from asphaltenes lose a neutral molecule with MW of 34 Da upon CAD, as well. High-resolution spectra, similar to the one shown in Figure 4.5, were carried out to verify that this loss corresponds to H_2S . Table 4.1 lists the relative abundances of fragment ions formed upon this loss for several molecular ions of different m/z values. Based on the fragment ions' relative abundances, a rough estimate for the relative heteroaromatic sulfur content may be obtained. Figure 4.6 shows the CAD mass spectra of molecular ions of m/z values near the center of the MWD for both coal and petroleum asphaltenes to illustrate the differences in the relative abundances of the fragment ions resulting from the loss of hydrogen sulfide.

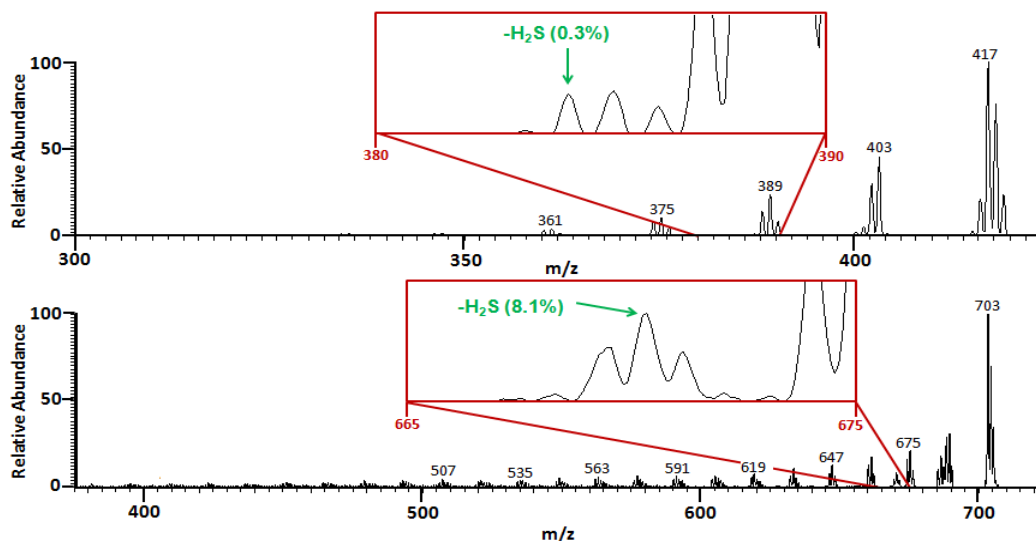


Figure 4.6 CAD mass spectra of ions of m/z 418 ± 1 derived from coal asphaltene (top) and ions of m/z 704 ± 1 derived from petroleum asphaltene (bottom) with a zoom window on the fragment ions formed upon loss of hydrogen sulfide, with their relative abundance compared to the most abundant fragment ion.

Based on the results presented in Figure 4.6, the relative heteroaromatic sulfur content is higher in petroleum asphaltene than in coal asphaltene. Table 4.1 shows that this is true for ions with a variety of different m/z values. Even though the nature of the hydrogen sulfide loss is not completely understood, these findings are in agreement with previously measured bulk elemental compositions of coal and petroleum asphaltene (0.1-1 wt% sulfur in coal asphaltene and 7-9 wt% sulfur petroleum asphaltene), providing some support for this technique's ability to compare relative heteroaromatic sulfur content.^{22,32}

Table 4.1 Molecular weight distributions (MWD) and average molecular weights (AVG MW) determined for molecules in coal and petroleum asphaltenes, as well as the estimated minimum total number of carbon atoms in all side chains, estimated core sizes, and relative abundances of the ions produced by neutral hydrogen sulfide loss, given for ions with selected m/z values. The differences between the petroleum and coal samples (petroleum – coal) are given in the last column.

	Coal	Petroleum	Difference (Petroleum – Coal)
MWD	200 Da - 800 Da	275 Da - 1450 Da	--
AVG MW	443 ± 33 Da	708 ± 14 Da	265 Da
<u>Ion of m/z 220</u>			
Carbons in Side Chains	3	--	--
Estimated Core Size	3	--	--
Relative Percent Hydrogen Sulfide Loss	0	--	--
<u>Ion of m/z 285</u>			
Carbons in Side Chains	4	--	--
Estimated Core Size	4	--	--
Relative Percent Hydrogen Sulfide Loss	1	--	--
<u>Ion of m/z 325</u>			
Carbons in Side Chains	4	--	--
Estimated Core Size	5	--	--
Relative Percent Hydrogen Sulfide Loss	0	--	--
<u>Ion of m/z 360</u>			
Carbons in Side Chains	5	5	0
Estimated Core Size	6	6	0
Relative Percent Hydrogen Sulfide Loss	1	1	0
<u>Ion of m/z 418</u>			
Carbons in Side Chains	4	6	2
Estimated Core Size	7	6	-1
Relative Percent Hydrogen Sulfide Loss	0	1	1
<u>Ion of m/z 456</u>			
Carbons in Side Chains	<u>4</u>	8	4
Estimated Core Size	<u>8</u>	7	-1
Relative Percent Hydrogen Sulfide Loss	<u>1</u>	2	1

Table 4.1, continued

	Coal	Petroleum	Difference (Petroleum – Coal)
<u>Ion of m/z 490</u>			
Carbons in Side Chains	5	11	6
Estimated Core Size	8	6	-2
Relative Percent Hydrogen Sulfide Loss	1	2	1
<u>Ion of m/z 515</u>			
Carbons in Side Chains	5	10	5
Estimated Core Size	9	7	-2
Relative Percent Hydrogen Sulfide Loss	1	2	1
<u>Ion of m/z 530</u>			
Carbons in Side Chains	5	12	7
Estimated Core Size	9	7	-2
Relative Percent Hydrogen Sulfide Loss	1	2	1
<u>Ion of m/z 606</u>			
Carbons in Side Chains	5	17	12
Estimated Core Size	10	7	-3
Relative Percent Hydrogen Sulfide Loss	1	4	3
<u>Ion of m/z 647</u>			
Carbons in Side Chains	5	17	12
Estimated Core Size	11	8	-3
Relative Percent Hydrogen Sulfide Loss	1	5	4
<u>Ion of m/z 677</u>			
Carbons in Side Chains	5	19	14
Estimated Core Size	12	8	-4
Relative Percent Hydrogen Sulfide Loss	1	6	5
<u>Ion of m/z 688</u>			
Carbons in Side Chains	6	22	16
Estimated Core Size	12	7	-5
Relative Percent Hydrogen Sulfide Loss	1	6	5
<u>Ion of m/z 704</u>			
Carbons in Side Chains	6	<u>22</u>	16
Estimated Core Size	12	<u>8</u>	-4
Relative Percent Hydrogen Sulfide Loss	1	<u>7</u>	6

Table 4.1, continued

	Coal	Petroleum	Difference (Petroleum – Coal)
<u>Ion of m/z 736</u>			
Carbons in Side Chains	5	17	12
Estimated Core Size	13	10	-3
Relative Percent Hydrogen Sulfide Loss	1	10	9
<u>Ion of m/z 780</u>			
Carbons in Side Chains	--	25	--
Estimated Core Size	--	8	--
Relative Percent Hydrogen Sulfide Loss	--	9	--
<u>Ion of m/z 810</u>			
Carbons in Side Chains	--	26	--
Estimated Core Size	--	9	--
Relative Percent Hydrogen Sulfide Loss	--	10	--
<u>Ion of m/z 850</u>			
Carbons in Side Chains	--	27	--
Estimated Core Size	--	9	--
Relative Percent Hydrogen Sulfide Loss	--	11	--
<u>Ion of m/z 875</u>			
Carbons in Side Chains	--	35	--
Estimated Core Size	--	7	--
Relative Percent Hydrogen Sulfide Loss	--	23	--

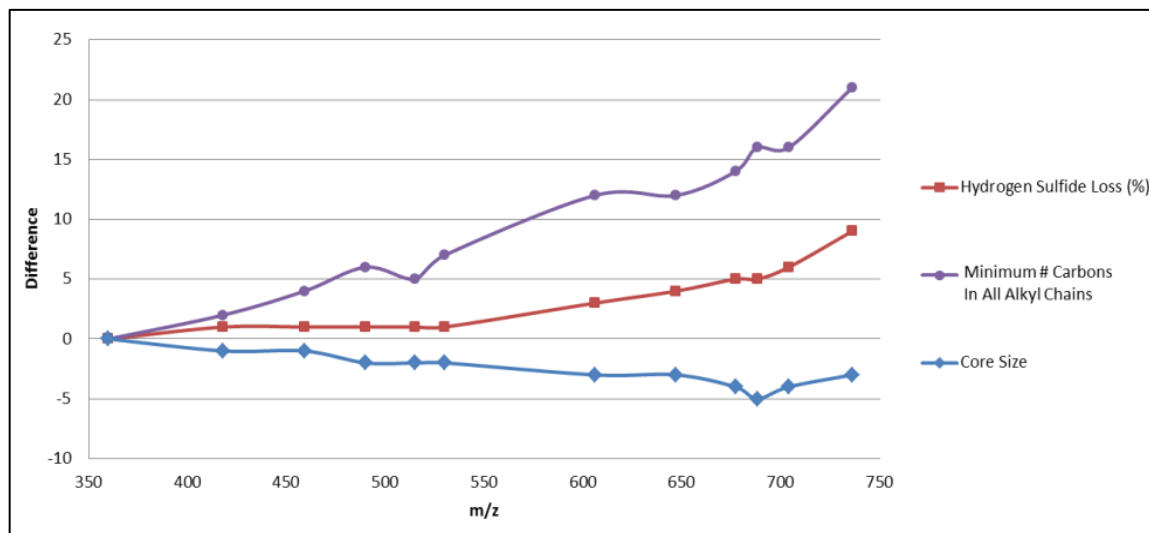


Figure 4.7 Graph illustrating the differences (petroleum – coal) between the coal asphaltenes and the petroleum asphaltenes as a function of their molecular size: relative abundances of ions produced from hydrogen sulfide loss, the estimated minimum total number of carbons in all side chains, and the approximate core size.

The differences between the coal and petroleum asphaltene samples shown in Table 4.1 are graphed as a function of the size of the ions in Figure 4.7. Figure 4.7 suggests that petroleum and coal asphaltenes are relatively similar in chain length, core size, and extent of hydrogen sulfide loss at low MW and that the differences gradually increase with MW. While bulk analysis methods can also measure these differences, they are unable to track how they change with MW like this method.

4.4 Conclusions

The MWDs collected for coal and petroleum asphaltenes by using APCI with carbon disulfide as the ionizing reagent in an LQIT were found to agree with a previous study that used laser deposition/ionization coupled to a time-of-flight mass

spectrometer.¹⁹ The observed MWD and average MWs for coal and petroleum asphaltene range from 200 up to 800 Da with 443 ± 33 Da average MW and from 275 up to 1500 Da with 708 ± 14 Da average MW, respectively. The CAD mass spectra for molecular ions of several m/z values showed a striking decrease in alkane carbon content relative to aromatic carbon content in petroleum (a total of about 35 carbons maximum in all side chains) vs. coal asphaltene (a total of about 6 carbons maximum in all side chains). Further, the core size of coal asphaltene was estimated to range from 3 up to 13 rings while that for petroleum asphaltene range from 6 up to 10 rings. Previous studies conducted on coal and petroleum asphaltene measured smaller core sizes than those presented here, which is likely due to the lack of appropriate model compounds needed to refine our methods.^{22,26,34} The measured trends reported here, on the other hand, are expected to be accurate. From these results it was concluded that the aromatic carbon to alkane carbon ratio in coal asphaltene is much higher than that of petroleum asphaltene, independent of the MW. Nevertheless, when comparing the most abundant molecules in both the petroleum and coal asphaltene, the molecules have similarly sized aromatic cores of about eight fused rings but very different total lengths of the alkyl side chains, with coal asphaltene having about 4 total carbons in alkyl chains and petroleum asphaltene having about 22 total carbons in alkyl chains. The lower alkane content measured for coal asphaltene than petroleum asphaltene agrees with bulk elemental compositions determined previously: 87-91 wt% carbon : 5-7 wt% hydrogen in coal asphaltene and 79-82 wt% carbon : 7-8 wt% hydrogen in petroleum asphaltene.^{22,32} The relative abundance of the fragment ion due to hydrogen sulfide loss from petroleum asphaltene was much higher than that of the coal asphaltene. This is also in agreement

with bulk elemental analysis carried out by others that showed that coal and petroleum asphaltene contain 0.1-1 wt% and 7-9 wt% sulfur, respectively.^{26,32} The agreement of these results with previous results collected using different techniques helps validate this technique.

4.5 References

1. Mullins, O.; Sheu, E., *Structure and Dynamics of Asphaltenes*. Plenum Press: New York, 1998.
2. Buenrostro-Gonzalez, E.; Groenzin, H.; Lira-Galeana, C.; Mullins, O., The Overriding Chemical Principles that Define Asphaltenes. *Energy Fuels* **2001**, *12*, 972-978.
3. Mullins, O.; Sheu, E.; Hammami, A.; Marshall, A., *Asphaltenes, Heavy Oils, and Petroleomics*. Springer: New York, 2007.
4. Ancheyta, J.; Betancourt, G.; Centeno, G.; Marroquin, G.; Alonso, F.; Garciafigueroa, E., Catalyst Deactivation During Hydroprocessing of Maya Heavy Crude Oil 1. Evaluation at Constant Operating Conditions. *Energy Fuels* **2002**, *16*, 1438-1443.
5. Yen, T.; Chilingarian, G., *Asphaltenes and Asphalts*. Elsevier: Amsterdam, 1994.
6. Potts, M. F. Crude Oil Fractionation Method. US Patent 3,320,158, 11/6/1964, 1967.
7. Nogueira, J., Refining and Separation of Crude Tall-Oil Components. *Sep. Sci. Technol.* **1996**, *31*, 2307-2316.
8. Ancheyta, J.; Betancourt, G.; Marroquín, G.; Centeno, G.; Castañeda, L.; Alonso, F.; Muñoz, J. A.; Gómez, M.; Rayo, P., Hydroprocessing of Maya Heavy Crude Oil in Two Reaction Stages. *Appl. Catal. A-Gen.* **2002**, *233*, 159-170.
9. Ancheyta-Juárez, J.; Betancourt-Rivera, G.; Marroquín-Sánchez, G.; Pérez-Arellano, A. M.; Maity, S.; Cortez, M.; del Río-Soto, R., An Exploratory Study for Obtaining Synthetic Crudes from Heavy Crude Oils via Hydrotreating. *Energy Fuels* **2001**, *15*, 120-127.
10. Trejo, F.; Centeno, G.; Ancheyta, J., Precipitation, Fractionation and Characterization of Asphaltenes from Heavy and Light Crude Oils. *Fuel* **2004**, *83*, 2169-2175.
11. Al-Muhareb, E.; Morgan, T.; Herod, A.; Kandiyoti, R., Characterization of Petroleum Asphaltenes by Size Exclusion Chromatography, UV-Fluorescence and Mass Spectrometry. *Petrol. Sci. Technol.* **2007**, *25*, 81-91.
12. Mullins, O., Rebuttal to Comment by Professors Herod, Kandiyoti, and Bartle on "Molecular Size and Weight of Asphaltene and Asphaltene Solubility Fractions from Coals, Crude Oils and Bitumen". *Fuel* **2007**, *86*, 309-312.

13. Herod, A.; Bartle, K.; Kandiyoti, R., Comment on a Paper by Mullins, Martínez-Haya, and Marshall “Contrasting Perspective on Asphaltene Molecular Weight. This Comment vs the Overview of A. A. Herod, K. D. Bartle, and R. Kandiyoti”. *Energy Fuels* **2008**, *22*, 4312-4317.
14. Mullins, O.; Martínez-Haya, B.; Marshall, A., Contrasting Perspective on Asphaltene Molecular Weight. This Comment vs the Overview of A. A. Herod, K. D. Bartle, and R. Kandiyoti. *Energy Fuels* **2008**, *22*, 1765-1773.
15. Mullins, O., The Modified Yen Model. *Energy Fuels* **2010**, *24*, 2179-2207.
16. Borton, D.; Pinkston, D.; Hurt, M.; Tan, X.; Azyat, K.; Scherer, A.; Tykwinski, R.; Gray, M.; Qian, K.; Kenttämä, H., Molecular Structures of Asphaltenes Based on the Dissociation Reactions of Their Ions in Mass Spectrometry. *Energy Fuels* **2010**, *24*, 5548-5559.
17. Sabbah, H.; Morrow, A.; Pomerantz, A.; Mullins, O.; Tan, X.; Gray, M.; Azyat, K.; Tykwinski, R.; Zare, R., Comparing Laser Desorption/Laser Ionization Mass Spectra of Asphaltenes and Model Compounds. *Energy Fuels* **2010**, *24*, 3589-3594.
18. Sabbah, H.; Morrow, A.; Pomerantz, A.; Zare, R., Evidence for Island Structures as the Dominant Architecture of Asphaltenes. *Energy Fuels* **2011**, *25*, 1597-1604.
19. Hortal, A.; Hurtado, P.; Martínez-Haya, B.; Mullins, O., Molecular-Weight Distributions of Coal and Petroleum Asphaltenes from Laser Desorption/Ionization Experiments. *Energy Fuels* **2007**, *21*, 2863-2868.
20. Badre, S.; Goncalves, C.; Norinaga, K.; Gustavson, G.; Mullins, O., Molecular Size and Weight of Asphaltene and Asphaltene Solubility Fractions from Coals, Crude Oils and Bitumen. *Fuel* **2006**, *85*, 1-11.
21. Groenzin, H.; Mullins, O., Molecular Size and Structure of Asphaltenes from Various Sources. *Energy Fuels* **2000**, *14*, 677.
22. Andrews, A.; Edwards, J.; Pomerantz, A.; Mullins, O.; Nordlund, D.; Norinaga, K., Comparison of Coal-Derived and Petroleum Asphaltenes by ¹³C Nuclear Magnetic Resonance, DEPT, and XRS. *Energy Fuels* **2011**, *25*, 3068-3076.
23. Mullins, O.; Sabbah, H.; Eyssautier, J.; Pomerantz, A.; Barre, L.; Andrews, A.; Ruiz-Morales, Y.; Mostowfi, F.; McFarlane, R.; Goual, L.; Lepkiewicz, R.; Cooper, T.; Orbulescu, J.; Leblanc, R.; Edwards, J.; Zare, R., Advances in Asphaltene Science and the Yen-Mullins Model. *Energy Fuels* **2012**, *26*, 3986-4003.

24. Morgan, T.; Alvarez-Rodriguez, P.; George, A.; Herod, A.; Kandiyoti, R., Characterization of Maya Crude Oil Maltenes and Asphaltenes in Terms of Structural Parameters Calculated from Nuclear Magnetic Resonance (NMR) Spectroscopy and Laser Desorption-Mass Spectroscopy (LD-MS). *Energy Fuels* **2010**, *24*, 3977-3989.
25. Alshareef, A.; Scherer, A.; Tan, X.; Azyat, K.; Stryker, J.; Tykwinski, R.; Gray, M., Formation of Archipelago Structures During Thermal Cracking Implicates a Chemical Mechanism for the Formation of Petroleum Asphaltenes. *Energy Fuels* **2011**, *25*, 2130-2136.
26. Andrews, A.; Shih, W.; Mullins, O.; Norinaga, K., Molecular Size Determination of Coal-Derived Asphaltene by Fluorescence Correlation Spectroscopy *Appl. Spectrosc.* **2011**, *65*, 1348-1356.
27. Wargadalam, V.; Norinaga, K.; Lino, M., Size and Shape of a Coal Asphaltene Studied by Viscosity and Diffusion Coefficient Measurements. *Fuel* **2002**, *81*, 1403-1407.
28. Pinkston, D.; Duan, P.; Gallardo, V.; Habicht, S.; Tan, X.; Qian, K.; Gray, M.; Müllen, K.; Kenttämaa, H., Analysis of Asphaltenes and Asphaltene Model Compounds by Laser-Induced Acoustic Desorption/Fourier Transform Ion Cyclotron Resonance Mass Spectrometry. *Energy Fuels* **2009**, *23*, 5564-5570.
29. de Hoffmann, E.; Stroobant, V., *Mass Spectrometry Principles and Applications*. 3rd ed.; John Wiley & Sons, Ltd: West Sussex, England, 2007.
30. Kim, Y.; Kim, S., Improved Abundance Sensitivity of Molecular Ions in Positive-Ion APCI MS Analysis of Petroleum in Toluene. *J. Am. Soc. Mass Spectrom.* **2010**, *21*, 386-392.
31. Owen, B.; Gao, J.; Borton, D.; Amundson, L.; Archibold, E.; Tan, X.; Azyat, K.; Tykwinski, R.; Gray, M.; Kenttämaa, H., Carbon Disulfide Reagent Allows the Characterization of Nonpolar Analytes by Atmospheric Pressure Chemical Ionization Mass Spectrometry. *Rapid Commun. Mass Spectrom.* **2011**, *25*, 1924-1928.

32. Long, R., *The Concept of Asphaltenes*. American Chemical Society: Washington D.C., 1981; Vol. 195.
33. Klein, G.; Kim, S.; Rodgers, R.; Marshall, A.; Yen, A., Mass Spectral Analysis of Asphaltenes. II. Detailed Compositional Comparison of Asphaltenes Deposit to its Crude Oil Counterpart for Two Geographically Different Crude Oils by ESI FT-ICR MS. *Energy Fuels* **2006**, 20, 1973-1979.
34. Calemma, V.; Iwanski, P.; Nali, M.; Scotti, R.; Montanari, L., Structural Characterization of Asphaltenes of Different Origins. *Energy Fuels* **1995**, 9, 225-230.

CHAPTER 5: COMPARISON OF THE STRUCTURES OF MOLECULES IN PETROLEUM ASPHALTENES BEFORE AND AFTER MILD AND HARSH HYDROCRACKING.

5.1 Introduction

As discussed in section 4.1, asphaltene are the heaviest fraction of crude oil and cause many problems during crude oil processing that increase production costs.¹⁻¹⁰ More needs to be known about asphaltene in order to be able to knowledgably devise a solution to these problems. Unfortunately, the study of asphaltene is not an easy task due to their extreme complexity. A better understanding of their molecular structures would greatly help in developing prevention strategies for the problems caused by asphaltene.¹¹ To date, only limited amount of work has been carried out to determine the molecular structures of asphaltene.¹²⁻¹⁵ Island and archipelago type structures have been proposed for molecules present in asphaltene.⁵ Island-type molecules have one aromatic core with alkyl chains branching off while archipelago-type molecules have several smaller aromatic cores linked by alkyl chains, with alkyl chains branching off.⁵ An example structure of both island-type molecules and archipelago-type molecules are shown in Figure 5.1. The studies that have been conducted thus far have concluded that the predominant molecular structural type present in asphaltene is the island type, with little evidence of archipelago-type structures.^{6,16-21}

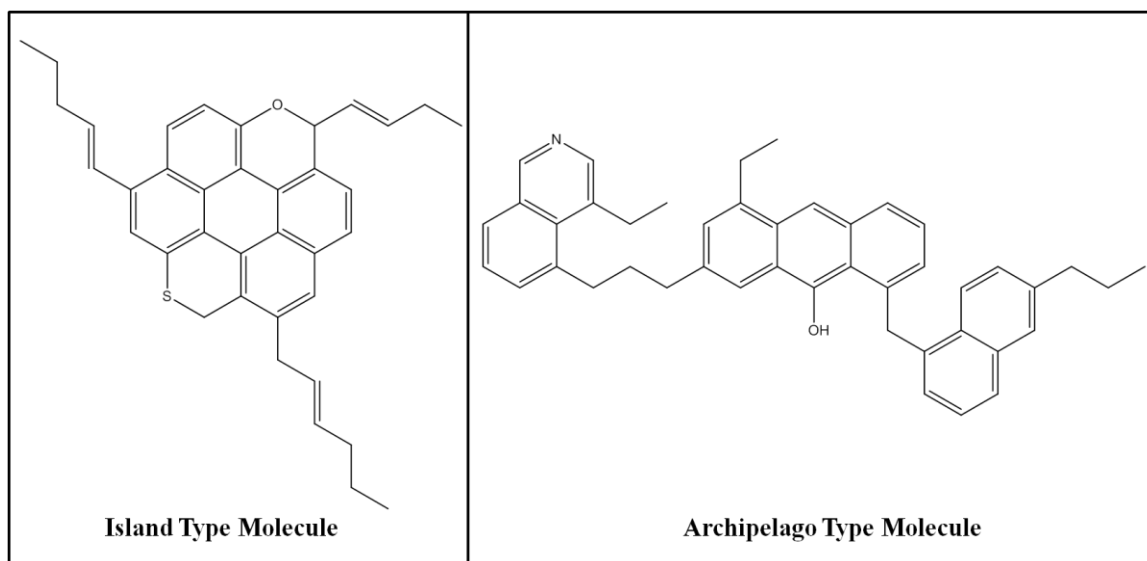


Figure 5.1 Example structures of an island-type asphaltene molecule (left) and an archipelago-type molecule (right).

One process that is currently utilized to partially upgrade asphaltenes into more useful compounds is hydrocracking.^{22,23} This process involves heating of the crude oil to a high temperature under a high pressure hydrogen atmosphere, resulting in catalytic hydrogenation of the molecules within the oil.^{24,25} The hydrogenation results in the removal of sulfur and nitrogen heteroatoms and saturation of double and triple bonds, thus converting molecules such as olefins into alkanes.^{24,25} Previous studies on hydrocracked asphaltenes by using bulk elemental analysis found that the asphaltenes became more hydrogen deficient and had a reduced amount of heteroatoms, such as sulfur and nitrogen.²⁶ Hence, it was concluded that during the hydrocracking process, the alkyl chains that branch off of the aromatic core are cleaved off.²⁶ Analysis of hydrocracked asphaltenes has yet to be studied at the molecular level by using mass spectrometry.

In the study discussed in this chapter, tandem mass spectrometry with collisionally-activated dissociation (CAD) was used to study the effects of “mild” and “harsh” hydrocracking conditions on the molecular structures of asphaltenes. The exact conditions of the hydrocracking processes were a trade secret of our industrial collaborators who donated the samples. The only information that we were provided was that some of the samples were hydrocracked at a low temperature and pressure while other samples were hydrocracked at a higher temperature and pressure. The same method that was used in the experiments described in Chapter 4 was used here. The sample was dissolved in carbon disulfide (CS₂) and ionized via atmospheric pressure chemical ionization (APCI). This method was chosen due to its ability to ionize a wide range asphaltenes model compounds by only producing one type of an ion per compound, the molecular ion (M⁺).²⁷

5.2 Experimental

Chemicals. All of the asphaltene samples studied here originated from an oil field in Russia. Two series of samples (obtained at two different times), each containing two sets (each set is a from a different feedstock) of samples, were analyzed during this study. All samples were collected under identical conditions. The first digit in the sample name denotes whether it belonged to the first or second series of samples. Of the ten samples analysed, four were unprocessed (U), four were processed under mild conditions (M), and two were processed under harsh conditions (H), which is denoted by the second digit of samples' name. The third digit of the samples' names indicates which feedstock was being processed from that series (i.e., 1H1 corresponds to sample 1U1 after the harsh

hydrocracking treatment). Table 5.1 provides a list of all the samples that were analyzed and the hydrocracking treatment they were exposed to. Carbon disulfide (CS₂) (>99.9%) was purchased from Sigma Aldrich (St. Louis, MO) and used without purification.

Instrumentation. A Thermo Scientific LTQ linear quadrupole ion trap (LQIT) mass spectrometer was used for mass spectrometric analyses. The asphaltenes samples were dissolved in carbon disulfide at a concentration of 0.5 g/mL and then introduced into the APCI source via direct infusion from a Hamilton 500 μ L syringe through the instrument's syringe pump at a rate of 20 μ L per minute. The APCI source was set at 450°C for the first series of samples and 300°C for the second series. This difference in temperature was due to a refinement in the mass spectrometric technique between the time when the first samples were analyzed and the time when the second set was received to prevent ion-molecule reactions during nebulization. The temperature was found to effect the molecular weight distribution (MWD) and the amount of energy required during CAD but since each series is not being directly compared to the other, these changes were found to be irrelevant). Several radical cations were isolated and subjected to CAD. An isolation window of 2 Da (selected m/z value \pm 1 Da) and a CAD energy of 35-60 arbitrary units was used. Both were controlled by the LTQ software.

Table 5.1 A list of the asphaltenes samples examined.

Asphaltene Sample	Processing
1U1	<u>U</u> nprocessed Feedstock
1M1	1U1 Processed Using <u>M</u> ild Hydrocracking Conditions
1H1	1U1 Processed Using <u>H</u> arsh Hydrocracking Conditions
1U2	<u>U</u> nprocessed Feedstock
1M2	1U2 Processed Using <u>M</u> ild Hydrocracking Conditions
1H2	1U2 Processed Using <u>H</u> arsh Hydrocracking Conditions
2U1	<u>U</u> nprocessed Feedstock
2M1	2U1 Processed Using <u>M</u> ild Hydrocracking Conditions
2U2	<u>U</u> nprocessed Feedstock
2M2	2U2 Processed Using <u>M</u> ild Hydrocracking Conditions

5.3 Results and Discussion

During this study, ten asphaltenes samples were examined that were exposed to none or various levels of hydrocracking treatment. Of the ten samples, four were different unprocessed feed stocks that were not exposed to hydrocracking, four were exposed to a mild hydrocracking process, and two were exposed to a harsh hydrocracking process. The samples were ionized using APCI with CS₂ as the ionization reagent to produce stable molecular ions. The MWDs measured for the both series of samples

(Figure 5.2 and 5.3) range from about 300 up to 1800 Da for the first series and 300 - 1400 Da for the second series. On the other hand, the center of the MWD, which was denoted by the most abundant peak in the distribution and indicated by a dashed red line in Figure 5.2 and 5.3, is shifted to a lower m/z value for samples subjected to the mild hydrocracking process and to an even lower m/z value for the samples subjected to the harsh hydrocracking process. For the first samples series, the center of the MWD shifted from ~750 Da for unprocessed asphaltenes to ~650 for asphaltenes that were mildly hydrocracked and to ~550 for asphaltenes that were harshly hydrocracked, with a similar trend observed for the second sample series. This shift in the center of the MWD indicates that the asphaltene molecules are being fragmented into smaller molecules during the hydrocracking process but it does not specify where the fragmentation is occurring in the molecule. The same trend is shown in Figure 5.3 for the unprocessed feedstocks and those subjected to mild hydrocracking from the second set of samples.

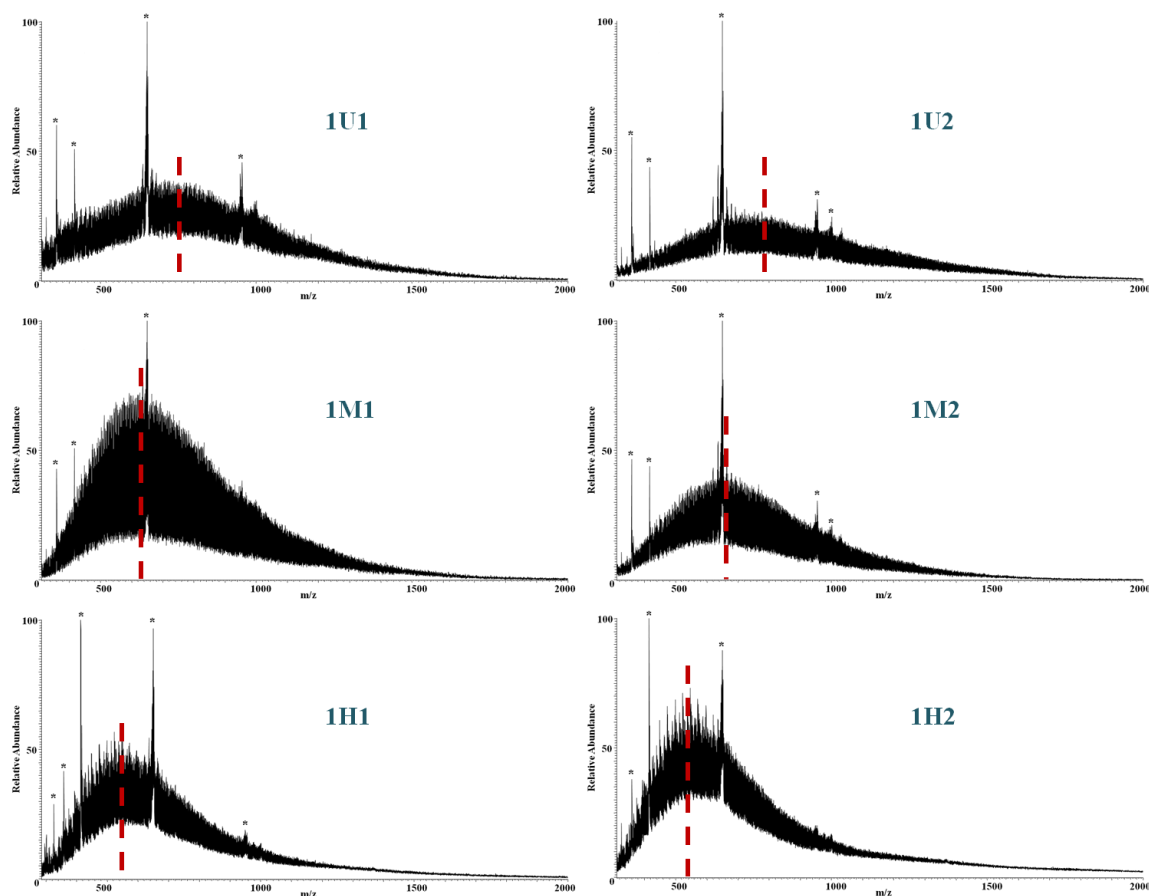


Figure 5.2 Mass spectra showing the MWD for the six samples in the first set of samples. The red dashed line indicates the center of the MWD (the most abundant compounds in the distribution). Comparing the mass spectra of the untreated samples (1U1 and 1U2) to those that were hydrocracked under different intensities (1M1 = 1M2 < 1H1 = 1H2) the center of the MWD shifts from 750 Da for 1U1 and 1U2 to 650 Da for 1M1 and 1M2 and to 550 Da for 1H1 and 1H2. The m/z values of ions with elevated relative abundances that are marked with a star are due to polyethylene glycol contamination.

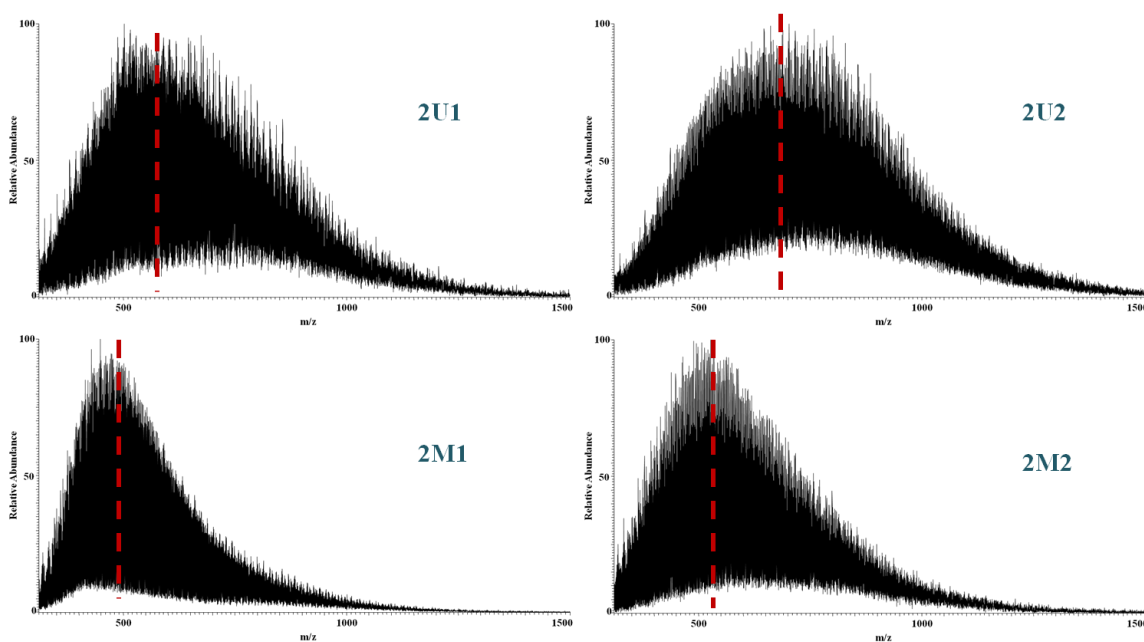


Figure 5.3 Mass spectra showing the MWD for four samples in the second set of samples. The red dashed line indicates the center of each MWD. Comparing the mass spectra measured for the hydrocracked feedstocks (2M1 and 2M2) to those of the corresponding untreated feedstocks (2U1 and 2U2) shows that hydrocracking shifts the centers of the MWDs to lower mass values, the same trend that was observed for the first set of samples.

Many ions derived from each sample were isolated and subjected to CAD to examine the structural changes caused by the hydrocracking processes. The major fragmentation pathway that was observed for each ion was the loss of neutral alkyl radicals of various lengths, with the loss of shorter radicals being more predominant than longer ones. The minimum combined length of the alkyl chains for a given set of molecular ions was approximated by isolating molecular ions with a narrow m/z range (2 m/z window), subjecting them to CAD, and determining the maximum number of apparent methylene losses (methylenes are actually not lost) in the mass spectrum, until the corresponding fragment ions' abundance is below two percent (value chosen

randomly) relative to the abundance of the most abundant ion, as described previously.¹² Based on Figure 5.4, which shows CAD mass spectra measured for ions of m/z 704 derived from 1U1, 1M1, and 1H1, increasing the intensity of the hydrocracking process shortens the lengths of the alkyl chains. Hence, the hydrocracking process breaks entire or partial alkyl chains off the aromatic core of the molecule. The same trend can be observed for the samples 1U2 (a total of 25 alkyl carbons lost), 1M2 (a total of 13 alkyl carbons lost), and 1H2 (a total of 7 alkyl carbons lost) in Figure 5.5, 2U1 (a total of 26 alkyl carbons lost) and 2M1 (a total of 8 alkyl carbons lost) in Figure 5.6, and 2U2 (a total of 30 alkyl carbons lost) and 2M2 (a total of 18 alkyl carbons lost) in Figure 5.7.

A rough estimate of the relative heteroaromatic sulfur present within an asphaltene sample may also be obtained using CAD. CAD mass spectra measured for molecular ions of asphaltene molecules occasionally show fragment ions formed from loss of a neutral molecule of MW of 34 Da. Previous model compound studies suggest that this loss corresponds to hydrogen sulfide.¹² High resolution experiments, conducted in our lab, have confirmed this assumption. As mentioned above, one of the goals of hydrocracking is to remove heteroatoms, such as sulfur.²⁶ If this was successful, the relative abundance of the fragment ions formed from hydrogen sulfide loss should decrease as the intensity of hydrocracking is increased. This is indeed what was observed, as shown in Figures 5.4 - 5.7.

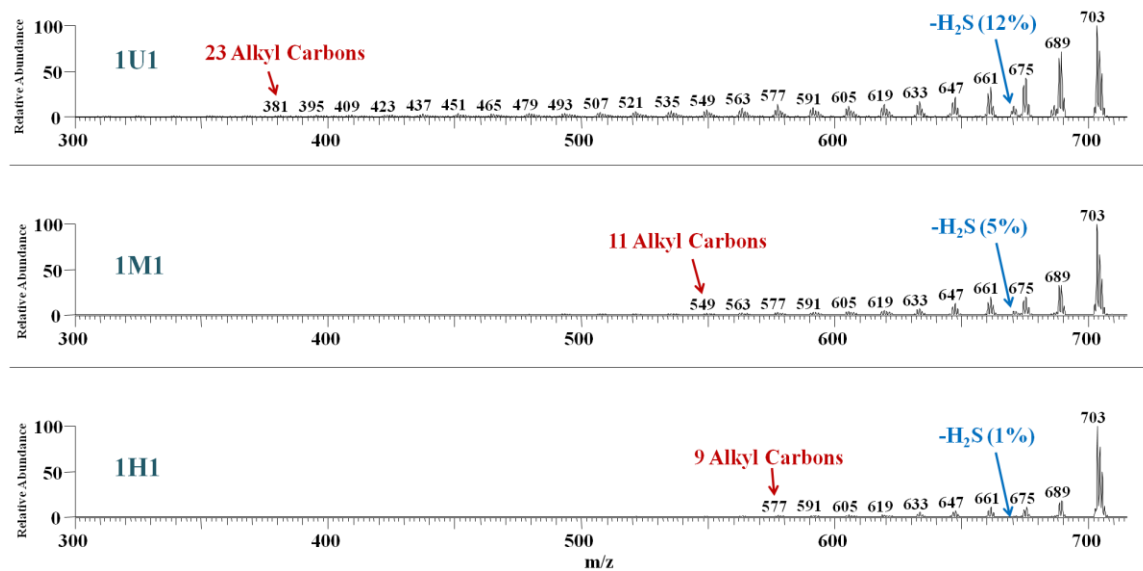


Figure 5.4 CAD mass spectra of ions of m/z 704 isolated from ionized asphaltene samples 1U1, 1M1, and 1H1. Comparing the mass spectra of the untreated sample (1U1) to those that were hydrocracked under different intensities (1M1 < 1H1), the number of alkyl carbons that brake off of the core is reduced and the relative abundance of the ions produced by hydrogen sulfide loss is reduced for hydrocracked samples.

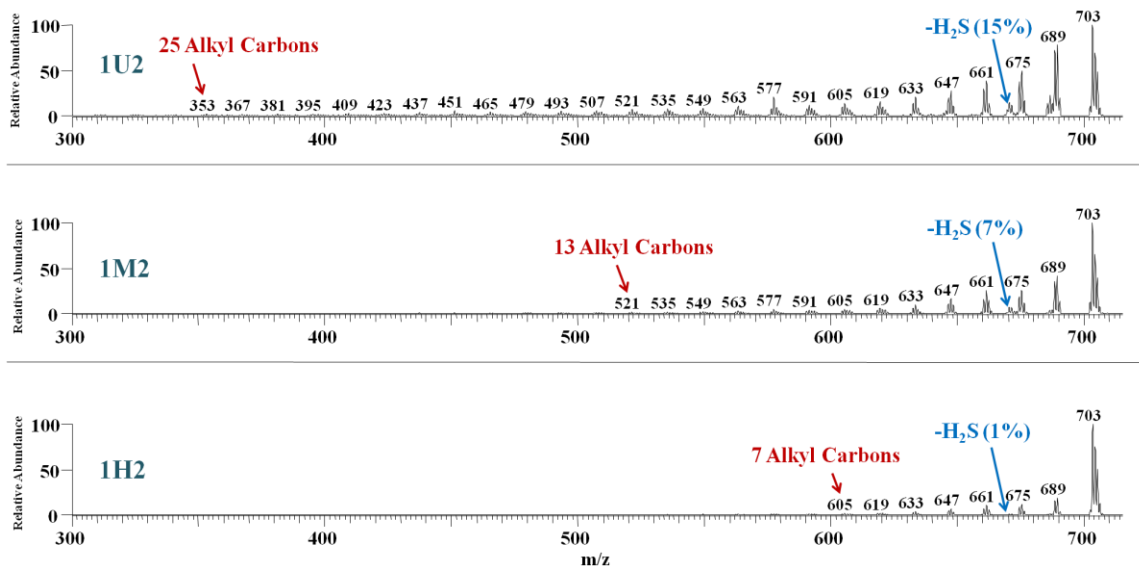


Figure 5.5 CAD mass spectra of ions of m/z 704 isolated from ionized asphaltene samples 1U2, 1M2, and 1H2. Comparing the mass spectra of the untreated sample (1U2) to those that were hydrocracked under different intensities (1M2 < 1H2) the number of alkyl carbons that brake off of the core is reduced and the relative abundance of the ions produced by hydrogen sulfide loss is reduced for hydrocracked samples.

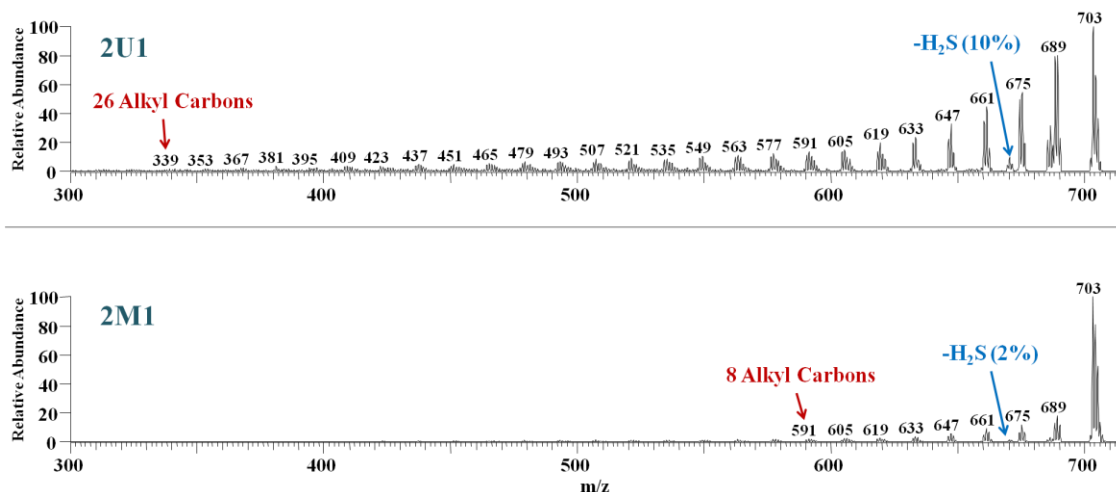


Figure 5.6 CAD mass spectra of ions of m/z 704 isolated from ionized asphaltene samples 2U1 and 2M1. Comparing the mass spectrum measured for the hydrocracked feedstock (2M1) to the mass spectrum of the corresponding untreated feedstocks (2U1) the number of alkyl carbons that brake off of the core is reduced and the relative abundance of the ions produced by hydrogen sulfide loss is reduced.

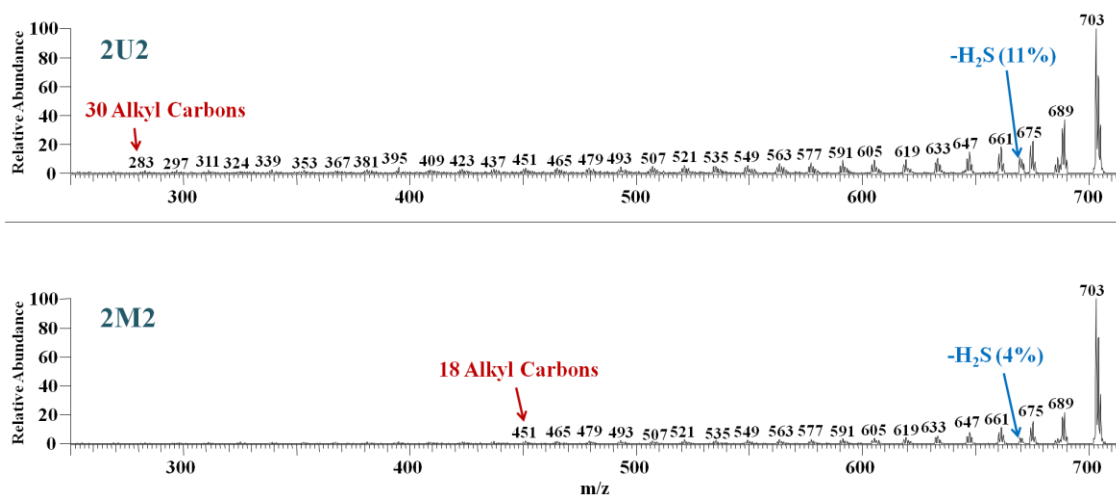


Figure 5.7 CAD mass spectra of ions of m/z 704 isolated from ionized asphaltene samples 2U2 and 2M2. Comparing the mass spectrum measured for the hydrocracked feedstock (2M2) to the mass spectrum of the corresponding untreated feedstocks (2U2) the number of alkyl carbons that brake off of the core is reduced and the relative abundance of the ions produced by hydrogen sulfide loss is reduced.

The breaking of alkyl chains and the reduction of sulfur content during hydrocracking was evident from the CAD of ions of varying m/z values for each of the sample sets studied but the effect was less obvious for ions of low m/z values than the ions of high m/z values (Figures 5.4 - 5.7). Figure 5.8 illustrates this for ions of m/z 460.

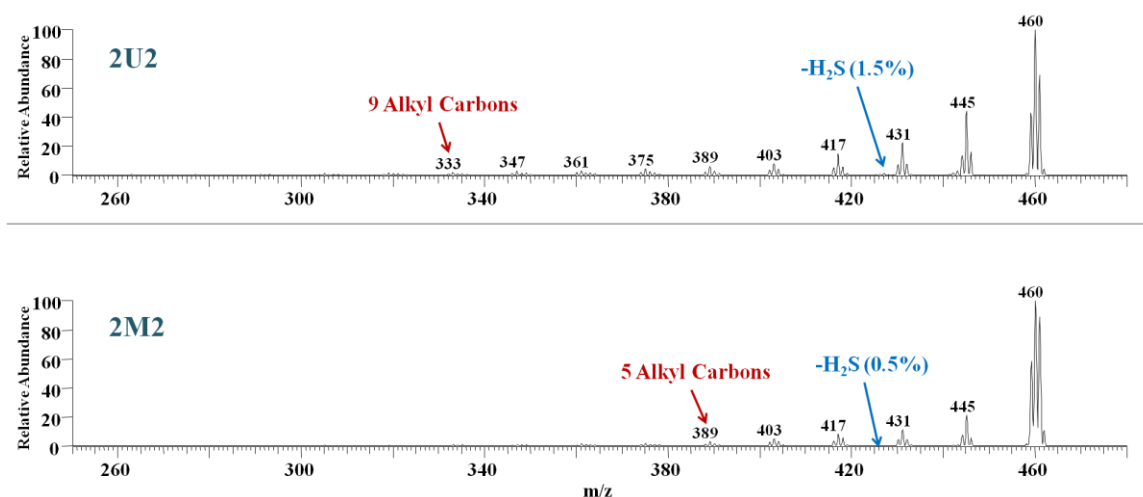


Figure 5.8 CAD mass spectra of ions of m/z 460 isolated from ionized asphaltene samples 2U2 and 2M2. Comparing the mass spectrum measured for the hydrocracked feedstock (2M2) to the mass spectrum of the corresponding untreated feedstocks (2U2) the number of alkyl carbons that brake off of the core is reduced and the relative abundance of the ions produced by hydrogen sulfide loss is reduced.

5.4 Conclusions

In this study, tandem mass spectrometry experiments using APCI with carbon disulfide to ionize asphaltenes samples in an LQIT provided insightful information regarding the effects of hydrocracking on the molecular structures of asphaltenes. For each of the asphaltenes samples, the center of the MWD shifted to lower mass after the sample was subjected to mild hydrocracking and even to lower mass after harsher

hydrocracking. While this information indicates that the asphaltene molecules are breaking down during hydrocracking, it does not specify where the breakdown is occurring within the molecules. CAD experiments indicated that the molecular breakdown during hydrocracking was due to the cleavage of alkyl chains off and heteroatoms out of the aromatic core of the molecule. The extent of this breakdown was found to increase when using harsher hydrocracking conditions. No observable change occurred to the aromatic cores. The shortening and/or cleavage of alkyl chains during hydrocracking is most likely what produces light alkanes²⁸ and more hydrogen deficient asphaltene molecules²⁶ that are known to be produced during asphaltene hydrocracking.²⁸

5.5 References

1. Ancheyta, J.; Betancourt, G.; Centeno, G.; Marroquin, G.; Alonso, F.; Garciafigueroa, E., Catalyst Deactivation During Hydroprocessing of Maya Heavy Crude Oil 1. Evaluation at Constant Operating Conditions. *Energy Fuels* **2002**, 16, 1438-1443.
2. Ancheyta, J.; Betancourt, G.; Marroquín, G.; Centeno, G.; Castañeda, L.; Alonso, F.; Muñoz, J. A.; Gómez, M.; Rayo, P., Hydroprocessing of Maya Heavy Crude Oil in Two Reaction Stages. *Appl. Catal. A-Gen.* **2002**, 233, 159-170.
3. Ancheyta-Juárez, J.; Betancourt-Rivera, G.; Marroquín-Sánchez, G.; Pérez-Arellano, A. M.; Maity, S.; Cortez, M.; del Río-Soto, R., An Exploratory Study for Obtaining Synthetic Crudes from Heavy Crude Oils via Hydrotreating. *Energy Fuels* **2001**, 15, 120-127.
4. Buenrostro-Gonzalez, E.; Groenzin, H.; Lira-Galeana, C.; Mullins, O., The Overriding Chemical Principles that Define Asphaltenes. *Energy Fuels* **2001**, 12, 972-978.
5. Mullins, O.; Sheu, E., *Structure and Dynamics of Asphaltenes*. Plenum Press: New York, 1998.
6. Mullins, O.; Sheu, E.; Hammami, A.; Marshall, A., *Asphaltenes, Heavy Oils, and Petroleomics*. Springer: New York, 2007.
7. Nogueira, J., Refining and Separation of Crude Tall-Oil Components. *Sep. Sci. Technol.* **1996**, 31, 2307-2316.
8. Potts, M. F. Crude Oil Fractionation Method. US Patent 3,320,158, 11/6/1964, 1967.
9. Trejo, F.; Centeno, G.; Ancheyta, J., Precipitation, Fractionation and Characterization of Asphaltenes from Heavy and Light Crude Oils. *Fuel* **2004**, 83, 2169-2175.
10. Yen, T.; Chilingarian, G., *Asphaltenes and Asphalts*. Elsevier: Amsterdam, 1994.
11. Hortal, A.; Hurtado, P.; Martínez-Haya, B.; Mullins, O., Molecular-Weight Distributions of Coal and Petroleum Asphaltenes from Laser Desorption/Ionization Experiments. *Energy Fuels* **2007**, 21, 2863-2868.
12. Borton, D.; Pinkston, D.; Hurt, M.; Tan, X.; Azyat, K.; Scherer, A.; Tykwinski, R.; Gray, M.; Qian, K.; Kenttämä, H., Molecular Structures of Asphaltenes Based on the Dissociation Reactions of Their Ions in Mass Spectrometry. *Energy Fuels* **2010**, 24, 5548-5559.

13. Mullins, O., The Modified Yen Model. *Energy Fuels* **2010**, 24, 2179-2207.
14. Sabbah, H.; Morrow, A.; Pomerantz, A.; Mullins, O.; Tan, X.; Gray, M.; Azyat, K.; Tykwinski, R.; Zare, R., Comparing Laser Desorption/Laser Ionization Mass Spectra of Asphaltenes and Model Compounds. *Energy Fuels* **2010**, 24, 3589-3594.
15. Sabbah, H.; Morrow, A.; Pomerantz, A.; Zare, R., Evidence for Island Structures as the Dominant Architecture of Asphaltenes. *Energy Fuels* **2011**, 25, 1597-1604.
16. Alshareef, A.; Scherer, A.; Tan, X.; Azyat, K.; Stryker, J.; Tykwinski, R.; Gray, M., Formation of Archipelago Structures During Thermal Cracking Implicates a Chemical Mechanism for the Formation of Petroleum Asphaltenes. *Energy Fuels* **2011**, 25, 2130-2136.
17. Andrews, A.; Edwards, J.; Pomerantz, A.; Mullins, O.; Nordlund, D.; Norinaga, K., Comparison of Coal-Derived and Petroleum Asphaltenes by ^{13}C Nuclear Magnetic Resonance, DEPT, and XRS. *Energy Fuels* **2011**, 25, 3068-3076.
18. Badre, S.; Goncalves, C.; Norinaga, K.; Gustavson, G.; Mullins, O., Molecular Size and Weight of Asphaltene and Asphaltene Solubility Fractions from Coals, Crude Oils and Bitumen. *Fuel* **2006**, 85, 1-11.
19. Groenzin, H.; Mullins, O., Molecular Size and Structure of Asphaltenes from Various Sources. *Energy Fuels* **2000**, 14, 677.
20. Morgan, T.; Alvarez-Rodriguez, P.; George, A.; Herod, A.; Kandiyoti, R., Characterization of Maya Crude Oil Maltenes and Asphaltenes in Terms of Structural Parameters Calculated from Nuclear Magnetic Resonance (NMR) Spectroscopy and Laser Desorption-Mass Spectroscopy (LD-MS). *Energy Fuels* **2010**, 24, 3977-3989.
21. Mullins, O.; Sabbah, H.; Eyssautier, J.; Pomerantz, A.; Barre, L.; Andrews, A.; Ruiz-Morales, Y.; Mostowfi, F.; McFarlane, R.; Goual, L.; Lepkowicz, R.; Cooper, T.; Orbulescu, J.; Leblanc, R.; Edwards, J.; Zare, R., Advances in Asphaltene Science and the Yen-Mullins Model. *Energy Fuels* **2012**, 26, 3986-4003.
22. Hoek, A.; Huizinga, T.; Esener, A.; Maxwell, I.; Stork, W.; van de Meerakker, F.; Sy, O., New Catalysts Improves Heavy Feedstock Hydro-Cracking. *Oil Gas J.* **1991**, 89, 77-82.
23. Šimáček, P.; Kubicka, D., Hydrocracking of Petroleum Vacuum Distillate Containing Rapeseed Oil: Evaluation of Diesel Fuel. *Fuel* **2010**, 89, 1508-153.
24. Miki, Y.; Yamadaya, S.; Oba, M.; Sugimoto, Y., Role of Catalyst in Hydrocracking of Heavy Oil. *J. Catal.* **1983**, 83, 371-383.

25. Eng, J.; Tiedje, J. Integrated Process for Refining Whole Crude Oil. US patent 3,617,501, 9/6/1968, 1971.
26. Miller, J.; Fisher, R.; Thiyagarajan, P.; Winans, R.; Hunt, J., Subfractionation and Characterization of Mayan Asphaltene. *Energy Fuels* **1998**, 12, 1290-1298.
27. Owen, B.; Gao, J.; Borton, D.; Amundson, L.; Archibold, E.; Tan, X.; Azyat, K.; Tykwinski, R.; Gray, M.; Kenttämää, H., Carbon Disulfide Reagent Allows the Characterization of Nonpolar Analytes by Atmospheric Pressure Chemical Ionization Mass Spectrometry. *Rapid Commun. Mass Spectrom.* **2011**, 25, 1924-1928.
28. Soodhoo, K.; Phillips, C. R., Non-Catalytic Hydrocracking of Asphaltenes: 1. Product Distributions. *Fuel* **1988**, 67, 361-374.

CHAPTER 6: A MASS SPECTROMETRIC STUDY COMPARING THE MOLECULAR STRUCTURE OF FIELD DEPOSIT ASPHALTENES AND HEPTANE PRECIPITATED ASPHALTENES

6.1 Introduction

As discussed in Chapters 4 and 5, asphaltenes are the heaviest fraction of crude oil and create many problems for the oil industry, both during the transportation of crude oil from a reservoir as well as during refinement.¹⁻¹¹ For this reason, asphaltenes have been studied at length to gain a better understanding into their bulk properties and behavior, with a recent push to learn more about their molecular structures.^{7,12-17} Asphaltenes are defined as being soluble in toluene and insoluble in heptane.¹⁸ To date, the vast majority of asphaltenes that have been studied were heptane precipitated asphaltenes (HPAs) in a laboratory setting,^{15,18-24} with no studies probing the molecular structures of field deposit asphaltenes (FDAs), the actual problematic compounds that clog crude oil pipelines, to determine if they are structurally similar to HPAs.²⁵ If FDAs are found to have dramatically different molecular structure than HPAs, then all of the characterization that has been conducted on HPAs will do little to solve the problems that are caused by FDAs.

In the study described in this chapter, tandem mass spectrometry with collisionally-activated dissociation (CAD) was used to study the structural differences of FDAs and HPAs that originated from the same oil well. The samples were dissolved in

carbon disulfide (CS₂) and ionized via atmospheric pressure chemical ionization (APCI). This ionization method was chosen because it ionizes the majority of the different types of molecules present in asphaltenes²⁶ to produce only one type of an ion per compound, the molecular ion (M⁺).²⁷

6.2 Experimental

Chemicals. Carbon disulfide (>99.9%), and n-heptane (99%) were purchased from Sigma Aldrich (St. Louis, MO) and used without purification. The FDA sample and the crude oil from which the HPA sample was precipitated originated from an oil well in Wyoming and were donated by Andy Yen at Nalco. The HPA sample was precipitated out by using a method derived from a published procedure.²⁸ The precipitation was achieved by adding 50 mL of n-heptane to 5 g of crude oil and then sonicating the mixture for 15 minutes to ensure adequate mixing. The mixture was then stored over night, filtered, and rinsed with n-heptane.

Instrumentation. A Thermo Scientific LTQ linear quadrupole ion trap (LQIT) mass spectrometer was used for mass spectrometric analyses. The asphaltenes samples were dissolved in carbon disulfide at a concentration of 0.5 g/mL and then introduced into the APCI source via direct infusion from a Hamilton 500 μ L syringe through the instrument's syringe pump at a rate of 20 μ L per minute. The APCI source was set to 300°C. The molecular ions of the asphaltene model compounds and asphaltene samples were isolated and subjected to CAD at a collision energy of 35 arbitrary units with an isolation window of m/z 2 (selected m/z value \pm 1). All parameters were controlled by the LTQ software.

6.3 Results and Discussion

Two asphaltene samples, one heptane precipitated from crude oil and one collected from an asphaltene deposit inside a crude oil transfer line, both originating from the same oil well, were studied to determine any structural differences in their molecular make up. The samples were dissolved in carbon disulfide and ionized using APCI to produce stable molecular ions. The full (MS^1) mass spectra measured for these ions yielded information about the samples MWDs. The CAD (MS^2) mass spectra measured for several isolated ions yielded information about the molecular structures of the compounds present in the samples. The average molecular weight (MW) of both samples was derived from the MWDs by using Equation 4.1 and the values are given in Table 6.1.

As described in Chapter 4, one of the structural features of asphaltenes that can be examined using CAD is the approximate minimum for the total number of carbons in the combined alkyl chains branching from the aromatic core. The minimum number of carbons in the alkyl chains was experimentally determined by isolating several molecular ions of different m/z values, subjecting them to CAD and determining the number of consecutive formal methylene losses (no methylenes are actually lost) in the mass spectrum until the corresponding fragment ions' abundance was below two percent (arbitrarily chosen) relative to the abundance of the most abundant ion. The same fragment ions that were used to determine the minimum combined length of the alkyl chains were used to determine the molecule's core size (methylene functional groups possibly left onto the core after benzylic cleavages of the alkyl chains were included in this estimate). The calculation of the number of fused rings that comprise the core is a rough estimate as it does not take into account the presence of heteroatoms and the exact

number of methylene groups left on the core is unknown, but these factors should not change the final results to a significant degree.

Another structural feature experimentally determined was the approximate relative heteroaromatic sulfur content in the samples. A rough estimate of the amount of heteroaromatic sulfur present in the ions was obtained from the abundance of the fragment ions formed by the loss of hydrogen sulfide (34 Da) relative to that of the most abundant fragment ion in the CAD mass spectrum. High resolution experiments confirmed that hydrogen sulfide is the molecule lost from the ions in this fragmentation (exact mass measurement: 33.96236 Da). Our preliminary results obtained for molecular ions of model compounds with sulfur containing heteroaromatic rings showed hydrogen sulfide loss upon CAD in a LQIT.¹²

Figure 6.1, below, displays a direct comparison of the MWD measured for the FDAs and HPAs samples. The observed MWD for both samples range from 100 up to 1200 Daltons (Da). The calculated weighted MW average for was slightly different for the two samples, with the HPAs having an average MW of 545 ± 8 Da and FDAs 494 ± 29 Da, indicating that HPAs are composed of larger molecules.

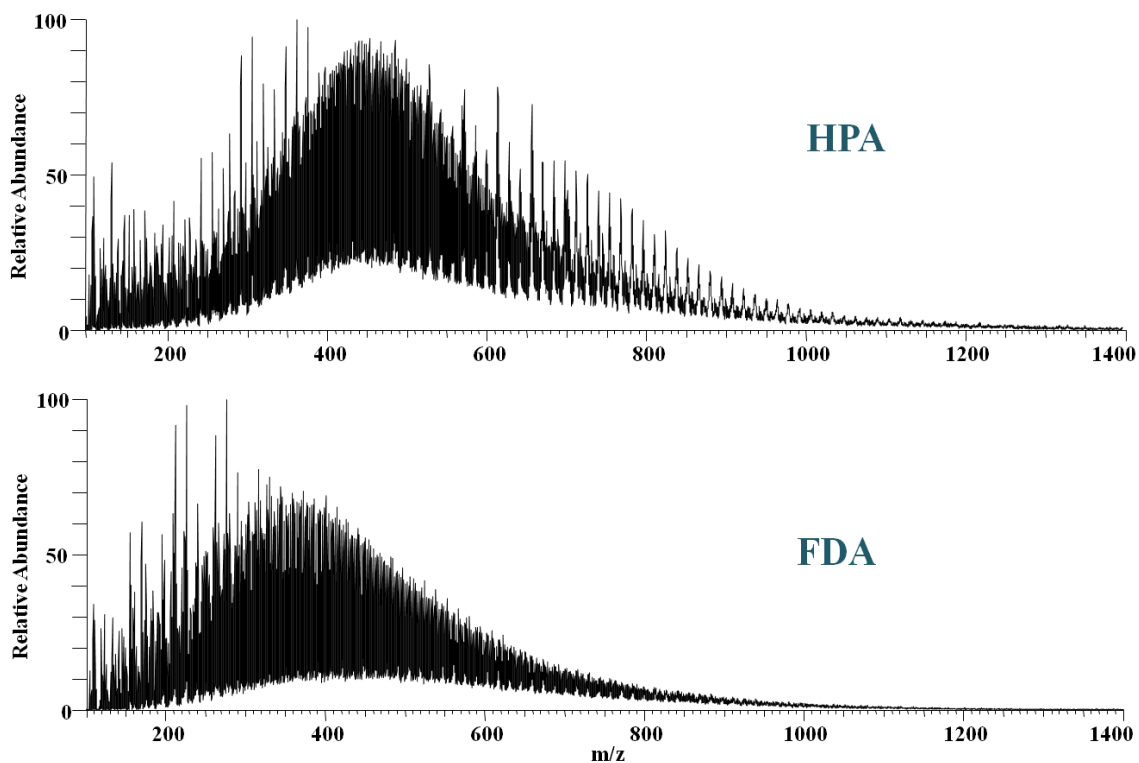


Figure 6.1 APCI/CS₂ mass spectra of HPAs (top) and FDAs (bottom).

Experiments using CAD were then conducted to probe the differences in molecular structures of the compounds present in each sample. As explained in Chapter 4, a relatively wide (2 m/z-units) window was used during the isolation event for the MS/MS experiments. Hence, the isolated ion population may contain between two and fifteen abundant isobaric ions (and several isomeric ions), all of which may contribute to the CAD mass spectrum.²⁵ As shown in Figure 4.3, substantial narrowing of this isolation window still shows the same dominant fragment ions; hence, data obtained using the broader isolation window should be fine for our qualitative comparison. Typical CAD mass spectra for ions of $m/z 442 \pm 1$ Da derived from HPAs and FDAs are shown in Figure 6.2. These CAD mass spectra are similar to the ones measured

previously for petroleum asphaltenes, depicting steadily decreasing abundances for fragment ions formed by the loss of larger alkyl radicals from the aromatic core.¹² CAD mass spectra of ions derived from asphaltenes yield an estimate of the number of carbons present in alkyl chains and the aromatic core and very rough estimate for their relative heteroaromatic sulfur content as described above. Figure 6.2 shows the CAD mass spectra of molecular ions for both HPAs and FDAs to illustrate the differences in the molecular structure for the two samples.

When looking at Figure 6.2, it can be noted that the most favored neutral fragments correspond to a series of alkyl radicals ranging from methyl up to an alkyl radical at least 12 carbons in length for HPAs and 21 carbons in length for FDAs. The decay in the abundances of the alkyl radicals as a function of their size suggests that shorter alkyl groups are much more prominent in asphaltenes molecules than longer alkyl groups. The results for ions of $m/z\ 422 \pm 1$, along with the other ions studied, are displayed in Table 6.1. These results suggest that in general, HPAs contain a smaller number of carbons in their alkyl chains than FDAs. The CAD mass spectra measured for ions with several m/z values (Table 6.1) show that the minimum total number of carbons in all side chains in HPAs and FDAs range from at least 12 up to at least 37 carbons and from at least 18 up to at least 40 carbons, respectively. Based on the results presented in Figure 6.2, the relative heteroaromatic sulfur content is higher in FDAs (10% relative abundance) than in HPAs (5% relative abundance). Table 6.1 shows that this is true for ions with a variety of different m/z values.

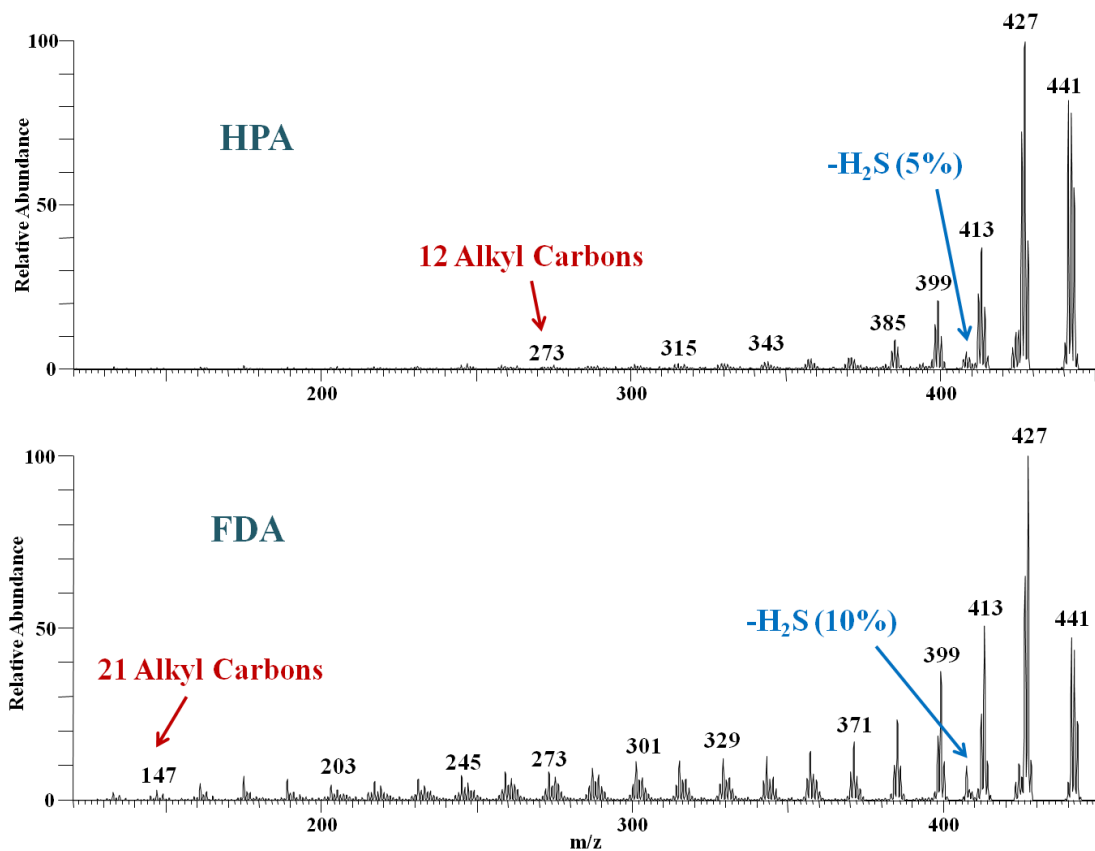


Figure 6.2 CAD mass spectra measured for ions of m/z 422 ± 1 derived from HPAs (top) and FDAs (bottom). The total number of carbons in the side chains and the relative abundance of the fragment ion produced due to the loss of hydrogen sulfide are labeled in the mass spectra.

Table 6.1 Molecular weight distributions (MWD) and average molecular weights (AVG MW) determined for molecules in FDAs and HPAs, as well as the estimated minimum total number of carbon atoms in all side chains and relative abundances of the ions produced by neutral hydrogen sulfide loss, given for ions with selected m/z values. The differences between the FDAs and HPAs (FDAs – HPAs) are given in the last column.

	FDAs	HPAs	Difference (FDAs – HPAs)
MWD	100 Da - 1200 Da	100 Da - 1200 Da	--
AVG MW	494 ± 29 Da	545 ± 8 Da	17
<u>Ion of m/z 423</u>			
Carbons in Side Chains	18	16	2
Relative Percent Hydrogen Sulfide Loss	3	4	-1
<u>Ion of m/z 442</u>			
Carbons in Side Chains	20	14	6
Relative Percent Hydrogen Sulfide Loss	6	3	3
<u>Ion of m/z 452</u>			
Carbons in Side Chains	20	12	8
Relative Percent Hydrogen Sulfide Loss	4	2	2
<u>Ion of m/z 509</u>			
Carbons in Side Chains	24	15	9
Relative Percent Hydrogen Sulfide Loss	5	4	1
<u>Ion of m/z 515</u>			
Carbons in Side Chains	22	17	5
Relative Percent Hydrogen Sulfide Loss	5	4	1
<u>Ion of m/z 536</u>			
Carbons in Side Chains	25	20	5
Relative Percent Hydrogen Sulfide Loss	5	5	0
<u>Ion of m/z 591</u>			
Carbons in Side Chains	27	23	4
Relative Percent Hydrogen Sulfide Loss	7.0	4	3
<u>Ion of m/z 606</u>			
Carbons in Side Chains	28	23	4
Relative Percent Hydrogen Sulfide Loss	15	5	10

Table 6.1, continued

	FDA _s	HPA _s	Difference (FDA _s – HPA _s)
<u>Ion of m/z 624</u>			
Carbons in Side Chains	29	28	1
Relative Percent Hydrogen Sulfide Loss	28	9	19
<u>Ion of m/z 722</u>			
Carbons in Side Chains	34	32	2
Relative Percent Hydrogen Sulfide Loss	29	24	5
<u>Ion of m/z 736</u>			
Carbons in Side Chains	34	32	2
Relative Percent Hydrogen Sulfide Loss	33	27	6
<u>Ion of m/z 755</u>			
Carbons in Side Chains	35	33	2
Relative Percent Hydrogen Sulfide Loss	18	7	11
<u>Ion of m/z 801</u>			
Carbons in Side Chains	40	37	3
Relative Percent Hydrogen Sulfide Loss	32	9	23
<u>Ion of m/z 822</u>			
Carbons in Side Chains	37	37	0
Relative Percent Hydrogen Sulfide Loss	31	10	21

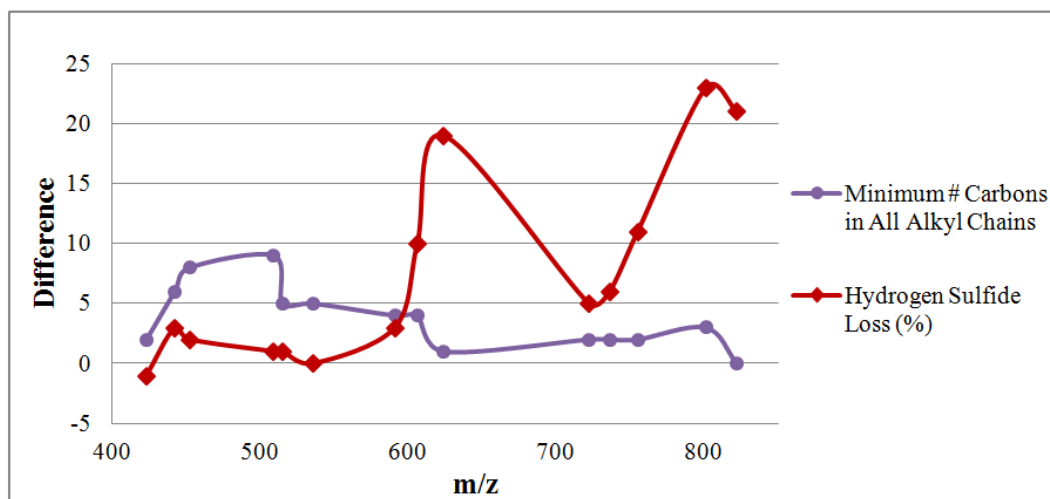


Figure 6.3 Graph illustrating the differences (FDAs – HPAs) between the FDAs and the HPAs as a function of their molecular size: relative abundances of ions produced from hydrogen sulfide loss and the estimated minimum total number of carbons in all side chains.

The differences between the FDAs and HPAs shown in Table 6.1 are graphed as a function of the size of the ions in Figure 6.3. Figure 6.3 suggests that ions of a wide range of different m/z values derived from FDAs and HPAs have similar alkyl chain lengths. However, while the extent of hydrogen sulfide loss from ions of small m/z-values is comparable for FDAs and HPAs, it can vary as much as by 23% for ions of greater m/z in these two samples. These results suggest that the molecules in FDAs and HPAs are quite similar structurally and hence, that HPAs are a suitable substitute for FDAs.

6.4 Conclusions

The MWDs measured for FDAs and HPAs by using APCI with carbon disulfide as the ionizing reagent in an LQIT were found to be quite similar. The observed MWD for both samples ranges from 100 up to 1200 Daltons (Da). The calculated weighted MW average for each sample was found to be 545 ± 8 Da for HPAs and 494 ± 29 Da for FDAs, indicating that HPAs are composed of somewhat larger molecules. The CAD mass spectra measured for molecular ions of several m/z values showed similar alkane carbon content for both samples, with FDAs having slightly higher alkane carbon content. The total number of carbons in all side chains in HPAs and FDAs was found to range from at least 12 up to at least 37 carbons and at least 18 up to at least 40 carbons, respectively. Finally, the relative abundance of the fragment ion due to hydrogen sulfide loss from ions derived from FDAs was much higher than that for the HPAs. While these differences are intriguing, the findings suggest that HPAs are indeed a good substitute for FDAs.

6.5 References

1. Ancheyta, J.; Betancourt, G.; Centeno, G.; Marroquin, G.; Alonso, F.; Garciafigueroa, E., Catalyst Deactivation During Hydroprocessing of Maya Heavy Crude Oil 1. Evaluation at Constant Operating Conditions. *Energy Fuels* **2002**, 16, 1438-1443.
2. Ancheyta, J.; Betancourt, G.; Marroquín, G.; Centeno, G.; Castañeda, L.; Alonso, F.; Muñoz, J. A.; Gómez, M.; Rayo, P., Hydroprocessing of Maya Heavy Crude Oil in Two Reaction Stages. *Appl. Catal. A-Gen.* **2002**, 233, 159-170.
3. Ancheyta-Juárez, J.; Betancourt-Rivera, G.; Marroquín-Sánchez, G.; Pérez-Arellano, A. M.; Maity, S.; Cortez, M.; del Río-Soto, R., An Exploratory Study for Obtaining Synthetic Crudes from Heavy Crude Oils via Hydrotreating. *Energy Fuels* **2001**, 15, 120-127.
4. Buenrostro-Gonzalez, E.; Groenzin, H.; Lira-Galeana, C.; Mullins, O., The Overriding Chemical Principles that Define Asphaltenes. *Energy Fuels* **2001**, 12, 972-978.
5. Idris, M.; Okoro, L., A Review on the Effects of Asphaltenes on Petroleum Processing. *Eur. Chem. Bull.* **2013**, 2, 393-396.
6. Mullins, O.; Sheu, E., *Structure and Dynamics of Asphaltenes*. Plenum Press: New York, 1998.
7. Mullins, O.; Sheu, E.; Hammami, A.; Marshall, A., *Asphaltenes, Heavy Oils, and Petroleomics*. Springer: New York, 2007.
8. Nogueira, J., Refining and Separation of Crude Tall-Oil Components. *Sep. Sci. Technol.* **1996**, 31, 2307-2316.
9. Potts, M. F. Crude Oil Fractionation Method. US Patent 3,320,158, 11/6/1964, 1967.
10. Trejo, F.; Centeno, G.; Ancheyta, J., Precipitation, Fractionation and Characterization of Asphaltenes from Heavy and Light Crude Oils. *Fuel* **2004**, 83, 2169-2175.
11. Yen, T.; Chilingarian, G., *Asphaltenes and Asphalts*. Elsevier: Amsterdam, 1994.
12. Borton, D.; Pinkston, D.; Hurt, M.; Tan, X.; Azyat, K.; Scherer, A.; Tykwinski, R.; Gray, M.; Qian, K.; Kenttämaa, H., Molecular Structures of Asphaltenes Based on the Dissociation Reactions of Their Ions in Mass Spectrometry. *Energy Fuels* **2010**, 24, 5548-5559.

13. Miller, J.; Fisher, R.; Thiyagarajan, P.; Winans, R.; Hunt, J., Subfractionation and Characterization of Mayan Asphaltene. *Energy Fuels* **1998**, *12*, 1290-1298.
14. Mullins, O., The Modified Yen Model. *Energy Fuels* **2010**, *24*, 2179-2207.
15. Pinkston, D.; Duan, P.; Gallardo, V.; Habicht, S.; Tan, X.; Qian, K.; Gray, M.; Müllen, K.; Kenttämäa, H., Analysis of Asphaltenes and Asphaltene Model Compounds by Laser-Induced Acoustic Desorption/Fourier Transform Ion Cyclotron Resonance Mass Spectrometry. *Energy Fuels* **2009**, *23*, 5564-5570.
16. Sabbah, H.; Morrow, A.; Pomerantz, A.; Mullins, O.; Tan, X.; Gray, M.; Azyat, K.; Tykwinski, R.; Zare, R., Comparing Laser Desorption/Laser Ionization Mass Spectra of Asphaltenes and Model Compounds. *Energy Fuels* **2010**, *24*, 3589-3594.
17. Sabbah, H.; Morrow, A.; Pomerantz, A.; Zare, R., Evidence for Island Structures as the Dominant Architecture of Asphaltenes. *Energy Fuels* **2011**, *25*, 1597-1604.
18. Groenzin, H.; Mullins, O., Molecular Size and Structure of Asphaltenes from Various Sources. *Energy Fuels* **2000**, *14*, 677.
19. Alboudwarej, H.; Beck, J.; Svrcek, W.; Yarranton, H., Sensitivity of Asphaltene Properties to Separation Techniques. *Energy Fuels* **2002**, *16*, 462-469.
20. Badre, S.; Goncalves, C.; Norinaga, K.; Gustavson, G.; Mullins, O., Molecular Size and Weight of Asphaltene and Asphaltene Solubility Fractions from Coals, Crude Oils and Bitumen. *Fuel* **2006**, *85*, 1-11.
21. Becker, C.; Qian, K.; Russell, D., Molecular Weight Distributions of Asphaltenes and Deasphalted Oils Studied by Laser Desorption Ionization and Ion Mobility Mass. *Anal. Chem.* **2008**, *80*, 8592-8597.
22. Qian, K.; Edwards, K.; Siskin, M.; Olmstead, W.; Mennito, A.; Dechert, G.; Hoosain, N., Desorption and Ionization of Heavy Petroleum Molecules and Measurement of Molecular Weight Distributions. *Energy Fuels* **2007**, *21*, 1042-1047.
23. Rahmani, S.; McCaffrey, W.; Elliott, J.; Gray, M., Liquid-Phase Behavior during the Cracking of Asphaltenes. *Ind. Eng. Chem. Res.* **2003**, *42*, 4101-4108.
24. Trejo, F.; Ancheyta, J.; Morgan, T.; Herod, A.; Kandiyoti, R., Characterization of Asphaltenes from Hydrotreated Products by SEC, LDMS, MALDI, NMR, and XRD. *Energy Fuel* **2007**, *21*, 2121-2128.

25. Klein, G.; Kim, S.; Rodgers, R.; Marshall, A.; Yen, A., Mass Spectral Analysis of Asphaltenes. II. Detailed Compositional Comparison of Asphaltenes Deposit to its Crude Oil Counterpart for Two Geographically Different Crude Oils by ESI FT-ICR MS. *Energy Fuels* **2006**, 20, 1973-1979.
26. Gaspar, A.; Zellermann, E.; Lababidi, S.; Reece, J.; Schrader, W., Impact of Different Ionization Methods on the Molecular Assignments of Asphaltenes by FT-ICR Mass Spectrometry. *Anal. Chem.* **2012**, 84, 5257-5267.
27. Owen, B.; Gao, J.; Borton, D.; Amundson, L.; Archibold, E.; Tan, X.; Azyat, K.; Tykwinski, R.; Gray, M.; Kenttämä, H., Carbon Disulfide Reagent Allows the Characterization of Nonpolar Analytes by Atmospheric Pressure Chemical Ionization Mass Spectrometry. *Rapid Commun. Mass Spectrom.* **2011**, 25, 1924-1928.
28. Bjorøy, Ø.; Fotland, P.; Gilje, E.; Høiland, H., Asphaltene Precipitation from Athabasca Bitumen Using an Aromatic Diluent: A Comparison to Standard *n*-Alkane Liquid Precipitants at Different Temperatures. *Energy Fuels* **2012**, 26, 2648-2654.

CHAPTER 7: EXAMINATION OF SOLVENT/REAGENT EFFECTS ON ATMOSPHERIC PRESSURE CHEMICAL IONIZATION OF ASPHALTENES IN A SEARCH FOR A REPLACEMENT FOR CARBON DISULFIDE

7.1 Introduction

As discussed in Chapters 4-6, asphaltenes are the heaviest fraction of crude oil and cause many problems during crude oil processing, thus increasing production costs.¹⁻¹¹ More needs to be known about asphaltenes in order to address these problems, but owing to their complexity, asphaltenes are not easy to study. Hence, only a limited amount of work has been carried out thus far to determine their molecular structures.¹²⁻¹⁶ For the proposed two different types of molecules believed to be present in asphaltenes, most of the data support island type structures (aromatic core with alkyl chains branching off), with only a small amount of evidence suggesting that archipelago-type molecules (several small aromatic cores linked by alkyl chains are also present.^{5,6,17-22}

The method that was utilized to analyze asphaltenes in the studies discussed in Chapters 4-6 proved very successful. The asphaltenes were ionized using an atmospheric pressure chemical ionization (APCI) source infused with the sample dissolved in carbon disulfide (CS₂) from an external syringe pump. CS₂ acts as the ionizing reagent during APCI, as discussed in section 2.2.1, and is known to produce solely stable molecular ions for asphaltene model compounds.²³ The molecular ions derived from asphaltenes were then isolated and subjected to collisionally activated dissociation (CAD) to determine

their structural features. The instruments that were used for these analyses were Thermo Scientific LTQ linear quadrupole ion traps (LQIT), which only can isolate ions with m/z range of 0.3 units or larger for the XL model and 0.8 units for the classic model (the classic model was used for the majority of these studies). Usually, an isolation window of m/z of 2 units was used for these experiments due to the extreme complexity of asphaltenes, which resulted in a low ion signal when smaller isolation windows were used. However, high resolution data collected both in our laboratory and in others have found that a 2 m/z -unit isolation window may result in isolation of an ion population that contains more than ten abundant isobaric ions, all of which may contribute to the CAD mass spectrum.^{24,25} For example, Figure 7.1 shows a high resolution mass spectrum of an isolated asphaltene ion cluster with a range of m/z values from 528.0 up to 528.5 Da that contains nine peaks with greater than twenty five percent relative abundance.

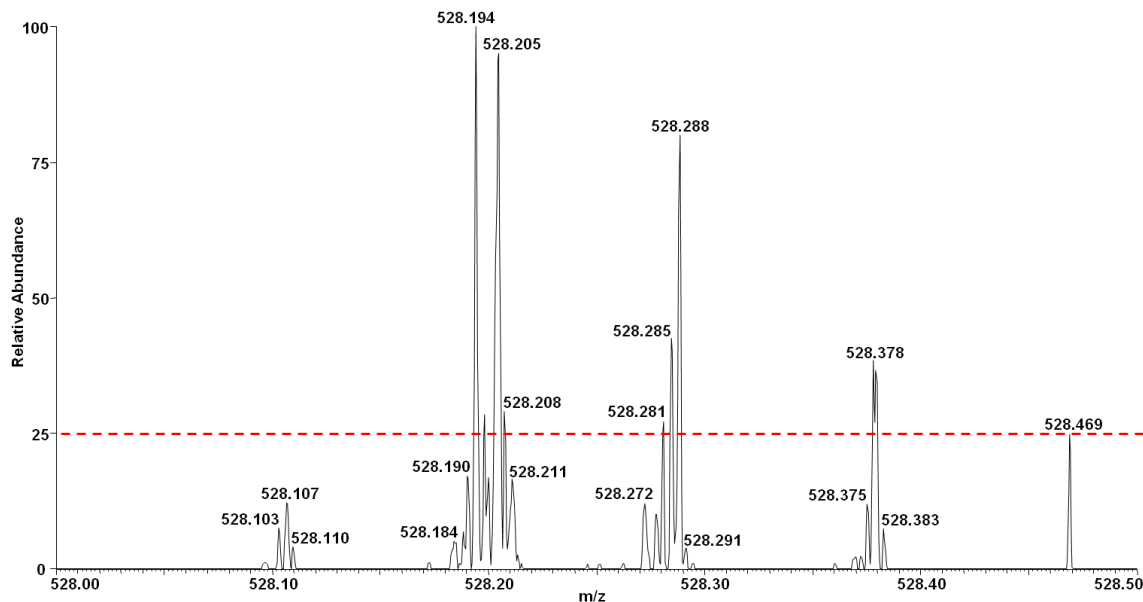


Figure 7.1 High resolution mass spectrum of an isolated asphaltene ion cluster of m/z ranging from 528.0 up to 528.5 Da. Nine peaks have greater than twenty five percent relative abundance, indicated by the red dashed line, illustrating the extreme complexity of asphaltenes.

To reduce the number of ions that contribute to a CAD mass spectrum measured for ions derived from asphaltenes, a chromatographic separation of the molecules is needed prior to mass spectrometric analysis. To develop a successful chromatographic method that can be used on-line with APCI, a solvent that can be used both in high performance liquid chromatography (HPLC) and APCI needs to be found. A solvent compatible with HPLC does not damage or corrode the internal components of the HPLC or the column and results in a good separation of the sample molecules. A solvent is considered compatible with APCI if it produces one ion per compound (i.e., the molecular ion M^{+} or the protonated molecule $M+H^{+}$). Promising work has already been conducted using preparatory HPLC of asphaltenes²⁶ but the solvent, N-methyl-2-pyrrolidone, used in these studies is not compatible with APCI due to its high proton

affinity (923.5 kJ/mol) and high boiling point, hindering its removal from the mass spectrometer after use.²⁷ CS₂ is also not compatible with HPLC.^{28,29}

To find a proper solvent for on-line HPLC/MS analysis, four solvents known to dissolve asphaltenes were tested to determine their compatibility with APCI: chloroform,³⁰⁻³³ dichloromethane (DCM),³⁴⁻³⁸ toluene,³⁹⁻⁴³ and tetrahydrofuran (THF).⁴⁴⁻⁴⁸ Tandem mass spectrometric analysis of an asphaltene sample and selected asphaltene model compounds was conducted using APCI with each of the four solvents. Both island type and archipelago type model compounds were studied. The mass spectrometric data collected for each solvent were compared to data collected using CS₂ as the solvent.

7.2 Experimental

Chemicals. The asphaltene sample used here originated from an oil field in Russia. The four asphaltene model compounds studied were provided by Professor Murray Gray (University of Alberta, Edmonton, Alberta, Canada). Figure 7.2 shows the structures of the asphaltene model compounds that were studied. Carbon disulfide (>99.9%), toluene (≥99.9%), dichloromethane (≥99.9%), chloroform (≥99.9%) with amylene stabilizer, and tetrahydrofuran (≥99.9%) were purchased from Sigma Aldrich (St. Louis, MO) and used without purification.

Instrumentation. A Thermo Scientific LTQ linear quadrupole ion trap (LQIT) mass spectrometer was used for mass spectrometric analyses. The asphaltenes sample and model compounds were dissolved in each solvent at a concentration of 0.5 g/mL and then introduced into the APCI source via direct infusion from a Hamilton 500 µL syringe

through the instrument's syringe pump at a rate of 20 μL per minute. The APCI source was set to 300°C. The ions derived from the model compounds and asphaltenes were isolated and subjected to CAD. A isolation windows of 1 m/z-unit (selected m/z value ± 0.5) and 2 m/z-units (selected m/z value ± 1) were used for isolation of ions derived from the model compounds and asphaltenes, respectively. All instrument parameters were controlled by the LTQ software.

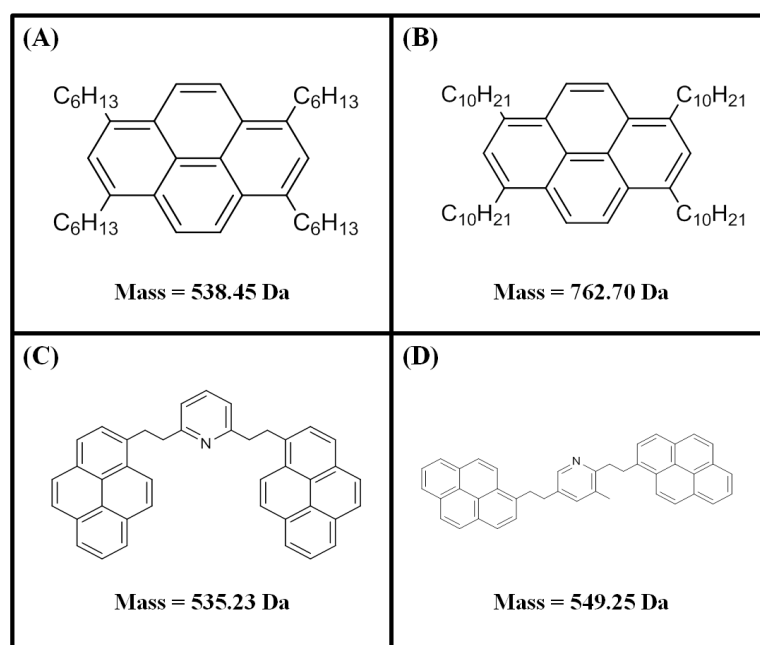


Figure 7.2 Structures and masses of the model compounds that were studied.

7.3 Results and Discussion

APCI of model compounds was studied first to determine the types of ions that are produced during APCI using each solvent. The same results were obtained for all model compounds. Hence, only the results obtained for model compound A are

discussed below. Figure 7.3 shows the mass spectrum of A obtained using APCI with CS₂ as the solvent/ionization reagent to serve as a comparison point for the mass spectra collected using the other solvents and shown in Figures 7.4 - 7.7.

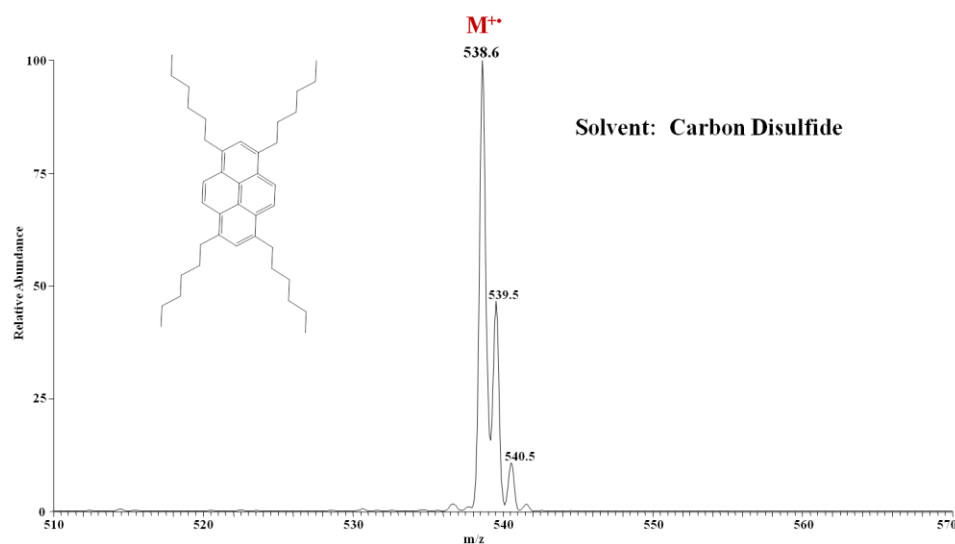


Figure 7.3 Mass spectrum of compound A when carbon disulfide is the solvent/ionization reagent for APCI. Stable molecular ion is the only type of ion produced (the additional peaks at m/z 539.5 and 540.5 are due to C¹³ isotopes).

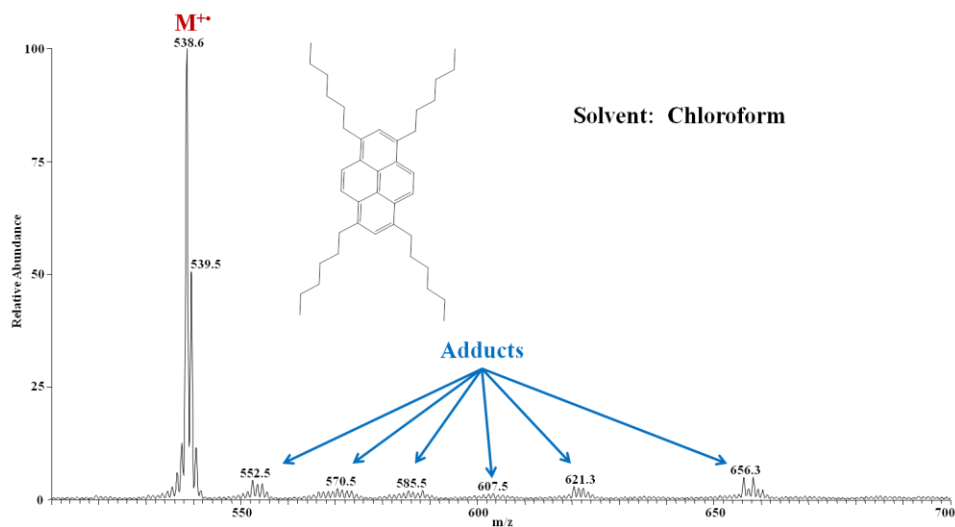


Figure 7.4 Mass spectrum of compound A when chloroform was the solvent/ionization reagent during APCI. Stable molecular ion along with many adduct ions formed from chloroform were detected (indicated with blue arrows).

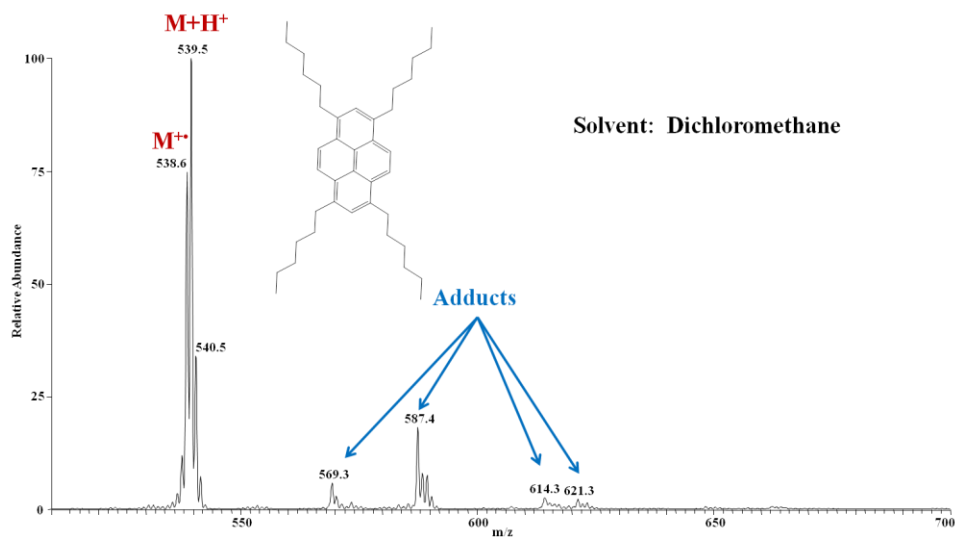


Figure 7.5 Mass spectrum of compound A when dichloromethane was used as the solvent/ionization reagent during APCI. Stable molecular ion, protonated molecule, and many additional adduct ions formed from dichloromethane during APCI (indicated with blue arrows) were formed.

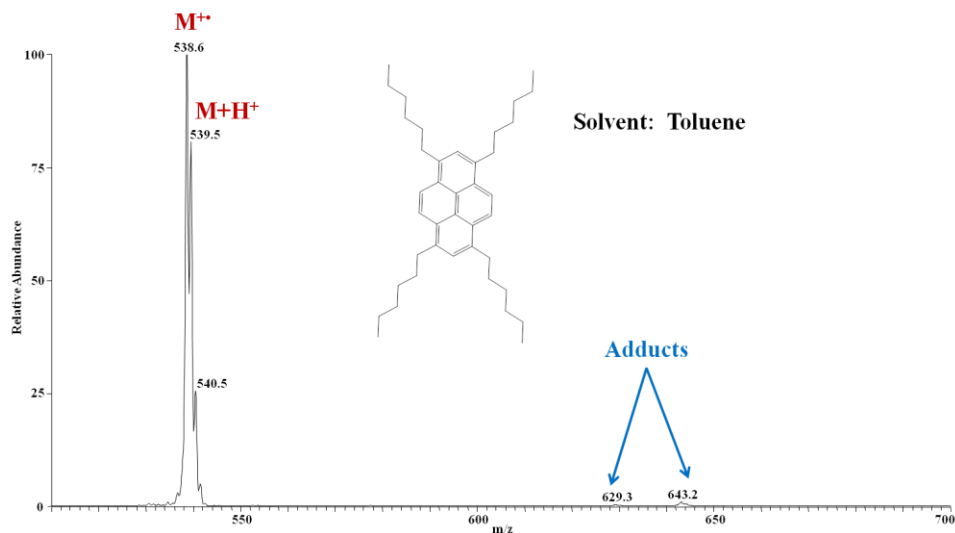


Figure 7.6 Mass spectrum of compound A when toluene was used as the solvent/ionization reagent during APCI. Stable molecular ion, protonated molecule, and two additional adduct ions (indicated by blue arrows) were formed.

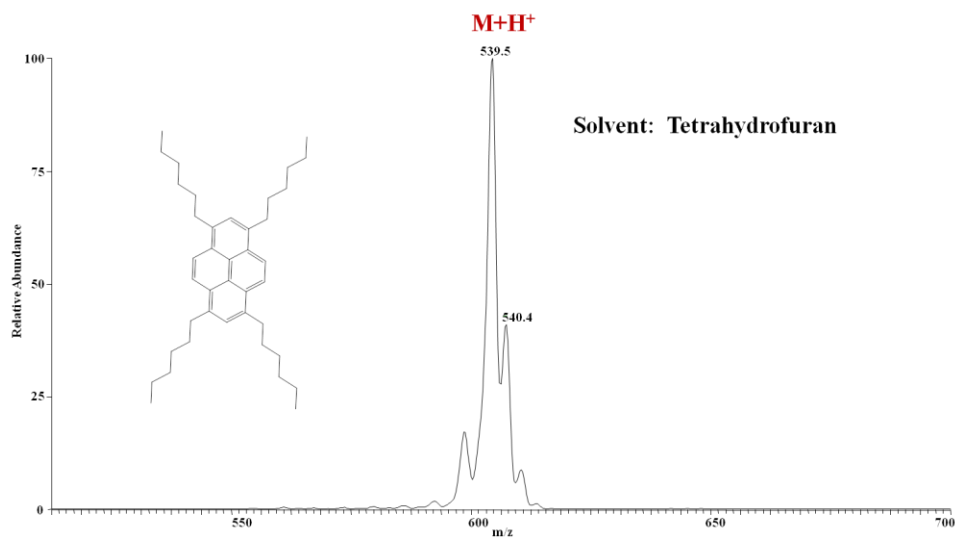


Figure 7.7 Mass spectrum of compound A when tetrahydrofuran was used as the solvent/ionization reagent during APCI. Stable protonated molecule is the only type of ion produced (the additional peak at m/z 540.4 is due to C^{13} isotopes).

Using the mass spectrum collected by using APCI with CS₂ as the solvent/ionization reagent (Figure 7.3) as a reference for the "ideal" spectrum (only one ion produced per molecule), the viability of each solvent for APCI of asphaltenes can be easily determined. For chloroform as the solvent (Figure 7.4), A forms abundant molecular ion but also a variety of adduct ions. The formation of adduct ions is undesirable for the analysis of asphaltenes due to further convolution of an already complex mixture. Adduct ions were also observed when DCM was used as the solvent (Figure 7.5), along with molecular ions and protonated molecules. Toluene as the solvent (Figure 7.6) produced minor adduct ions along with abundant molecular ion and protonated molecule. THF (Figure 7.7) was the only new solvent that did not produce any adduct ions but instead was found to produce solely protonated molecules for all model compounds (with the exception of compound B that was found to produce only molecular ions).

CAD of the adduct ions observed for the model compounds was then conducted to learn how they fragment. Figure 7.8 shows the CAD mass spectra for three of the adduct ions produced from compound A when using chloroform, ions of m/z of 607.5 (top left), 621.3 (top right), and 656.3 (bottom). All the adduct ions displayed fragment ions that can be attributed to the solvent, with the loss of HCl being evident for all three adduct ions. The same was found to be true for DCM (Figure 7.9). The adducts that formed with toluene were able to be attributed to toluene as shown in Figure 7.10.

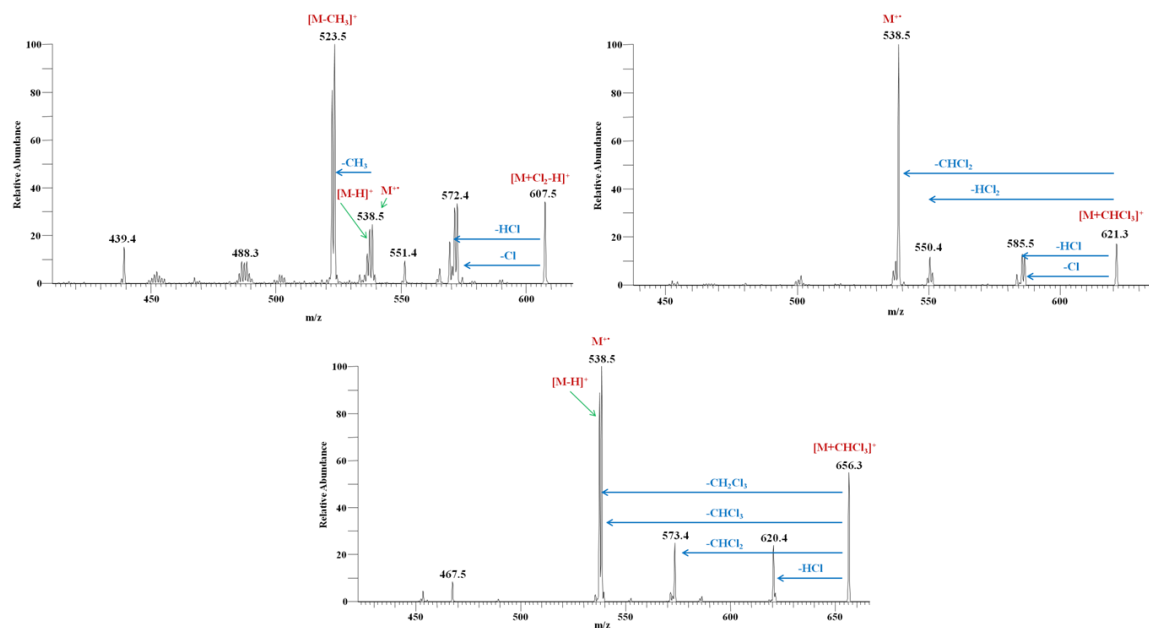


Figure 7.8 CAD mass spectra of three adduct ions formed upon APCI of A when chloroform was the solvent/ionization reagent.

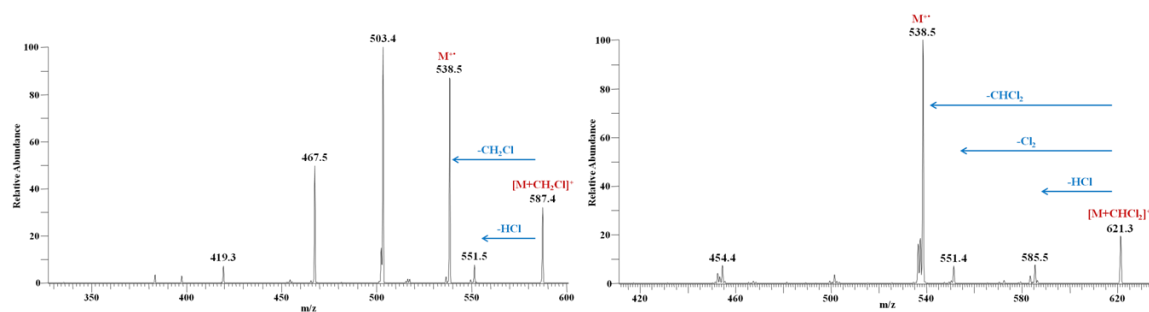


Figure 7.9 CAD mass spectra of two adduct ions formed upon APCI of A when DCM was the solvent/ionization reagent.

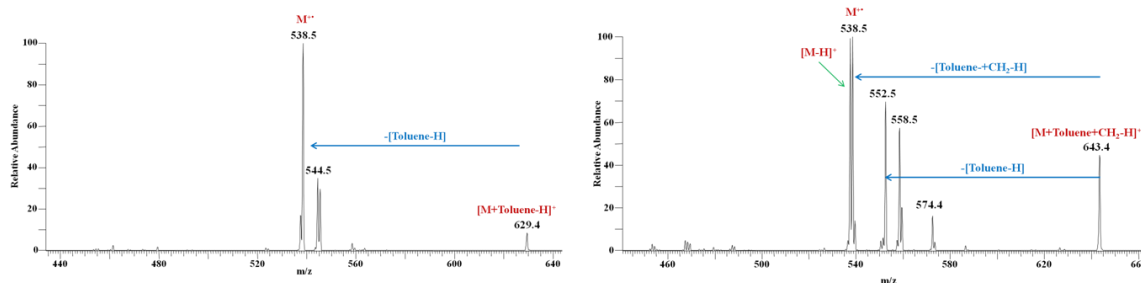


Figure 7.10 CAD mass spectra of two adduct ions formed upon APCI of A when toluene was the solvent/ionization reagent.

The fragmentation patterns of both the protonated model compounds and their molecular ions were also studied to determine whether the change from CS₂ to THF changes the CAD mass spectra produced for ions derived from asphaltenes. Some changes are likely since CS₂ produces molecular ions but THF protonated molecules. Figure 7.11 shows MS² - MS⁴ mass spectra for both the protonated molecules (left) and the molecular ions (right) for A. These CAD mass spectra show vastly different fragmentation patterns for protonated molecules and molecular ions. Hence, different fragmentation patterns are also expected when CAD mass spectra are measured for isolated protonated molecules and molecular ions derived from asphaltenes.

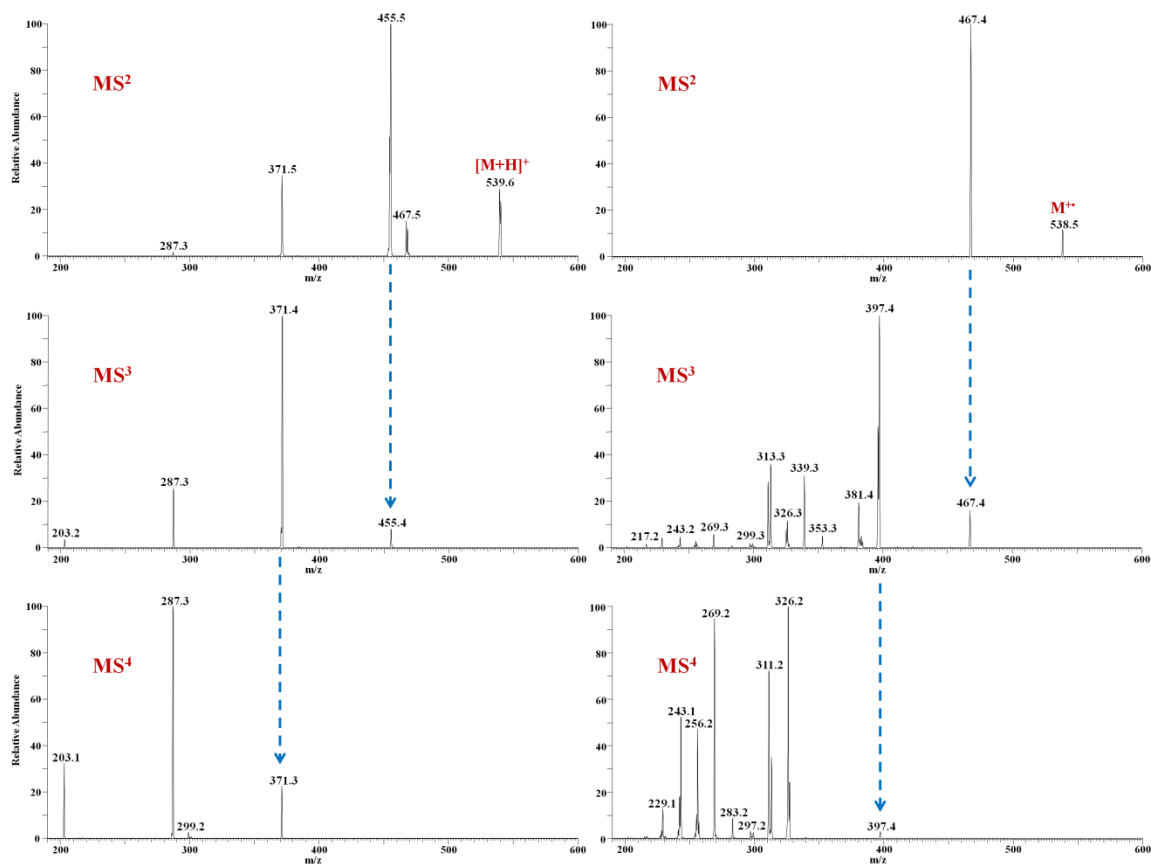


Figure 7.11 CAD mass spectra of the protonated molecules (left) and the molecular ions (right) formed upon APCI of A when toluene was the solvent/ionization reagent.

Each solvent was then used in conjunction with APCI to ionize an actual asphaltene sample. Figure 7.12 shows the molecular weight distribution (MWD) of the same asphaltene sample dissolved in each of the solvents of interest, along with CS₂ for comparison.

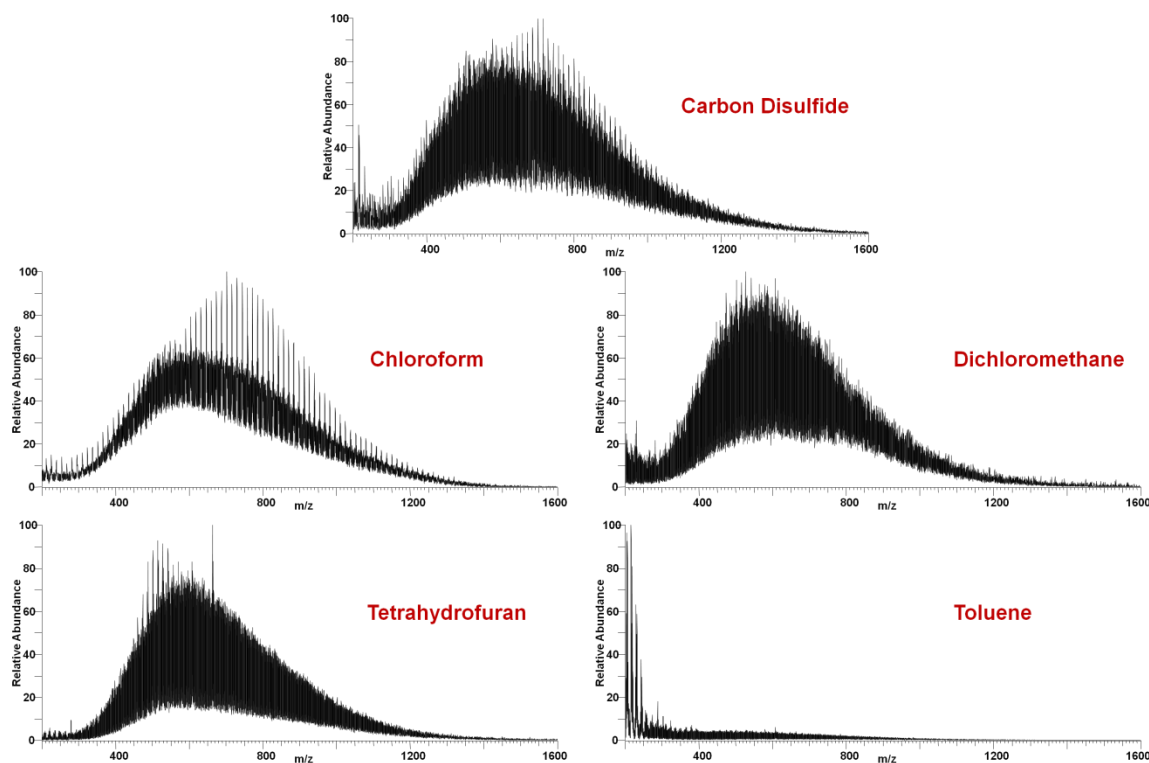


Figure 7.12 Mass spectra of the asphaltene sample dissolved in carbon disulfide (top), chloroform (middle left), dichloromethane (middle right), tetrahydrofuran (bottom left), and toluene (bottom right).

The mass spectra in Figure 7.12 show that all of the solvents, except toluene, have little effect on the MWD of the sample. The MWD ranges from about 300 Da to 1400 Da for CS₂, chloroform, DCM, and THF. Toluene, on the other hand, produces very abundant solvent related ions at low m/z-values that suppress the signal of the ions derived from asphaltenes at higher m/z values. CAD was then conducted on several isolated ions to determine whether adduct ions similar to those that were found for the model compounds would also be observed for asphaltenes. Figures 7.13 - 7.16 compare CAD mass spectra for ions of $m/z\ 600 \pm 1$ for the new solvents (red) and CS₂ (black).

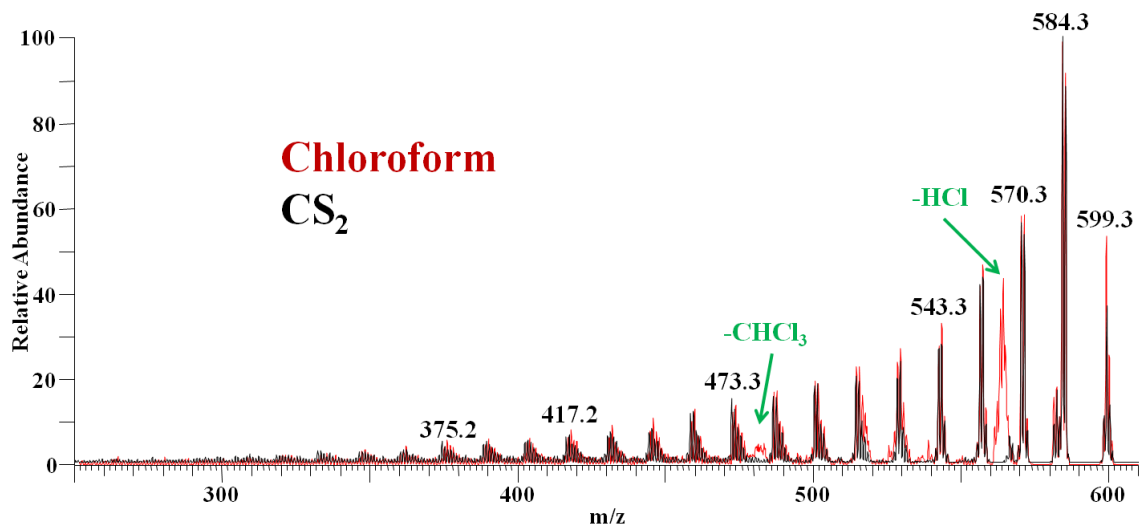


Figure 7.13 CAD mass spectrum collected for ions of m/z values of 600 ± 1 when chloroform was used as the solvent (red) overlaid with the CAD mass spectrum collected for the same ions when CS_2 was used as the solvent (black). Two new fragment ion clusters are observed in the CAD mass spectrum with chloroform as the solvent. These new fragment ions are due to adducts.

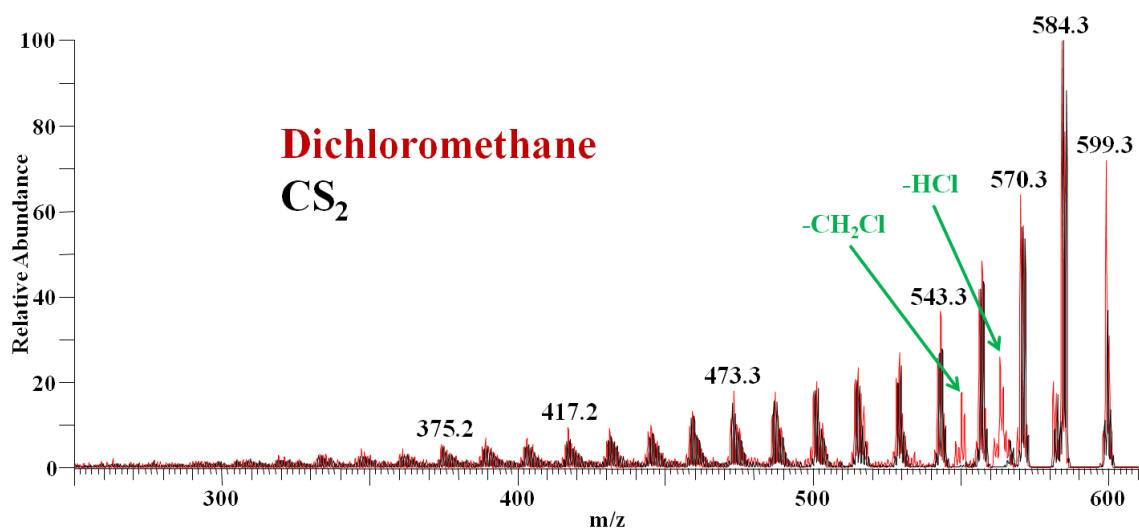


Figure 7.14 CAD mass spectrum collected for ions of m/z values of 600 ± 1 when DCM was used as the solvent (red) overlaid with the CAD mass spectrum collected for the same ions when CS_2 was used as the solvent (black). Two new fragment ion clusters are observed in the CAD spectrum with DCM as the solvent. These new fragment ions are due to adducts.

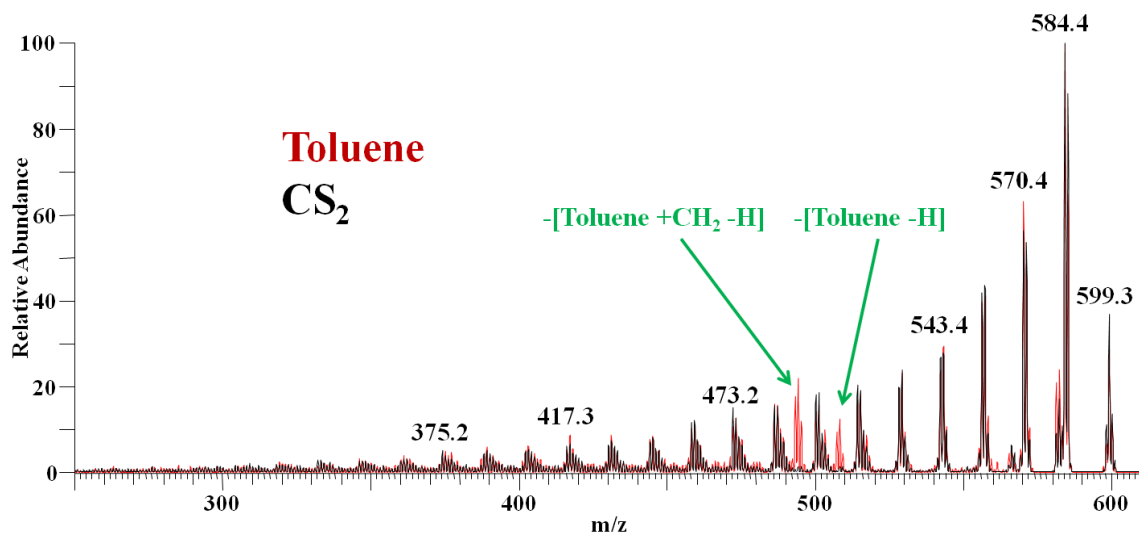


Figure 7.15 CAD mass spectrum collected for ions of m/z 600 ± 1 when toluene was used as the solvent (red) overlaid with the CAD mass spectrum collected for the same ions when CS_2 was used as the solvent (black). Two new fragment ion clusters are observed in the CAD spectrum with toluene as the solvent. These new fragment ions are due to adducts.

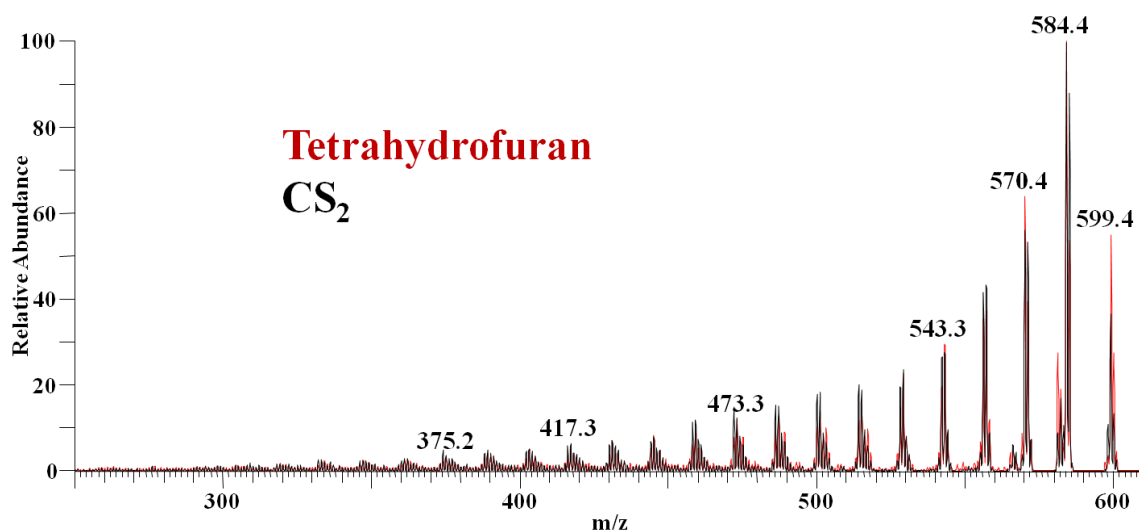


Figure 7.16 CAD mass spectrum collected for ions of m/z 600 ± 1 when THF was used as the solvent (red) overlaid with the CAD mass spectrum collected for the same ions when CS_2 was used as the solvent (black). No new fragment ion clusters are observed in the CAD spectrum with THF as the solvent.

A typical CAD mass spectrum of an asphaltene sample ionized using APCI with CS₂ as the solvent/ionization reagent (black CAD spectra in Figures 7.13 - 7.16) has several distinct features: some fragment ions are produced from water loss (-18 Da from parent ion), hydrogen sulfide loss (-34 Da from parent ion), and the loss of a methyl radical (-15 Da from parent ion) with many additional consecutive formal methylene losses (no methylenes are actually lost) that form a decay profile. In Figures 7.13 - 7.15, new fragment ions appear in the CAD mass spectra when the solvents chloroform, DCM, or toluene were used. These new fragment ions are a direct result of the adduct ions that are formed during APCI of asphaltene molecules, as observed with the model compounds. The new fragment ions that are produced with chloroform correspond to the losses of HCl and CHCl₃ from the parent ion. The fragment ions formed using DCM correspond to losses of HCl and CH₂Cl from the parent ion. Lastly, the fragment ions that were the result of fragmentation of toluene adduct ions correspond to losses of [toluene - H] and [toluene + CH₂ - H]. The fragment ions corresponding to the loss of HCl for chloroform and DCM overlap with the fragment ions formed from the loss of hydrogen sulfide. The relative abundances of the fragment ions produced from the loss of hydrogen sulfide may yield information regarding the sulfur content of the molecule, which cannot be determined with the overlapping peaks generated by solvent adduct ions. For the solvent THF, the CAD mass spectrum is almost identical to the mass spectrum collected CS₂ is the solvent (Figure 7.16). This result is surprising as it indicates that ionized asphaltenes fragment in a very similar fashion whether they are ionized to form molecular cations or protonated molecules. This is very interesting since the model

compounds analyzed here fragment very differently depending on whether they are radical cations or protonated molecules, as shown in Figure 7.11.¹²

7.4 Conclusions

In this study, mass spectrometry results obtained using APCI with chloroform, THF, DCM, and toluene as the solvent/ionization reagent were compared to those obtained using carbon disulfide for asphaltene model compounds and real asphaltenes. The purpose of these experiments was to find a solvent that is suitable for on-line HPLC separation of asphaltenes prior to mass spectrometric analysis in order to simplify the mixtures prior to analysis. Hence, the solvent has to be compatible with HPLC (i.e., does not degrade or damage the columns) and with APCI (i.e., produce only one ion per compound). Three of the four solvents studied, toluene, chloroform, and DCM, produced several different ions for the asphaltene model compounds upon APCI. This will convolute the CAD mass spectra measured for asphaltenes by producing new solvent dependent/related fragment ions. THF was found to only form one ion per model compound, the protonated molecule, except for one model compound **B** that was found to produce the molecular ion. The CAD mass spectra measured for isolated ions derived from the asphaltene sample ionized by APCI using THF as the solvent/ionization reagent were almost identical to the mass spectra obtained using CS₂. These results suggest that THF is a suitable, HPLC compatible, replacement for CS₂ when analyzing asphaltenes using APCI.

7.5 References

1. Ancheyta, J.; Betancourt, G.; Centeno, G.; Marroquin, G.; Alonso, F.; Garciafigueroa, E., Catalyst Deactivation During Hydroprocessing of Maya Heavy Crude Oil 1. Evaluation at Constant Operating Conditions. *Energy Fuels* **2002**, 16, 1438-1443.
2. Ancheyta, J.; Betancourt, G.; Marroquín, G.; Centeno, G.; Castañeda, L.; Alonso, F.; Muñoz, J. A.; Gómez, M.; Rayo, P., Hydroprocessing of Maya Heavy Crude Oil in Two Reaction Stages. *Appl. Catal. A-Gen.* **2002**, 233, 159-170.
3. Ancheyta-Juárez, J.; Betancourt-Rivera, G.; Marroquín-Sánchez, G.; Pérez-Arellano, A. M.; Maity, S.; Cortez, M.; del Río-Soto, R., An Exploratory Study for Obtaining Synthetic Crudes from Heavy Crude Oils via Hydrotreating. *Energy Fuels* **2001**, 15, 120-127.
4. Buenrostro-Gonzalez, E.; Groenzin, H.; Lira-Galeana, C.; Mullins, O., The Overriding Chemical Principles that Define Asphaltenes. *Energy Fuels* **2001**, 12, 972-978.
5. Mullins, O.; Sheu, E., *Structure and Dynamics of Asphaltenes*. Plenum Press: New York, 1998.
6. Mullins, O.; Sheu, E.; Hammami, A.; Marshall, A., *Asphaltenes, Heavy Oils, and Petroleomics*. Springer: New York, 2007.
7. Nogueira, J., Refining and Separation of Crude Tall-Oil Components. *Sep. Sci. Technol.* **1996**, 31, 2307-2316.
8. Potts, M. F. Crude Oil Fractionation Method. US Patent 3,320,158, 11/6/1964, 1967.
9. Trejo, F.; Centeno, G.; Ancheyta, J., Precipitation, Fractionation and Characterization of Asphaltenes from Heavy and Light Crude Oils. *Fuel* **2004**, 83, 2169-2175.
10. Yen, T.; Chilingarian, G., *Asphaltenes and Asphalts*. Elsevier: Amsterdam, 1994.
11. Idris, M.; Okoro, L., A Review on the Effects of Asphaltenes on Petroleum Processing. *Eur. Chem. Bull.* **2013**, 2, 393-396.
12. Borton, D.; Pinkston, D.; Hurt, M.; Tan, X.; Azyat, K.; Scherer, A.; Tykwinski, R.; Gray, M.; Qian, K.; Kenttämä, H., Molecular Structures of Asphaltenes Based on the Dissociation Reactions of Their Ions in Mass Spectrometry. *Energy Fuels* **2010**, 24, 5548-5559.

13. Mullins, O., The Modified Yen Model. *Energy Fuels* **2010**, 24, 2179-2207.
14. Sabbah, H.; Morrow, A.; Pomerantz, A.; Mullins, O.; Tan, X.; Gray, M.; Azyat, K.; Tykwinski, R.; Zare, R., Comparing Laser Desorption/Laser Ionization Mass Spectra of Asphaltenes and Model Compounds. *Energy Fuels* **2010**, 24, 3589-3594.
15. Sabbah, H.; Morrow, A.; Pomerantz, A.; Zare, R., Evidence for Island Structures as the Dominant Architecture of Asphaltenes. *Energy Fuels* **2011**, 25, 1597-1604.
16. Hortal, A.; Hurtado, P.; Martínez-Haya, B.; Mullins, O., Molecular-Weight Distributions of Coal and Petroleum Asphaltenes from Laser Desorption/Ionization Experiments. *Energy Fuels* **2007**, 21, 2863-2868.
17. Alshareef, A.; Scherer, A.; Tan, X.; Azyat, K.; Stryker, J.; Tykwinski, R.; Gray, M., Formation of Archipelago Structures During Thermal Cracking Implicates a Chemical Mechanism for the Formation of Petroleum Asphaltenes. *Energy Fuels* **2011**, 25, 2130-2136.
18. Andrews, A.; Edwards, J.; Pomerantz, A.; Mullins, O.; Nordlund, D.; Norinaga, K., Comparison of Coal-Derived and Petroleum Asphaltenes by ^{13}C Nuclear Magnetic Resonance, DEPT, and XRS. *Energy Fuels* **2011**, 25, 3068-3076.
19. Badre, S.; Goncalves, C.; Norinaga, K.; Gustavson, G.; Mullins, O., Molecular Size and Weight of Asphaltene and Asphaltene Solubility Fractions from Coals, Crude Oils and Bitumen. *Fuel* **2006**, 85, 1-11.
20. Groenzin, H.; Mullins, O., Molecular Size and Structure of Asphaltenes from Various Sources. *Energy Fuels* **2000**, 14, 677.
21. Morgan, T.; Alvarez-Rodriguez, P.; George, A.; Herod, A.; Kandiyoti, R., Characterization of Maya Crude Oil Maltenes and Asphaltenes in Terms of Structural Parameters Calculated from Nuclear Magnetic Resonance (NMR) Spectroscopy and Laser Desorption-Mass Spectroscopy (LD-MS). *Energy Fuels* **2010**, 24, 3977-3989.
22. Mullins, O.; Sabbah, H.; Eyssautier, J.; Pomerantz, A.; Barre, L.; Andrews, A.; Ruiz-Morales, Y.; Mostowfi, F.; McFarlane, R.; Goual, L.; Lepkowitz, R.; Cooper, T.; Orbulescu, J.; Leblanc, R.; Edwards, J.; Zare, R., Advances in Asphaltene Science and the Yen-Mullins Model. *Energy Fuels* **2012**, 26, 3986-4003.

23. Owen, B.; Gao, J.; Borton, D.; Amundson, L.; Archibold, E.; Tan, X.; Azyat, K.; Tykwinski, R.; Gray, M.; Kenttämä, H., Carbon Disulfide Reagent Allows the Characterization of Nonpolar Analytes by Atmospheric Pressure Chemical Ionization Mass Spectrometry. *Rapid Commun. Mass Spectrom.* **2011**, *25*, 1924-1928.
24. Klein, G.; Kim, S.; Rodgers, R.; Marshall, A.; Yen, A., Mass Spectral Analysis of Asphaltene. II. Detailed Compositional Comparison of Asphaltene Deposit to its Crude Oil Counterpart for Two Geographically Different Crude Oils by ESI FT-ICR MS. *Energy Fuels* **2006**, *20*, 1973-1979.
25. Shi, Q.; Hou, D.; Chung, K.; Zhao, S.; Zhang, Y., Characterization of Heteroatom Compounds in a Crude Oil and Its Saturates, Aromatics, Resins, and Asphaltenes (SARA) and Non-basic Nitrogen Fractions Analyzed by Negative-Ion Electrospray Ionization Fourier Transform Ion Cyclotron Resonance Mass Spectrometry *Energy Fuels* **2009**, *24*, 2545-2553.
26. Loegel, T.; Danielson, N.; Borton, D.; Hurt, M.; Kenttämä, H., Separation of Asphaltenes by Reversed-Phase Liquid Chromatography with Fraction Characterization. *Energy Fuels* **2012**, *26*, 2850-2857.
27. Hunter, E.; Lias, S., Evaluated Gas Phase Basicities and Proton Affinities of Molecules: An Update. *J. Phys. Chem.* **1998**, *27*, 413-656.
28. Xiao, J.; Meyererhoff, J., High-Performance Liquid Chromatography of C₆₀, C₇₀, and Higher Fullerenes on Tetraphenylporphyrin-Silica Stationary Phases Using Strong Mobile Phase Solvents *J. Chromatogr. A* **1995**, *715*, 19-29.
29. Xiao, J.; Savina, M.; Martin, G.; Francis, A.; Meyerhoff, M., Efficient HPLC Purification of Endohedral Metallofullerenes on a Porphyrin-Silica Stationary Phase. *J. Am. Chem. Soc.* **1994**, *116*, 9341-9342.
30. Al-Muhareb, E.; Morgan, T.; Herod, A.; Kandiyoti, R., Characterization of Petroleum Asphaltenes by Size Exclusion Chromatography, UV-Fluorescence and Mass Spectrometry. *Petrol. Sci. Technol.* **2007**, *25*, 81-91.
31. Dettman, H.; Inman, A.; Salmon, S., Chemical Characterization of GPC Fractions of Athabasca Bitumen Asphaltenes Isolated Before and After Thermal Treatment. *Energy Fuel* **2005**, *19*, 1399-1404.
32. Kempe, M., Antibody-Mimicking Polymers as Chiral Stationary Phases in HPLC. *Anal. Chem.* **1996**, *68*, 1948-1953.
33. Becart, I.; Chevalier, C.; Biesse, J., Quantitative Analysis of Phospholipids by HPLC with a Light Scattering Evaporating Detector – Application to Raw Materials for Cosmetic Use. *J. High Res. Chromatog.* **13**, *13*, 126-129.

34. Rogel, E.; Ovalles, C.; Moir, M., Determination of Asphaltenes in Crude Oil and Petroleum Products by the on Column Precipitation Method. *Energy Fuel* **2009**, 23, 4515-4521.
35. Christy, A.; Hopland, A.; Barth, T.; Kvalheim, O., Quantitative Determination of Thermal Maturity in Sedimentary Organic Matter by Diffuse Reflectance Infrared Spectroscopy of Asphaltenes. *Org. Geochem.* **1989**, 14, 77-81.
36. Christy, A.; Dahl, B.; Kvalheim, O., Structural Features of Resins, Asphaltenes and Kerogen Studied by Diffuse Reflectance Infrared Spectroscopy. *Fuel* **1989**, 68, 430-435.
37. Ôi, N.; Kitahara, H., Enantiomer Separation by HPLC with Some Urea Derivatives of L-Valine as Novel Chiral Stationary Phases. *J. Liq. Chromatogr.* **1986**, 9, 511-517.
38. Dark, W.; McFadden, W.; Bradford, D., Fractionation of Coal Liquids by HPLC with Structural Characterization by LC-MS. *J. Chromatogr. Sci.* **1977**, 15, 454-460.
39. Liu, Y.; Sheu, E.; Chen, S.; Storm, D., Fractal Structure of Asphaltenes in Toluene. *Fuel* **1995**, 74, 1352-1356.
40. Freer, E.; Radke, C., Relaxation of Asphaltenes at the Toluene/Water Interface: Diffusion Exchange and Surface Rearrangement. *J. Adhesion* **2004**, 80, 481-496.
41. Storm, D.; Sheu, E.; DeTar, M.; Barresi, R., A Comparison of the Macrostructure of Ratawi Asphaltenes in Toluene and Vacuum Residue. *Energy Fuel* **1994**, 8, 567-569.
42. Meier, M.; Selegue, J., Efficient Preparative Separation of C₆₀ and C₇₀. Gel Permeation Chromatography of Fullerenes Using 100% Toluene as Mobile Phase. *J. Org. Chem.* **1992**, 57, 1924-1926.
43. Gügel, A.; Müllen, K., Separation of C₆₀ and C₇₀ on Polystyrene Gel with Toluene as Mobile Phase. *J. Chromatogr. A* **1993**, 628, 23-29.
44. Acevedo, S.; Méndez, B.; Rojas, A.; Layrisse, I.; Rivas, H., Asphaltenes and Resins from the Orinoco Basin. *Fuel* **1985**, 64, 1741-1747.
45. León, O.; Rogel, E.; Espidel, J.; Torres, G., Asphaltenes: Structural Characterization, Self-Association, and Stability Behavior. *Energy Fuel* **2000**, 14, 6-10.

46. Schwager, I.; Lee, W.; Yen, T., Molecular Weight and Association of Coal-Derived Asphaltenes. *Anal. Chem.* **1977**, 49, 2363-2365.
47. Ikegami, T.; Hara, T.; Kimura, H.; Kobayashi, H.; Hosoya, K.; Cabrera, K.; Tanaka, N., Two-Dimensional Reversed-Phase Liquid Chromatography Using Two Monolithic Silica C18 Columns and Different Mobile Phase Modifiers in the Two Dimensions. *J. Chromatogr. A* **2006**, 1106, 112-117.
48. Ertürk, S.; Aktaş, E.; Ersoy, L.; Fıçıcıoğlu, S., An HPLC Method for the Determination of Atorvastatin and its Impurities in Bulk Drug and Tablets. *J. Pharmaceut. Biomed.* **2003**, 33, 1017-1023.

CHAPTER 8: DEVELOPMENT OF A HIGH-THROUGHPUT LASER-INDUCED ACOUSTIC DESORPTION PROBE WITH RASTER SAMPLING COUPLED TO ATMOSPHERIC PRESSURE CHEMICAL IONIZATION

8.1 Introduction

The analysis of thermally labile and nonvolatile analytes by mass spectrometry has long been a struggle but the development of soft ionization techniques such as matrix assisted acoustic desorption (MALDI) and electrospray ionization (ESI) have gone a long way in improving the analysis of those molecules.¹⁻⁵ On the other hand, both MALDI and ESI preferentially ionize the most polar molecules with easily ionizable functional groups and are unable to ionize nonpolar compounds, such as hydrocarbons.^{6,7} Laser-induced acoustic desorption (LIAD) was then developed for the evaporation of thermally labile and nonvolatile analytes that could then be ionized using any ionization method. LIAD involves firing a pulsed laser at the backside of a thin foil to generate acoustic waves that propagate through the foil and evaporate the intact neutral analyte molecules from the front side of the foil.⁸⁻¹¹ To date, much of the research utilizing LIAD was performed using high vacuum instruments such as Fourier-transform ion cyclotron resonance (FT-ICR) mass spectrometers capable of electron ionization (EI) and chemical ionization (CI).¹²⁻¹⁶ LIAD coupled with these ionization methods inside of an FT-ICR has been shown to facilitate mass spectrometric analysis of biomolecules, such as peptides, and various petroleum samples, ranging from saturated hydrocarbons to

asphaltenes.¹⁵⁻¹⁸ The increasing popularity of atmospheric pressure ionization techniques has led to the coupling of LIAD to ESI and atmospheric pressure chemical ionization (APCI).^{7,19,20} Careful considerations are required when choosing what ionization method to couple with LIAD. If the ionization method has an inherent bias, such as ESI, the method will suffer from that same bias and will be unable to analyze nonpolar compounds. LIAD/APCI has been successfully used to analyze both polar and nonpolar hydrocarbons.^{7,20} Nevertheless, LIAD/APCI does have its limitations, such as being able to only sample a small fraction of the analyte molecules deposited on the surface of the LIAD foil, and the inability to efficiently desorb large thermally labile molecules, such as asphaltenes.

Work conducted using a high-power LIAD probe that was developed for high-vacuum experiments demonstrated that higher laser power densities produce stronger acoustic waves that can desorb larger analytes.^{21,22} The same high-power LIAD probe was used in the initial LIAD/APCI experiments.^{7,22} While high-power LIAD/APCI allowed for the analysis of larger compounds compared to fiber LIAD, the shot to shot reproducibility was poor, especially for asphaltene samples. It is believed that the long laser beam path was a major factor leading to the poor reproducibility. The long beam path results in beam divergence causing a large loss in laser power density between the laser exit slit and the back of the foil. Non-optimal alignment of the mirrors inside the probe also resulted in laser power density to be lost. Further, the alignment of the inner mirrors is quite time consuming due to the inability to make fine adjustments, and the alignment easily drifts as a result of vibrations. Another major weakness of the conventional LIAD probe, described in section 2.6.4, is that only about 26.5 mm² of a foil

with a total surface area of 227 mm² can be irradiated by the laser (Figure 2.16). Thus, only around twelve percent of the total sample deposited on the foil is utilized. In an effort to eliminate these problems, a new high-power LIAD probe capable of rastering the sample was developed.

8.2 Experimental

All experiments were performed using a Thermo Scientific LTQ linear quadrupole ion trap (LQIT) equipped with an APCI source and operated in the positive ion mode. The APCI source was operated at 300 °C, with a sheath gas flow rate of 40-50 (arbitrary units), and an auxiliary gas rate of 5 (arbitrary units). The instrument transfer capillary was kept at 275 °C. The ionization reagent for LIAD/APCI was either carbon disulfide directly infused into the source at 20 µl/min, or no solvent was used allowing the nitrogen nebulizer gas to serve as the chemical ionization reagent. The use of both carbon disulfide and nitrogen as ionization reagents produced molecular ions for all analyte molecules desorbed through LIAD

A Continuum Minilite Nd:YAG laser (model Continuum Minilite II, model ML 1) set to 532 nm wavelength with 12 mJ nominal power (at 532 nm) at a repetition rate of 10 Hz, 1 cm⁻¹ line width, < 3 mrad divergence, and beam diameter of 3 mm, was used to perform LIAD. Kinematically mounted high-power reflective mirrors were used to control the light beam path in the new LIAD setup.⁷ The sample was deposited onto the LIAD foil using the dry drop method, described previously.¹⁶

8.3 Novel High Throughput LIAD Probe

Many of the design limiting factors that played a role in the development of the initial LIAD probes for FT-ICR, such as desorbing the molecules on axis with the electron beam and the magnetic field, that required the inner mirror assembly are no longer an issue.^{22,23} This allowed the removal of the inner mirror assembly eliminating alignment and laser power densities issues associated with them. To further reduce the reproducibility problems and loss of laser power density that were present in the first LIAD/APCI setup on a LQIT,⁷ a new LIAD probe was designed with three telecentric lenses to focus and re-collimate then refocus the laser beam as it travels to the backside of the foil (laser spot on the back of the foils was around 0.3 mm in diameter). The focusing and recollimating of the laser beam minimizes beam divergence over the three foot beam path.

The probe was constructed of two identical brass tubes (295 mm long, 0.736" outer diameter, and 0.535"-40 threads) with three lens holders (0.5" long, 0.5" aperture inner diameter) one at each end and one in the center. The lens holders contained a telecentric lens (Plano-Convex Lens, 0.5" diameter, $f = 150.0$ mm, Ar-coated). One of the brass tubes acts as a spacer that is twice the focal length of the lenses resulting in the beam being focused via the first lens and recollimated by the second lens as shown in Figure 8.1. The third lens focuses the laser beam onto the backside of the foil. By changing the distance of the third lens from the foil the focusing volume at the foil can be manipulated. Each of the brass tubes had clearance holes drilled along their length to help facilitate cooling when the laser was fired. The minimization of heating inside of the brass tubes helps reduce the expansion of the metal lens holders and spacer tubes.

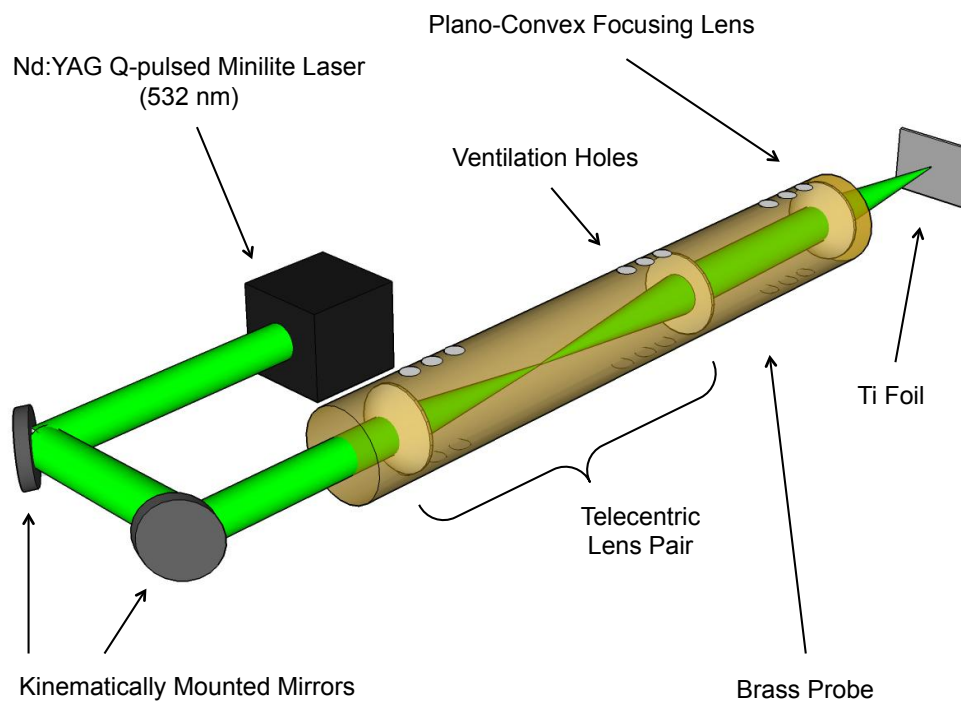


Figure 8.1 Depiction of the novel high-throughput LIAD probe. The lens holders that are threaded into the spacer tubes are not shown in this diagram (reproduced from Reference 23).

The probe shown in Figure 8.1 fits into an adapter built into the raster assembly that connects to the atmospheric ionization chamber on the front of the LQIT. The other end of the probe is held in place via a custom holder secured to a breadboard that sits on the table in front of the instrument. The probe has to be removed every time a new sample foil is introduced and can be done without moving the external kinematically mounted mirrors preventing the need for realignment of the laser between each sample. A photograph of the high throughput probe is provided in Figure 8.2.

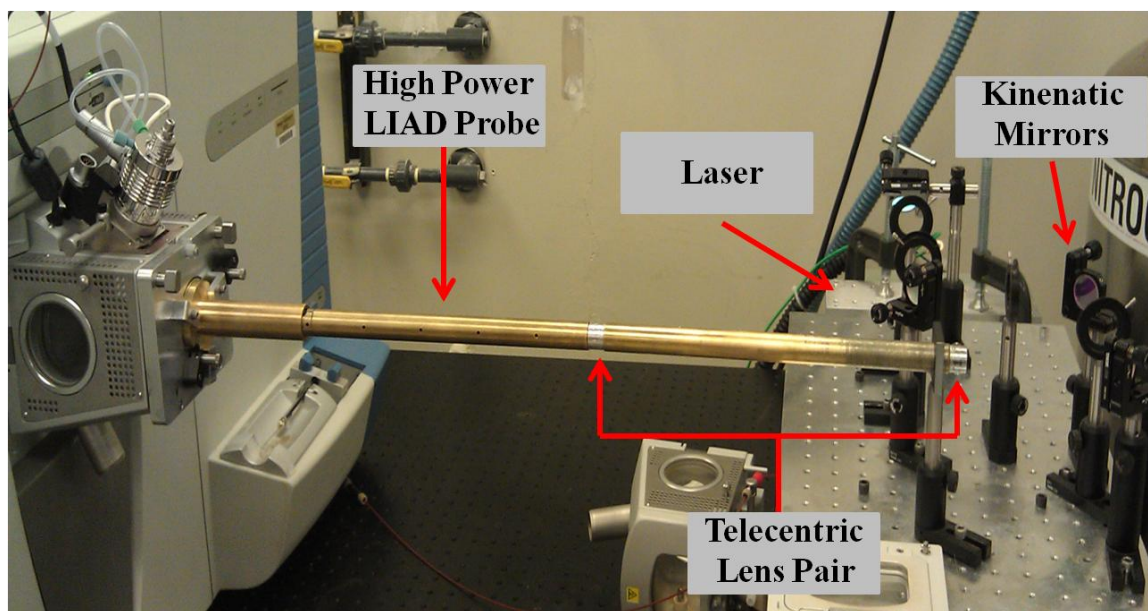


Figure 8.2 Image of the novel high-throughput LIAD probe. The probe is held by the raster assembly on the left and a custom holder on the right. The new probe can easily be removed to change sample without disturbing any of the kinematic mirrors shown on the right side of the image (picture reproduced from Reference 23).

8.3.1 New LIAD Probe Performance

The new high-throughput LIAD probe greatly increases the ease of laser beam alignment to the back of the foil when compared to the original setup.^{7,22} The telecentric lenses also greatly reduce the amount of power lost as the laser beam travels to the foil. The original LIAD setup suffered from about 75% loss in laser power by the time the beam hit the LIAD foil.²² The new probe containing the telecentric lenses was found to only lose 2% of the initial laser power. The reduction in the amount of power increased the maximum potential power density on the backside of the foil from 2000 MW/cm⁻² to 8200 MW/cm⁻². The power densities were measured using an Ophir power meter (model no. 7Z0287), placed either at the head of the laser or where the foil is placed.

The new probe was then evaluated by testing its ability to desorb asphaltenes the spectrum of which is shown in Figure 8.3. The asphaltene sample was dissolved in carbon disulfide at a concentration of roughly 1mg/mL and deposited on the titanium foil using the dry drop method, as described previously.¹⁶ The titanium foil was then placed into the raster assembly (described below) and the asphaltenes were desorbed using LIAD. The desorbed asphaltene molecules were ionized using APCI with nitrogen as the ionization reagent. The corona discharge ionizes the nitrogen to form N_2^{+*} which in turn abstracts an electron from an asphaltene molecule, forming a radical cation. The measured molecular weight distribution (MWD) of the asphaltenes was found to range from m/z 200 up to m/z 1050. These results are in good agreement with previous measurements using LIAD/EI (70 eV) as shown in Figure 8.3. The initial LIAD/APCI setup did not yield signals for asphaltenes⁷ but the higher power that is able to reach the foil using the new probe, better desorption of molecules such as asphaltenes can be achieved.

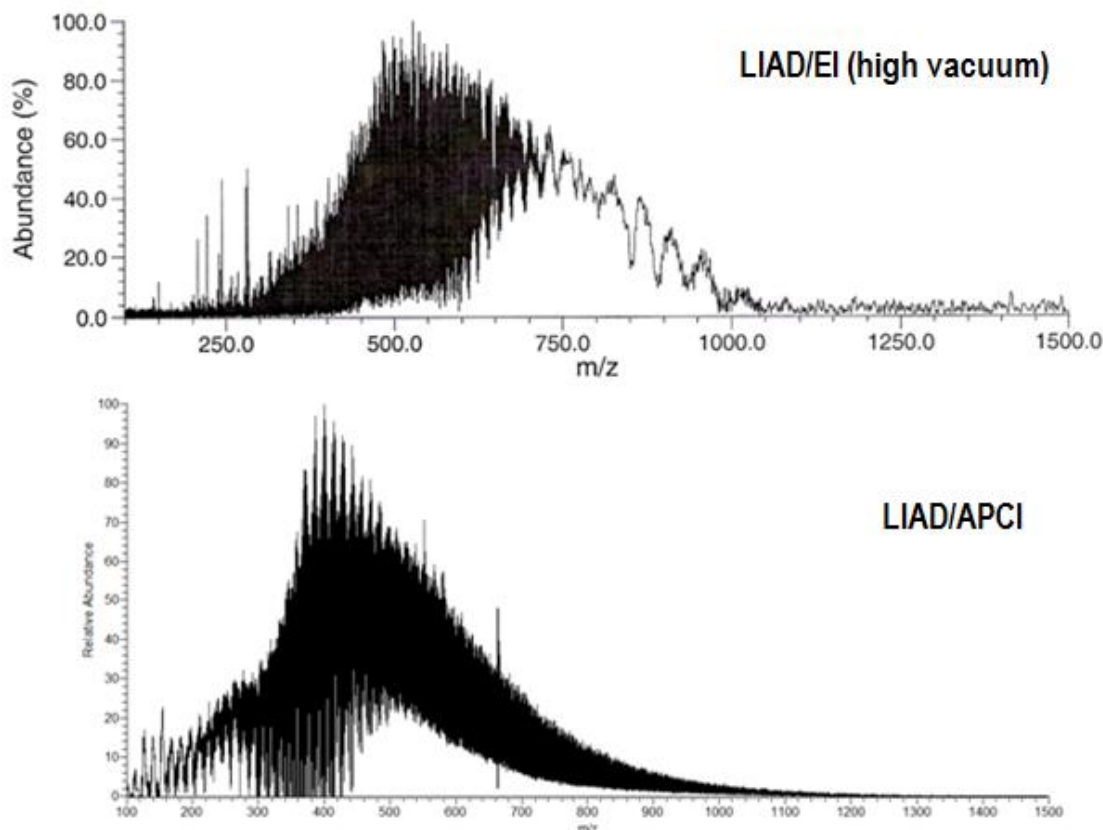


Figure 8.3 Mass spectrum of Khafji asphaltenes measured using high vacuum LIAD/EI (70 eV) in a 3T FT-ICR (top) and a mass spectrum of the same asphaltene sample ionized via LIAD/APCI using nitrogen as the chemical ionization reagent in a LQIT. The MWDs measured using both methods are in good agreement with one another (reproduced from Reference 23).

8.4 Novel High-Throughput LIAD Raster Assembly

In order to utilize more than twelve percent of the analyte deposited onto the LIAD foil when using the traditional LIAD probe, a rastering assembly was built. For the assembly to be successful, it needed to allow for the movement of the foil in the x- and y-directions with a fixed laser beam path to be able to sample a significant portion of the surface and allow the new high-throughput probe to be maneuvered in the z-direction to change the focal volume and power density of the laser beam at the backside of the

LIAD foil. The setup also needs to allow for easy addition and removal of LIAD foils that will not disturb the optics to prevent the need to realign the laser between each sample.

The raster LIAD assembly bolts to the front of the ionization chamber of the Thermo Scientific LQIT after removal of the original front access door, as shown in Figure 8.4. The same bolts (#4/40) and 90° lock pins that attached the original door also attach the assembly. The assembly contains an adjustable brass holder (inner diameter 0.74", outer diameter 1.03") to hold the final 3.75" tip of the probe for the high throughput in place. The adjustments allow optimization of the probe time in the x- and y-directions to overlap the analyte plume produced during LIAD with the corona discharge needle for more efficient ionization. The holder also allows for movement of the probe in the z-direction to change the focal volume and power density of the laser beam at the backside of the foil. The LIAD foil is held in place via four screws with washers at each corner of the foil stage. The stage is attached to the assembly by two perpendicular threaded rods (1/32" thread) that allow movement of the stage in the x- and y-directions enabling a large portion of the foil to be sampled. The movement of the threaded rods is achieved by manually turning one of two knobs that connected to via a cable drives. One knob will move the stage in the y-direction (up and down) and the other knob controls movement in the x-direction (right and left). Detailed pictures of the rastering assembly are shown in Figure 8.5.

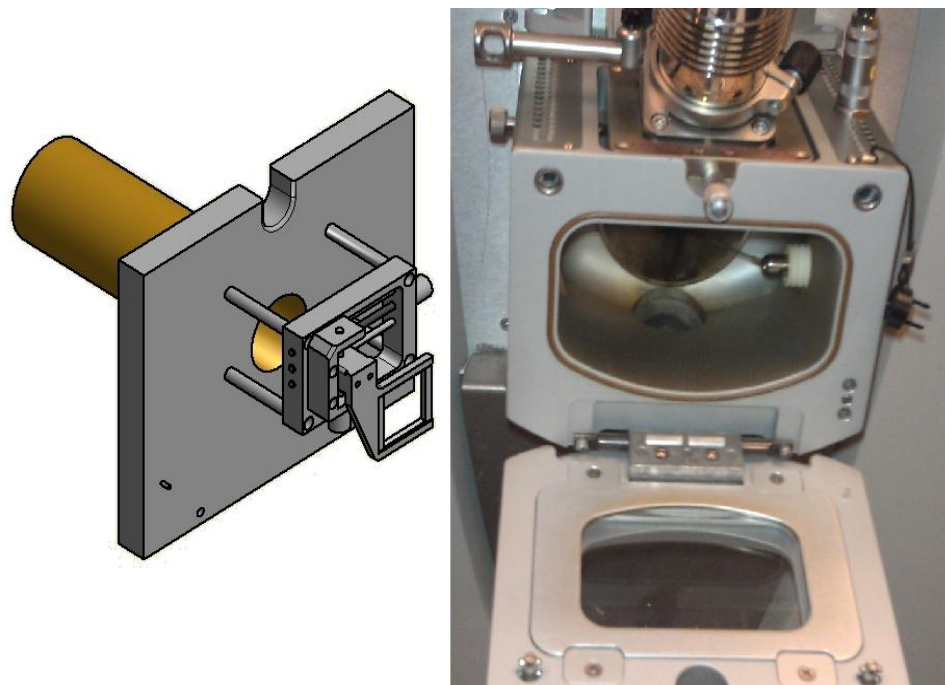


Figure 8.4 CAD drawing of the rastering assembly (left) and a photo of the Thermo Scientific LQIT ionization chamber with the front access door open (right). The rastering assembly replaces the front door while using the original hardware for attachment (reproduced from Reference 23).

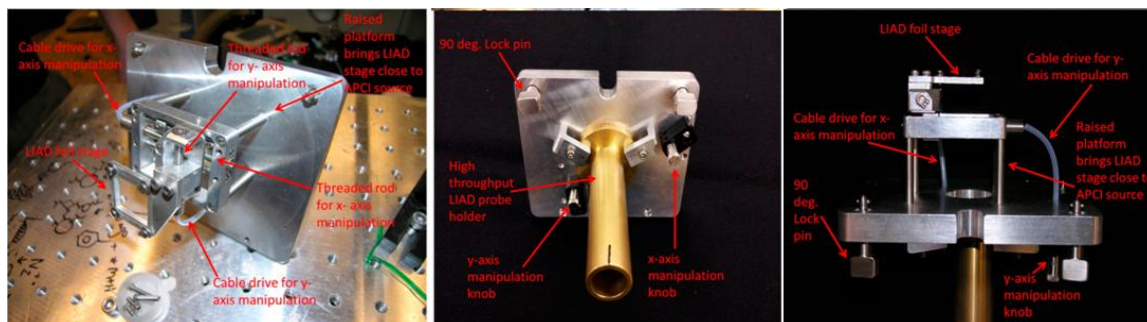


Figure 8.5 Images of the raster LIAD assembly (reproduced from Reference 23).

8.4.1 Performance

The new LIAD assembly that is able to raster significantly increases the area of the foil that can be irradiated compared to the traditional LIAD probe, as shown in Figure 8.6. Roughly about 133 mm² of the foil was sampled using the raster assembly compared to 26.5 mm² for the conventional setup. That indicates that five times more sample can be analyzed.

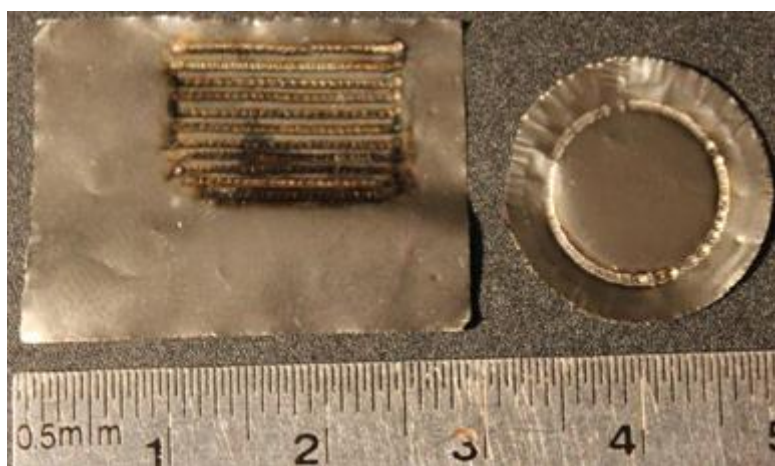


Figure 8.6 Image comparing a foil used in the raster LIAD assembly to a foil used in the conventional LIAD probe (reproduced from Reference 23).

The previous work conducted on the conventional LIAD/APCI found that a quarter of the sample (6.63 mm² of the foil) had to be evaporated using LIAD to produce an adequate signal-to-noise ratio.⁷ That meant that only four experiments could be conducted per foil. The raster assembly is able to sample roughly 133 mm² of the foil surface, but only half of that surface area can be used to allow a space in between the sampling rows on the back of the foil. Allowing for space in between sampling rows helps prevent overlap of consecutive shots as to maximum amount of analyte molecules

able to be desorbed with any given laser pulse. With that in mind, around ten experiments can now be conducted per foil, almost three times as many than the conventional setup. With the increased foil size and sampling area, multiple analytes can be placed on the foil in different areas (discussed in more detail in Chapter 9), further increasing the through-put of this method.

The use of the new raster assembly also helps improve sensitivity and reproducibility. The increased sampling surface area available allows prolonged LIAD experiments which increases the number of mass spectra that can be collected by the LQIT. That then can be averaged to reduce the affect of uneven sample on the surface of the foil or low sample concentration. The effects of being able to average a large number of mass spectra after an experiment using the raster LIAD assembly is shown in Figure 8.7. The top image in Figure 8.7 is a total ion chromatogram collected during a 3.75 minute raster LIAD experiment utilizing the entire available sampling surface area and resulting in the collection of about 920 mass spectra. The signal obtained in the first 30 seconds of the total ion chromatogram is a collection of background mass spectra to allow for background subtraction. The peaks in the chromatogram correspond to areas of the foil that contained a higher concentration of analyte and low intensity areas of the chromatogram correspond to sections of the foil that had lower concentrations of analyte. The dry drop method that was used to deposit the sample to the foil does not generally form a uniform sample layer onto the foil. A better sample deposition method was developed to solve this problem, as described in Chapter 9.

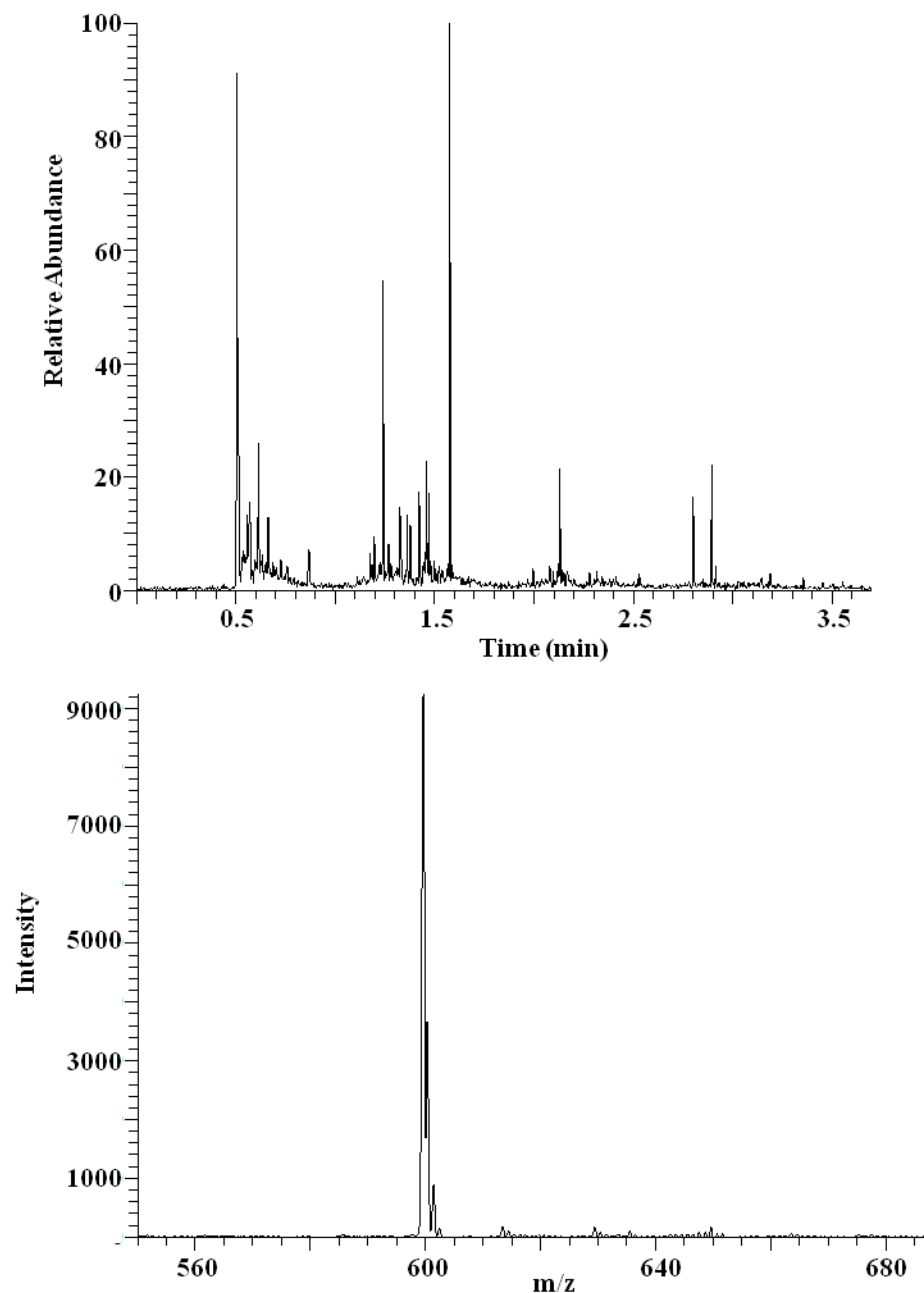


Figure 8.7 Total ion current as a function of time for a raster LIAD experiment (top). The mass spectrum, on bottom, was produced by averaging all of the ~922 mass spectra collected between $t = 0.50$ min to $t = 3.75$ min and subtracting the background ($t = 0$ min to $t = 0.50$ min). The desorbed octaethyl porphyrin molecules (MW = 600 Da) were ionized using APCI with carbon disulfide as the chemical ionization reagent (reproduced from Reference 23).

8.5 Conclusions

A new high-throughput LIAD probe using a telecentric lens pair along with a raster assembly was developed to improve the capabilities of LIAD/APCI. The new probe increases the laser power density that reaches the LIAD foil to 98% of the initial laser output from the 25% that was achieved using the conventional LIAD probe via the reduction of beam divergence.²² The increase in laser power at the LIAD foil allows for better desorption of heavy analytes, such as asphaltenes, that could not be analyzed using the previous method.⁷

The raster assembly was created so that a greater surface area of the LIAD foil can be sampled. The assembly can be easily attached to the ionization chamber of the Thermo Scientific LQIT by removing the front door. The rastering stage moves in the x-y plane by a person twisting one of two knobs attached to two perpendicular threaded rods. The knobs have since been replaced with electric motors under computer control to automate the system. The raster assembly was found to improve sensitivity and reproducibility by increasing the number of mass spectra that can be collected and averaged during the course of a LIAD experiment. More experiments can also be conducted per LIAD foil because of the dramatic increase in available sampling area using the raster setup (133 mm²) over the conventional setup (26.5 mm²).

8.6 References

1. Whitehouse, C.; Dreyer, R.; Yamashita, M.; Fenn, J., Electrospray Interface for Liquid Chromatographs and Mass Spectrometers. *Anal. Chem.* **1985**, *57*, 675-679.
2. Yamashita, M.; Fenn, J., Electrospray Ion Source. Another Variation on the Free Jet Theme. *J. Phys. Chem.* **1984**, *88*, 4451-4459.
3. Karas, M.; Bahr, U.; Gießmann, U., Matrix Assisted Laser Desorption Ionization Mass Spectrometry. *Mass Spectrom. Rev.* **1991**, *10*, 335-357.
4. Fenn, J.; Mann, M.; Meng, C.; Wong, S.; Whitehouse, C., Electrospray Ionization for Mass Spectrometry of Large Biomolecules. *Science* **1989**, *246*, 64-71.
5. Tanaka, K.; Waki, H.; Ido, Y.; Akita, S.; Yoshida, Y.; Yoshita, T., Protein and Polymer Analysis up to m/z 100,000 by Laser Ionization Time-Of-Flight Mass Spectrometry. *Rapid Commun. Mass Spectrom.* **1988**, *2*, 151-153.
6. Marshall, A.; Rogers, R., Petroleomics: The Next Grand Challenge for Chemical Analysis. *Acc. Chem. Res.* **2004**, *37*, 53-59.
7. Gao, J.; Borton, D.; Owen, B.; Jin, Z.; Hurt, M.; Amundson, L.; Madden, J.; Qian, K.; Kenttämäa, H., Laser-Induced Acoustic Desorption/Atmospheric Pressure Chemical Ionization Mass Spectrometry. *J. Am. Soc. Mass Spectrom.* **2011**, *22*, 531-538.
8. Golovlev, V.; Allman, S.; Garrett, W.; Taranenko, N.; Chen, C., Laser-Induced Acoustic Desorption. *Int. J. Mass Spectrom. Ion Process.* **1997**, *169-170*, 69-78.
9. Lindner, B., On the Desorption of Electrosprayed Organic Compounds from Supporting Metal Foils by Laser Induced Pressure Waves. *Int. J. Mass Spectrom. Ion Process.* **1991**, *103*, 203-218.
10. Pérez, J.; Petzold, C.; Watkins, M.; Vaughn, W.; Kenttämäa, H., Laser Desorption in Transmission Geometry Inside a Fourier-Transform Ion Cyclotron Resonance Mass Spectrometer. *J. Am. Soc. Mass Spectrom.* **1999**, *10*, 1105-1110.
11. Pérez, J.; Ramírez-Arizmendi, L.; Petzold, C.; Guler, L.; Nelson, E.; Kenttämäa, H., Laser-Induced Acoustic Desorption/Chemical Ionization in Fourier-Transform Ion Cyclotron Resonance Mass Spectrometry. *Int. J. Mass Spectrom.* **2000**, *198*, 173-188.
12. Campbell, J.; Crawford, K.; Kenttämäa, H., Analysis of Saturated Hydrocarbons by Using Chemical Ionization Combined with Laser-Induced Acoustic Desorption/Fourier Transform Ion Cyclotron Resonance Mass Spectrometry. *Anal. Chem.* **2004**, *76*, 959-963.

13. Crawford, K.; Campbell, J.; Fiddler, M.; Duan, P.; Qian, K.; Gorbaty, M.; Kenttämää, H., Laser-Induced Acoustic Desorption/Fourier Transform Ion Cyclotron Resonance Mass Spectrometry for Petroleum Distillate Analysis. *Anal. Chem.* **2005**, *77*, 7916-7923.
14. Duan, P.; Fu, M.; Pinkston, D.; Habicht, S.; Kenttämää, H., Gas-Phase Reactions of $\text{ClMn}(\text{H}_2\text{O})^+$ with Polar and Nonpolar Hydrocarbons in a Mass Spectrometer. *J. Am. Chem. Soc.* **2007**, *129*, 9266-9267.
15. Duan, P.; Qian, K.; Habicht, S.; Pinkston, D.; Fu, M.; Kenttämää, H., Analysis of Base Oil Fractions by $\text{ClMn}(\text{H}_2\text{O})^+$ Chemical Ionization Combined with Laser-Induced Acoustic Desorption/Fourier Transform Ion Cyclotron Resonance Mass Spectrometry. *Anal. Chem.* **2008**, *80*, 1847-1853.
16. Pinkston, D.; Duan, P.; Gallardo, V.; Habicht, S.; Tan, X.; Qian, K.; Gray, M.; Müllen, K.; Kenttämää, H., Analysis of Asphaltenes and Asphaltene Model Compounds by Laser-Induced Acoustic Desorption/Fourier Transform Ion Cyclotron Resonance Mass Spectrometry. *Energy Fuels* **2009**, *23*, 5564-5570.
17. Somuramasami, J.; Kenttämää, H., Evaluation of a Novel Approach for Peptide Sequencing: Laser-Induced Acoustic Desorption Combined with $\text{P}(\text{OCH}_3)^{2+}$ Chemical Ionization and Collision-Activated Dissociation in a Fourier Transform Ion Cyclotron Resonance Mass Spectrometer. *J. Am. Soc. Mass Spectrom.* **2007**, *18*, 525-540.
18. Petzold, C.; Ramirez-Arizmendi, L.; Heidbrink, J.; Perez, J.; Kenttämää, H., Gas-Phase Reactions of Charged Phenyl Radicals with Neutral Biomolecules Evaporated by Laser-Induced Acoustic Desorption. *J. Am. Soc. Mass Spectrom.* **2002**, *13*, 192-194.
19. Cheng, S.; Cheng, T.; Chang, H.; Shiea, J., Using Laser-Induced Acoustic Desorption/Electrospray Ionization Mass Spectrometry to Characterize Small Organic and Large Biological Compounds in the Solid State and in Solution Under Ambient Conditions. *Anal. Chem.* **2009**, *81*, 868-874.
20. Nyadong, L.; McKenna, A.; Hendrickson, C.; Rodgers, R.; Marshall, A., Atmospheric Pressure Laser-Induced Acoustic Desorption Chemical Ionization Fourier Transform Ion Cyclotron Resonance Mass Spectrometry for the Analysis of Complex Mixtures. *Anal. Chem.* **2011**, *83*, 1616-1623.

21. Shea, R.; Petzold, C.; Campbell, J.; Li, S.; Aaserud, D.; Kenttämää, H., Characterization of Laser-Induced Acoustic Desorption Coupled with a Fourier Transform Ion Cyclotron Resonance Mass Spectrometer. *Anal. Chem.* **2006**, *78*, 6133-6139.
22. Shea, R.; Habicht, S.; Vaughn, W.; Kenttämää, H., Design and Characterization of a High-Power Laser-Induced Acoustic Desorption Probe Coupled with a Fourier Transform Ion Cyclotron Resonance Mass Spectrometer. *Anal. Chem.* **2007**, *79*, 2688-2694.
23. Borton, D.; Amundson, L.; Hurt, M.; Dow, A.; Madden, J.; Simpson, G.; Kenttämää, H., Development of a High-Throughput Laser-Induced Acoustic Desorption Probe and Raster Sampling For Laser-Induced Acoustic Desorption/Atmospheric Pressure Chemical Ionization. *Anal. Chem.* **2013**, *85*, 5720-5726.

CHAPTER 9: DESIGN AND DEVELOPMENT OF A DRYING GAS CHAMBER FOR PREPARING LIAD FOILS

9.1 Introduction

As previously mentioned in Chapter 8, laser induced acoustic desorption (LIAD) is a technique for the evaporation of nonvolatile neutral molecules into the gas phase. It has proven useful for the mass spectrometric analysis of biomolecules and large hydrocarbons.¹⁻⁴ The ability to couple LIAD to almost any ionization technique has been shown to be beneficial for the mass spectrometric analysis of a variety of analytes.⁵⁻⁸ LIAD uses a pulsed laser beam focused onto the backside of a metal foil that contains a layer of the analyte on the front side.^{5-7,9} When the laser hits the backside of the foil acoustic waves are generated. They propagate through the foil and evaporate neutral analyte molecules from the front side that are then ionized.^{7,9} In these experiments, good reproducibility and large signal depend on the uniformity of the analyte layer on the foil.¹⁰

Previous sample deposition methods utilized for LIAD foil preparation were discussed in Chapter 2.6.3. Electrospray deposition can be used to create a rather uniform sample layer on the foil surface but is only effective for polar analytes.¹¹ The deposition of nonpolar analytes, such as petroleum samples, is normally performed using the dry drop method.² The downside to this method is that the analyte layer on the

surface of the foil is highly non-uniform, likely because the solvent moves towards the outside of the foil during sample deposition since the adhesion forces of the solvent to the foil are weaker than the cohesion forces between the solvent molecules. This migration of the solvent as it evaporates results in areas of high and low analyte concentration on the foil surface. In an effort to minimize this effect, the foil is softly spun to redistribute the analyte more evenly as the solvent is evaporating. This is a difficult process that requires much practice as spinning too fast will cause the sample to fall off of the foil and spinning too slowly will not effectively redistribute the analyte solution. The dry drop method cannot be used for thermally labile compounds because the foil is slightly heated to help facilitate evaporation of solvent.

Both electrospray deposition and dry drop methods were most effective with the circular LIAD foils for the original probes. The raster LIAD assembly discussed in Chapter 8 requires larger foils that are rectangular in shape. For these foils, the dry drop method produces layers of analyte molecules that are even less uniform and the foil is too large for the spray cone formed during electrospray deposition to cover entire foil. A chamber utilizing drying gas to facilitate evaporation of the solvent was developed for the rectangular foils to resolve the problems faced using the other sample deposition methods.

9.2 Design and Construction of the Drying Gas Chamber

The chamber that was made to address the problems of non-uniform sample deposition onto LIAD foils consists of four parts that are denoted A, B, C, and D. Part A is the base block shown in Figure 9.1 consisting of a milled piece of stainless steel that is

2.505" long x 1.495" wide x 1.455" tall. A rectangular region that is 1.314" long x 1.054" wide x 0.715" deep was removed from the center of A. In the bottom of the cavity formed from the removal of the rectangular block two addition wells were milled to collect solvent that may leak off the edges of the foil. The wells were 0.592" long x 0.273" wide x 0.681" deep and were separated by a 0.145" spacing centered along the length of A. The top surface of A also contains four threaded holes that are 1.000" deep for 6-32 bolts in each of the corners located 0.250" from both the long and short sides. Figure 9.2 gives all of the relevant dimensions are for A and all other components.

Part B holds the LIAD foil and was constructed of Teflon with dimensions 1.300" long and 1.000" wide and was designed to fit into the cavity of A. A centered 0.14" deep cavity was recessed into the top of B that is 1.008" long x 0.870" wide. Two 0.13" diameter clearance holes were drilled through the recessed region of B directly above the solvent collection wells in A. Both holes were placed 0.491" from the long side of the block and 0.385" from the short side of the block with 0.371" space between the holes, measurements were made from the center of the holes. After B is placed into A, a rectangular titanium foil can be inserted into the recessed cavity of B. The foil dimensions are 1.004" long x 0.841" wide x 12.7 μm thick. The same foil sheets as those used to make the conventional circular LIAD foils were used to make these foils.

Parts C1 and C2 are interchangeable forming mandrels made from stainless steel and are mushroom shaped when viewed from the side. The lower and upper sections of C1 and C2 have dimensions of 1.000" long x 0.850" wide and 1.299" long x 0.998" wide x 0.185" tall. A notch cut at a 90-degree angle transitions the upper and lower sections of C1. A rectangular shape cut out was removed from the center of C1 with dimensions

0.801" long x 0.661" wide. C1 is placed on top of B with the lower section of C1 fitting into the recessed cavity in B. C1 forms a seal between the foil edges and B, allowing the foil to be exposed in the cut out in the center of C1. The area of exposed foil is where the analyte is deposited after the chamber is fully assembled. C2 can be used instead of C1 to allow for two separate regions for sample deposition, so a foil can be produced with two different analytes on different section of the foil. C2 is identical to C1 except C2 has a 0.980" wide divider through its center, so that the two identical cutouts of 0.350" long x 0.661" wide are formed.

The last piece of the assembly is the lid, part D. D sits onto the top of A and is fastened to A with four 6-32 allen head bolts, each 1" in length. The bolts pass through clearance holes in D (0.250" from each edge) and thread into the tapped holes in A. A circular viton o-ring, 0.799" ID and 3/32" thick, sits in a 0.130" deep recessed circular channel centered on the lid both horizontally and vertically with an outer radius of 0.510" on the underside of D. The o-ring helps to compress C1/C2 into B as the lid is tightened down with the bolts, effectively sealing the edges of the titanium foil to prevent solvent from leaking off of the foil. A second viton o-ring, 19/16" ID and 3/32" thick, rests in a rectangular channel of the same depth but with dimensions of 1.740" long x 1.380" wide centered on the lid horizontally and vertically. In the center of D a clearance hole with a 0.380" was drilled.

When the bolts holding A and D together are fully tightened the large o-ring on the underside of D forms a seal between A and D to prevent excess leakage of drying gas from the chamber as solvent is evaporated off of the foil. A 19/22-19/38 rubber septum is then placed into the clearance hole in D with two 22-gauge needles are inserted into the

septum with one of the needles having a 90 degree bend in the shaft so that the tip will be parallel with the titanium foil once passed through the septum. The bent needle is then attached to a compressed gas cylinder of an inert dry gas, such as argon or nitrogen. The bend in the needle is required so the gas is not blowing directly onto the surface of the foil, which would blow away the sample in the area leaving a region of bare foil. The second needle was used as the exhaust allowing the drying gas to leave the chamber to prevent pressure build up.

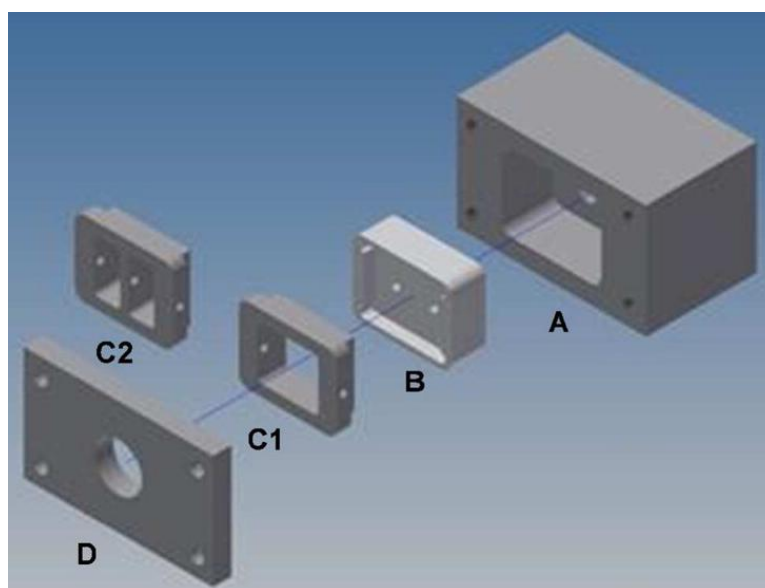


Figure 9.1 The parts of the LIAD foil sample preparation chamber. Each part is labeled for easy referencing in the description of the chamber above. **A** is the base and contains the primary cavity, **B** the foil holder, **C1/C2** are the forming mandrels, and **D** is the lid. **C1** and **C2** are interchangeable mandrels with **C1** allowing only one analyte to be deposited on the foil surface and **C2** allowing two analytes to be deposited on the foil surface (reproduced from Reference 10).

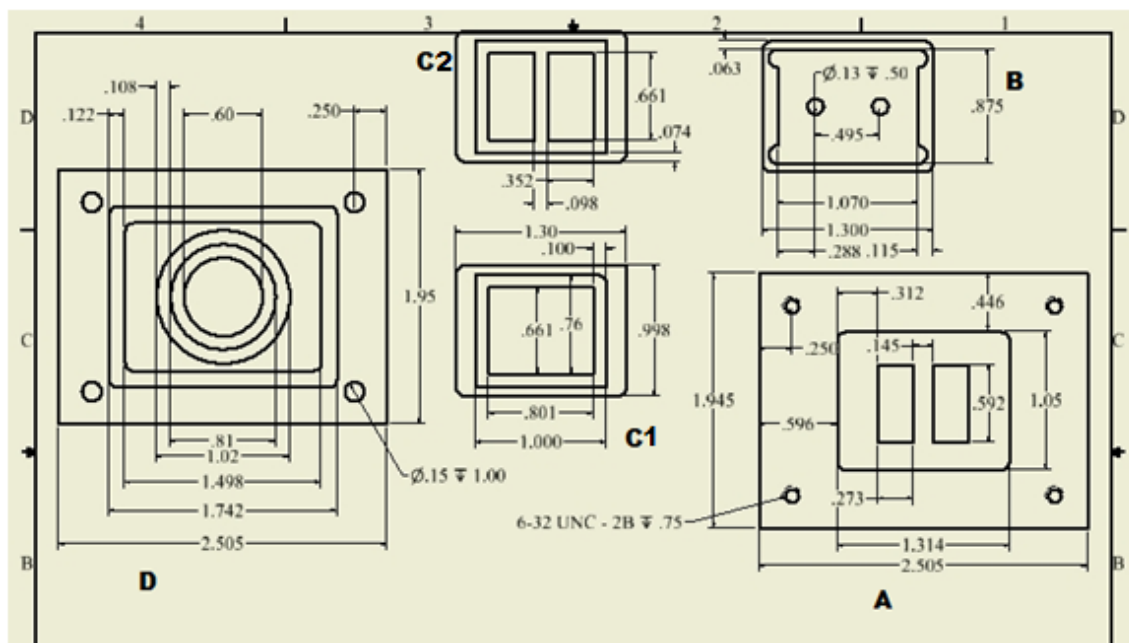


Figure 9.2 Computer aided design of the components of the LIAD foil drying gas chamber, dimensions given in inches (reproduced from Reference 10).

The sample is added after the chamber is fully assembled and the foil is inside but before the septum is inserted. The analyte solution is pipetted onto the surface of the foil until a thin layer of solvent covers the entire foil surface. The more volatile the solvent the faster the evaporation but solvents with low volatility, such as water, can also be used. The septum is then inserted while letting the drying gas flow at a low rate (just a few bubbles per second when the needle is inserted into water) over the sample. For very volatile solvents, such as carbon disulfide, 10 minutes is normally more than enough time to evaporate all of the solvent. Once the solvent has fully evaporated, the septum is removed to check the condition of the foil. If the sample concentration is too low, the previous steps are repeated until the desired concentration is achieved.

The sample layer on the surface of the foil is visually more uniform than when using the dry drop method as shown in Figure 9.3. The foils presented in Figure 9.3 had asphaltenes deposited on their surface. Asphaltenes are primarily made up of nonpolar hydrocarbons and hence cannot be deposited using electrospray. Figure 9.4 shows the total ion chromatogram from a LIAD rastering experiment using a foil that was prepared with the dry drop method (top) and a foil prepared using the drying gas chamber (bottom). The signal in the total ion chromatogram produced while a foil prepared using the drying gas chamber was rastered was much more stable, indicating that the sample layer was more uniform than that produced using the dry drop method. The drying chamber also simplifies the production of the regular foils needed for raster LIAD experiments. The forming mandrel C2 was found to successfully produce foils with two distinct sections of analyte as shown in Figure 9.5. The ability to analyze foils with two separate analytes on them will further help increase sample throughput for LIAD experiments.



Figure 9.3 Comparison of a LIAD foil with asphaltenes deposited on it by using the dry drop method (left) and a LIAD foil with asphaltenes deposited on it by using the drying gas chamber (right). A visual comparison of the two samples indicates that the sample is deposited much more uniformly using the drying gas chamber (reproduced from Reference 10).

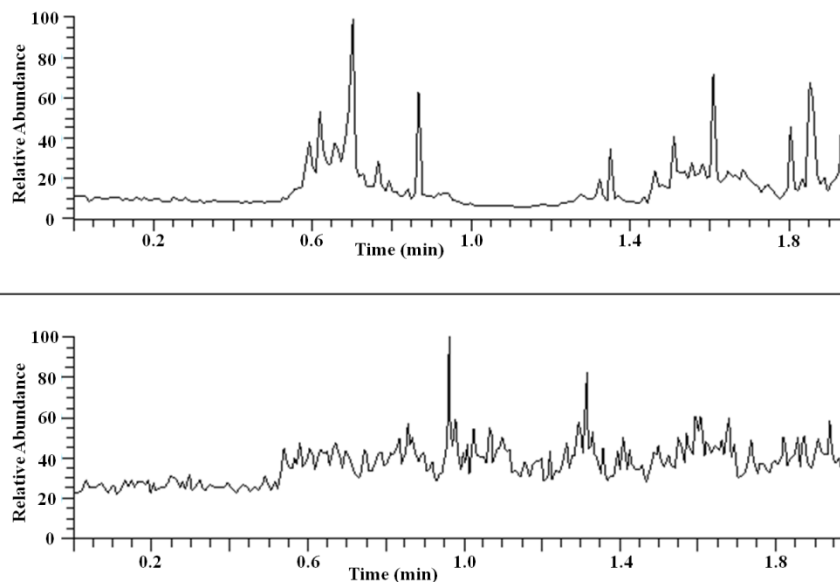


Figure 9.4 The total ion chromatogram generated upon LIAD rastering a foil prepared using the dry drop method (top) compared to a total ion chromatogram generated upon LIAD rastering a foil prepared using the drying gas chamber (bottom). The laser began firing at 0.5 minutes for both experiments; the sporadic signal is a result of variations in the sample layer uniformity. The signal in the bottom chromatogram is more consistent than in the top chromatogram, indicating that a much more uniform layer of analyte was deposited onto the foil when using the drying gas chamber (reproduced from Reference 10).



Figure 9.5 A LIAD foil prepared using forming mandrels C2 in the drying gas chamber. Brilliant green was deposited on the left side of the foil and octaethyl porphyrin was deposited on the right side (reproduced from Reference 10).

9.3 Conclusions

A LIAD foil preparation chamber was developed to deposit samples on the new rectangular foils that are required for the new raster LIAD assembly presented in Chapter 8. The chamber uses inert drying gas to evaporate solvent in order to leave a uniform analyte sample layer on the foil surface. The chamber can be used to prepare foils of both polar and nonpolar analytes, unlike electrospray deposition, and it produces a more uniform sample layer than the dry drop method. The deposition chamber also has interchangeable forming mandrels that allow for either one or two analytes to be deposited onto the surface.

9.4 References

1. Duan, P.; Qian, K.; Habicht, S.; Pinkston, D.; Fu, M.; Kenttämää, H., Analysis of Base Oil Fractions by $\text{ClMn}(\text{H}_2\text{O})^+$ Chemical Ionization Combined with Laser-Induced Acoustic Desorption/Fourier Transform Ion Cyclotron Resonance Mass Spectrometry. *Anal. Chem.* **2008**, 80, 1847-1853.
2. Pinkston, D.; Duan, P.; Gallardo, V.; Habicht, S.; Tan, X.; Qian, K.; Gray, M.; Müllen, K.; Kenttämää, H., Analysis of Asphaltenes and Asphaltene Model Compounds by Laser-Induced Acoustic Desorption/Fourier Transform Ion Cyclotron Resonance Mass Spectrometry. *Energy Fuels* **2009**, 23, 5564-5570.
3. Somuramasami, J.; Kenttämää, H., Evaluation of a Novel Approach for Peptide Sequencing: Laser-Induced Acoustic Desorption Combined with $\text{P}(\text{OCH}_3)^{2+}$ Chemical Ionization and Collision-Activated Dissociation in a Fourier Transform Ion Cyclotron Resonance Mass Spectrometer. *J. Am. Soc. Mass Spectrom.* **2007**, 18, 525-540.
4. Petzold, C.; Ramirez-Arizmendi, L.; Heidbrink, J.; Perez, J.; Kenttämää, H., Gas-Phase Reactions of Charged Phenyl Radicals with Neutral Biomolecules Evaporated by Laser-Induced Acoustic Desorption. *J. Am. Soc. Mass Spectrom.* **2002**, 13, 192-194.
5. Golovlev, V.; Allman, S.; Garrett, W.; Taranenko, N.; Chen, C., Laser-Induced Acoustic Desorption. *Int. J. Mass Spectrom. Ion Process.* **1997**, 169-170, 69-78.
6. Lindner, B., On the Desorption of Electrosprayed Organic Compounds from Supporting Metal Foils by Laser Induced Pressure Waves. *Int. J. Mass Spectrom. Ion Process.* **1991**, 103, 203-218.
7. Pérez, J.; Petzold, C.; Watkins, M.; Vaughn, W.; Kenttämää, H., Laser Desorption in Transmission Geometry Inside a Fourier-Transform Ion Cyclotron Resonance Mass Spectrometer. *J. Am. Soc. Mass Spectrom.* **1999**, 10, 1105-1110.
8. Shea, R.; Petzold, C.; Campbell, J.; Li, S.; Aaserud, D.; Kenttämää, H., Characterization of Laser-Induced Acoustic Desorption Coupled with a Fourier Transform Ion Cyclotron Resonance Mass Spectrometer. *Anal. Chem.* **2006**, 78, 6133-6139.

9. Pérez, J.; Ramírez-Arizmendi, L.; Petzold, C.; Guler, L.; Nelson, E.; Kenttämää, H., Laser-Induced Acoustic Desorption/Chemical Ionization in Fourier-Transform Ion Cyclotron Resonance Mass Spectrometry. *Int. J. Mass Spectrom.* **2000**, 198, 173-188.
10. Borton, D.; Amundson, L.; Hurt, M.; Dow, A.; Madden, J.; Simpson, G.; Kenttämää, H., Development of a High-Throughput Laser-Induced Acoustic Desorption Probe and Raster Sampling For Laser-Induced Acoustic Desorption/Atmospheric Pressure Chemical Ionization. *Anal. Chem.* **2013**, 85, 5720-5726.
11. McNeal, C.; Macfarlane, R.; Thurston, E., Thin Film Deposition by the Electrospray Method for Californium-252 Plasma Desorption Studies of Involatile Molecules. *Anal. Chem.* **1979**, 51, 2036-2039.

VITA

VITA

Matthew Robert Hurt was born in Normal, IL on May 27, 1987. While growing up he greatly enjoyed science and animals and wanted to become a zoologist. When he started taking honors chemistry his sophomore year of high school, he realized that was the subject for him. He went on to take AP chemistry his junior and decided that he wanted biochemistry to be his major in college. He graduated from Normal Community West High School in Normal, IL, in 2005, and enrolled at Northern Illinois University in Dekalb, IL as a biochemistry major. Through the course of his studies he found out that he preferred the field of analytical chemistry more than biochemistry. His senior year he conducted undergraduate research with the Dr. Ryzhov studying ion-molecule reactions in a 3D ion trap mass spectrometer. While there, he found working with mass spectrometers to be quite fascinating and became interested in furthering his education and working more with mass spectrometers in graduate school. Upon hearing this Dr. Ryzhov suggested applying to Purdue University because of its outstanding reputation in the field of mass spectrometry. In 2009, Matthew graduated *cum laude* from NIU with a B.S. in chemistry and minor in biology and enrolled at Purdue University. The summer after graduation he had the honor of presenting the work that he conducted under Dr. Ryzhov at the annual American Society of Mass Spectrometry Conference in Philadelphia. A few weeks after the conference, he arrived at Purdue University and

began his graduate career early as a summer student (or “Zero Year”) in the group of Dr. Hilikka I. Kenttämäa. He greatly enjoyed the research and the people in Dr. Kenttämäa’s and officially joined her research group later that year. The following years were mainly dedicated to graduate research; however, in 2012, he was married to Deepali Mehta, a graduate student in physical chemistry (Zwier Group), who he met his first year of graduate school. In December 2013, he earned a Ph.D. in analytical chemistry from Purdue University.